AD-A071 781 NAVAL OCEAN SYSTEMS CENTER SAN DIEGO CA F/G 4/1
PROCEEDINGS OF CONFERENCE ON ATMOSPHERIC REFRACTIVE EFFECTS ASS--ETC(U)
JUN 79 J H RICHTER
UNCLASSIFIED NOSC-TD-260 NL

1 OF 2
AD
A071781

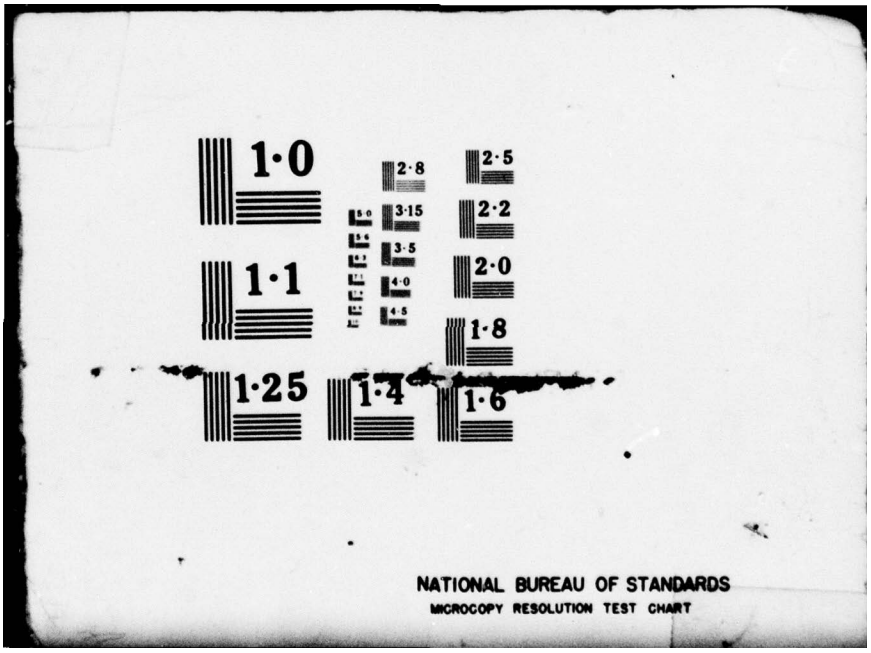
1·0
1·1
1·25
2·8
3·15
3·5
4·0
4·5
2·5
2·2
2·0
1·8
1·4
1·6
NATIONAL BUREAU OF STANDARDS
MICROCOPY RESOLUTION TEST CHART

NOSC

NOSC TD 260

NOSC TD 260

Technical Document 260

PROCEEDINGS OF CONFERENCE ON ATMOSPHERIC REFRACTIVE EFFECTS ASSESSMENT

23 — 25 January 1979, San Diego, California

JH Richter
Conference Chairman

15 June 1979

Conference Proceedings: May 1973 — January 1979

Prepared for
Naval Material Command
Code 08T24

Approved for public release; distribution unlimited

NAVAL OCEAN SYSTEMS CENTER
SAN DIEGO, CALIFORNIA 92152

NAVAL OCEAN SYSTEMS CENTER, SAN DIEGO, CA 92152

AN ACTIVITY OF THE NAVAL MATERIAL COMMAND

SL GUILLE, CAPT, USN
Commander

HL BLOOD
Technical Director

ADMINISTRATIVE INFORMATION

Work was done under 62759, ZF52551002, NCND, MP33, from May 1973 to January 1979.

Released by
JH Richter, Head
EM Propagation Division

Under authority of
JD Hightower, Head
Environmental Sciences Department

UNCLASSIFIED

SECURITY CLASSIFICATION OF THIS PAGE (When Data Entered)

REPORT DOCUMENTATION PAGE

READ INSTRUCTIONS BEFORE COMPLETING FORM

1. REPORT NUMBER
NOSC Technical Document 260 (TD 260)

2. GOVT ACCESSION NO.

3. RECIPIENT'S CATALOG NUMBER
Rept. for

4. TITLE (and Subtitle)
PROCEEDINGS OF CONFERENCE ON ATMOSPHERIC REFRACTIVE EFFECTS ASSESSMENT, 23 - 25 JANUARY 1979, SAN DIEGO, CALIFORNIA

5. TYPE OF REPORT & PERIOD COVERED
May 1973 - January 1979

6. PERFORMING ORG. REPORT NUMBER

7. AUTHOR(s)
JH Richter - Conference Chairman
Juergen H. Richter

8. CONTRACT OR GRANT NUMBER(s)
NOSC-TD-260

9. PERFORMING ORGANIZATION NAME AND ADDRESS
Naval Ocean Systems Center
San Diego, California 92152
161p.

10. PROGRAM ELEMENT, PROJECT, TASK AREA & WORK UNIT NUMBERS
62759 ZF52551002 NCND
MP33

11. CONTROLLING OFFICE NAME AND ADDRESS
Naval Material Command
Code 08T24
F52551

12. REPORT DATE
15 June 1979

13. NUMBER OF PAGES
172

14. MONITORING AGENCY NAME & ADDRESS (if different from Controlling Office)

15. SECURITY CLASS. (of this report)
Unclassified

15a. DECLASSIFICATION/DOWNGRADING SCHEDULE

16. DISTRIBUTION STATEMENT (of this Report)
Approved for public release; distribution unlimited

17. DISTRIBUTION STATEMENT (of the abstract entered in Block 20, if different from Report)

18. SUPPLEMENTARY NOTES

19. KEY WORDS (Continue on reverse side if necessary and identify by block number)
Anomalies--propagation
Ducts--propagation
Electromagnetic radiation
Radar clutter
Refraction

20. ABSTRACT (Continue on reverse side if necessary and identify by block number)
Twenty-three papers presented at the conference on atmospheric refractive effects assessment are reproduced. The papers cover the areas of Naval operations and refractive effects assessment systems; refractive effects modeling; refractivity measurement techniques and propagation measurements; and refractivity forecasting and climatologies.

DD FORM 1 JAN 73 1473 EDITION OF 1 NOV 65 IS OBSOLETE
S/N 0102-LF-014-6601

UNCLASSIFIED 393159
SECURITY CLASSIFICATION OF THIS PAGE (When Data Entered)

CONFERENCE ON ATMOSPHERIC REFRACTIVE EFFECTS ASSESSMENT

23-25 January 1979, San Diego, CA

INTRODUCTION

The effect of atmospheric refraction on shipboard radars was noticed as early as the first radars became operational toward the end of World War II. In the years following, extensive theoretical and experimental investigations led to a good qualitative understanding of the phenomenon. However, the difficulty in obtaining precise geophysical measurements and the mathematical complexity required for quantitative performance calculations prevented operational assessments of refractive effects. Between 1950 and 1970, a number of refractive effects manuals were developed which proved too cumbersome and complex for routine operational use. In recognition of the increased importance of refractive phenomena on Fleet Operations, COMTHIRDFLT arranged in May 1973 for a Navy conference on "Refractive Effects on Electromagnetic Propagation" with the purpose to review the status and to influence future direction of refractivity measurement and assessment. As a result of this meeting an ad hoc group on refractivity problems was tasked by CNO to prioritize the findings and coordinate the Navy's effort in refractive effects assessment. In November 1973, the ad hoc group recommended the development of new refractivity sensors, refractivity forecasting techniques, increased training of Navy personnel and a real-time shipboard assessment system. A little over four years have passed during which the R&D community performed work in the recommended areas. We are today at the point where a number of accomplishments produced by this effort are being used under operational conditions and an even greater number are ready for shipboard use. It seems to be appropriate and timely to bring the R&D and the Navy operational community together to review the status of refractivity assessment, to coordinate fleet implementation and to optimize usage of refractivity information.

J. H. RICHTER
Head, EM Propagation Division

ELECTROMAGNETIC PROPAGATION ASSESSMENT

Juergen H. Richter, Herbert G. Hughes, Robert B. Rose

EM Propagation Division

Naval Ocean Systems Center

San Diego, CA 92152

ABSTRACT

The concept of electromagnetic (EM) propagation assessment systems and their present status are described. Specifically, systems for ionospheric radio, tropospheric radio, and electrooptical (EO) propagation are presented. Some of the sensing requirements of geophysical input parameters are discussed.

1. INTRODUCTION

Any system which relies on propagation of electromagnetic including electrooptic waves in the earth's environment is to some extent propagation limited. There are a number of examples. Solar disturbances affecting the ionosphere can result in complete disruption of the Navy's vital high frequency (hf) communications and surveillance network. Refractive layers in the lower atmosphere can cause "holes" in shipboard radar coverage. Oceanic ducting phenomena may be exploited for over-the-horizon detection capabilities. Aerosols (clouds) are often the limiting factors in electrooptical systems. A mere qualitative understanding of atmospheric effects on EM/EO propagation is not sufficient for optimum deployment of military systems. Therefore, the concept of real-time assessment systems useable under operational conditions has been developed. These systems are based on mini- or microcomputers with interactive graphic displays providing quantitative performance data for specific equipments and geometries under existing and, potentially, also forecast geophysical conditions. The status of assessment systems for ionospheric radio, tropospheric radio and EO propagation and sensing requirements of geophysical input parameters are discussed.

2. PROPAGATION ASSESSMENT SYSTEMS

Independent of the location within the frequency spectrum and the specific application (e.g. surveillance, communications, navigation, etc.) all propagation assessment systems share some basic features. All deal with the geophysical environment; all require a careful analysis of the sensitivity of the systems addressed to environmental parameters (which in turn defines geophysical sensing requirements); all require verified models which relate environmental conditions to systems performance; all need carefully planned operational implementations involving optimum hardware selection, man-machine interface questions, optimum displays, interface with other existing or planned equipment; and, finally, all have to demonstrate that they are affordable by either proving a quantitative pay-off through actual savings or by showing increased tactical or strategic capabilities. In recognition of the commonality of these basic features, the Navy has established an exploratory development program in "Atmospheric Effects on EM/EO Propagation" which is managed by the Naval Ocean Systems Center. A significant portion of the

Frequency Band / Implementation	Ionospheric Radio Propagation	Tropospheric Radio Propagation	EO Propagation
Exploratory Development Assessment System	PROPHET	IREPS	PREOS
Interim Operational Implementation	PROPHET CLASSIC PROPHET FOTACS	Interim E/WEPS	
Operational	Frequency Management	E/WEPS (SESC)	E/WEPS (SESC)

Table 1. Status and Plans for EM/EO Assessment Systems

effort under this program is in support of a family of assessment systems listed in Table 1 (Richter, et al., 1979). In the area of ionospheric radio propagation the PROPHET (pseudoacronym for propagation forecasting terminal) system (Richter, Rothmuller, Rose, 1977) has demonstrated its utility in initial deployments at a Naval Communications Station. CLASSIC PROPHET is a smaller desk top calculator version specifically geared to tactical applications. A limited, non real-time propagation assessment capability has been incorporated into FOTACS (Fleet Operational Telecommunications Automated Control System, Caldwell, 1978) which shortly will be installed in all Navy CAMS (Communications Area Master Station). FOTACS is a forerunner for a comprehensive frequency management system which should include all present and planned PROPHET capabilities.

In the area of tropospheric radio propagation, the Integrated Refractive Effects Prediction System (IREPS) (Richter and Hitney, 1977) has undergone further development and a smaller version using a desk top calculator has been made available. This represents an interim version of an Environment/Weapons Effects Prediction System (E/WEPS). The operational implementation of E/WEPS may be in the frame of a Shipboard Environmental Support Center (SESC) which includes meteorological information and displays (e.g. the Naval Environmental Display Station or NEDS) and underwater acoustic propagation assessment.

3. IONOSPHERIC RADIO PROPAGATION ASSESSMENT

Radio propagation in the frequency range below approximately 50 MHz is dependent on ionospheric conditions. The composition and structure of the ionosphere is primarily influenced by solar emissions and is quite predictable if those emissions remain constant. However, during solar disturbances, ionospheric conditions change so that communication links may be interrupted, surveillance systems may be rendered useless and navigation systems may be grossly inaccurate (Rose, et al., 1971). The space environmental processes affecting ionospheric propagation are quite complex and an extensive numerical computational capability is required for the quantitative assessment of communications or surveillance ranges and navigation corrections. To accomplish this task, a propagation assessment and forecasting terminal (PROPHET) has been developed which accepts space environmental data from a variety of sensors and provides, real-time, quantitative data of systems performance under operational conditions. The various emissions during a solar flare and their effects on the ionosphere are schematically indicated in Figure 1. Ultraviolet and x-ray radiation reach the ionosphere a few minutes after the eruption of a flare and cause increased D-layer ionization with resulting increased absorption for hf frequencies. With a delay of up to several hours high energy protons and α-particles also cause increased D-layer ionization and resulting hf absorption, mostly in the polar regions, which is the reason that this phenomenon is called polar cap absorption (PCA). One or two days after a flare, low energy plasma reaches the ionosphere causing magnetic storms, aurorae, increased D-layer ionization and enhanced ionization in the E-layer of the ionosphere (sporadic E). All the solar flare emissions need to be known if one wants to calculate and forecast their effects on the ionosphere and the resulting communication, surveillance, electronic warfare, or navigation systems performance. However, most of the radiation or particles never reach the surface of the earth; they have to be measured before they are absorbed in the ionosphere. This is being done by

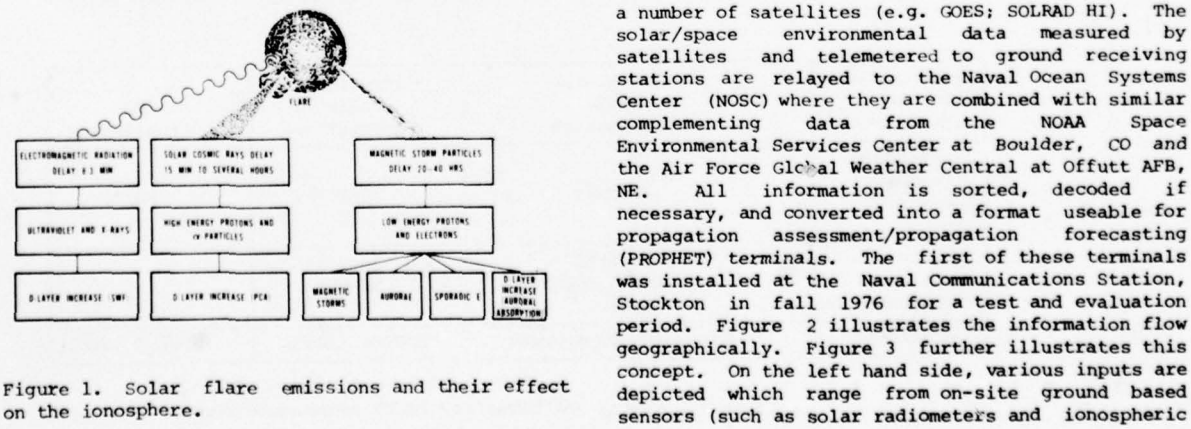

FLARE EMISSIONS AND IONOSPHERE EFFECTS

Figure 1. Solar flare emissions and their effect on the ionosphere.

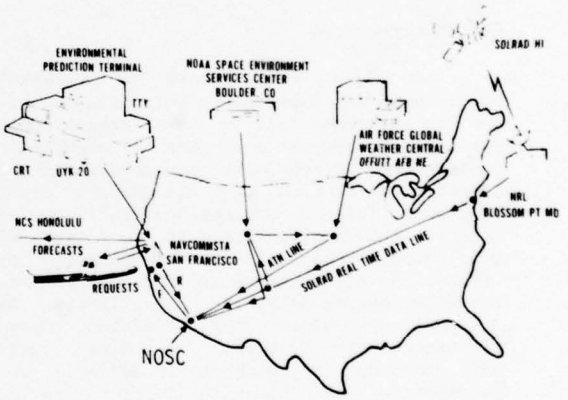

Figure 2. Information flow for the PROPHET environmental prediction terminal.

a number of satellites (e.g. GOES; SOLRAD HI). The solar/space environmental data measured by satellites and telemetered to ground receiving stations are relayed to the Naval Ocean Systems Center (NOSC) where they are combined with similar complementing data from the NOAA Space Environmental Services Center at Boulder, CO and the Air Force Global Weather Central at Offutt AFB, NE. All information is sorted, decoded if necessary, and converted into a format useable for propagation assessment/propagation forecasting (PROPHET) terminals. The first of these terminals was installed at the Naval Communications Station, Stockton in fall 1976 for a test and evaluation period. Figure 2 illustrates the information flow geographically. Figure 3 further illustrates this concept. On the left hand side, various inputs are depicted which range from on-site ground based sensors (such as solar radiometers and ionospheric

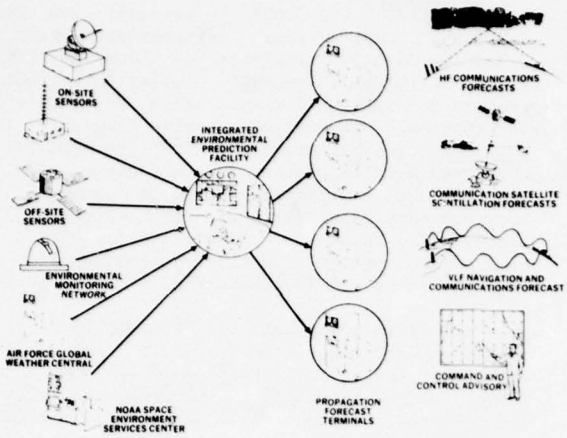

Figure 3. PROPHET: information flow and products.

sounders), to satellite sensors, as well as data and support from the Air Force and NOAA. The input data are sorted, converted and relayed to various propagation forecast terminals. On the right hand side of Figure 3 a few applications are illustrated. They cover hf and vlf communications, ionospheric scintillations affecting satellite communication, vlf navigation, command and control advisory, and many others. A PROPHET terminal itself consists of a stand alone minicomputer system with an interactive graphic display and a hard copy unit. The minicomputer used is a AN/UYK-20 supported by two magnetic tape drives. An additional input/output capability is provided by a teletype and paper tape reader/punch.

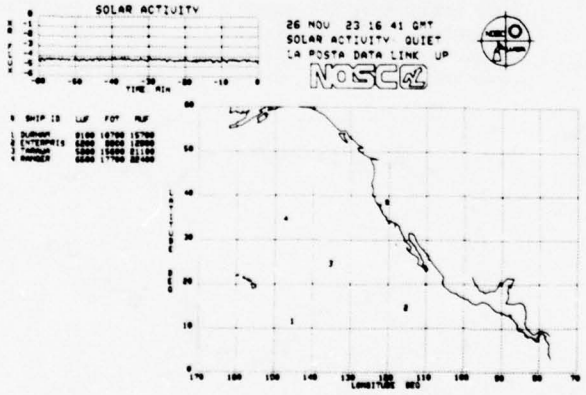

Figure 4. PROPHET display of hf propagation between Naval Communications Station (asterisk at 121°W, 38°N) and various ships.

One major objective in the development of the PROPHET products was simplicity in presentation and ease in operation and understanding. Figure 4 is an example of how these objectives were met. On the graphic display a map appears of the area of concern for the communications controller. For the Naval Communications Station at Stockton (shown by an asterisk in the map) this is the eastern Pacific. At the upper left hand corner a smaller graph is displayed and labeled SOLAR ACTIVITY. This graph displays the solar 1-8Å x-ray flux received during the past hour. The communications controller enters the geographic coordinates of the ships with which he wants to communicate. After he has done this, the ships' position and their names appear on the map including the frequency band which can be used based on the real time space environmental data stream input into PROPHET. From this display, the communications controller can see that he has to use a frequency between 6.2-12.9 MHz in order to communicate with the ship Enterprise. The frequency of optimum transmission (FOT) is 8.8 MHz. The map and its information is updated every few minutes. The information shown in Figure 4 may also be displayed in tabular form, as shown in Figure 5, which is a useful presentation when many communication circuits are being controlled at once.

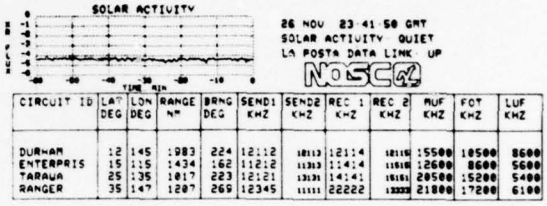

CIRCUIT ID	LAT DEG	LON DEG	RANGE NM	BRNG DEG	SEND1 KHZ	SEND2 KHZ	REC 1 KHZ	REC 2 KHZ	MUF KHZ	FOT KHZ	LUF KHZ
DURHAM	12	145	1983	224	12112	12113	12114	12115	15500	10500	8600
ENTERPRIS	15	115	1434	162	11212	11313	11414	11515	12600	8600	5600
TARAWA	25	135	1017	223	12121	13131	14141	15151	20500	15200	5400
RANGER	35	147	1207	269	12345	11111	22222	33333	21800	17200	6100

Figure 5. Tabular presentation of the information in Figure 4.

A very important PROPHET capability is the ability to produce ray traces which depict the path of the electromagnetic wave fronts. Figure 6 is an example of a ray trace diagram over a 3000 km path. A number of important propagation features are evident from this presentation. No communications are possible for ranges out to approximately 1250 km. This so-called skip zone may be of advantage if an unwanted receiver is located within this range. Focusing, i.e. several rays are concentrated in a small area, occurs between 1250-1350 km and, because of the different travel times of the rays, signal degradation through interference may be expected. A similar

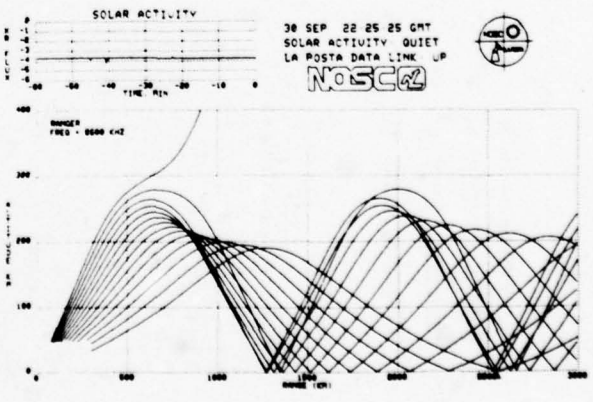

Figure 6. PROPHET ray trace presentation.

interference must be expected at larger ranges (2500-2700) where rays deflected once from the ionosphere and rays deflected twice (after being reflected from the ocean's surface) are superimposed. Another application of the ray trace picture is the selection of specific antennas having launch angles favoring desired rays and suppressing undesired rays for a particular optimum coverage situation.

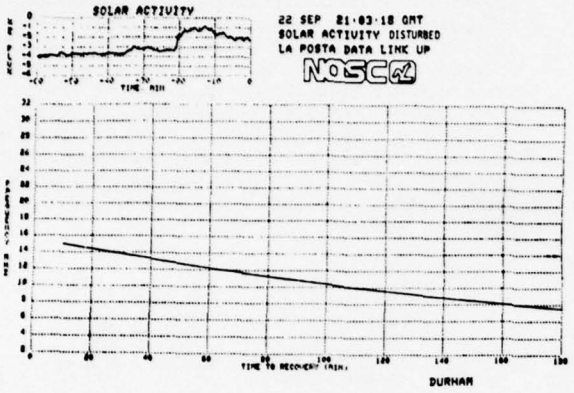

Figure 7. LOF recovery prediction for a solar flare event.

The correlation between 1-8Å x-ray flux and the lowest observed frequency (LOF) led to the development of an empirical model which permits the prediction of the LOF as soon as the peak x-ray flux has been reached (Rose, et al., 1974). This capability has important implications. Figure 7 is an example of a high x-ray flux associated with a flare which has stabilized in the last few minutes. If for instance a communications path had been operated prior to the flare at a frequency of 6 MHz, then it would take over three hours until communication could be resumed at this frequency. If, however, the frequency would be changed to 15 MHz, communications could be re-established in only a few minutes. The recognition that a solar flare (and not equipment failure) was the cause of the communications blackout and the knowledge of when to resume communications as a function of frequency is of critical operational importance.

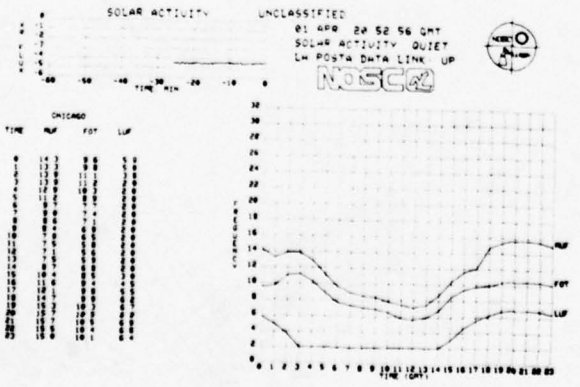

Figure 8. Propagation link performance prediction for undisturbed ionospheric conditions.

Finally, the PROPHET terminal has stored extensive statistical information which is otherwise usually available in look up tables. Figure 8 shows a PROPHET display of predicted propagation link performance based on statistical information. The maximum useable frequency (MUF), the lowest useable frequency (LUF) and the FOT are displayed both in tabular form and graphically for the particular propagation path of concern. It is believed that easy retrieval of information from large data bases and the simplification of bookkeeping chores frees the operator for more creative tasks and increases his or her efficiency.

The primary emphasis with PROPHET has been on hf communications. Even though hf communications represents only a small portion of the Navy's total communications capability, the need for accurate propagation assessment will increase in the future for several reasons. First, it can be shown that sizeable electric power consumption savings can be achieved by radiating optimum power levels for respective propagation conditions and providing area coverage without redundant transmitters. Both can be done with accurate, real-time propagation assessment information. Secondly, the lesser use of the hf spectrum reduces the available number of qualified operators having long experience and good understanding of propagation phenomena. Again, PROPHET can replace this capability. Thirdly, any further reduction in available frequencies in the hf spectrum and transmission facilities will require a more efficient management of the available resources which can be achieved only by a PROPHET concept.

Besides the hf communications aspects, another potentially very important capability has been incorporated into PROPHET for correcting the Omega navigation system under disturbances of the polar ionospheres (for so-called Polar Cap Absorptions or PCAs caused by particles emitted from the sun and concentrated by the earth's magnetic field around the poles). An example of a resulting position error is shown in Figure 9 in which the actual position may be in error by as much as 7-8 nmi.

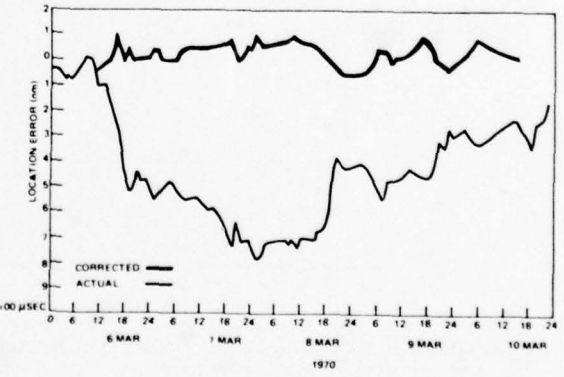

Figure 9. Omega location error for a PCA with and without corrections.

Models have been developed (Argo, 1975) and implemented into PROPHET which correct for these disturbances so that Omega retains its specified accuracy of ±1 nmi. The particular example in Figure 9 is based on hyperbolic ranging using the

Omega stations in Norway and Hawaii. It should be pointed out that disturbances of this kind can last for days. Figure 10 shows the oceanic areas affected by a PCA and the corrective measures required. This kind of a correction may become of increased importance should commercial air carriers replace expensive inertial navigation systems with much cheaper Omega receivers. Densely traveled routes (like the North Atlantic) most certainly require corrective measures.

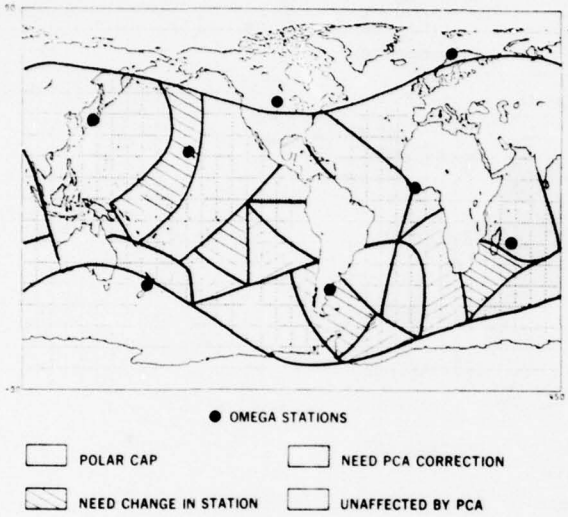

Figure 10. PCA effects on Omega coverage for oceanic areas.

A special version of PROPHET called CLASSIC PROPHET (Rose, 1976; Rose and Martin, 1977; Rose, Martin and Levine, 1978) has been developed for tactical applications using a graphics capable desk top calculator (Tektronix 4051). Figure 11 shows the information flow and examples of presentations. Unlike PROPHET which receives real-time satellite sensed environmental data, CLASSIC PROPHET requires manual input of this information. Examples of CLASSIC PROPHET products are shown on the bottom of Figure 11. For example, on the left side a display shows the hf bands that can be received by a number of stations for a given transmitter location. This information can be readily used to select a transmission frequency to eliminate or minimize reception by unwanted receivers. The other two displays on the bottom of Figure 11 show bearing quality (variance of bearing angle for direction finding) on the ordinate versus time and frequency respectively. These displays may be used to select either times of transmission or frequencies that result in either poor to good fixes for direction finding applications. Initial operational use of CLASSIC PROPHET systems has convincingly demonstrated the excellent utility of such systems.

The eventual capability and configuration of the PROPHET concept has not been fully defined yet and will strongly depend on further test and evaluations in an operational environment. Table 2 lists the models, their application, their purpose and status for FOTACS, the present PROPHET and its future version. Present plans call for the deployment of three units and a test and evaluation period of approximately three years. At the end of this period decisions will be made as to which models listed in Table 2 will be made in a final operational implementation which will be part of a frequency management system.

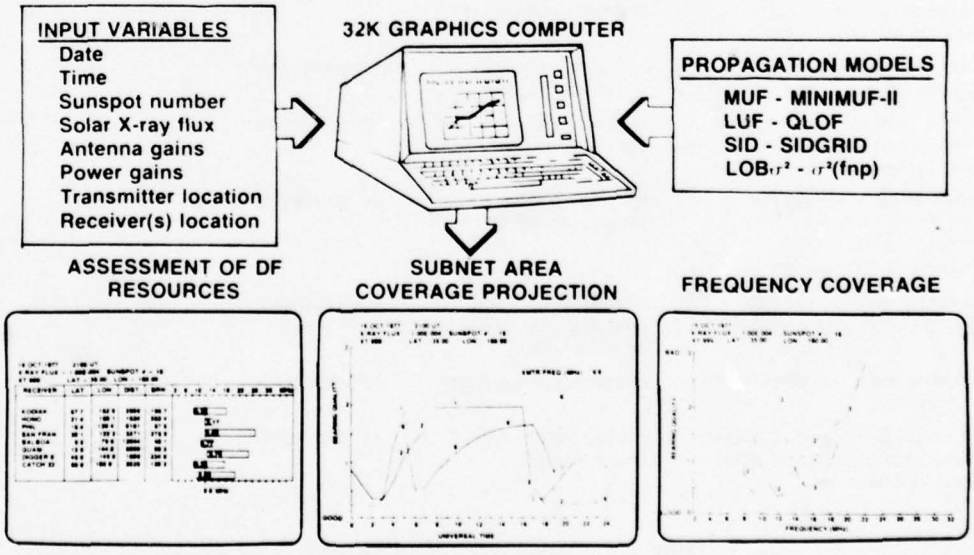

Figure 11. CLASSIC PROPHET information flow and displays.

Model	System	Action	Status	FOTACS	Pres. PROPHET	Future PROPHET
Flare detection	all hf, vlf navigation and comm	Warning	operational		X	X
Flare detection	all hf, vlf nav/comm	hf comm-freq shift reroute traffic	operational		X	X
SID GRID	all hf	hf comm freq shift reroute traffic	operational	X	X	X
SPA/vlf	vlf nav Omega	phase correction factor	developed			X
SPA inversion	all hf, vlf	estimate x-ray flare size (independent of satellite) feed sid grid	in progress			X
PCA/vlf	vlf navig	phase correction factor for transpolar circuits	developed			X
PCA/hf	all polar hf	hf comm-advice signal strength loss-freq shift	developed			X
PCA/vhf	all polar satellite	vhf comm-advice signal loss	developed			X
QLOF	all hf	hf comm-normal operations, freq management	operational	X	X	X
LOF split	covert hf systems	opt freq selection against known rcvrs	operational			X
MINIMUF	all hf	hf comm-normal ops freq. management	operational	X	X	X
15 min update to MINIMUF using auroral E fields	all hf	correct MUF est. (real time) minimize errors (to < 1 MHz est) (feeds MINIMUF)				X
Raytrace	all hf	hf comm-normal ops. antenna selection	operational		X	X
Launch angle multipath using quasi parabolic	all hf	hf comm-normal ops. antenna selection	near completion			X
Polar and auroral ionosphere	all hf vhf satellite	hf comm, auroral & polar circuits	in progress			X
Earth's magnetic field variations (ground)	ASW & any magnetically sensitive	corrections for field changes	in progress			X
Mixing Shock front from auroral disturbances	all hf	hf comm-midlatitude (feeds MINIMUF)	in progress			X
Scintillation grid	vhf/uhf satellite comm	advisory-dB fade probability based on location	operational	X	X	X
Omega correction factors	Omega vlf	correction factors	operational		X	X
DMSP topside sounder ionospheric updates	hf & satellite comm	correct MUF est. (real time)	in conception			X

Table 2. Present and Future PROPHET Capabilities

4. TROPOSPHERIC RADIO PROPAGATION ASSESSMENT

Non-standard variations in the vertical distribution of water vapor (and to a lesser degree of temperature and pressure) may result in atmospheric layers which refract electromagnetic waves, thereby altering their expected propagation paths. This phenomenon is schematically illustrated in Figure 12. The waves emanating from a shipboard radar are refracted by a layer in such a way that an area above the layer may be illuminated insufficiently for the detection of an airborne target thereby creating a "hole" in radar coverage. At the same time, energy may be ducted beyond the horizon and be intercepted at unexpectedly distant ranges. A propagation

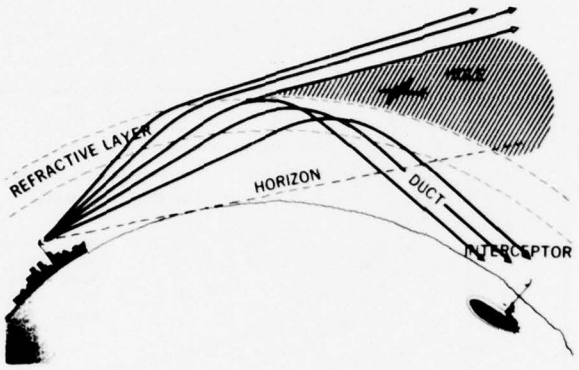

Figure 12. Schematic presentation of the effects a refractive layer may have on a shipboard radar.

assessment system for real-time shipboard assessment of these phenomena has been developed and is known as the Integrated Refractive Effects Prediction System (IREPS) (Hitney and Richter, 1976; Hitney and Richter, 1977; Richter and Hitney, 1977).

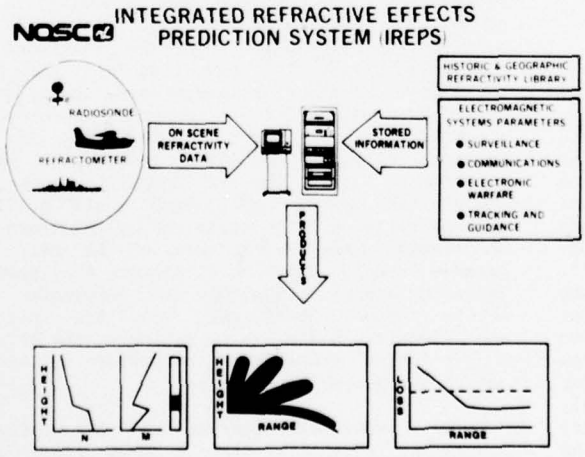

Figure 13. Block diagram of IREPS information flow and products.

Figure 13 shows a block diagram of the IREPS information flow. A stand alone minicomputer system with an interactive graphic display accepts environmental information from meteorological balloons (radiosonde), aircraft mounted refractometers, and surface observations. Stored in the computer are the parameters of the surveillance, communications, electronic warfare, and weapons systems of concern. In addition, extensive climatological data are stored which permit a statistical assessment of refractive conditions as a function of geographic area and season. With this information, IREPS provides a number of products which are designed to be easily understood and immediately useful to the operator. A detailed description of IREPS, its present and future capabilities are given in a companion paper by Hitney (1979) and shall, therefore, not be discussed any further in this paper.

5. ELECTROOPTICAL PROPAGATION ASSESSMENT

A significant concentrated and coordinated effort has started within the Navy to assess the performance of electrooptical systems. Table 3 lists examples of EO systems and the reasons for which they are attractive to the Navy. The special capabilities offered for the various applications in Table 3 have to be weighed against the serious performance degradations that EO systems may experience as a result of changing environmental conditions. A Navy wide coordinated effort for EO systems performance has been described by Schefer (1977). Additional coordination and guidance has since been provided. Specifically, the Under Secretary of Defense for Research and Engineering has formulated six goals to be followed by the three different services (Army, Navy, Air Force). The goals are:

- Relate atmospheric transmission effects to sensor system performance.

- Accurately model the propagation effects of naturally-occurring and man-made aerosols.

- Relate the production, transport, and dissipation of naturally-occurring aerosols to measurable or predictable meteorological parameters.

- Accurately model the propagation effects of atmospheric molecular absorption.

- Assess the performance of weapons systems based on validated propagation models applied to historical or derived standard meteorological measurements or models.

- Develop atmospheric sensor systems to support EO systems operations.

The fundamental nature of these goals reflects the fact that much of the basic knowledge in the area of EO propagation is still missing. This coupled with the fact that there are presently no operational shipboard EO systems in the Navy results in a different emphasis on EO assessment system development than for the systems previously described. Consequently the major emphasis is presently on development and verification of models, sensitivity analyses, and sensor development.

APPLICATION	CAPABILITY
IMAGING (e.g. low light level television, forward looking infrared system) SEARCH AND TRACK (e.g. infrared search and track system)	passive surveillance (covertness), night vision, high resolution
RANGING (e.g. laser range finder) DESIGNATING (e.g. laser designator)	high pointing accuracy
COMMUNICATIONS (e.g. ship to ship, ship or satellite to submarine communication system)	covertness, water penetration

Table 3. EO Systems of Navy Interest

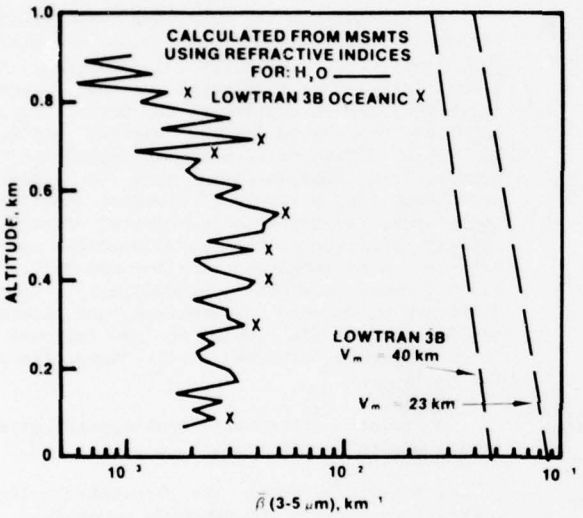

Figure 14. Aerosol extinction coefficient variations with altitude based on measured dropsize distributions and on LOWTRAN 3B.

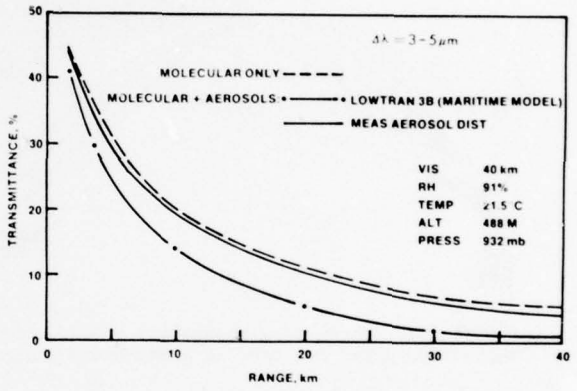

Figure 15. Transmission versus range calculations.

Of the atmospheric parameters affecting EO propagation (e.g. aerosols, molecular absorption, turbulence, refraction) aerosols extinction is the key problem in the Navy's EO propagation program. For example, in Figure 14 the aerosol extinction coefficient for the 3-5 μm band is plotted as a function of altitude. The solid line is calculated from dropsize distribution measurements obtained with a light scattering spectrometer (PMS ASSP-100) flown on an aircraft (Snyder and Hughes, 1978). The aerosol refractive index was assumed to be pure water. (The crosses indicate calculations for selected altitudes using the oceanic refractive index of LOWTRAN 3B.) The dashed curves are the average aerosol extinctions based on LOWTRAN 3B for visibilities of 23 and 40 km respectively representing the range of reported visibility conditions. The extinction values based on LOWTRAN 3B decrease exponentially with height while the extinction calculated from aerosol measurements shows a slight increase with altitude up to height of the convectively mixed layer (approximately 600 m) and a decrease above. The extinction calculated from LOWTRAN 3B is more than an order of magnitude greater than the extinction calculated from the measurements. To estimate what this means in terms of systems performance, transmittance was plotted against range in Figure 15 for the distributions in Figure 14. Figure 15 shows that for longer ranges there might be a serious underestimation of systems performance using the reported meteorological visibility as an input to LOWTRAN. If, for example, a value of 10% transmittance was the performance limit for a specific system, the calculations based on LOWTRAN would predict a maximum range of 14 km while the calculations based on aerosol measurements predict 22 km. This example should serve to illustrate the need for improved transmission models (in particular their marine aerosol portions) and the kind of considerations necessary to estimate the effect of a particular atmospheric parameter or modeling aspect on systems performance.

Of particular concern to a performance assessment capability for a broad range of EO systems is the number of measurements at different wavelengths necessary to characterize the entire frequency spectrum of interest (usually the visible and infrared region). Theoretical considerations

and experimental data showed correlations between the total liquid water content and extinction and subsequently the possibility of scaling aerosol extinction at one wavelength to that of another (Biberman, Roberts and Seekamp, 1977). This kind of scaling was tested for marine aerosols by Hughes and Jensen (1978) and one of the results is shown in Figure 16. A reasonable straightline correlation (in a log-log presentation) between the aerosol extinction coefficients calculated from dropsize distribution measurements between 3.5 and 10.6 μm is evident in two categories: poor and good visibilities. The dropsize spectrometer used for these data could not measure particle radii in excess of 14.7 μm. Since the aerosol measurements

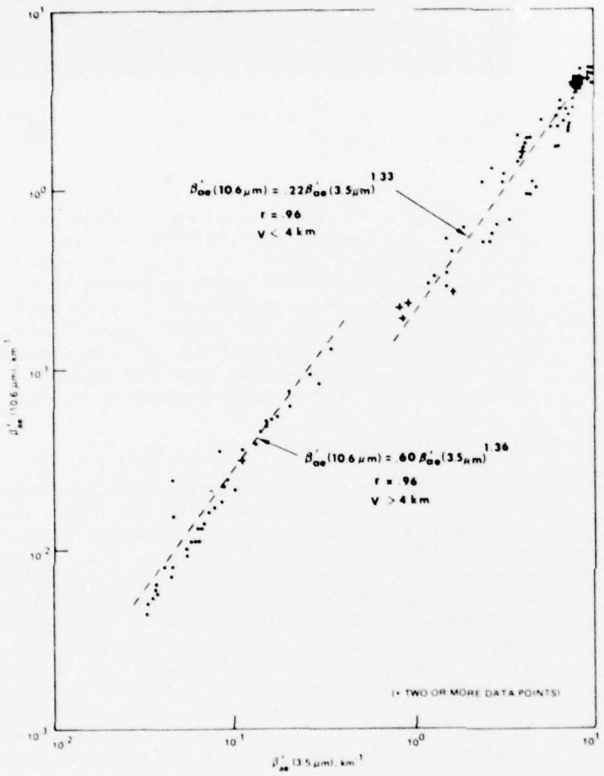

Figure 16. Calculated aerosol extinction coefficients β_{ae} for 10.6 μm vs. those for 3.5 μm.

for better visibilities (v > 4 km) did not show particles with radii in excess of 10 μm one can assume that larger particles did not play a significant role. However, for the poor visibilities (v < 4 km) particles were measured in the largest size range and one can assume that the truncation of the distribution (by the inability to measure larger particles) would affect the results. To check this assumption the aerosol distributions for visibility ranges of less than 4 km were extrapolated to contain aerosols with maximum radii r_2 of 20, 25, and 30 μm respectively. Figure 17 shows the result of this extrapolation which causes the two regression lines to become more in agreement. The development of these scaling laws is clearly encouraging even though a number of questions need to be investigated such as aerosol refractive index changes for different air masses.

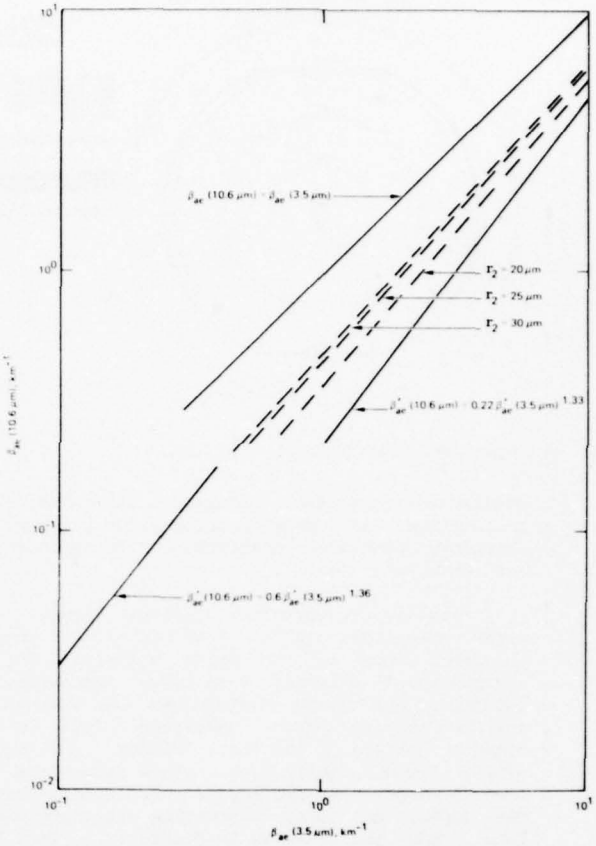

Figure 17. Increased extinction coefficients (dashed lines) for 10.6 μm vs. those at 3.5 μm for increased particle radii as indicated and compared with the regression analysis in Figure 16.

The primary effort on the development of shipboard real-time assessment system called PREOS (for prediction of performance and range for EO systems) centers presently on the selection of proper transmission models and their tailoring and incorporation into suitable hardware. The hardware is defined by E/WEPS of which PREOS is one building block. Since, as previously pointed out, there are presently no operational shipboard EO systems in the Navy, important applications of available PREOS capabilities are sensitivity analyses studies and systems performance simulation.

An example of what a PREOS display might provide is shown in Figure 18. After the operator has supplied environmental input data (such as visibility, scene luminance, etc.) and specified the system to be assessed (low light level television in this example) PREOS might give a range contour of detecting a specific target (in this case an aircraft carrier) as a function of aspect angle. This information is useful in determining ranges within which a target is safe from detection or conversely is likely to be detected. A very important tactical application of propagation assessment systems is in trade-off decisions. Various active and passive detection and intercept techniques based on electromagnetic, electrooptic or acoustic measures are or will be

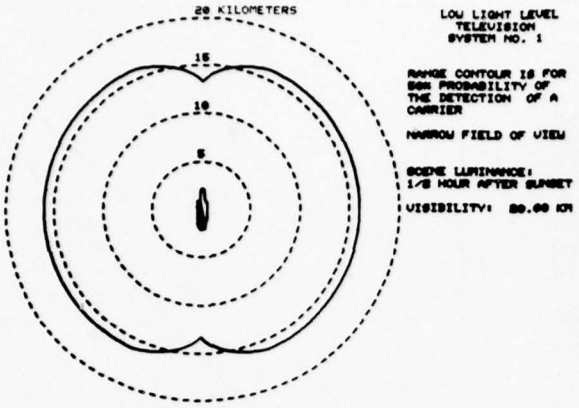

Figure 18. PREOS sample display.

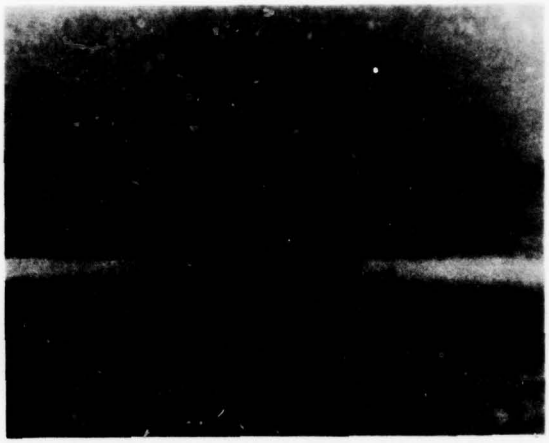

Figure 20. Photograph of a surface ship distorted by refractive layers.

available to the ship's commander. A comprehensive propagation assessment capability can provide the necessary quantitative information to optimize all available resources.

Finally, frequently observed mirages over ocean areas led to an investigation of ducting phenomena close to the water surface. The two questions of interest were range extensions or reductions and image distortions for visible and infrared imaging systems operating close to the ocean's surface. Feinberg, Hitney and Hughes (1978) found significant range reductions for 10.6 μm propagation for superadiabatic lapse rates. One aspect of image distortion was incorporated into PREOS and is shown in Figure 19. The left side of this figure shows temperature T and modified refractivity M as a function of height. The object's contour has to be supplied to PREOS which will then provide an expected image for refractivity conditions encountered (based on ray tracing techniques). In the case of Figure 19 an isothermal temperature profile was assumed to extend from the surface to a height of 15 m which is the base of a 4° temperature inversion extending to a height of 20 m. Situations like this are not uncommon in the Southern California offshore area during Santa Ana conditions (dry desert air, heated additionally by subsidence, and advected over the ocean). Figure 20 shows a photograph of a surface ship during a Santa Ana occurrence during which the base of the temperature inversion was measured to be as low as 10 m above sea level. The similarity of the image provided by PREOS in Figure 19 and an observed example shown in Figure 20 is striking. An important aspect of the PREOS capability shown in Figure 19 is the possibility of reconstructing the object's true contours from a distorted image if the vertical refractivity profile is known.

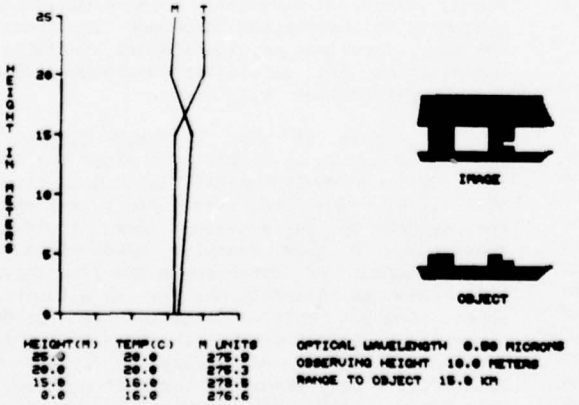

Figure 19. Image distortion analysis caused by refractive layers.

6. CONCLUSIONS

It has been demonstrated that propagation assessment systems are feasible and have proven very effective to the operational users. Their pay off reaches from actual savings, to improved understanding of sensor performance, optimization of resource allocation, and tactical exploitation of propagation phenomena. The major question is no longer if propagation assessment will be part of Naval operations but rather how to combine, integrate and implement various assessment capabilities for optimum operational utilization. In the area of ionospheric propagation a comprehensive frequency management system appears to be the proper host for real-time propagation assessment. Tropospheric radio propagation, electrooptical propagation, perhaps underwater acoustics propagation, may be best combined with oceanographic and meteorological data in a shipboard environmental support center.

7. REFERENCES

Argo, P. E., 1975: Modeling Omega PCA Phase Advances, Naval Electronics Laboratory Center Technical Report 1950.

Biberman, L. M., R. E. Roberts and L. N. Seekamp, 1977: A Comparison of Electrooptical Technologies for Target Acquisition and Guidance; part 2: Analysis of the Grafenwoehr Atmospheric Transmission Data, Institute for Defense Analysis Paper P-1218.

Caldwell, J. F., 1978: Fleet Operational Telecommunications Automated Control System (FOTACS): System Description, Naval Ocean Systems Center Technical Note 551.

Feinberg, R., H. V. Hitney and H. G. Hughes, 1978: Marine Boundary Layer Effects in the Infrared, Naval Ocean Systems Center Technical Note 555.

Hitney, H. V. and J. H. Richter, 1976: Integrated Refractive Effects Prediction System (IREPS), Naval Engineers Journal, p. 257-262.

Hitney, H. V. and J. H. Richter, 1977: Integrated Refractive Effects Prediction System (IREPS), Proceedings of URSI Commission F. Open Symposium on Propagation in Non-Ionized Media, La Baule, France, April 28-May 6.

Hitney, H. V., 1979: Integrated Refractive Effects Prediction System (IREPS) and Environment/Weapons Effects Prediction System (E/WEPS), Proceedings of the Atmospheric Refractive Effects Assessment Conference, Naval Ocean Systems Center (in press).

Hughes, H. G. and D. R. Jensen, 1978: Extinction of IR Wavelengths by Aerosols in Coastal Fog, Applied Optics, 17, 2138-2140.

Richter, J. H. and H. V. Hitney, 1977: IREPS: A Refractive Effects Assessment System, Proc. 7th Technical Exchange Conference, El Paso, TX. Published by ASL, WSMR, NM 88002, pp 72-76.

Richter, J. H., I. J. Rothmuller, and R. B. Rose, 1977: PROPHET: Real Time Propagation Forecasting Terminal, Proc. 7th Technical Exchange Conference, El Paso, TX. Published by ASL, WSMR, NM 88002, pp 77-81.

Richter, J. H., H. V. Hitney, H. G. Hughes and R. B. Rose, 1979: Electromagnetic Propagation Assessment, Proc. 8th Technical Exchange Conference, Colorado Springs, CO. Published by Dept. of the Air Force, Headquarters Air Weather Service, Scott AFB, IL 62225.

Rose, R. B., D. G. Morfitt, and M. P. Bleiweiss, 1971: System Performance Degradation Due to Varying Solar Emission Activity: SOLRAD Applications Study - Task II, Naval Electronics Laboratory Center Technical Report 1774.

Rose, R. B., J. R. Hill and M. P. Bleiweiss, 1974: Sudden Ionospheric Disturbance Grid, Naval Electronics Laboratory Center Technical Report 1938.

Rose, R. B., 1976: Tactical Applications of HF Skywave Propagation Forecasts, part II, Naval Electronics Laboratory Center Technical Note 3212.

Rose, R. B. and J. N. Martin, 1977: Estimated *HFDF* Propagation Error Based upon the Position of the Operating Frequency in the Propagation Bandwidth, Naval Ocean Systems Center Technical Note 182.

Rose, R. B., J. N. Martin and P. H. Levine, 1978: MINIMUF-3: A Simplified HF MUF Prediction Algorithm, Naval Ocean Systems Center Technical Report 186.

Schefer, M. H., 1977: The Proposed Navy Exploratory Development Electrooptical Meteorology Project, Proc. 7th Technical Exchange Conference, El Paso, TX. Published by ASL, WSMR, NM 88002, pp 178-183.

Snyder, F. P. and H. G. Hughes, 1978: Aerosol Distributions with Altitude at Sea for High Visibilities - A Case Study, Naval Ocean Systems Center Technical Note 537.

INTEGRATED REFRACTIVE EFFECTS PREDICTION SYSTEM (IREPS) AND ENVIRONMENT/WEAPONS EFFECTS PREDICTION SYSTEM (E/WEPS)

Herbert V. Hitney
Naval Ocean Systems Center
EM Propagation Division
San Diego, CA 92152

ABSTRACT

IREPS (the Integrated Refractive Effects Prediction System) has been under exploratory development at NOSC since 1974. An advanced development program has started to develop the E/WEPS (the Environment/Weapons Effects Prediction System). A review of the current status of IREPS and its continuing development as a software module of E/WEPS will be presented. Recently developed IREPS displays will be shown and discussed relative to their intended tactical uses, especially for carrier applications. The E/WEPS RDT&E program, as currently envisioned, consists of a near-term interim assessment capability based on the Hewlett-Packard Model 9845 programmable calculator (PROCAL) and a final fully militarized advanced development model (ADM) assessment system. The program to deploy the interim PROCALs and work with the carrier and air wing personnel to further refine the assessment capabilities of E/WEPS will be discussed. The relationship of the interim E/WEPS to the final ADM E/WEPS will also be presented. Finally, the development plans for the ADM E/WEPS will be discussed and will include consolidation of the Naval Environmental Display Station (NEDS) with E/WEPS and other environmental support functions to form a proposed Shipboard Environmental Support Center (SESC). Also considerations of life-cycle costs, degree of militarization and standardization required, test and evaluation, and logistics support requirements will be presented.

1. INTRODUCTION

It has long been recognized that anomalous distributions of temperature and humidity in the lower atmosphere can be responsible for significant changes in electromagnetic (EM) wave propagation and the resulting enhancement or degradation of naval sensor and weapons systems. Such anomalous propagation effects were first seriously studied during and immediately after World War II and many of these studies are summarized in Kerr (1951). During recent years numerous computational algorithms have been developed that have allowed a near-real time atmospheric refractive effects assessment system to be developed. IREPS has been under development at NOSC since 1974 and continues to be developed and refined. The basic IREPS system is described by Hitney and Richter (1976) and is based on mathematical models developed by several investigators. IREPS has been an exploratory development (category 6.2 RDT&E) project that has resulted in successful demonstration of the concept of on-board assessment systems. Because of the success of the exploratory development program, an advanced development program (category 6.3 RDT&E) was begun in 1978 to specify and develop militarized hardware to host the assessment system's software. This militarized hardware is to be known as the Environment/Weapons Effects Prediction System (E/WEPS). Because the development of E/WEPS will take several years, an interim assessment system based on the Hewlett-Packard Model 9845 programmable calculator (PROCAL) has been developed and will be deployed to all operational carriers during 1979. This interim E/WEPS will be maintained by Hewlett-Packard for the estimated three to five year life of the systems. It is hoped that the interaction of operational and R&D personnel concerned with the interim E/WEPS will provide valuable guidance in developing the fully militarized E/WEPS.

2. REFRACTIVE EFFECTS

The term "refractive effects" usually refers to the property of a medium (here the lower atmosphere) to refract or bend an EM wave as it passes through the medium. However, as the term is used here, it takes on the wider meaning which includes all propagation effects of or related to the lower atmosphere that affect the performance of EM systems. As such the term includes not only refraction and ducting, but also reflection from the sea surface, multipath interference, diffraction around the earth's surface, tropospheric scattering, sea clutter, and many other propagation mechanisms and processes. For most naval EM systems, the occurrence of ducting in the troposphere provides the most dramatic impact on system performance.

2.1 Surface-Based Ducts from Elevated Layers

Over ocean areas there often exists a cool, moist marine air mass extending vertically from the ocean surface to an altitude of a few hundred metres. The air mass above this altitude can be much warmer and drier than the marine air for a variety of meteorological reasons, and it creates a transition region or refractive layer in which the air warms up and dries out very rapidly with increasing altitude. The rapid warming and drying of the air can cause the refractive index (and refractivity) to decrease with height fast enough

to refract an upward traveling EM wave downward as illustrated in the example shown in Figure 1. If the refractive layer is strong enough to cause the downward traveling wave to strike the surface, then a surface-based duct will be formed. As Figure 1 illustrates, such a surface-based duct can result in severe alterations in the performance of EM systems. In the example, a shipboard air-search radar can experience loss of air coverage in a radar "hole" above the refractive layer due either to reduced signal levels or masking from sea clutter return at the same range enhanced by the duct. Also note that the radar signal propagates beyond the normal horizon and can be intercepted by hostile surface platforms. Surface-based ducts are generally rare over most ocean areas, but in some important operating areas such as the Southern California off-shore area, the eastern Mediterranean, and the northern Indian Ocean they can occur from 20 to 40% of the time on a yearly basis.

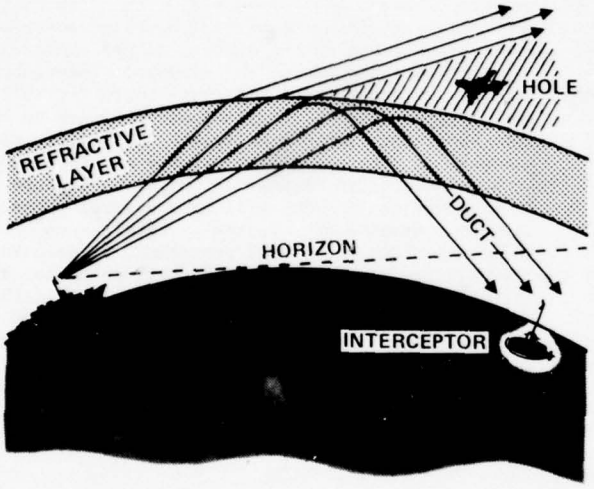

Figure 1. Example of a surface-based duct showing the effects on a shipboard air-search radar.

2.2 Elevated Ducts

If the refractive layer shown in Figure 1 occurs at a higher elevation such that the downward traveling wave does not strike the surface, then an elevated duct will be formed as illustrated in Figure 2. The primary effect that elevated ducts have is to create a region (or hole) above the duct where severely reduced signals from an emitter within or above the elevated duct will result. As the example of Figure 2 shows, an airborne early-warning radar located in the elevated duct will experience a radar hole in which the detection of air targets will be much reduced. Although this effect will be most pronounced for radar systems, communications systems (excluding hf) can also be affected. Elevated ducts generally occur in the lowest 3 km of the atmosphere, but on occasion have been observed up to 6 km.

2.3 Evaporation Ducts

A very persistent ducting mechanism is created over most ocean areas by the rapid decrease of moisture immediately adjacent to the ocean's surface. For continuity reasons, the air adjacent to the ocean is saturated with water vapor and the

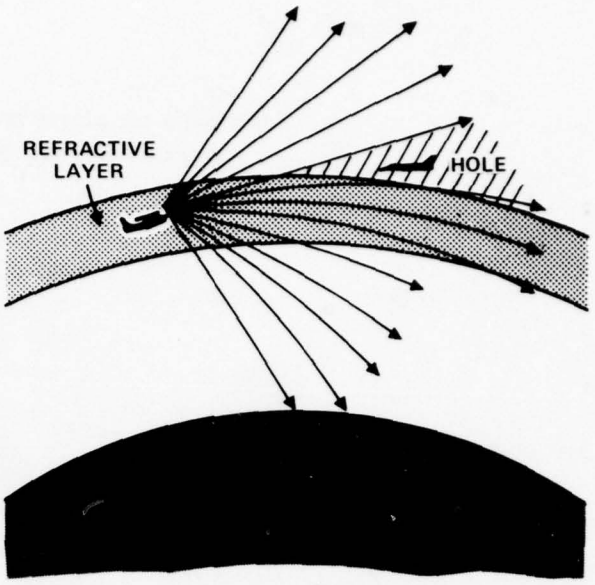

Figure 2. Example of an elevated duct showing the effects on an airborne early-warning radar.

relative humidity is thus 100%. This high relative humidity decreases very rapidly in the first few metres to an ambient value which varies depending on the meteorological conditions existing at the time. The rapid decrease in moisture also causes the refractive index of the air to decrease very rapidly such that a trapping layer and surface duct are formed immediately adjacent to the surface. This type of duct is much thinner and weaker than surface-based ducts created by elevated refractive layers and usually only affects frequencies above 3 GHz. For radars and other EM systems operating at these high frequencies, Figure 3 illustrates that over-the-horizon detections and interceptions are possible. The strength of the evaporation duct is quite variable and depends on the air and sea temperature, and ambient surface wind speed, and humidity. The evaporation duct tends to be stronger at equatorial latitudes, during the summer months, and during the daytime.

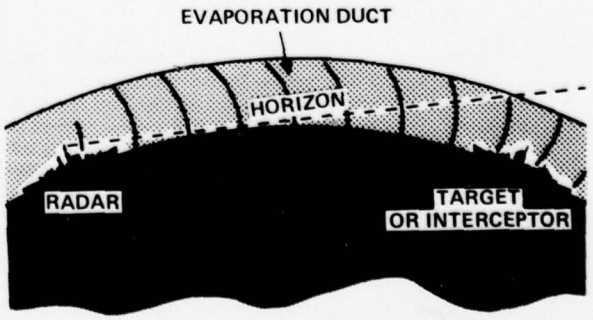

Figure 3. Example of an evaporation duct showing the enhancement of both detection and intercept ranges for a shipboard surface-search radar.

3. IREPS

IREPS is an exploratory development project to develop, validate, and implement a minicomputer based software system that accepts refractivity of the lower atmosphere and calculates and displays the pertinent propagation effects and resulting enhancement or degradation in the performance of specific EM systems. The development of IREPS is primarily a model and computer software development consisting of: adapting existing mathematical models and developing new models where needed, validating the resulting models by carefully controlled radiometeorological measurements taken both by NOSC and others, compiling a comprehensive world-wide climatology of refractive effects which can be called on to supplement on-scene refractivity data, developing the computer software necessary to implement the resulting models and climatology handling routines on IREPS, and demonstration and evaluation of IREPS during actual fleet exercises.

3.1 The IREPS Concept

Figure 4 illustrates the IREPS concept in a block diagram form. Central to IREPS is a hardware data processing system which is usually based on a minicomputer. The essential elements of the hardware system besides the central processor are an interactive terminal and graphics display, a graphics-capable hard copy unit, a mass storage device to store the programs and the climatological data, and a cassette reader that is compatible with the AN/AMH-3 airborne microwave refractometer. On-scene refractivity data is supplied to IREPS from either a radiosonde balloon, the refractometer cassette, or surface measurements made aboard the IREPS host ship. Two types of stored information are available to IREPS. The first type is the climatological data stored in a historic and geographic refractivity library from which IREPS can generate products that display the probabilities of occurrence of various refractive effects for any latitude, longitude, season, and time of day. The second type of stored information consists of the parameters of those EM systems for which IREPS will calculate and display refractive effects. IREPS can accommodate a wide variety of EM systems for surveillance, communications, electronic warfare, and weapons tracking and guidance. Once the appropriate on-scene refractivity data has been entered into IREPS, the system can generate one or more products that either display refractive conditions, a summary of refractive effects for a wide variety of systems, or specific effects on particular systems.

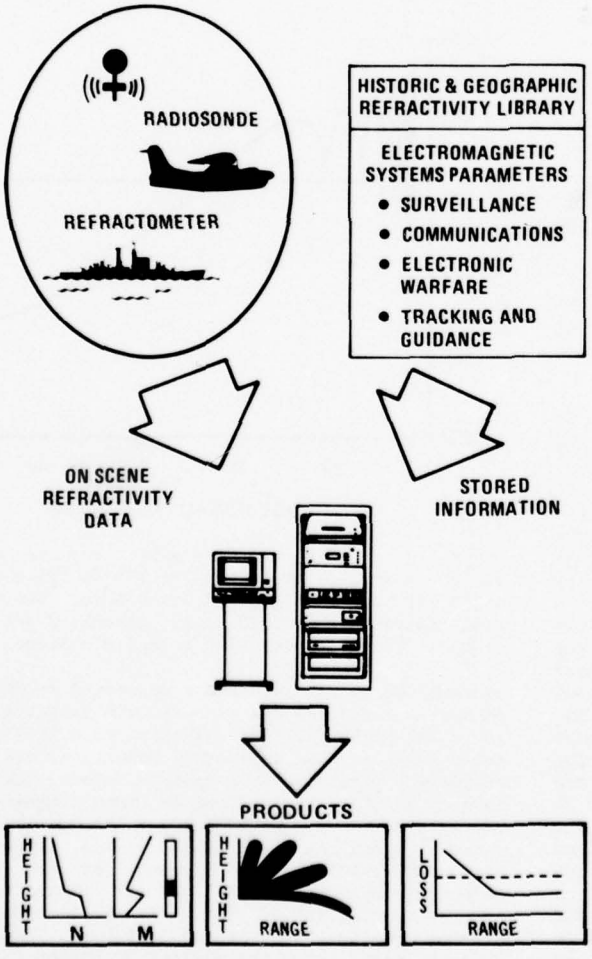

Figure 4. The IREPS concept in block-diagram form.

3.2 The IREPS Displays

Figure 5 shows an example of the basic refractive conditions plot generated by IREPS. Both the refractivity in N units and the modified refractivity in M units are plotted versus height. The bar to the right shows the presence of any ducts by the shaded area. The example shows a surface-based duct generated by an elevated refractive layer occurring at 1000 ft. Figure 6 shows the propagation conditions summary product from IREPS which is a plain language narrative description of the propagation conditions and effects on EM systems in general. The refractive conditions are the same as those in Figure 5. The summary is broken down into three categories for surface-to-surface, surface-to-air, and air-to-air geometries. Figure 7 shows an example of a coverage diagram which is undoubtedly the most useful IREPS product. The example is for a 1300

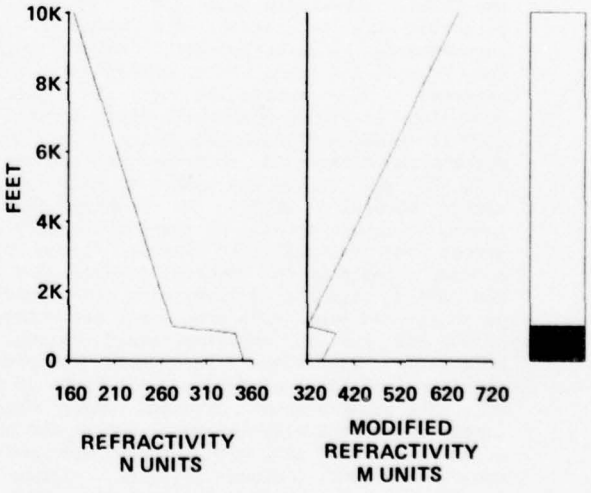

Figure 5. Refractive conditions plot for a surface-based duct extending up to 1000 ft.

SURFACE TO SURFACE

EXTENDED RANGES AT ALL FREQUENCIES

SURFACE TO AIR

EXTENDED RANGES FOR ALTITUDES UP TO	**1,000.0 FEET**
POSSIBLE HOLES FOR ALTITUDES ABOVE	**1,000.0 FEET**

AIR TO AIR

EXTENDED RANGES FOR ALTITUDES UP TO	**0.0 FEET**
POSSIBLE HOLES FOR ALTITUDES ABOVE	**1,000.0 FEET**

Figure 6. Propagation conditions summary for the refractive conditions shown in Figure 5.

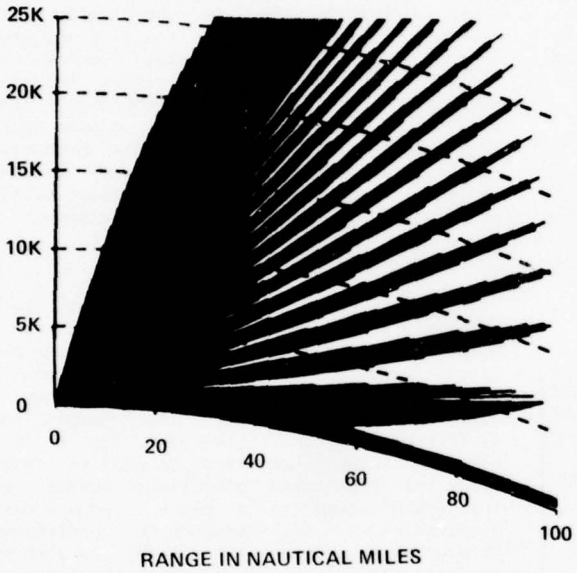

Figure 7. Coverage display for a SPS-12 air-search radar located at 80 ft for a 90% probability of detection of a 1 m^2 target for the refractive conditions of Figure 5.

MHz SPS-12 air-search radar for 90% probability of detection of a 1 m^2 target. The shaded area on the curved-earth range-versus-height display indicates the region in space where detections would be expected. The example is for the refractive conditions of Figure 5 which is characterized by a 1000 ft high surface-based duct. The coverage display shows extended coverage within the first 1000 ft and to 100 nmi caused by this duct. At higher elevation angles the display shows the lobing structure created by the interference of the direct and sea-reflected wave. Figure 8 shows another example of the coverage display for a 420 MHz APS-96 airborne early-warning radar operating at 16 kft and based on a free space detection range of 200 nmi for an arbitrary-sized target. The refractive conditions in this example are characterized by an elevated duct between 15 and 18 kft. The example shows extended radar detection capability in the elevated duct but at the expense of a radar "hole" or region of reduced detection above the duct. Figure 9 is an example of a one-way path loss versus range display for a 5700 MHz SPS-10 surface-search radar operating at 170 ft above the ocean surface and for a target at 50 ft above the ocean surface. Path loss is the ratio of

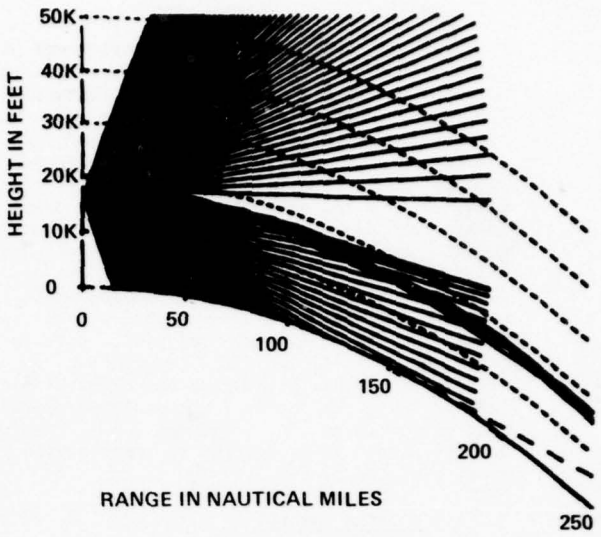

Figure 8. Coverage display for an APS-96 airborne early warning radar operating at 16 kft based on a free space range of 200 nmi for an arbitrary target and in the presence of an elevated duct between 15 and 18 kft.

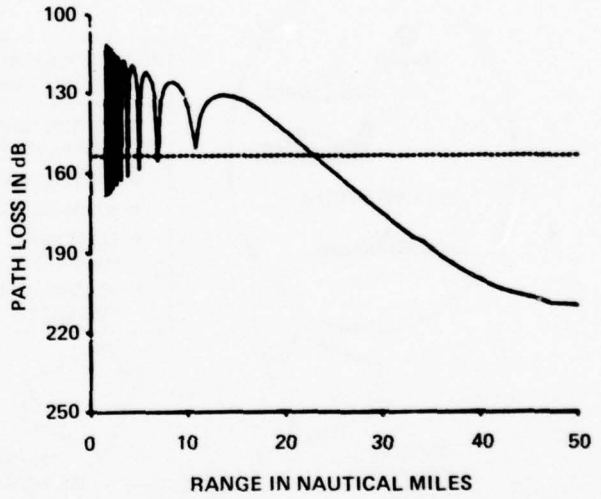

Figure 9. Path loss display for an SPS-10 surface-search radar mounted at 170 ft for a target at 50 ft and a standard atmosphere. The dashed line indicates the path loss threshold for a 50% probability of detection of a 1000 m^2 target.

transmitted to received power expressed in dB. The dashed line denotes the one-way path loss threshold for a 50% probability of detection of a 1000 square metre target. The refractive conditions are for a standard atmosphere. The example shows the path loss oscillating up and down at close ranges due to the interference of the direct and sea-reflected waves. Since the path loss values exceed the threshold briefly at a number of the nulls, detection would not be expected at these ranges. At a range of about 23 nmi, the path loss curve crosses the threshold for the last time, therefore this display shows the maximum detection range to be 23 nmi.

In addition to the products that have been presented in the above examples, IREPS can generate other displays that assist the operator in loading and evaluating on-scene refractivity data, in editing refractivity data or EM systems parameters, or requesting the climatological data.

3.3 Tactical Uses of IREPS Products

There seem to be many tactical uses for the various IREPS products as determined from actual fleet exercises. Several of the more important ones will be presented in this section, but this discussion is not intended to be all-inclusive.

One of the most important uses of the IREPS products is as an aid in determining the optimum flight profiles for attack aircraft to avoid detection by hostile radar systems. For instance, a normal tactic to avoid detection is to fly as close to the ocean surface as possible, but for the example presented in Figure 7 such a low altitude would be the worst altitude for penetration. In the case of such a surface-based duct, it would be much better to fly above the duct or to fly down one of the interference nulls to avoid detection. Similarly an ECM aircraft can use the coverage diagram to plan a flight profile to minimize his detection or to maximize the efficiency of his jamming equipment.

Another important use of the coverage diagrams is in stationing of airborne assets to minimize the effects of radar holes. For instance in the example of Figure 8, the radar hole would become smaller and smaller the higher the aircraft would fly above 18 kft and could completely disappear for altitudes below 15 kft. Another use for the coverage diagram is in stationing of all types of aircraft to maximize vhf communications to the various surface units and other airborne units. Special communications systems such as the Multi-Channel Jezebel Relay (MCJR) used to relay sonobuoy information to the Tactical Support Center on a carrier via a helicopter or S-3 aircraft can be greatly affected by refractive effects also. A coverage diagram tailored to the MCJR can be used to optimize stationing of the relaying platform and will indicate the possibility of OTH communication from low altitudes due to surface-based ducts which can allow an ASW helicopter to use its dipping sonar simultaneously with the MCJR. Also the IREPS products can be used to determine the appropriate EMCON conditions based on the propagation conditions that currently exist.

4. E/WEPS

E/WEPS is an advanced development project to develop a militarized hardware and software system and supporting documentation to perform the IREPS functions (and potentially other assessment system functions) aboard major combatant ships.

4.1 E/WEPS Objectives

The final objective of the E/WEPS project is to specify, construct, TECHEVAL, OPEVAL, and obtain approval for service use for an advanced development model (ADM) to perform assessment system functions. Many factors go into the development of an ADM and a number of them are specified in the next section. The process to develop such an ADM E/WEPS will take several years if done properly and will result in a lack of assessment system capabilities within the fleet until at least the late 1980s. Because of the long delay in initial operational capability, an interim E/WEPS based on a Hewlett-Packard model 9845 programmable calculator is being implemented and deployed aboard all operational carriers. The HP 9845 has the capability to generate all of the IREPS products and produce a high-quality graphics hard-copy output, but at a reduced speed of operation. The interim E/WEPS has been used aboard the USS RANGER for several months with highly successful results. It is anticipated that all of the operational carriers will have an interim E/WEPS capability by the end of CY 1979. It is hoped that the early interaction of the operational personnel of the various ships and airwings with the R&D personnel involved in the development of IREPS and E/WEPS will result in a far improved ADM E/WEPS for eventual use.

4.2 Advanced Development Model Factors

There are a multitude of factors to be considered in the development of an ADM that have been mandated by CNO. A partial list of those factors that must be considered in the development of the E/WEPS ADM are:

1) Functional performance requirements
2) MIL-E-16400 requirements
3) Life-cycle costs
4) Design-to-cost
5) Navy standardization program
6) Reliability/maintainability/availability
7) Test and evaluation requirements
8) Integrated logistics support
9) Manpower and training
10) Shipboard installation requirements
11) Resource sharing

5. SESC

It has recently been proposed that a Shipboard Environmental Support Center (SESC) be developed that consolidates the functions of E/WEPS with the Naval Environmental Display Station (NEDS-2) and the Integrated Command ASW Prediction System (ICAPS). NEDS-2 is a proposed shipboard version of the shorebased NEDS that has been developed by Fleet Numerical Weather Central (FNWC) to receive and display weather data generated by FNWC. ICAPS is an assessment system developed by NAVOCEANO for underwater acoustics environmental effects. The SESC is proposed to be situated on all carriers in the meteorological office and on selected other capital ships. Because of the NEDS requirement for high data rate communications from FNWC and considerable mass storage, it is expected that the NEDS-2 requirements will dominate those of E/WEPS and ICAPS except for the central processor requirements. It is hoped that by combining all three of these functions into one system a much greater capability will result at a lesser cost than implementing each one alone.

6. REFERENCES

Hitney, H. V. and J. H. Richter, 1976: Integrated Refractive Effects Prediction System, Naval Engineers Journal, 88, no. 2, 257-262.

Kerr, Donald E., 1951: Propagation of Short Radio Waves, McGraw-Hill Book Company.

THE FLENUMWEACEN RADAR PROPAGATION ANALYSIS MODEL

Leo Clarke and William Pertle

Fleet Numerical Weather Central

Monterey, California 93940

ABSTRACT

Following a one year operational evaluation by Pacific Coast fleet units, the FLENUMWEACEN Radar Propagation Model became operational in July 1977. Subsequently requests for Radar Propagation Analysis (RPA) support have increased from less than one hundred per month to more than six hundred per month.

The execution of RPA at FLENUMWEACEN has been automated with in-house turnaround time of less than one hour except in unusual cases. The RPA model is radar specific and treats each user's request as a separate calculation based on a free space detection range (FSDR) for each specific radar mode of operation and target configuration. The RPA model assumes a nonleaky duct, specular reflection from the sea surface, and a layered horizontally homogeneous atmosphere. The output is a ratt-graphic coverage diagram representing probabilities of detection (PD) at specific heights and ranges in a two dimensional matrix. A tabular N-profile is included at the end of each message, and represents the refractive index profile upon which the coverage diagrams are based.

1. RADAR PROPAGATION ANALYSIS MODEL

1.1 Introduction

Following a one year operational evaluation by Pacific Coast fleet units, the Fleet Numerical Weather Central (FLENUMWEACEN) Radar Propagation Analysis Model became operational in July 1977. Subsequently, fleet requests for Radar Propagation Analysis (RPA) support have increased from less than one hundred per month to more than six hundred per month (Figure 1).

1.2 Model Description

The RPA model utilizes nonleaky duck and coherent ray theory to compute atmospherically induced electromagnetic energy gain/loss from a free space reference level. The calculations consider a one-way path from an isotropic antenna.

A refractive index profile is customarily computed from an atmospheric sounding (raob). The model incorporates a variable vertical grid which incorporates all the significant levels of the sounding. Under this system the basic input data is inventoried and, if necessary, is expanded by a progressive interpolation technique to improve the accuracy of the ray tracing integrations. This technique generates no new extrema or minima, but rather fits a curve to the discrete data. If the refractive index profile extends to less than fifty thousand feet, it is extrapolated to that altitude with an exponential model. The RPA model initially was basically an inverted FACT (Fast Asymptotic Coherent Transmission) model which is used by FLENUMWEACEN to compute transmission loss as a function of range and frequency at fixed source and receiver depths in underwater acoustics, Spofford (1974).

The RPA model driver converts the refractive index profile to an analogous underwater sound velocity profile. The driver then executes the FACT model once for each level in the analogous sound velocity profile. The propagation loss is returned in arrays for formatting via the output package. The RPA modeling includes

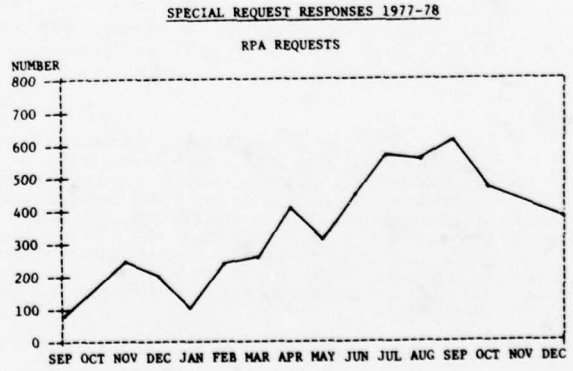

Figure 1

an evaporative duct on all oceanic soundings because of the well known inability of the radiosonde to portray temperature moisture profiles in the first thirty meters above the surface. The FLENUMWEACEN planetary boundary layer model (PBL) calculates the presence or absence of the ocean surface radar evaporation duct (REVAP) using ocean interface parameters calculated in the PE model. This duct is nearly always present over the oceans and is strongest in the tropics (on the average, but can be extreme in other regions when dry air is present). This duct is of importance in extending the range of radars in over-the-horizon (OTH) SFC to SFC and low level radar coverage. Enhanced detection ranges occur for frequencies of 3 to 20 Ghz and are proportional to the strength of the duct gradient in N units. Antenna location relative to the top of the duct also effects enhancement (lowest antennas within the duct usually have the greatest OTH range).

Due to the possible enhancement or degradation of radar systems caused by an evaporation duct, FLENUMWEACEN combines the evaporative duct output from the FLENUMWEACEN PBL model with the input sounding sent in by the requesting unit, or with a nearby land sounding, if desired. In this manner, the effects of an evaporative duct can be incorporated into the radar propagation model by modifying the bottom of the input sounding.

The manner in which the evaporative duct is added to the sounding is accomplished by decoding the ship position and extracting the duct information from the PBL fields. A message will be added to the RATTGRAPHIC output if the evaporative duct has been added. If for some reason the evaporative duct cannot be added, then no message will appear. In the event that a land sounding is used, a caveat figure 2 will appear in the output to alert users to possible problems.

DATA COMPUTED BASED ON RAOB SOUNDING FOR (LAND STATION)
AND BLENDED WITH FNWC SURFACE DUCT AT (POSITION)
RPA COMPUTED FROM LAND RAOB IS SUBJECT TO CONTINENTAL
ATMOSPHERIC CONDITIONS WHICH MAY DIFFER FROM MARITIME
ENVIRONMENT. EXISTENCE OF FRONTAL ZONE OR AIRMASS
DISCONTINUTITIES IN AREA WILL ALSO REDUCE ACCURACY.
RELIABILITY OF RPA IS INVERSELY PROPORTIONAL TO DISTANCE
BETWEEN SOUNDING AND OP AREA AND TO ELEVATION OF
OBSERVATION. RECOMMEND THESE VARIATIONS BE CONSIDERED AS
APPROPRIATE.

Figure 2

1.3 Model Input

Input to the model requires:

a. antenna height
b. radar frequency
c. maximum horizontal range of the analysis
d. an input sounding
e. three pairs of Free Space Detection Ranges (FSDR);

and their associated Probabilities of Detection (PD). FSDRs have been computed at FLENUMWEACEN for standard PDs based upon a one square meter target area for a number of radars (Figure 3).

RADAR SYSTEMS SUPPORTED BY FLENUMWEACEN

RADAR PROPAGATION ANALYSIS MODEL

AN/SPS-5C	AN/SPS-48V
AN/SPS-5D	AN/SPS-49
AN/SPS-6C	AN/SPG-51C
AN/AWG-9	AN/SPS-52
AN/AWG-10	AN/SPS-52B
AN/SPS-1	AN/SPS-53
AN/SPS-12	AN/SPS-53A
AN/SPS-21A	AN/SPS-53K
AN/SPS-21D	AN/SPS-53L
AN/SPS-29C	AN/SPG-55B
AN/SPS-29E	AN/SPS-55
AN/SPS-3	AN/SPS-58
AN/SPS-32	AN/SPS-58A
AN/SPS-33	AN/SPG-6
AN/SPS-35	AN/SPS-61
AN/SPS-37	AN/SPS-62
AN/SPS-37A	AN/APS-8
AN/SPS-39	AN/APS-96
AN/SPS-39A	AN/APS-115
AN/SPS-4	AN/APS-12
AN/SPS-4B	F111 RADAR
AN/SPS-4C	MK-25 MOD-3
AN/SPS-4D	
AN/SPS-43	
AN/SPS-43A	
AN/SPN-43	
AN/SPS-48	
AN/SPS-48A	

Figure 3

These calculations were made using a FORTRAN computer program RGCALC, Blake (1972). For other than standard U. S. Navy shipboard radars, FSDRs must be supplied by the user or can be calculated by FLENUMWEACEN if sufficient data is supplied.

The input sounding is customarily a radiosonde sounding which includes, as a

minimum: pressure, temperature, and dew point depression. The height of each level, if included, will be utilized, otherwise, it will be calculated.

The input sounding is the most frequent cause of ambiguous results. The sounding should contain as many levels in the lower atmosphere as is possible. It is essential that the sounding include complete moisture information and include dewpoint depression in the levels below 500 millibars. Deck launched radiosondes should be launched well clear of any unusual shipboard thermal conditions to avoid inadvertent thermal anomalies.

1.4 Model Output

The AUTODIN message does not refer to radar frequency or location. However, the radar designation is included in the coverage diagram heading necessitating a CONFIDENTIAL classification. The message text is in grid form with an altitude (feet) versus range (nm) graphic display. The output, called a coverage diagram, shows areas of probability of detections (Figure 4).

```
RDR PROP IMESCON8090
1.  IN RESPONSE TO REF A THE FOLLOWING RADAR
PROPAGATION ANALYSIS IS PROVIDED.
2.ALTITUDE      0. TO   50000. .
  STATION              77110712Z
 FOLLOWING IS COVERAGE DIAGRAM WHERE LETTER A REPRESENTS
COVERAGE WITH GREATER THAN 90. PER CENT PROBABILITY OF
DETECTION (PD), LETTER B REPRESENTS GREATER THAN 50. PER CENT
PD BUT LESS THAN 90. PER CENT PD AND LETTER C REPRESENTS
GREATER THAN 10. PER CENT PD BUT LESS THAN 50. PER CENT PD.
THE VERTICAL AXIS IS ALTITUDE IN FEET AND THE HORIZONTAL AXIS
IS RANGE IN NM.
THE RECEIVER HEIGHT FOR THIS MSG IS     77 FEET.
THE RADAR TYPE FOR THIS MSG IS SPX99A
     0.        38.       77.       115.      154.      192.      230.
50000.AAAAAAAAAAAAAABAAABAAA AAAAB BAAAABC  BBAAAABBC       CCBBBBBB
40879.AAAAAAAAAAAAAABAAABBAAAB BAAAAB  CBAAAAABB       CBBBBBBBBBBBC
31759.AAAAAAAAAAAABAAACAAAB AAAAAC BAAAAAABB      CBBBBBBBBBBBCCC
28812.AAAAAAAAAAAAAACAAAB AAAAA BAAAAAABC      CBBBAABBBBBBBCCC
25866.AAAAAAAAAAAAAACAAABCAAAAB CAAAAAABB     CBBAAAAABBBBBCCC
25367.AAAAAAAAAAAAAABBAAAAB BAAAAAABC         BBBAAAAABBBBBCC
19291.AAAAAAAAAAAABAAA AAAAA BAAAAAAB    CBAAAAAAAAABBBCC
10381.AAAAAAAAAAAAAAAABAAAAAABCBAAAAAAAAAABBBCC
 8704.AAAAAAAAAAAAAAAAAAAAAAABAAAAAAAAAAAABBBC
 7028.AAAAAAAAAAAAAAAAAAAAAAAAAAAAAAAAAAABBBC
 6611.AAAAAAAAAAAAAAAAAAAAAAAAAAAAAAAAAABBBC
 5802.AAAAAAAAAAAAAAAAAAAAAAAAAAAAAAAAABBBC
 4993.AAAAAAAAAAAAAAAAAAAAAAAAAAAAAABBC
 2585.AAAAAAAAAAAAAAAAAAAAAAAB
 2215.AAAAAAAAAAAAAAAAAAAAB
 1913.AAAAAAAAAAA
 1808.AAAAAAAAAAAAAAAAAAAAB                CBAAAAAAAAAAAAAAAAAAAAABBB
 1703.AAAAAAAAAAAAAAAAAAAABC               BAAAAAAAAAAAAAAAAAAABBBBBB
 1598.AAAAAAAAAAAAAAAAAAABC                BBBBBAAAAAAAAAAAAAABC BBBB
 1545.AAAAAAAAAAAAAAAAAAABB               CBBBBBBAAAAAAAAAAAAABC BBBB
 1493.AAAAAAAAAAAAAAAAAAABB               BBBBBBBBAAAAAAAABAAAAB  BBBB
   71.A                       CAABBBCC                       BBCCCCC
   22.AAB                      CCCC
    0.A
     0.        38.       77.       115.      154.      192.      230
THE EVAPORATIVE DUCT HAS BEEN ADDED TO THE BOTTOM OF THE SOUNDING
SECTION HERE.
```

Figure 4

The output can be interpreted directly. For example in Figure 4, the letter "A" represents the area where there is greater than 90% probability of detection. Letter "B" represents greater than 50% probability of detection but less than or equal to 90%; letter "C" represents greater than 10% probability of detection but less than or equal to 50%; and blank areas indicate 10% probability of detection or less. The last paragraph of each RPA message contains a tabular listing of the refractive index profile with heights in feet, N units for each level, N gradient and description of the refraction of each layer, i.e., trapping, super, normal, or subrefractive (Figure 5).

3.THE ABOVE RADAR PROPAGATION ALALYSIS WAS DERIVED FROM THE SOUNDING GIVEN BELOW. THE REFRACTION COLUMN TELLS IF THE REFRACTION IN THE LAYER BETWEEN TWO LEVELS IS NORMAL, SUB, SUPER OR TRAPPING.

HEIGHTS FEET	REFRACTIVE INDEX N UNITS	N/1000 FT.	REFRACTION
0.	422.0		
22.	375.0	-2180.0	TRAPPING
71.	371.3	-73.6	TRAPPING
1493.	350.6	-14.6	NORMAL
1545.	342.2	-160.7	TRAPPING
1598.	332.9	-176.0	TRAPPING
1703.	313.0	-190.2	TRAPPING
1808.	292.5	-194.7	TRAPPING
1913.	273.5	-181.7	TRAPPING
2215.	261.5	-39.5	SUPER
2585.	258.1	-9.3	NORMAL
4993.	246.6	-4.8	NORMAL
5802.	236.3	-12.8	NORMAL
6611.	224.5	-14.6	NORMAL
7028.	221.2	-7.9	NORMAL
8704.	208.6	-7.5	NORMAL
10381.	197.3	-6.8	NORMAL
19291.	149.9	-5.3	NORMAL
25367.	119.6	-5.0	NORMAL
25866.	117.4	-4.3	NORMAL
28812.	107.0	-3.5	NORMAL
31759.	97.1	-3.4	NORMAL
40879.	68.8	-3.1	NORMAL
50000.	40.9	-3.1	NORMAL

Figure 5

1.5 Radar Propagation Request and Data Input Messages

When possible, the initial RPA request for service should be sent several working days before the first RPA product is required. Thereafter, standard operational message requests are appropriate unless there is a change in radar parameter input, or if several months have elapsed since RPA was last provided to your command. Sample initial request messages are provided in Figure 6.

When the sounding is provided by the user, it must be in the format described in Figure 7. Deviations in the format may cause nonrecognition of the message as an RPA request due to the similarity of normal sounding data messages required by other fleet directives.

```
FM  (YOUR COMMAND)
TO  AIG 7608 (PACIFIC)
    AIG 7641 (ATLANTIC)
BT
(CLASSIFICATION)//N03149//
RADAR PROP ANALYSIS REQUEST (U)
1.  REQ RPA IAW FOLLOWING PARAMETERS:
A.  (RPA PRODUCT ADDRESSEES)
    USS  (YOUR SHIP)
    USS  (SHIP IN COMPANY)
    INFO (EMBARKED STAFF)
B.  (RADAR TYPE(S), SPS-40B)
C.  (DISCRETE RADAR FREQUENCY(S), MHZ)
D.  (ANTENNA HEIGHT(S) ABOVE SEA LEVEL, FT)
E.  (MAXIMUM HORIZONTAL ANALYSIS RANGE(S), NM)
F.  (TIME PERIOD DESIRED, IE:  12Z 24 JAN 79 to 12Z 27 JAN 79)
G.  *(APPROXIMATE POSITION OF RADAR(S) FOR EACH TIME PERIOD
    REQUESTED, LAT/LONG)
2.  (REPEAT PARAGRAPH 1.  INFORMATION FOR EACH SEPARATE RPA
    MESSAGE DESIRED.)
3.  UPPER AIR SOUNDINGS WILL BE PROVIDED BY USS (SHIP),
(OR) UTILIZE (LAND STATION, E.G. SAN DIEGO)
SOUNDING (STATION NUMBER IF KNOWN), (OR) REQUEST SELECT
UPPER AIR STATION OF OPPORTUNITY.  (NOTE THAT REPORTING
RELIABILITY OF MANY LAND STATIONS IS LESS THAN 100%.)
BT
* LAND STATION SOUNDING UTILIZATION ONLY.
```

Figure 6

```
FM {SHIP PROVIDING}
FM {SHIP PROVIDING SOUNDING}
TO AIG 7608 {PACIFIC}
   AIG 7641 {ATLANTIC}
BT
{CLASSIFICATION}//N03149//
RADAR PROP ANALYSIS REQUEST {U}
UUAA {MANDATORY LEVELS - WMO 36.3}
UUBB {SIGNIFICANT LEVELS - WMO 36.3}
BT
```

Figure 7

The message SSIC of 03149 (vice 03144) and the subject line "RADAR PROP ANALYSIS REQUEST" are critical in decoder recognition. The sounding indicators UUAA and UUBB must be in the left column and must not be preceded by any information such as paragraph numbers, INTERNATIONAL RADIO CALL SIGN (IRCS), etc., DIRNAVOCEANMET (1978). UUCC/UUDD information may also be included if it is desired to combine a normal upper air report required by fleet directive with the RPA request, as RPA request soundings are also read into the FLENUMWEACEN data base, NAVAIR (1975).

1.6 RPA Model Operation

Execution of RPA is initiated upon receipt of an upper air sounding at FLENUMWEACEN. Requests supported by land raob's are automatically executed when the required raob is received via the AWN data collection network. Request supported by a ship's own raob is executed on receipt of the sounding via AUTODIN. The TSCREEN program searches all AUTODIN input, saving RPA request soundings in a permanent file. The RADFIND program extracts the sounding and it is displayed for quality control and possible correction. Subsequent to error-checking the sounding, the RPA job is executed, generating an AUTODIN transmit tape.

1.7 Response Time

The entire RPA execution process from receipt at communications to transmission of response is usually less than one hour. In some cases, the time has been less than twenty-five minutes. However, when the sounding has several errors, or when the computer assets are not available, it may take in excess of three hours, Figure 8. User response indicates an average of two to three hours from transmission of request to receipt of product. This generally agrees with the FLENUMWEACEN one-way AUTODIN overhead of one hour for immediate messages.

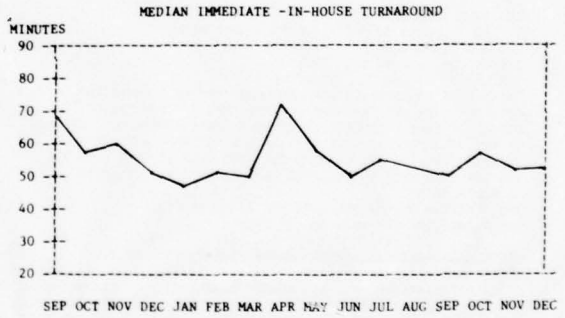

Figure 8

1.8 Independent Evaluations

User response to request for evaluation of the RPA product have indicated that the coverage diagram is easy to interpret, and normally valid. In most cases, observed detection ranges and effects of propagation were consistent with predictions. However, significant atmospheric changes were observed to invalidate results. Understanding and awareness of anomalous propagation conditions aided in antenna/frequency selection and, for multiple radar units,

optimum radar selection. The RPA product in general has been accepted as a valuable and reliable addition to fleet support, and one user stated "The RPA support provided was a significant factor in the success of our operations." Probably the most common complaint was the long turnaround time. In view of the fact that FLENUMWEACEN in-house time is generally less than one hour, the major delay seems to be in fleet communications. Many of the users surveyed indicated a desire for onboard capability to generate RPA (such as IREPS).

REFERENCES:

Blake, L. V., 1972: A Fortran Computer Program to Calculate the Range of a Pulse Radar. Washington D. C., NRL Report 7448, 1-5

DIRNAVOCEANMET, 1978: Ballistic Winds and Density, Chaff Winds, Radiological Fallout and Radar Propagation Forecasts. Bay St Louis, MS, DIRNAVOCEANMET NOTICE 3140, 11-18

NAVAIR, 1975: International Meteorological Codes 1974 and Worldwide Synoptic Broadcasts. Washington, D. C., NAVAIR 50-1p-11, 57-63

Spofford, C. W., 1974: The FACT Model, Maury Center Report 109. Arlington, VA, Office of Naval Research, 52 pp

REVISED FNWC RADAR PROPAGATION MODEL

Claude P. Hattan
Naval Ocean Systems Center
EM Propagation Division
San Diego, CA 92152

ABSTRACT

The U.S. Navy operates in an environment which often produces dramatic refractive effects on fleet microwave systems. A variety of technical papers and manuals are or have been employed by the fleet to assess the effect of refraction on these systems. The greatest majority of these assessment methods are of little utility to the fleet as they are not fast, accurate, and/or simple enough. In recent years NOSC has developed a minicomputer-based assessment system which allows near-real time evaluation of refractive effects on Naval sensors. This system is the Integrated Refractive Effects Prediction System or IREPS. As IREPS products and prototype hardware are introduced to operational units they will only be installed on those ships with meteorological capabilities. In order to provide other units with the benefit of IREPS-type products a computer program has been developed for Fleet Numerical Weather Central (FNWC) as a replacement for their Radar Propagation Analysis (RPA), which will allow FNWC to provide these units with IREPS-compatible propagation information. A description of the propagation models used in the program and the necessary inputs required for operation are given. Examples of the produces are also presented.

1. INTRODUCTION

The effects of refractivity on microwave systems have long been a subject of interest for the U.S. Navy. A considerable amount of time and money has been spent studying the problem and proposing techniques for assessing these effects. However, the majority of these methods are either too technical or too complex for most fleet personnel to use. In recent years advances in computer technology have enabled NOSC to develop a minicomputer - based assessment system called the Integrated Refractive Effects Prediction System (IREPS). This system, which is intended for eventual deployment aboard those ships with meteorological capability (primarily CVs), allows near real-time evaluation of the effects of the refractive conditions on specific microwave systems. IREPS - capable ships can have a definite tactical advantage over those units which are not so equipped.

At the present time Fleet Numerical Weather Center (FNWC) provides its users with a Radar Propagation Analysis (RPA) based on models developed for underwater acoustics. Operational units will soon be faced with the problem of reconciling two different propagation products with the deployment of an interim-IREPS capability this year. To eliminate any confusion NOSC is providing FNWC with a program intended for use in replacing the present RPA. This program, which is based on the IREPS models, will allow FNWC to provide its users IREPS-compatible propagation information. The program will also be upward-compatible with IREPS and as improvements are made to IREPS they can be incorporated into the FNWC RPA program.

The principal program products will be coverage diagrams and a narrative propagation summary. The coverage diagram program, and the models for producing these plots, described in this paper require three types of inputs to produce an output: environmental data, the radar system operating parameters, and the target size. The environmental inputs required are: the refractivity (N unit) values as a function of altitude, the relative humidity near the surface, the air temperature, the sea surface temperature, and the wind speed. The required radar parameters are: the frequency, the antenna height, the radar free-space range against a known target cross-section, the antenna pattern, and the antenna elevation angle. The output is a 51 line by 60 character line printer "plot." Each element in this array will be X'ed if the radar detection threshold for the desired target is exceeded at any point in that array element and left blank when this threshold is not exceeded. Additionally, a plot of refractivity versus height and a profile list are available.

2. MODELS

Radar coverage diagrams indicate those areas in the far field of a radar where a target might be detected. Cover diagrams may be obtained by tracing a series of rays through the atmosphere for varying elevation angles at the transmitting

antenna. The length of each ray is determined by the antenna pattern and the free-space range of the radar. If the radar is on a surface ship then the length of each ray is modified by the coherent interference between direct and sea-reflected rays. There is an implicit assumption of a horizontal stratification and homogeneity of the atmosphere in the ray trace models used to draw the cover diagrams in this program.

Airborne system cover diagrams are drawn by tracing each ray to a range defined by the product of the radar free-space range and the antenna pattern function for that ray, assuming that the ray is not trapped. When the transmitter is in a trapping layer the duct is assumed to be uniformly illuminated to twice the free space range. Downgoing rays are only traced to the surface.

Surface-based transmitting antennas produce divergent beams which allow energy to arrive at a target in the far field by two paths, for targets above the radar horizon (tangent ray): a direct and a sea-reflected path. The energy arriving at the target is the vector sum of the two signals arriving by the different paths. The phase difference between the two signals gives rise to an interference pattern. Ray optic methods adequately describe the field, at least when the total phase difference is greater than one-quarter wavelength. The vector sum is further modified by the surface roughness and the spherical nature of the reflecting surface.

Well below the radar horizon the field is mainly due to diffraction from the earth's surface. (At much greater ranges the field is dominated by scattering from irregularities in the troposphere but this field is generally well below radar receiver thresholds.) NOSC has a tropospheric waveguide program which can provide the series solutions to the diffraction field problem, but the program requires a substantial investment in computer time and is not amenable to "hands off" operation. Accordingly, the IREPS models use solutions obtained by curve fitting waveguide program solutions to obtain the diffraction field strength for evaporation ducts. Empirical models are used for the diffraction field solutions for ground-based ducts due to elevated layers.

In the vicinity of the horizon optical methods don't adequately describe the field and the diffraction field series solutions converge very slowly. This region is sometimes referred to as the intermediate region. The IREPS models obtain the field strength in this region by linearly interpolating between interference region and diffraction region values.

3. PRODUCTS

An example of a refractivity plot is given in Figure 1. The figure indicates the presence of two elevated trapping layers. At the right hand side of the figure the N-gradient at the plotted height is given. The gradients are characterized to indicate the presence of subrefractive, super-refractive, trapping, and normal layers. The ordinate and abscissa values are fixed at 20,000 feet and 100 to 400 N-units respectively. Figure 2 is a sample of the data used to generate

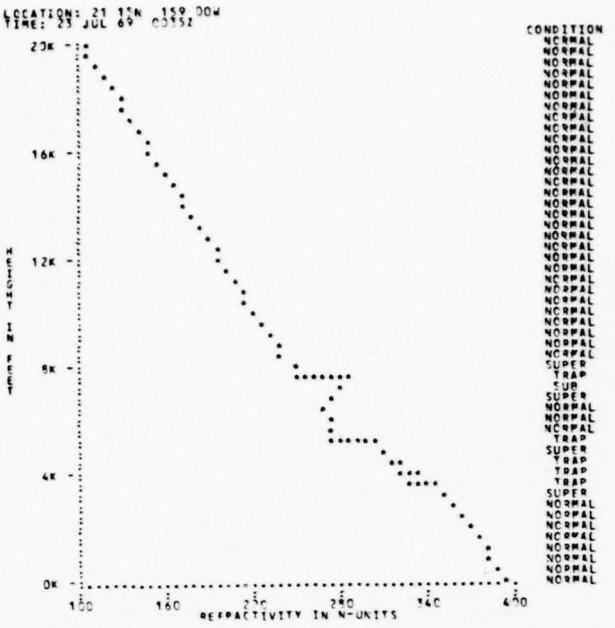

Figure 1. Refractivity plot.

the profile plot. The location and time of the radiosonde profile are labeled at the top and the evaporation duct input parameters and calculated evaporation duct height are given below this. The N-unit values and corresponding height values are listed below the evaporation duct parameters. M-unit values are calculated and displayed also. A narrative refractive conditions summary for the profile of Figure 1 is shown in Figure 3. The surface-to-surface category in this example reflects the effects of the evaporation duct on the higher frequency bands. The air-to-air category indicates that there are actually five trapping layers in this profile and that airborne systems flying at any of these elevations should expect some anomalous propagation effects as indicated. Surface-to-air propagation should be normal as there are no ground-based ducts from elevated layers.

LOCATION: 21 15N 159.00W
TIME: 23 JUL 69 0035Z

WIND SPEED = 20.0 KNOTS
RELATIVE HUMIDITY = 90.0 %

SEA TEMPERATURE = 20.0 C
AIR TEMPERATURE = 19.0 C
DUCT HEIGHT = 50.0 FT

LEVEL	HEIGHT(FEET)	N-UNITS	M-UNITS
1	0.0	304.0	304.0
2	500.0	309.0	413.9
3	1000.0	332.0	426.8
4	1500.0	338.0	440.8
5	2000.0	369.0	444.7
6	2500.0	362.0	481.6
7	3000.0	355.0	499.5
8	3300.0	344.0	501.0
9	3450.0	344.0	509.7
10	3500.0	339.0	509.4
11	3650.0	339.0	511.6
12	3700.0	330.0	507.2
13	3850.0	328.0	512.2
14	3900.0	335.0	521.6
15	4100.0	332.0	528.3
16	4250.0	320.0	525.1
17	4700.0	315.0	550.9
18	5000.0	304.0	563.3
19	5250.0	298.0	569.3
20	5400.0	295.0	571.5
21	6000.0	288.0	580.1
22	6250.0	285.0	602.0
23	7000.0	270.0	610.9
24	7050.0	289.0	626.1
25	7400.0	258.0	642.0
26	7500.0	253.0	643.5
27	7750.0	252.0	651.6
28	9100.0	244.0	691.5
29	20300.0	100.0	1071.2

Figure 2. Refractivity list.

```
                    PROPAGATION CONDITIONS SUMMARY

LOCATION: 21 15N  159 00W
TIME: 23 JUL 69  00352

SURFACE TO SURFACE:
   EXTENDED RANGES FOR ALL FREQUENCIES ABOVE  4 GHZ

SURFACE TO AIR:
   NORMAL RANGES AT ALL ALTITUDES.

AIR TO AIR:
   EXTENDED RANGES FOR ALTITUDES BETWEEN    3395. AND    3500. FT
   EXTENDED RANGES FOR ALTITUDES BETWEEN    3514. AND    3700. FT
   EXTENDED RANGES FOR ALTITUDES BETWEEN    3953. AND    4250. FT
   EXTENDED RANGES FOR ALTITUDES BETWEEN    4409. AND    5250. FT
   EXTENDED RANGES FOR ALTITUDES BETWEEN    7041. AND    7700. FT
   POSSIBLE HOLES FOR ALTITUDES BETWEEN    3500. AND    3514. FT
   POSSIBLE HOLES FOR ALTITUDES BETWEEN    3700. AND    3953. FT
   POSSIBLE HOLES FOR ALTITUDES BETWEEN    4250. AND    4409. FT
   POSSIBLE HOLES FOR ALTITUDES BETWEEN    5250. AND    7041. FT
   POSSIBLE HOLES FOR ALTITUDES ABOVE    7730. FT
```

Figure 3. Narrative summary.

The most important product of the revised FNWC RPA is the coverage diagram. Figure 4 is a sample

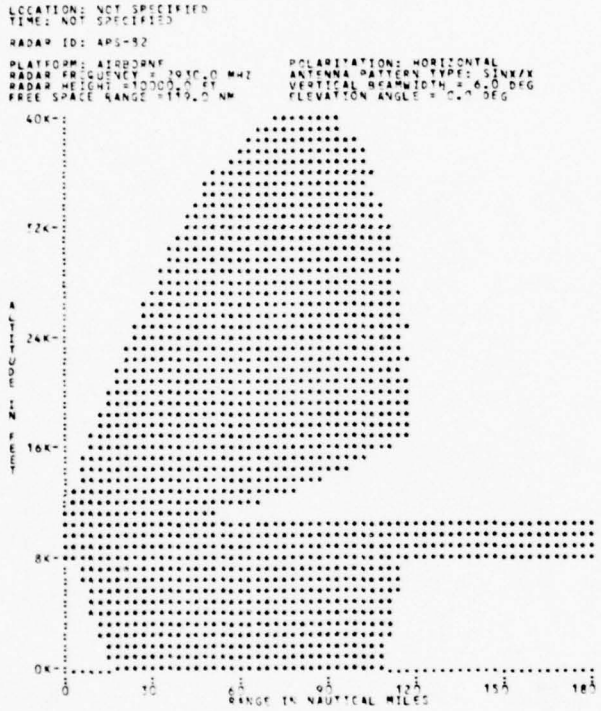

Figure 4. Coverage diagram for an airborne system.

of a coverage diagram for an airborne system with the aircraft flying in an elevated duct extending from 8300 feet to 11,000 feet. The extended range in the elevated duct is clearly shown as well as a radar "hole" above the duct. Figure 5 is an example of a coverage diagram for a surface based system, in this case an AN/SPS-28 air search radar. The profile used to generate this diagram was that of a 1000 foot surface duct from an elevated layer. Such a strong duct is a relatively common occurrence off the Southern California coast. Extended ranges near the surface result from this duct. The lobes shown are due to the coherent interference between the direct and sea-reflected rays. The height scales for the coverage diagrams are user designated in 5000 foot increments from 5000 feet to 50000 feet. Range scales are user optional in 60 nautical mile increments from 60 to 300 nautical miles. The range increment was chosen to fit the AUTODIN line width.

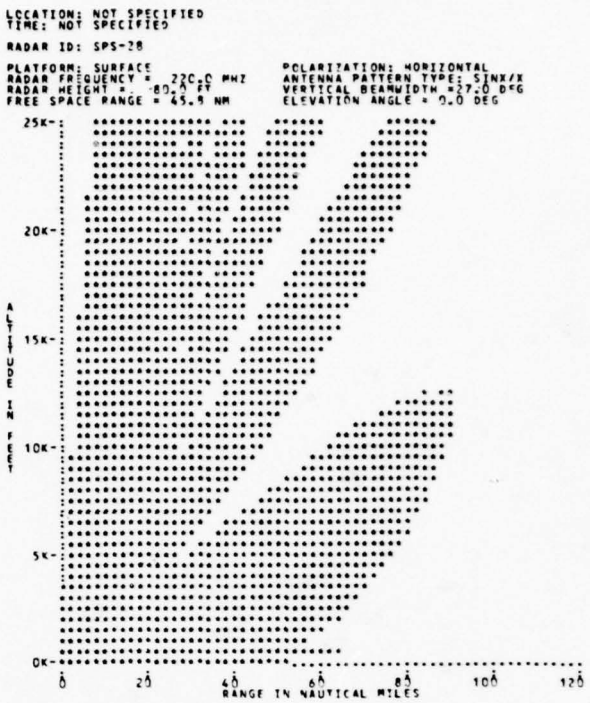

Figure 5. Coverage diagram for a surface-based system.

OPERATIONAL EMPLOYMENT OF AIRBORNE MICROWAVE REFRACTOMETER

Commander Kenneth D. Denbow

Carrier Airborne Early Warning Squadron

One Hundred Sixteen

FPO San Francisco 96601

Introduction

The Airborne Microwave Refractometer (AMR) provides the operational commander an essential capability to utilize existing atmospheric conditions to enhance the tactical effectiveness of his task force. Modern warfare is highly dependent on use of the electromagnetic spectrum for command and control communications, radar detection, ESM and ECM. All of these elements are highly affected by existing atmospheric conditions and a knowledge of what these conditions are, in real-time, is mandatory for successful offensive and defensive operations.

The effect of anomalous propagation has long been known (and utilized) in determining sonar performance in water. The ASW commander deploys his forces and modifies his tactics based on accurate data which determines existing propagation conditions in the area of operations. Similiarly, submarine forces use the existing data to determine optimum depth and tactics for attack to avoid detection and maximize the probability of a successful attack. Sophisticated equipment has been developed to measure water temperature, salinity, density and other factors which effect sonar conditions, and elaborate studies have been conducted to determine exactly what the effect of anomalous conditions will be on a specific sonar. The results have been a detailed, accurate data base for the ASW commander/submarine commander to utilize in successfully completing the assigned mission.

A similar capability is required for the detection and measurement of anomalous propogation of electromagnetic waves in the atmosphere to enable the carrier strike group commander to employ his forces in a manner to optimize the probability of success in assigned missions. In this paper I will discuss the operational use of anomalous conditions in strike warfare at sea, AAW, and command and control communication. This will be followed by a brief discussion on desired capabilities for the E-2 series aircraft in equipment and software to enable this valuable command and control platform to meet the needs of the operational commander. Throughout the paper, the assumption is made that the reader has an understanding of the principals and the effect of refractive "layers" on electromagnetic propagation.

Strike Warfare at Sea

The effectiveness of an air strike against surface ships is extremely dependent upon the survivability of the strike vehicle, whether that vehicle is a manned aircraft raid or an attack by cruise missiles such as HARPOON or TOMAHAWK. Survivability can be enhanced by denying the enemy electromagnetic detection capability through the proper choice of run-in altitude based on existing refractive layers. Active methods of denial of electromagnetic detection can also use atmospheric phenomena to optimize the effectiveness of the jamming.

A dramatic demonstration of the tactical exploitation of atmospheric effects on strike survivability was provided in the Third Fleet exercise VALIANT HERITAGE conducted in 1976. E-2B aircraft of VAW-113 were equipped with AMR's during the exercise and determined a strong refractive layer at 1500 feet MSL. Two consecutive strikes were controlled against a TARTAR equipped surface ship. Reconstruction of the exercise revealed that the first strike, flying at 200 feet MSL and lower were detected at a range of 80 miles (well beyond the radar horizon) and tracked on a 1:1 blip/scan ratio throughout the strike. The second strike flew essentially the same profile except at an altitude of 200 feet above the 1500 foot layer. Detection on the second strike occurred at a range of 8 miles - and was made visually by the lookouts. While the first strike was engaged by missiles, the second strike was unopposed due to the short warning time and lack of electronic detection. Radar performance of the surface ship was constant throughout both strikes, and the remainder of the day.

The effectiveness of jamming in support of strike operations is vastly increased if the jammer is on the same side of a refractive layer as the victim radar. The radiated ECM energy is affected in the same manner as radar energy. Thus, the use of refractive layers to "trap" the jamming energy in the same altitude structure as the victim radar antenna magnifies the jamming effectiveness. Conversely, a layer between the radar antenna and the jammer "insulates" the radar antenna from the jamming energy and causes a deterioration of jamming effectiveness. It is readily apparent that jammer altitude selection is highly dependent on an accurate knowledge of layer composition. Against a surface radar, an altitude of 1000 feet MSL would be an excellent choice with a layer at 1200 feet, but would be a very poor choice with an 800 foot layer.

AAW

The consideration of refractive layers in force AAW defense is as essential to task force survival as it is to strike group survival. In much the same manner as ASW forces are positioned depending on water conditions, force detection platforms should be positioned based on existing atmospheric conditions. The operational commander has long used the "fade chart" designed for each radar antenna system to preclude "holes" in coverage by varying ship station. However, these charts are accurate only on a standard day. He must have the data available to station his forces on a "non-standard" day.

Altitude of CAP stations, airborne ESM platforms, and AEW stations are particularly dependent upon atmospheric conditions. Stationing on the wrong side of a layer can essentially negate the sophisticated radar and passive detection systems of these aircraft. As an example, again, referring to the experience gained by VAW-113 while deployed with the OPEVAL version of the AMR during exercise KANGAROO II in the South Pacific in 1977, an F-14 was vectored against a low flying F-111. Bogey altitude was estimated as 1000 feet (actually at 100 feet). An extremely strong layer existed between 1000 and 1300 feet. The F-14 chose a run-in altitude of 5000 feet. Detection was made visually when the controller called a merged plot. Yet this same F-14 was able to detect F-111's at ranges in excess of 80 miles both before and after this particular intercept - as long as the bogey and interceptor were on the same side of the layer.

During the same exercise, the E-2 determined a strong layer at an altitude of 18000 feet. A station was chosen below this layer to optimize low flyer detection, which was successful with detection ranges beyond that normally expected. However, a zero detection rate resulted for high flyers; i.e., bogies above the layer.

Similarly, EA-6 and S-3 ESM assets had an extremely low detection rate during this exercise, despite exceptionally good performance before and after. Although it is not documented, my opinion is that their performance was degraded by not taking into account the severe atmospheric anomolies present in the South Pacific off Australia. It was documented that the Australians (Orange Forces) utilized data on existing layer and ducts to plan their mission profiles.

Approximately midway through the exercise, CTF-77 recognized the requirement to consider atmospheric conditions in AAW. Cap station and AEW station altitudes were adjusted based on E-2 crew interpretation of AMR readouts. While performance of Blue AAW improved, the restrictions on ability to accurately read the AMR paper tape output precluded optimizing AAW stationing. The lack of IREPs equipment aboard Enterprise also precluded using the more accurate data contained on the AMR magnetic tape.

Command and Control Communications

The factors mentioned above for radar performance are equally as important to the operational commander when considering his command and control communications, particularly UHF. Modern task force operations are highly dependent on data links and UHF communications. The advantages of UHF Link 11 over HF Link 11 in allowing effective command and control while still denying the enemy long range locating data via HF-DF is obvious, as is the security of using UHF secure voice circuits vice unsecure HF circuits. However, stationing of AAW units is constrained by the maximum range of UHF propagation. While theoretically "line of sight", UHF can be trapped by atmospheric layers, with ranges in excess of 100 miles being experienced. It was not uncommon in the Gulf of Tonkin to have covered UHF communications between YANKEE station and the North SAR station via NAVY RED (an Un-relayed circuit) - a distance of more than 120 miles!

Control of CAP via LINK-4A from a surface platform, particularly at the mid and low altitudes, can be seriously degenerated when the CAP nears a refractive layer. The situation is anomalous to the blind zone of sonar caused by a temperature layer in the water, with the energy "splitting" and leaving an area in which the UHF energy cannot penetrate. While common sense would tell the pilot of the interceptor to climb to regain communications, an accurate knowledge of atmospheric conditions might indicate that descending below the layer would be the proper action.

UHF Link 11 with the E-2C, P3C and S-3A can also be optimized with a knowledge of refractive conditions. Does a datum 100 miles from the force necessarily mean that the force must shift to HF Link 11 if real time data are to be received from the ASW platform flying MAD traps at 100 feet? Can an E-2C 150 miles from the force necessarily maintain reliable UHF Link 11 at an altitude of 25,000 feet? A knowledge of the atmospheric anomolies can greatly aid the force commander in answering these and myriad other essential questions in the command and control area.

E-2 Required Capabilities

Once the staff of the operational commander has been shown the advantages to be gained by considering the need to determine anomalous conditions, the questions immediately arise as to what type of equipment is required to obtain the data, and then, what is the optimum air wing platform on which to mount the equipment. At the risk of sounding parochial, I maintain the only viable platform is the E-2 series aircraft for the following reasons:

1. The E-2 is the only aircraft embarked which must always climb through the atmosphere to perform its mission. In my experience, there is no mission of the E-2 which cannot be carried out at an altitude of 10,000 feet or more, unless anomalous conditions exist. It is axiomatic that the AMR equipment must be carried through the anomalous conditions in order to detect it.

2. The E-2 interfaces with every airwing mission, normally as a primary or secondary command and control agency.

3. The E-2 maintains communications, both voice and data link, with force commander during all missions.

4. The E-2 has the onboard computer and data link hardware necessary to process the AMR data with only minor modification required.

The capabilities required in the E-2 fall into two areas. First, the capability to immediately translate AMR data into a useful form for onboard use in determining optimum E-2 station altitude and optimum altitude for aircraft under the control of the E-2. Second, the E-2 must have the capability to get AMR data back to the force commander in real time for his use in deploying his force and in strike planning.

The OPEVAL report from VAW-113 thoroughly documents the limited use of the paper tape line graph in enabling the E-2 crew to accurately determine the existence and strength of layers. Far more useful was a simple log, kept by the co-pilot, of "N" values (refractive index) at each 100 feet of altitude. Most useful, however, was the IREPS computer installed on Enterprise during Valiant Heritage. The IREPS printout gave a graphic display of the effect of layers on a specific radar with the target at various altitudes. This display, however, was not available until the E-2 recovered and the magnetic tape was hand carried to the IREPS computer. Thus, the information was not usable by the force commander for approximately 4½ - 5 hours after the E-2 launched nor to E-2 crews until the 3rd launch of the day!

The IREP's personnel stated that the IREPs program is relatively small, and that it was entirely feasible to utilize the L-304 computer already in the E-2 to run the program and display the resulting graph of radar performance on the CRT display. Thus, the only modification to the E-2 required would be a capability to insert the magnetic tape data into the computer and a program to process the data and generate the display. This program would be short enough to be included on the magnetic data tape, and would thus be only a transit program which would essentially require little, if any, dedicated computer memory. Most of the memory required for both the program and the data could come from track store files and interceptor control files with the memory being returned to its original purpose after processing the data.

If one assumes the E-2 were to control a strike against a MOSKVA class ship, the scenario might run as follows:

1. The E-2 launches and climbs to station while the strike rendevous.

2. The E-2 CICO loads the AMR data tape into the computer and requests a display of HEADNET "C" performance.

3. The E-2 CICO determines optimum run in altitude and passes it to the strike leader via covered UHF voice.

4. The IREPs program and data are dumped from the computer and normal ATDS operations follow.

If going against a multi-ship formation, the E-2 CICO could query the computer for the other air search radars in the force as well.

The data on the frequency, etc., of radar which are required for the IREP's computations are already stored in the ATDS computer of the E-2C to enable the passive detection system to perform its function. In the E-2B, this data would have to be entered manually by the operator. In both cases, additional memory requirements are negligible.

The capability to relay the information back to the force commander should be done via a data link, for further processing aboard ship. The two data link systems equipment installed in the E-2, Link 11 and Link 4A, could be adapted to send this data. Due to its higher data rate, the Link 4A equipment would appear to be the logical choice. This could be done in a number of ways, one of which is to simply modify the Link 4A program such that the data transmitted was from the AMR magnetic tape data stores vice the normal UTM's and control data. This would cost the E-2 the ability to control interceptors via Link 4 during the brief period that the AMR data were being relayed, but would achieve full Link 4 capability once the relay was complete. The scenario in this case would be:

1. The E-2 launches and climbs to station, obtaining AMR data enroute.

2. The E-2 CICO loads the AMR magnetic tape into the L-304 computer.

3. The E-2 CICO enters a function code into the computer which causes the Link 4A system to broadcast the AMR data vice normal control data.

4. After a specified length of time or upon receiving directions from the surface station, the E-2 CICO enters another function code which returns the Link 4A to normal operations.

The equipment required to accomplish this capability is the same as needed to provide the onboard readout capability; i.e., the capability to read the magnetic tape into the computer and a transit program to cause the Link 4A to transmit AMR data vice Intercept Control data. No new shipboard equipment is required as the ship's Link 4A receiver can be used to receive the data. The only operational penalty is that the E-2 has no Link 4A capability while AMR data is being processed, and the ship has only one way data link capability (on a different frequency from the AMR data frequency). This latter drawback can be overcome if the ship uses a second UHF receiver to receive the AMR data. The loss of capability should be no more than 5 - 10 minutes.

Conclusions

This paper has discussed the value of atmospheric data to a force commander. The minor modifications to the E-2 series aircraft to obtain

this capability has been shown to be feasible and have a low cost factor. VAW-116 has already submitted a proposal to install a tape read capability in the E-2 series aircraft which would be compatible with the AMR tape cassette. Although the primary reason for submitting this proposal was for the input of PDS data and for data extraction, approval would also facilitate the effort to obtain and process AMR data. This tape drive capability has been favorably endorsed by the E-2 CORE committee and may soon be a reality.

The operational requirement for data on atmospheric anomalies should elicit support for AMR capability from all operational commanders. The success of offensive and defensive task force missions demands the capability to measure and utilize atmospheric conditions.

HYBRID RAY-MODE FORMULATION OF TROPOSPHERIC PROPAGATION

S. H. Cho, C. G. Migliora and L. B. Felsen
Department of Electrical Engineering
Polytechnic Institute of New York
Farmingdale, New York 11735

SUMMARY

High-frequency propagation in an elevated tropospheric duct is analyzed here by a new method involving an appropriate mixture of ray-optical fields and whispering gallery mode fields guided along the concave side of the duct boundary. In this formulation, ray fields may be regarded as expressing the remainder field when a guided mode series is truncated or, alternatively, a certain number of guided modes accounts for omitted higher order reflected rays. To explore the theory on a simple example, the duct is modeled by a single circular boundary separating an interior higher refractive index region from an exterior region with lower index. Source and observation points are assumed to be widely separated, and both are located on the duct boundary. The electric line source Green's function is first derived in terms of eigenmodes involving whispering gallery plus continuous spectrum contributions, and is then converted to the hybrid ray-mode alternative form. It is shown that the number of modes and rays required in the hybrid formulation is far less than when the field is expressed solely either in terms of modes or in terms of rays. A numerical example for typical tropospheric conditions indicates that a few of the lowest-loss modes are adequate to describe the field when source and observation points are on the boundary, rendering the ray contribution negligible. However, ray fields are expected to assume greater importance when the observation point, source point, or both, are located inside the duct.

1. INTRODUCTION AND CONCLUSIONS

In an elevated tropospheric duct, high frequency signals are guided with little attenuation by the outer boundary separating the duct (higher refractive index) medium from the exterior. The wave types responsible for this low-loss propagation mechanism are the whispering gallery (W.G.) modes, which have appreciable field strengths only in thin layers adjacent to the boundary. For an elevated source inside the duct, the field observed at long range may comprise many W.G. modes whose propagation and attenuation coefficients must be calculated very accurately for reliable prediction of the observed phase and amplitude of the transmitted signal. Because of interference between oscillatory modal fields, the total field is very sensitive to the contributions from the various relevant modal constituents.

An alternative procedure for calculating high-frequency fields is in terms of geometric-optical rays. Here, the presence of the concave boundary between the duct and exterior regions implies the existence of ray contributions undergoing many reflections before reaching a distant observation point inside the duct, and especially near the boundary. These multiply reflected ray fields of high order are not only tedious numerically but the notion of a ray-optical field becomes invalid when the ray travels too close to the boundary; in that event, one can no longer identify a local plane wave field (the boundary disturbs the phase front) which forms the foundation for a ray description.

The above observations suggest that a highly efficient and physically appealing method for analyzing high frequency tropospheric propagation would involve a mixture of rays and modes such that the fields extending relatively far from the duct boundary would be expressed in terms of rays while the fields clinging close to the boundary would be expressed in terms of W.G. modes. We have shown that such a hybrid formulation can indeed be achieved when the boundary is perfectly conducting (Ishihara, T. and L. B. Felsen, 1978) or characterized by a surface impedance (Ishihara, T and L. B. Felsen, 1979). The present paper extends this analysis to the tropospheric case where the boundary separates two media with different refractive indeces descriptive of tropospheric conditions. To establish the theory on the simplest model, the duct and exterior media are taken to be homogeneous, the duct boundary circular, and the propagation problem two-dimensional. Generalization to radial inhomogeneities and spherical geometry should pose no difficulties after the two dimensional model has been solved.

The analysis begins with the formulation of the exact electric line source Green's function in the two-medium cylindrical geometry. To include only the guiding effects of the interface between the source point Q and observation point P, without azimuthal periodicity of the field, the problem is posed in an infinitely extended angular space, equivalent to placing a "perfect absorber" at two radial planes. Such an absorber introduces spurious scattering effects from the radial coordinate origin, which are subsequently subtracted during the asymptotic (high-frequency) calculation of the field (Felsen, L. B. and N. Marcuvitz, 1973). The asymptotic Green's function is expressed in alternative forms comprising a) a discrete spectrum of proper eigenmodes plus a proper continuous spectrum, and b) a mixture of geometric optical fields, modal fields and a remainder integral, the contribution from the latter being negligible under suitable conditons. The detailed analysis, and corresponding numerical calculations for a model troposphere, have been performed for the special case when P and Q are widely separated and both are located on the interface. The mode-plus-continuous-spectrum representation has been used as a reference solution, with which the hybrid ray-mode formulation is compared. It is found that relatively few of the most tightly bound whispering gallery modes fully describe the field, rendering the ray contribution negligible. Therefore, this case is not best suited to demonstrating the utility of a ray-mode mixture. It is anticipated that this situation will change when the source point, the observation point, or both, are removed from the interface since the most tightly bound modal fields then have exponentially small amplitudes (Pappert, R. A. and C. L. Goodhart, 1977). Nevertheless, we have truncated the mode series by omitting some of the most tightly bound W.G. modes in order to force the ray contribution to be non-trivial. Under these circumstances, however, the validity of ordinary ray optics is being strained. The results show qualitative agreement that improves as the number of modes is increased and the number of rays reduced.

In summary, although the ray-optical field is unimportant for the present special example when all of the lowest-loss (most tightly bound) W. G. modes are included, the hybrid ray-mode formulation does demonstrate a systematic means for calculating the ducted fields in the most efficient numerical, and in a physically significant, manner. The number of rays and modes included in the representation is determined from well-defined criteria. Thus, the representation can be regarded as using rays to account quantitatively for the remainder field in a truncated mode series, or as using modes to account quantitatively for the remainder field in a truncated ray series, with the number of either being far less than when only one or the other is used exclusively. The method should have strong potential for dealing with lateral and longitudinal duct inhomogeneities, and with scattering by obstacles or localized scattering centers within the duct. These aspects are presently under study.

2. ALTERNATIVE FIELD REPRESENTATION

A. Green's function formulation

The physical model consists of two dielectric media separated by a cylindrical interface with radius $\rho = a$. The refractive indeces in medium 1 ($\rho < a$) and in medium 2 ($\rho > a$) are n_1 and n_2, respectively, with $n_1 > n_2$ but $n_1 \simeq n_2$. An electric line source is placed on the interface at an angular position $\phi = \phi'$. Since we are interested only in the guiding effects of the interface from the source point Q to an observation point P, it is necessary to remove the angular (2π) periodicity of the field in the cylindrical geometry. To this end, we place along two radial planes (which may be along a single diameter as in Fig. 1) a "perfect absorber for angularly propagating waves" which has the effect of extending the ϕ domain from its original $0 \leq \phi \leq 2\pi$ to $-\infty < \phi < \infty$, (Felsen, L. B. and N. Marcuvitz, 1973). Thus, waves originating at the source travel toward $|\phi| \to \infty$ without reflections, and the ϕ-dependence of the fields is not restrained to be periodic. The ficticious "perfect absorber" is, however, known to have the property of introducing a scattering center at the origin $\rho = 0$, which gives rise to spurious diffraction effects (Felsen, L. B. and N. Marcuvitz, 1973). These spurious contributions must be removed from the desired field representation. Since we are interested only in the lowest order asymptotic solution with respect to the large parameter $k_1 a$, where k_1 is the wavenumber in medium 1, this deletion can be accomplished when performing the asymptotic field calculation.

In the configuration of Fig. 1, the line-source-excited field (Green's function) $G(\rho, \phi; a, \phi')$ can be constructed in the following integral form (Felsen, L. B. and N. Marcuvitz, 1973):

$$G(\rho, \phi; a, \phi') = \frac{1}{2\pi} \int_C \hat{g}(\rho, a; \nu) \exp(i\nu |\phi - \phi'|) \, d\nu \tag{1}$$

where

$$\hat{g}(\rho, a; \nu) = \begin{cases} g(\rho, a; \nu) & \text{for } \mathrm{Re}(\nu) \geq 0 \\ g(\rho, a; -\nu) & \text{for } \mathrm{Re}(\nu) \leq 0 \end{cases} \tag{2}$$

and C is the integration path shown in Fig. 2. The radial Green's function $g(\rho, a; \nu)$ is obtained by imposing continuity on the tangential electric and magnetic fields at $\rho = a$, with the source placed at $\rho = a$:

$$g(\rho, a; \nu) = \frac{i\pi}{4} \begin{cases} \dfrac{\psi_1(k_1\rho)\psi_2(k_1 a)}{1 - R(\nu)} & , \ \rho \leq a \\ \dfrac{\psi_1(k_1 a)\psi_2(k_2 a)}{1 - R(\nu)} \dfrac{H_\nu^{(1)}(k_2\rho)}{H_\nu^{(1)}(k_2 a)} & , \ \rho \geq a \end{cases} \tag{3}$$

Here,

$$\psi_1(k_1\rho) = 2 J_\nu(k_1\rho) = H_\nu^{(1)}(k_1\rho) + H_\nu^{(2)}(k_1\rho) , \tag{4}$$

$$\psi_2(k_1\rho) = H_\nu^{(1)}(k_1\rho) + R(\nu) H_\nu^{(2)}(k_1\rho) , \tag{5}$$

$$R(\nu) = \frac{H_\nu^{(1)}(k_1 a)}{H_\nu^{(2)}(k_1 a)} \cdot \bar{R}(\nu) , \tag{6}$$

$$\bar{R}(\nu) = \frac{\left[H_\nu^{(1)'}(k_1 a)/H_\nu^{(1)}(k_1 a) \right] - \left[k_2/k_1 \, H_\nu^{(1)'}(k_2 a)/H_\nu^{(1)}(k_2 a) \right]}{\left[-H_\nu^{(2)'}(k_1 a)/H_\nu^{(2)}(k_1 a) \right] + \left[k_2/k_1 H_\nu^{(1)'}(k_2 a)/H_\nu^{(1)}(k_2 a) \right]} \tag{7}$$

and the wave numbers for the media on the concave and convex sides of the interface, respectively, are $k_i = k_o n_i$ ($i = 1, 2$), with k_o representing the wave number in free space, and n_i representing the refractive index.

From (3), the resonance equation for angularly propagating modes is

$$1 - R(\nu_q) = 0 \tag{8}$$

or equivalently

$$\frac{J_{\nu_q}'(k_1a)}{J_{\nu_q}(k_1a)} - \frac{k_2}{k_1}\frac{H_{\nu_q}^{(1)'}(k_2a)}{H_{\nu_q}^{(1)}(k_2a)} = 0 \tag{9}$$

The resonance equation in (9) has two sets of roots, one set near $J_\nu'(k_1a) = 0$ or $J_\nu(k_1a) = 0$ and the other set near $H_\nu^{(1)'}(k_2a) = 0$ or $H_\nu^{(1)}(k_2a) = 0$ as shown in Fig. 2. The first set of roots represents whispering gallery modes trapped on the concave side of the boundary, while the second set describes fields similar to the creeping waves on a perfectly conducting convex surface. Since k_1a is much larger than unity and k_2 is very close to k_1, (9) can be approximated near $\nu = k_1a$ in terms of Airy functions (Abramowitz and Stegun, 1964):

$$\frac{V'(t_q)}{V(t_q)} - (1-\Delta n)\frac{W_1'(t_q + x_D)}{W_1(t_q + x_D)} = 0 \tag{10}$$

where $\Delta n = n_1 - n_2 << 1$ and,

$$\nu_q = k_1a + (k_1a/2)^{1/3}t_q \ , \tag{11a}$$

$$x_D = 2\Delta_n (k_1a/2)^{2/3} \tag{11b}$$

$$V(t) \equiv Ai(t) \tag{12}$$

$$W_1(t) \equiv Ai(t) - i\,Bi(t) \tag{13}$$

When ν is not near k_1a, one may employ the Debye approximations (see A(4) in Appendix 1) in (9) to obtain:

$$\exp(-i\pi/2)\exp(i2\zeta(w_m))\cdot\frac{\cos w_m - \sqrt{\cos^2 w_m - 2\Delta n}}{\cos w_m + \sqrt{\cos^2 w_m - 2\Delta n}} = 1 \tag{14}$$

where

$$\zeta(w) = k_1a\,[\cos w - (\pi/2 - w)\sin w]\ , \quad \nu = k_1a\sin w\ . \tag{15}$$

Equation (14) is valid for those whispering gallery modes where the Debye approximation may be applied (see (A 14) appendix 1). A similar equation can be obtained for the creeping waves, but the contributions from the modes with ν_q far from k_2a are negligible. Thus one may use (10) for all relevant ν_q in the creeping wave contribution.

For the special case when the observation point also lies on the interface (i.e., $\rho = a$), (3) reduces on use of the Wronskian relation for the cylindrical functions to

$$g(a,a;\nu) = \frac{1}{k_1a\left[\dfrac{J_\nu'(k_1a)}{J_\nu(k_1a)} - \dfrac{k_2}{k_1}\dfrac{H_\nu^{(1)'}(k_2a)}{H_\nu^{(1)}(k_2a)}\right]} \tag{16}$$

This case shall be considered first.

B. Guided mode and continuous spectrum representation

The integration contour in (1) can be deformed around the singularities of the integrand in the upper half of the ν-plane since the integrand decays at infinity there. Applying Cauchy's theorem, one may write the Green's function in (1) as (Fig. 2):

$$G(a,\phi;a,\phi') = \frac{1}{2\pi}\int_0^{i\infty}[g(a,a;\nu) - g(a,a;-\nu)]\exp(i\nu|\phi-\phi'|)d\nu + \sum_{m=1}^{M}\bar{G}_m + \sum_{\ell=1}^{\infty}\bar{G}_\ell \tag{17}$$

where

$$\bar{G}_q = \frac{i}{k_1a}\frac{\exp(i\nu_q|\phi-\phi'|)}{\dfrac{\partial}{\partial\nu}\left[\dfrac{J_\nu'(k_1a)}{J_\nu(k_1a)} - (1-\Delta n)\dfrac{H_\nu^{(1)'}(k_2a)}{H_\nu^{(1)}(k_2a)}\right]_{\nu=\nu_q}} \tag{18}$$

With $q = m$ or ℓ in (18), $\bar{G}_m$ and $\bar{G}_\ell$ represent the whispering gallery modes and creeping waves, respectively. When we employ the Airy function approximation near $\nu = k_1a$, then

$$\bar{G}_q \sim \frac{-i}{2}\left(\frac{2}{k_1 a}\right)^{1/3} \frac{\exp(ik_1 d)\exp\left[\, i\,(k_1 a/2)^{1/3} t_q \,\right]}{\left\{ t_q - (1-\Delta n)(t_q + x_D) + (1-\Delta n)\Delta n \left[\frac{W_1'(t_q + x_D)}{W_1(t_q + x_D)}\right]^2 \right\}} \tag{19}$$

where d is $a|\phi-\phi'|$.

The branch cut integral in (17) can be written as

$$I = I_{c_o} + I_{s_1} + I_{s_2} \tag{20}$$

where

$$I_{c_o} = \frac{1}{2\pi} \int_{C_o} g_1(a,a;\nu) \exp(i\nu\,|\phi - \phi'|)\, d\nu \tag{21}$$

$$I_{s_1} = \frac{1}{2\pi} \int_{o}^{i\infty} [\, g_2(a,a;\nu) - g(a,a;-\nu)] \exp(i\nu\,|\phi-\phi'|) d\nu \tag{22}$$

$$I_{s_2} = \frac{-1}{2\pi} \int_{-i\infty}^{o} g_1(a,\, a\,;\, \nu) \exp(i\,\nu\,|\phi-\phi'|) d\nu \tag{23}$$

$$g(a,a;\nu) = g_1(a,a;\nu) + g_2(a,a;\nu) \tag{24}$$

$$g_1(a,a;\nu) = \frac{i\pi}{4} \psi_2^2(k_1 a)/[\,1 - R(\nu)] \tag{25a}$$

$$g_2(a,a;\nu) = \frac{i\pi}{4} H_\nu^{(2)}(k_1 a)\, \psi_2(k_1 a) \tag{25b}$$

and the integration path C_o lies along the imaginary axis in the ν-plane (Fig. 3). It can be shown (Appendix 1) that I_{s_1} and I_{s_2} are $O\left(\frac{1}{k_1 a}\right)$ and represent spurious diffraction effects associated with the origin ($\rho = 0$). These integrals may therefore be neglected. Thus, the continuous spectrum is expressed as $I \sim I_{c_o}$ in (20) and I_{c_o} can be simplified as follows (see Appendix 1):

$$I_{c_o} \sim \frac{1}{\pi} \int_{o}^{\infty} \frac{\exp[\,-k_1 a\,|\phi-\phi'|\sinh v\,]\, dv}{2\Delta n/\cosh^2 v - i\,4\exp[\,-2ik_1 a(\cosh v - v\sinh v\,]\exp[\,-\pi k_1 a \sinh v\,]} \tag{26}$$

This integral is in a convenient form for numerical calculation. Thus, the Green's function in (17) becomes

$$G(a,\phi\,;a,\,\phi') = \sum_{m=1}^{M} \bar{G}_m + \sum_{\ell=1}^{\infty} \bar{G}_\ell + I_{c_o} \tag{27}$$

with $\bar{G}_m$ or G_ℓ given in (18) and I_{c_o} given in (26). For $\bar{G}_\ell$, and for $\bar{G}_m$ with $\nu_m \simeq k_1 a$ or $k_2 a$, one may employ the simplified expression in (19).

C. Hybrid ray-mode representation

To obtain a hybrid representation containing a mixture of ray and whispering gallery mode fields, we return to I_{c_o} in (21), deform the integration contour to the right across some of the whispering gallery poles, perform a partial ray expansion of the integrand over the deformed path, and then provide an estimate for the remainder integral. A typical deformed contour $\bar{C}$ is shown in Fig. 3. It can be shown that the integrand of I_{c_o} behaves properly as $|\nu| \to \infty$ to legitimize the deformation. We now express $g_1(a,a;\nu)$ in the integrand in (21) as

$$g_1(a,a;\nu) = \frac{\psi_2^2(k_1 a)}{1 - R(\nu)} = \psi_2^2(k_1 a)\left[\, 1 + R(\nu) + \ldots + R^n(\nu) + \frac{R^{n+1}(\nu)}{1 - R(\nu)}\right] \tag{28}$$

where $\psi_2(k_1 a)$ and $R(\nu)$ are given in (5) and (6), respectively. Employing Debye approximations and choosing $\bar{C} = C_N$ as defined below, the integral becomes (see Fig. 4)

$$\bar{I} = \frac{1}{4\pi} \sum_{n=0}^{N} \int_{C_N} [\,1 + \bar{R}(w)]^2\, \bar{R}^n(w) \exp[\, i\, q_n(w)\,]\,(-i)^n dw + E_N \bar{M} \tag{29}$$

where

$$q_n(w) = k_1 a\, \{\, |\phi-\phi'| \sin w + 2(n+1)[\,\cos w - (\tfrac{\pi}{2} - w)\sin w]\,\} \tag{30}$$

$$R_{N\bar{M}} = \frac{1}{4\pi} \int_{\bar{C}_N} \frac{[1+\bar{R}(w)]^2 \bar{R}^{N+1}(w) \exp[iq_N(w)] \exp[i2\zeta(w)](-i)^{N+1}}{1 - \bar{R}(w) \exp[i2\zeta(w)](-i)} dw \tag{31a}$$

$$\zeta(w) = k_1 a [\cos w - (\pi/2 - w) \sin w] \tag{31b}$$

and

$$\nu = k_1 a \sin w \tag{31c}$$

The integral in (29) can be evaluated by the saddle point method (see Fig. 4). The saddle points w_n are determined by $dq_n(w)/=0^1$, and the integration path $\bar{C}_N$ is deformed into $\bar{C}_n$ (local steepest descent path). It may be shown that this deformation is possible, and the saddle point evaluation then yields:

$$\bar{I} = \sum_{n=0}^{N} G_n + R_{N\bar{M}} \tag{32a}$$

where

$$G_n = \frac{e^{i\pi/4}}{4} \sqrt{\frac{2}{\pi k_1 D_n}} (-i)^n [1+\bar{R}(w_n)]^2 \bar{R}^n(w_n) \exp(i k_1 D_n) \tag{32b}$$

with

$$\bar{R}(w) = \frac{\cos w_n - \sqrt{\cos^2 w_n - 2\Delta n}}{\cos w_n + \sqrt{\cos^2 w_n - 2\Delta n}} \tag{33a}$$

$$w_n = \pi/2 - |\phi - \phi'|/2(n+1) \tag{33b}$$

and

$$D_n = 2(n+1) a \sin[|\phi - \phi'| / 2(n+1)] \tag{33c}$$

The expression for G_n in (32) represents a geometric-optical ray field reflected n times from the concave side of the boundary on its travel from the source point to the observation point (see Fig. 5). At each reflection, the field amplitude changes by the reflection coefficient $\bar{R}(w_n)$. The remainder integral $R_{N\bar{M}}$ in (30) is taken over the local steepest descent path $\bar{C}_N$ corresponding to the last ray (n = N) included in the expansion. The subscript $N\bar{M}$ signifies that $\bar{M}$ whispering gallery modes lie to the right of w_N. The residues of those modes with $0 < \mathrm{Re}\, w_m < \mathrm{Re}\, w_N$ must be extracted from the sum in (27) since they were eliminated by deformation of C_o into $\bar{C}_N$. Thus,

$$G(a, \phi; a, \phi') = \sum_{n=0}^{N} G_n + \sum_{m=1}^{\bar{M}} \bar{G}_m + \sum_{\ell=1}^{L_N} \bar{G}_\ell + R_{N\bar{M}} \tag{34}$$

The upper limit of L_N instead of infinity on the creeping wave sum indicates that the path $\bar{C}_N$ may intercept the pole sequence w_ℓ as shown in Fig. 4. Actually, this is of little practical consequence since the contributions from the higher order creeping waves are very small. It is shown in Appendix 2 that

$$R_{N\bar{M}} \sim \frac{-|\bar{R}(w_N)|}{1 + |\bar{R}(w_N)|} G_N \tag{35}$$

provided that the saddle point w_N does not lie near poles w_m with $m = \bar{M}$ or $\bar{M}+1$.

3. NUMERICAL RESULTS

Numerical calculations were performed for a model troposphere with the following parameters: f = 900 MHz, a = 6369 km, Δn = 30 units, for variable range $d = a|\phi - \phi'|$. The guided-mode-plus-continuous-spectrum representation in (27) was used as a reference solution. It was found that 30 whispering gallery modes (i.e., M = 30) is adequate to yield accurate field values when the earth's boundary is assumed to lie at ρ = 6368 km. In fact, the maximum number of whispering gallery modes without the earth's surface is about $k_1 a/\pi$ ($\simeq 3\times10^7$), and the decay factor does not increase very much as the number of modes increases. With the presence of the earth's surface, it is found that the decay factor becomes large for the higher order modes lying beyond the 40th mode (Cho, S. H. and J. R. Wait, 1978). Therefore, the number of modes providing the major contribution to the total field ranges from 30 to 40. For large distances d, as considered here, the contributions from the creeping waves and the continuous spectrum are negligible.

The hybrid ray-mode calculation from (34) was performed for various combinations of rays and whispering gallery modes, but the number of modes $\bar{M}$ always included all of the modes having very small decay factors (these have poles lying between $\pi/2 - \sqrt{2\Delta n}$ and $\pi/2$). With the physical parameters chosen above, the number of these modes is six. The number of rays N was chosen such that $w_N < \pi/2 - \sqrt{2\Delta n}$. The physical interpretation of this condition is similar to that for the perfectly conducting boundary, and is schematized in Fig. 6. Also, the creeping waves are neglected in the hybrid representation, and the rays blocked by the earth's surface are eliminated in the calculation of the total field in order to compare the result with the field based on the whispering gallery modes only, in the presence of the earth. The rays

eliminated (i.e., blocked by the earth's surface) are indicated in Fig. 6(b). In Fig. 7(a), the amplitude of the total field is normalized to the field in the free space, with the distance between source and observation points measured along the interface.

The numerical results show that the modes having very small decay factors account completely for the total field, thereby rendering the ray-optical contribution and the remainder $R_{N\bar{M}}$ negligible. Thus, the hybrid ray-optical field formulation does not really show up to its best advantage for the present example where the source and observation points are both on the interface since a few tightly bound low-loss modes account efficiently for the observed field at long ranges. Nevertheless, the validity of the method is confirmed because the mode sum may legitimately be terminated after inclusion of only the lowest-loss modes, with the truncation error quantified by the (negligible) ray-optical field.

To force a situation where the geometric-optical field is not negligible, it is necessary to choose $\bar{M}$ so that not all low-loss modes are included. Accordingly, we have calculated the field also for $\bar{M} = 3, 4$. The results are shown in Fig. 7(b). The agreement with the reference solution is now poorer than before but the correct general trend is preserved. Since now $w_N > \pi/2 - \sqrt{2\Delta n}$, the ray reflection coefficient cannot be approximated by Debye formulas but requires use of the Airy function:

$$\bar{R}(t) \cong \frac{\dfrac{W_1'(t)}{W_1(t)} - \dfrac{W_1'(t+x_D)}{W_1(t+x_D)}}{\dfrac{-W_2'(t)}{W_2(t)} + \dfrac{W_1'(t+x_D)}{W_1(t+x_D)}} \tag{36}$$

with

$$t = (k_1 a/2)^{2/3} \bar{w}_n^2 \quad , \quad \bar{w} = \pi/2 - w \tag{36a}$$

It should be emphasized that the validity of the ray-optical formulation is strained in this parameter range since the rays strike the interface almost at grazing incidence.

When the source and (or) observation points are moved from the interface into the region $\rho < a$, the influence of the tightly bound whispering gallery modes with $\pi/2 - \sqrt{2\Delta n} < w_m < \pi/2$ is de-emphasized since their field decays rapidly away from the boundary (Pappert, R.A. and C.L. Goodhart, 1977). It is then expected that modes with $w_m < \pi/2 - \sqrt{2\Delta n}$ become important, thereby providing a better framework for the hybrid representation. This aspect is now being studied.

APPENDIX 1 - Approximation of continuous spectrum integral.

From (3) and the relation for the Hankel functions,

$$H_{-\nu}^{(2)}(k_1 a) = \exp(\pm i \nu \pi)\, H_{\nu}^{(2)}(k_1 a) \tag{A1}$$

one obtains

$$g(a, a, -\nu) = \frac{i\pi}{4} \frac{[\exp(i2\nu\pi)\, H_{\nu}^{(1)}(k_1 a) + H_{\nu}^{(2)}(k_1 a)]\psi_2(k_1 a)}{1 - \exp(i2\nu\pi)R(\nu)} \tag{A2}$$

Substituting (A2) into (22),

$$I_{s_1} = -\frac{i}{8} \int_0^{i\infty} \frac{\exp(i2\nu\pi)\, H_{\nu}^{(1)^2}(k_1 a)[1+\bar{R}(\nu)]^2}{1 - \exp(i2\nu\pi)\, \dfrac{H_{\nu}^{(1)}(k_1 a)}{H_{\nu}^{(2)}(k_1 a)}\, \bar{R}(\nu)} \exp(i\nu|\phi - \phi'|)\, d\nu \tag{A3}$$

One may employ Debye approximations for $|\nu - k_1 a| > (\frac{k_1 a}{2})^{1/3}$

$$H_{\nu}^{(2)}(ka) \sim \sqrt{\frac{2}{\pi k a \cos w}}\, \exp[\pm i \zeta(w) \mp i\pi/4] \tag{A4}$$

$$H_{\nu}^{(2)}(ka) \sim \sqrt{\frac{2\cos w}{\pi k a}}\, \exp[\pm i \zeta(w) \pm i\pi/4]$$

where

$$\zeta(w) = ka[\cos w - (\pi/2 - w)\sin w] \tag{A4a}$$

and (A4) is valid for $|\arg(\zeta(w)^{2/3})| < 2\pi/3$.

Let

$$\nu = k_1 a \sin w \tag{A5a}$$

and

$$d\nu = k_1 a \cos w\, dw = i k_1 a \cosh v\, dv \tag{A5b}$$

where the last equality is valid on the imaginary axis in the ν-plane (Abramowitz and I. Stegun, 1964). Using the Debye approximation in (A4), with (A5a, b), in (A3), one may obtain:

$$I_{s_1} \sim -\frac{1}{4\pi}\int_o^\infty \frac{[1+\bar{R}(v)]^2 \exp[-k_1 a\,(\pi+|\phi-\phi'|)\sinh v\,]\exp[i2k_1 a(\cosh v - v\sinh v)]}{1-(-i)\exp[i2k_1 a(\cosh v - v\sinh v)]\exp(-\pi k_1 a\sinh v)}\,dv$$

$$\sim -\frac{i}{4\pi}[1+\bar{R}(0)]^2\left[\frac{\exp(i2k_1 a)}{(\pi+|\phi-\phi'|)k_1 a}+(-i)\bar{R}(o)\frac{\exp(i4k_1 a)}{(2\pi+|\phi-\phi'|)k_1 a}+\text{-----}\right]+O\left(\frac{1}{k_1^2 a^2}\right) \quad (A6)$$

where

$$\bar{R}(0)=\frac{1-\sqrt{1-2\Delta n}}{1+\sqrt{1-2\Delta n}}$$

The asymptotic result in (A6) follows on geometric series expansion of the integrand and evaluation of each integral in the series by integration by parts. Similarly,

$$I_{s_2} = -\frac{i}{8}\int_o^{i\infty}\frac{\exp(i2\nu\pi)[H_\nu^{(1)}(k_1 a)]^2[1+\bar{R}(\nu)]^2\exp(-i\nu|\phi-\phi'|)}{1-\bar{R}(\nu)\exp(i2\nu\pi)H_\nu^{(1)}(k_1 a)/H_\nu^{(2)}(k_1 a)}\,d\nu$$

$$\sim -\frac{i}{4}[1+\bar{R}(o)]^2\left[\frac{\exp(i2k_1 a)}{(\pi-|\phi-\phi'|)k_1 a}+(-i)\bar{R}(o)\frac{\exp(+i4k_1 a)}{(2\pi-|\phi-\phi'|)k_1 a}---\right]+O\left(\frac{1}{k_1^2 a^2}\right) \quad (A7)$$

To deal with the integral I_{c_o} in (21), we write:

$$I_{c_0}=\frac{-i}{(\pi k_1 a)^2}\int_{-i\infty}^{i\infty}\frac{\exp(i\nu|\phi-\phi'|)\,d\nu}{[J_\nu'(k_1 a)-J_\nu(k_1 a)Z(\nu)][H_\nu^{(2)'}(k_1 a)-Z(\nu)H_\nu^{(2)}(k_1 a)]} \quad (A8)$$

where

$$Z(\nu)=\frac{k_2}{k_1}\,\frac{H_\nu^{(1)'}(k_2 a)}{H_\nu^{(1)}(k_2 a)} \quad (A9)$$

The denominator in (A8) may be rewritten as:

$$D=\frac{1}{2}\left\{H_\nu^{(1)'}(k_1 a)H_\nu^{(2)'}(k_1 a)-Z(\nu)[H_\nu^{(1)}(k_1 a)H_\nu^{(2)'}(k_1 a)+H_\nu^{(1)'}(k_1 a)H_\nu^{(2)}(k_1 a)]\right.$$

$$\left.+Z^2(\nu)H_\nu^{(2)}(k_1 a)H_\nu^{(1)}(k_1 a)+[H_\nu^{(2)'}(k_1 a)-Z(\nu)H_\nu^{(2)}(k_1 a)]^2\right\} \quad (A10)$$

Using Debye approximations from (A4),

$$D\sim\frac{1}{2}\,\frac{2\cos w}{\pi k_1 a}\left[\left(1+\frac{Z^2(w)}{\cos w}\right)+\exp(-i\pi/2)\left(1-\frac{Z(w)}{\cos w}\exp(i\pi/2)\right)^2\exp(-i2\zeta(w))\right] \quad (A11)$$

where

$$Z(w)=\frac{k_2}{k_1}\exp(i\pi/2)\cos w_2 \quad (A12)$$

with

$$\cos w_2 \sim \sqrt{1-\left(\frac{k_1}{k_2}\sin w\right)^2} \quad (A12a)$$

Thus, on the imaginary axis, for $v \geq 0$,

$$D\sim\frac{1}{2}\,\frac{2\cosh v}{\pi k_1 a}\left[\frac{2\Delta n}{\cosh^2 v}+\exp(-i\pi/2)\left(1+\sqrt{1-\frac{2\Delta n}{\cosh^2 v}}\right)^2\exp(-2i\zeta(v))\right] \quad (A13)$$

where $\zeta(v)$ is given by (31b) with $w = iv$. It follows that

$$I_{c_0}\sim\frac{1}{\pi}\int_o^\infty\frac{\exp(-k_1 a|\phi-\phi'|\sinh v)\,dv}{\left[\frac{2\Delta n}{\cosh^2 v}+4(-i)\exp(-\pi k_1 a\sinh v)\exp[-2ik_1 a(\cosh v - v\sinh v)]\right]} \quad (A14)$$

Here, the contribution from $-i\infty$ to 0 in (A8) is neglected since it is $O\left(\frac{1}{k_1 a}\right)$ (see A(6)).

APPENDIX 2 - Approximation of $R_{N\bar{M}}$

From (30),

$$R_{N\bar{M}} = \frac{1}{4\pi} \int_{C_N} \frac{[1+\bar{R}(w)]^2 [\bar{R}(w)]^{N+1} (-i)^{N+1} \exp(i q_N(w)) \exp[i2\zeta(w)]}{1 - \bar{R}(w) \exp[i2\zeta(w)](-i)} \tag{A15}$$

We now rewrite

$$\frac{(-i)\exp[i2\zeta(w)]\,\bar{R}(w)}{1-(-i)\exp[i2\zeta(w)]\,\bar{R}(w)} = -\frac{1}{2}\left[1 - \frac{1+(-i)\exp[2i\zeta(w)]\bar{R}(w)}{1+(-i)\exp[2i\zeta(w)]\bar{R}(w)}\right] \tag{A16}$$

$$= -\frac{1}{2}\left[1 + i\tan\left[\zeta(w) + \frac{\theta(w)}{2} + \pi/4\right] - i\frac{1}{2}\ln|\bar{R}(w)|\right] \tag{A17}$$

where

$$\bar{R}(w) = \exp[i\theta(w)]\exp[\ln|\bar{R}(w)|] \tag{A18}$$

If the saddle point w_N for the last ray satisfies

$$\zeta(w_N) + \frac{\theta(w_N)}{2} + \pi/4 = j\pi \tag{A19}$$

where j is an integer, then the remainder term becomes approximately (see (32))

$$R_{N\bar{M}} \sim -\frac{1}{2} G_N \left[1 - \frac{1-\bar{R}(w_N)}{1+\bar{R}(w_N)}\right] = -G_N \frac{|\bar{R}(w_N)|}{1+|\bar{R}(w_N)|} \tag{A20}$$

This result is used in (35).

[1] Note that the phase function $q_n(w)$ does not include the phase of the reflection coefficient terms that appear as amplitudes. Therefore, the ray paths do not have lateral shifts on the boundary. For the case of interest here, the shift effects are negligible when the Debye approximation can be applied.

REFERENCES

Abramowitz, M. and I. Stegun, 1964, "Handbook of Mathematical Functions," U.S. Government Printing Office.

Cho, S.H. and J.R. Wait, 1978, "Analysis of Microwave Ducting in an Inhomogeneous Troposphere," Pure and Applied Geophysics, Vol. 116, Birkhäuser Verlag, Basel, Switzerland.

Felsen, L.B. and N. Marcuvitz, 1973, "Radiation and Scattering of Waves," Chap. 6, Prentice Hall, Englewood Cliffs, New Jersey.

Ishihara, T. and L.B. Felsen, 1978, "High Frequency Fields Excited by a Line Source on a Perfectly Conducting Concave Cylindrical Boundary, IEEE Trans. on Antennas and Propagation, Vol. AP-26, pp. 757-767.

Ishihara, T. and L.B. Felsen, 1979, "High Frequency Fields Excited by a Line Source Located on a Concave Cylindrical Impedance Surface," to be published in IEEE Trans. on Antennas and Propagation.

Pappert, R.A. and C.L. Goodhart, 1977, "Case Studies of Beyond-the-Horizon Propagation in Tropospheric Duct Environments, Radio Science, Vol. 12, No. 1, pp. 75-88.

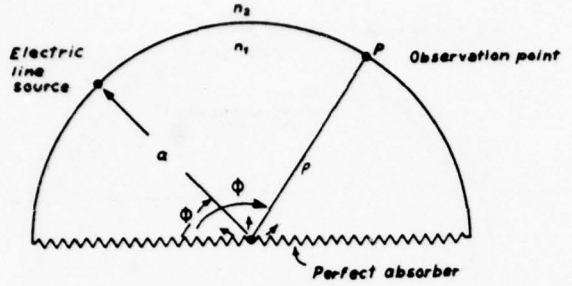

Fig. 1 Physical configuration. The "perfect angular absorber" introduces a scattering center at $\rho = 0$.

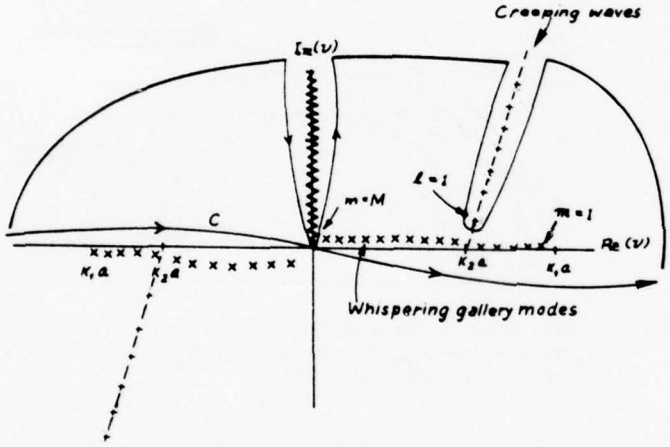

Fig. 2 Integration paths and singularities in complex ν-plane.

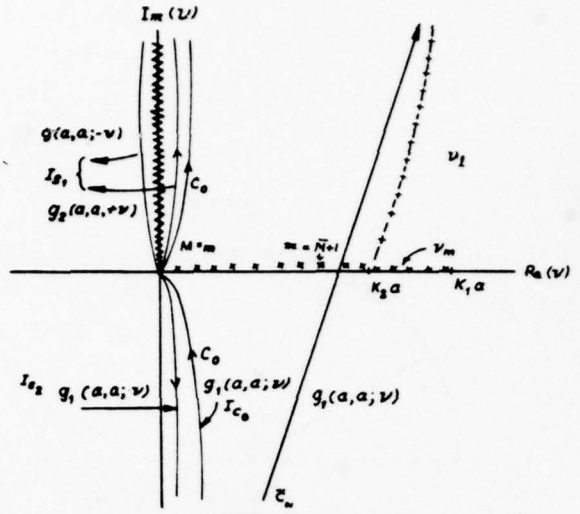

Fig. 3 Integration path decomposition in complex ν-plane. Also shown are the integrals I_{c_o}, I_{s_1} and I_{s_2}. When the integration contour C_o is changed to $\bar{C}_N$ with the same integrand, one obtains in addition to the integral along $\bar{C}_N$ the residues representing the whispering gallery modes from m = M to m = $\bar{M}$ +1.

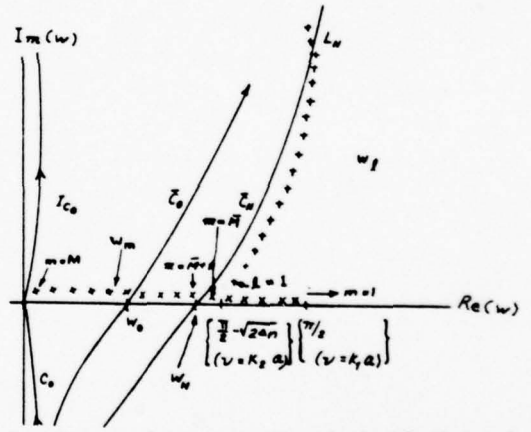

Fig. 4 Steepest descent paths and singularities in w-plane ($\nu = k_1 a \sin w$). The saddle points for the direct ray and the N times reflected ray (last ray) are w_o and w_N, respectively. When the remainder integral (see equation (31a)) is along $\bar{C}_N$, one has in addition to the integral the contributions from the whispering gallery mode poles m = $\bar{M}$ + 1 to M. Also the deformed path may capture creeping waves with $\ell \geq N$.

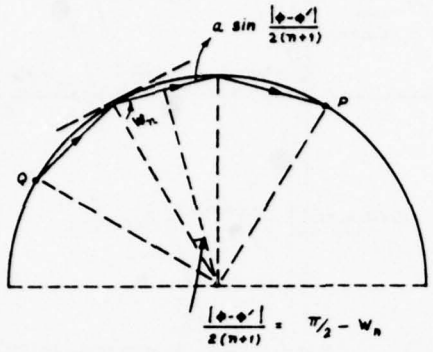

Fig. 5 Geometric optical ray path (n = 2).

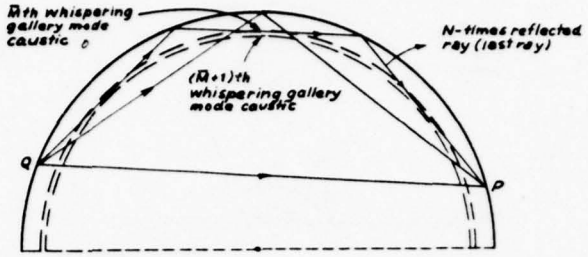

Fig. 6(a) In this sketch, without the earth's boundary, the effects of modes with caustics smaller than the Mth mode caustic are accounted for by ray optical fields with N = 2.

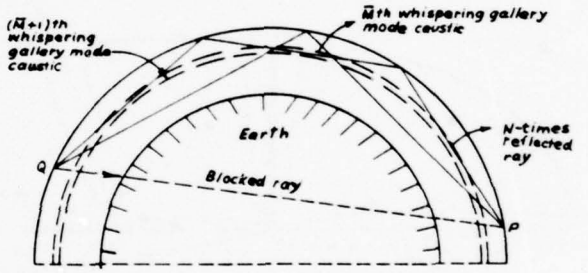

Fig. 6(b) In this sketch, in presence of the earth's boundary, the direct ray is blocked and omitted from the calculation.

Fig. 6 Pictorial representation of ray-mode combination. The $\bar{M}$ whispering gallery modes included are those whose caustics fit between the interface and the N-times reflected ray trajectory.

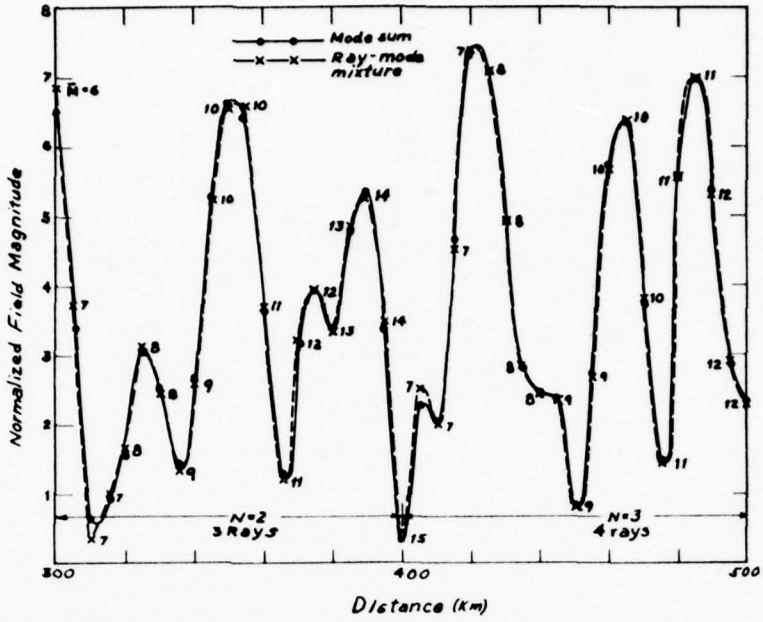

Fig. 7(a) $M \geq 6$ so that all whispering gallery modes with very small loss are included. The ray-optical contribution is very small.

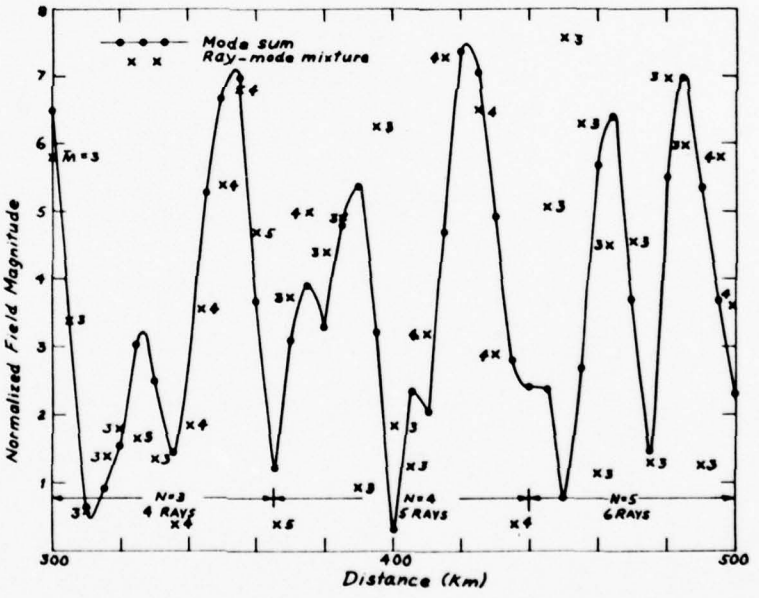

Fig. 7(b) $3 \leq M < 6$ so that some of the whispering gallery modes with very small loss are omitted. The ray-optical remainder may now be appreciable.

Fig. 7 Comparison of mixture of rays and whispering gallery modes with whispering gallery mode sum. The reference solution involves summation over 30 whispering gallery modes and is shown as the solid curve. The hybrid representation of modes and rays is shown as the dashed curve, and M and N indicate the number of modes and rays, respectively. Actually computed points are indicated by $\cdot$ for the mode sum and X for the ray-mode mixture, respectively, with the number next to X denoting M. The number N of included rays is shown near the bottom scale. The direct ray (n=0) is omitted from the calculation (see Fig. 6(b)).

CASE STUDIES OF TROPOSPHERIC PROPAGATION IN LATERALLY HOMOGENEOUS GUIDES

R. A. Pappert

EM Propagation Division

Naval Ocean Systems Center

San Diego, CA 92152

C. L. Goodhart

Megatek Corporation

1055 Shafter St.

San Diego, CA 92106

ABSTRACT

It has long been recognized that waveguide concepts can be used to at least qualitatively explain much anomalous tropospheric radio wave propagation and the advent of the electronic computer has made it possible in recent times to perform detailed case study comparisons between theory and experiment. In this paper several case studies which have been treated by waveguide concepts, which follow closely Budden's formalism, are reviewed. Points of discrepancy between calculation and observation are singled out along with some problem areas worthy of further study.

1. INTRODUCTION

For several years an effort at this laboratory has been directed towards waveguide computer modeling of propagation for a broad class of horizontally stratified refractivity structures. These include shallow surface ducts and ground based or earth detached ducts produced by elevated layers as well as the simultaneous occurrence of combinations of such environments. The computer modeling has advanced to the stage where it has been possible to perform detailed case study comparisons between theory and experiment and the intent of this paper is to review some of those case studies pointing out some of the areas of discrepancy along with some of the remaining problem areas.

2. APPROACH

Since waveguide formalism is well documented by a number of authors (Kerr, 1951; Brekhovskikh, 1960; Budden, 1961; Wait, 1972), the essence of the present approach will be reviewed only very briefly. First, the developments are in terms of an earth flattened geometry where earth curvature is included in the index of refraction. Therefore, in the usual terminology n in Figure 1 is the modified refractive index referenced to 1 at the ground and its height behavior for a combination surface duct and elevated layer is shown schematically. In the numerical methods used, the modified refractivity profile is approximated by linear segments. The number of linear segments is essentially unlimited. The normal modes are found subject to the boundary conditions of outgoing wave at the top and outgoing wave in the ground. The fundamental mode equation can be developed quite simply in terms of plane wave reflection coefficients. In Figure 1 is shown an infinitesimal vacuum gap at height b above the ground. The gap is also shown expanded with the inclusion of an upgoing and downgoing plane wave determined by the complex angle θ. If R_b is the plane wave reflection coefficient from everything above b, then R_b operating on the upgoing wave U gives the downgoing wave D. Similarly if $\bar{R}_b$ is the plane wave reflection coefficient from everything below b, then $\bar{R}_b$ operating on the downgoing wave D gives another upgoing wave. The self consistency requirement that the original upgoing wave equal the upgoing wave generated by the reflection processes yields the fundamental mode equation shown in Figure 1.

3. SOLVING THE MODE EQUATION

Crucial to any successful waveguide program is the determination of all significant complex zeros of the fundamental mode

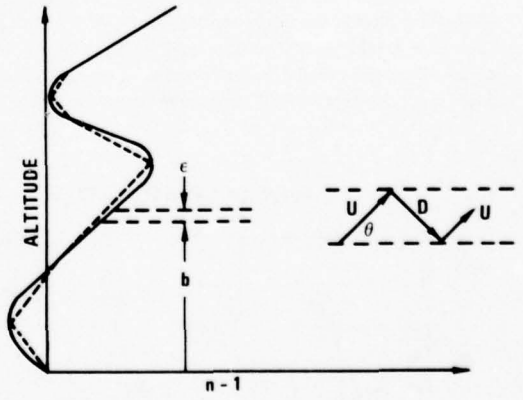

$$R_b(\theta)U = D$$

$$\bar{R}_b(\theta)R_b(\theta)U = \bar{R}_b(\theta)D = U$$

$$\left(1 - \bar{R}_b(\theta)R_b(\theta)\right)U = 0 \therefore 1 - \bar{R}_b(\theta)R_b(\theta) = 0$$

$$G(\theta_r, \theta_i) = \bar{R}_b(\theta)R_b(\theta) \models 1$$

Figure 1. Method of Approach and Mode Equation Development

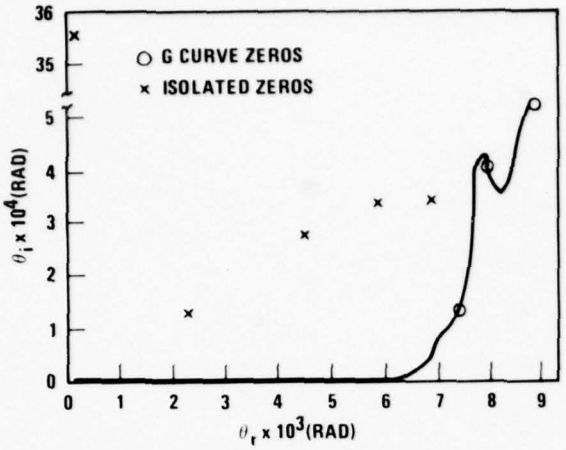

Figure 2. Zero Locations in the Complex Eigenangle Space

equation. One solution of the equation is $\theta = 0$. Using this knowledge and plotting the G curve defined in Figure 1 allows for one method of root extraction. An example is shown in Figure 2. The vertical axis is the imaginary part of θ and the horizontal axis the real part. The 0's denote solutions on the G curve traced from the origin. As will be seen there are also solutions, represented by X's in Figure 2, which do not fall on the G curve which emanates from the origin. It is believed these are isolated zeros (i.e., zeros on curves for which $|R\,\bar{R}| = 1$ closes upon itself). It is known (Pappert and Goodhart, 1978) that simple transformations can be used to change the topology of the complex θ space and we believe although by no means have proven that any mode of significance can be obtained by tracing a G curve from the origin. That is to say that a transformation can be made for which each of the X's in Figure 2, for example, can be made to fall along a G curve traced from the origin. Questions concerning the occurrence of isolated solutions as well as what can be done by transforming the topology of the eigenangle space are certainly difficult areas deserving of additional study.

Another method which by no means has been fully exploited for finding the mode solutions is based on an ingenious algorithm developed by Shellman and Morfitt (1976). It is based on searching the periphery of a rectangular region of the eigenangle space for zero or 180° phase contours of a modal function.

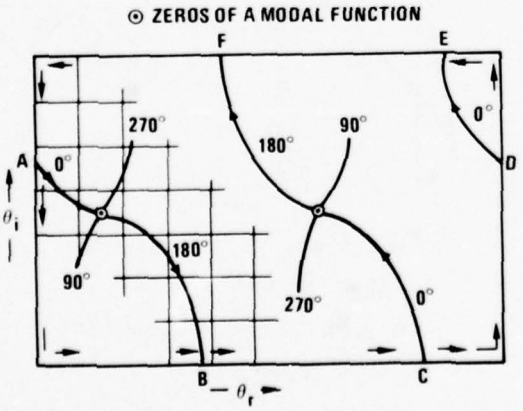

Figure 3. Schematic of Root Finding Method

The modal function is required to be analytic within and on the boundary of the search rectangle. The latter requirement guarantees that the phase contours must either terminate on zeros of the modal function or enter and exit the search rectangle (see Figure 3). To meet the requirement of analyticity within and on the boundary of the search rectangle generally requires considerable but straightforward transformation of the modal function shown in Figure 1. The method has been used successfully for trilinear profiles (Goodhart and Pappert, 1977); that is, modified refractivities approximated by three linear segments. The method certainly could, and we believe should, be extended to include a broader class of profiles. Lengthy computer times can be anticipated in using the method in the upper UHF band because the proximity of modal solutions can require very small mesh squares to be used in the two-dimensional search algorithm.

4. CASE STUDIES

To give an idea of the dynamic frequency range to which the waveguide formalism has been applied, we begin with a recent numerical study made of ducting in the HF band (Pappert and Goodhart, submitted to Radio Science). In a recent study P. Hansen (1977) reported measurements over a 235 km southern California all ocean path in the frequency range from 4 to 32 MHz. No skywave contamination existed for the path. Hansen found that above about 20 MHz the average signal levels considerably exceeded predictions based on standard ground wave theory. Available during a 24 hour period of Hansen's measurements were nine refractivity profiles recorded at four different sites which were in reasonable proximity to Hansen's path. Each refractivity provided an environment for which waveguide calculations were performed. Figure 4 shows measured and calculated path losses. The average path losses are at the midpoint of the error bars which represent one standard deviation on each side of the average. It will be seen that the calculated averages and the experimental averages are in good agreement. Disparity between the calculated and observed standard deviation is attributed to the likelihood of lateral inhomogeneity of the guide at any given time which has not been taken into account in the calculations.

A major purpose of Hansen's measurements was to check out Barrick's (1971) surface roughness theory for ground wave propagation. An area deserving study concerns the question of whether Barrick's theory applies in the presence of ducting environments; although it seems likely that surface roughness effects, except perhaps for the highest sea states, would be subdominant to the field enhancement due to the ducting at frequencies above about 20 MHz.

Figure 5 shows a case study made at 65 MHz. It applies to offshore San Diego measurements during a period when an inversion layer characterized by a 40 M unit deficit existed between about 600 and 1000 ft (Pappert and Goodhart, 1977). Shown are measured and calculated height gain behavior for a 120 nautical mile range with the receiver at 100 ft. The vertical axis is altitude and the horizontal axis is signal level in dB relative to free space. Also shown is the height gain for a "normal" nonducting environment. Enhancement of the signal due to ducting near the midpoint of the duct is about 40 dB and it should be noted that there is no evidence of a radar hole above the layer. On the contrary the signal levels above the layer are also much enhanced over the normal field. Clearly the waveguide model does an excellent job of predicting signal levels in this single mode case. The case study of Figure 5 is also of interest because it is a

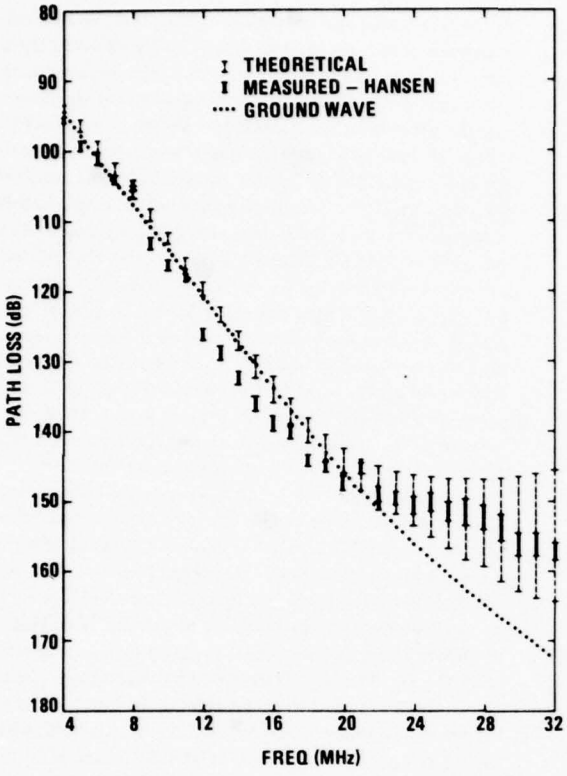

Figure 4. Case Study of Ducting at HF Frequencies

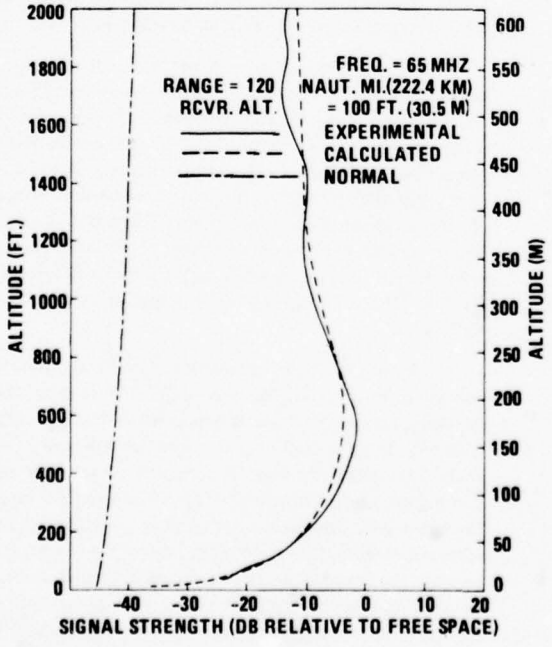

Figure 5. Height Gain Curves for Ground Based Duct

case for which calculations have been made using a phase integral method (Hayes, 1973). In particular, the method in this instance has been used to determine the reflection coefficient referenced to the ground for the layer structure shown schematically in Figure 6. K is the free space wave number and $z_{01,2}$ are zeros of the quantity q and are indicated schematically by the X's on the layer structure. If the zeros are sufficiently separated the exponential term in the denominator of R_0 is very small relative to one and the formula reduces to the conventional form given in standard textbooks. The modified form discussed by Hayes allows for leakage through the layer by virtue of the exponential term in the denominator.

Figure 7 shows a comparison of the phase integral calculation with the full wave and experimental results (Pappert, 1974). It will be seen that the phase integral method does quite an adequate job in this instance. Although much remains to be done in assessing the adequacy and utility of phase integral methods, they do seem to offer promise in applications such as IREPS (Richter and Hitney, 1977) where approximate but quick computational methods are required.

Figure 8 shows for the same environment which applied to Figure 5 height gains along with normal signal levels at 3.3 GHz for a 120 nautical mile range and receiver altitude of 500 ft (Pappert and Goodhart, 1977). The comparison between calculated and experimental results is quite good. This case is an example of signal level calculation by waveguide concepts when the number of modes is on the order of 100. The large number of modes points out the need, of course, for approximate methods such as ray hop, phase integral, GTD or hybrid methods. Nevertheless the results of Figure 8 show that with enough fortitude waveguide calculations can be carried at least to the several GHz range even for elevated layers and of course a reliable waveguide program can be used as a tape measure to assess the accuracy of approximate methods.

Figure 9 shows additional results close to 3 GHz (Pappert and Goodhart, 1977; Hitney, Pappert, Hattan and Goodhart, 1978). Shown are calculated and measured path losses as a function of range for a transmitter at 68 ft and a receiver at 3000 ft. The range covers the line of sight region, the

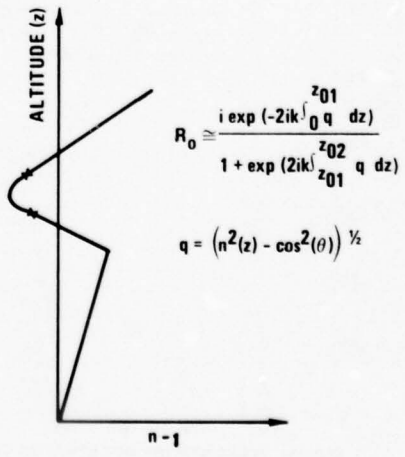

Figure 6. Phase Integral Method

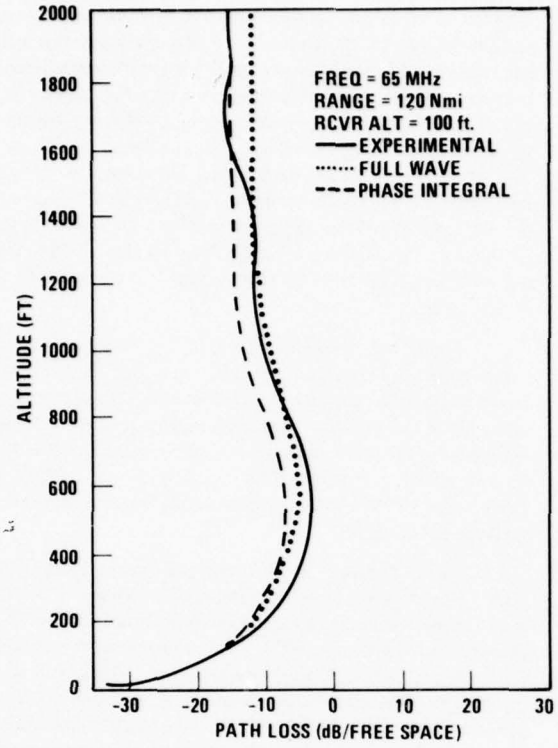

Figure 7. Phase Integral Comparison with Measurement and Full Wave Calculation

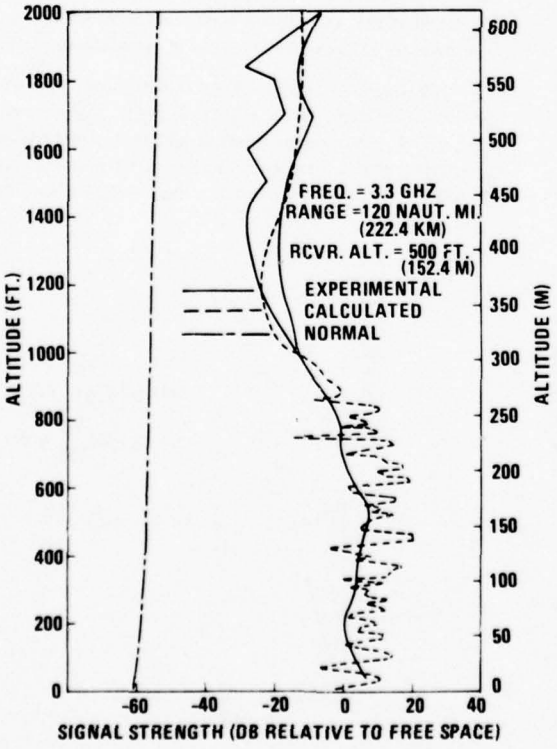

Figure 8. Height Gain Curve for Ground Based Duct

diffraction region and the region well beyond the horizon. Two waveguide results are shown. One is for the elevated layer environment shown in insert (b) of Figure 9, which was indicated by radiosonde measurements made during the period of the measurements and the other is for the surface duct shown in insert (c) which meteorological data indicated might have existed at the time of the measurements. The arrows are crude measures of the horizon for a direct ray ($\cong$ 75 naut. mi.) for a ray once reflected from the elevated layer ($\cong$ 170 naut. mi.) and for a ray twice reflected from the elevated layer ($\cong$ 290 naut. mi.). Observe that the waveguide calculated path loss for the elevated layer shows a large increase in the neighborhood of the arrows consistent with what might be expected on the basis of a ray hop picture and greatly overestimates the observed path loss beyond the first horizon. The waveguide calculation for the very strong evaporation duct gives reasonable agreement with the beyond the horizon signal. However, especially because of the difference between the experimental and shallow surface duct results close to the horizon we don't believe the shallow surface duct has been definitely established as the source of the lowly attenuated mode or modes propagating beyond the horizon. A possible alternative explanation is that there are many weakly attenuated modes of the elevated layer system which although not directly excited by the transmitter may be excited by mode conversion processes due to possible lateral inhomogeneity of the layer. This suggested explanation is shown schematically in Figure 10. The layer is indicated by the top two horizontal lines. The source and its image gives in the line of sight region a typical two source interference pattern, as indicated, which falls off at the horizon. If the layer is laterally inhomogeneous it would be expected that mode conversion from the direct field to weakly attenuated modes of the system would occur in the line of sight region. These weakly attenuated modes would then propagate beyond the horizon and radiate energy out as indicated, either by virtue of large scale lateral inhomogeneity or because of turbulence. The drawback in pursuing a model like this is of course that we know little about the large scale lateral inhomogeneity to be expected even on a statistical basis.

Figure 11 shows another in-flight path loss with range behavior recorded in an offshore San Diego environment. The feature of interest is the rather sudden recovery to nearly free space signal at about 65 naut. mi. The radiosonde data during the period of the measurement indicated the rather strong elevated layer at about 1500 ft. Waveguide calculations based on the elevated layer are shown by the dashed line in Figure 12 and as will be seen cannot explain the observation. An alternative explanation which we have pursued in rather cursory fashion is based on the following phenomenon which is used in integrated optics technology.

Figure 13 shows two identical guides and their individual modal height gain. The normal modes for the coupled system are the symmetric and antisymmetric combination g_1 and g_2, each with their individual propagation constants β_1 and β_2 respectively. If the field distribution as a function of x is taken to be expression g in Figure 13 it follows that at x = 0 the energy is localized about the lower guide, but at a coupling distance $\pi/(\beta_2 - \beta_1)$ the energy is localized about the upper guide. Based on this primitive notion we have examined quite arbitrarily whether such a coupling between the very strong evaporation duct shown in insert (c) of Figure 9 and the elevated layer might be responsible for the June 13th recovery. The result shown in Figure 14 for the combined system cannot explain the observed recovery and we are

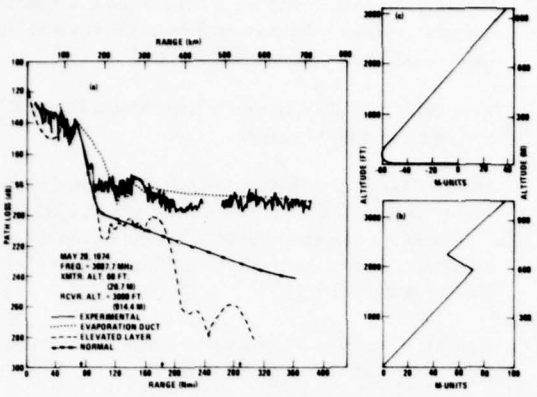

Figure 9. Measured and Calculated Path Loss Versus Range

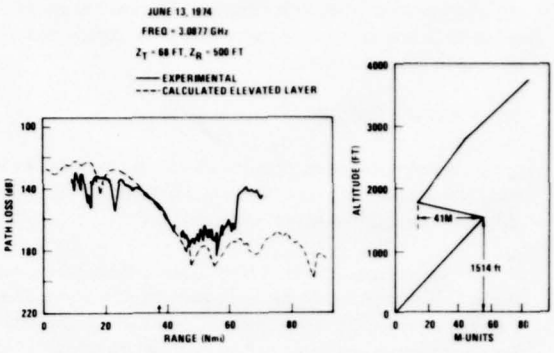

Figure 12. Measured and Calculated Path Loss Versus Range for Earth Detached Duct.

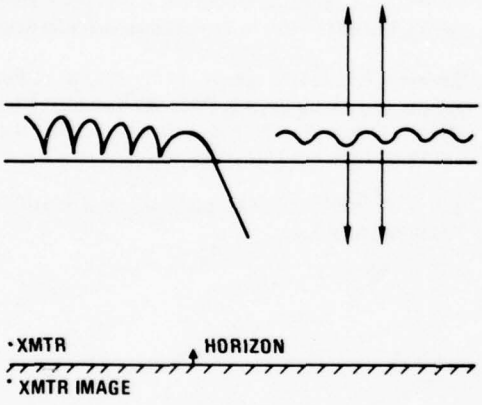

Figure 10. Schematic of Beyond The Horizon Radiation From Elevated Layer

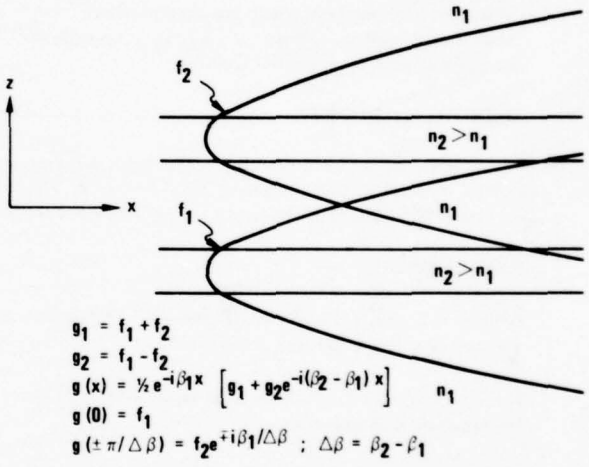

Figure 13. Schematic of Coupling of Two Identical Waveguides

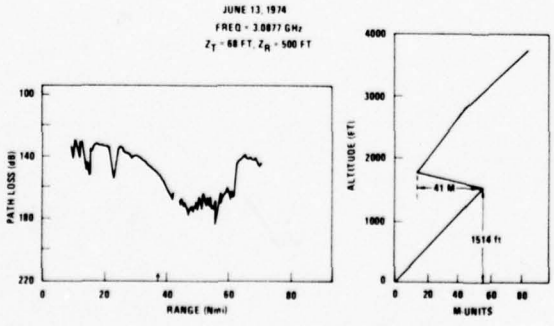

Figure 11. Measured Path Loss Versus Range

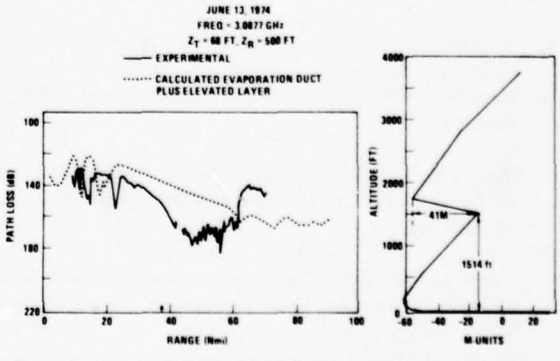

Figure 14. Measured and Calculated Path Loss Versus Range for Combination Surface and Earth Detached Duct

still at a loss to explain such behavior. The most likely explanation seems to be lateral inhomogeneity though no data is available relating to that possibility.

5. CONCLUSIONS

Two root finding methods which have been used with some success have been reviewed and the feeling is that this is still an area worthy of future research.

Several case studies of tropospheric ducting have been selected to illustrate the breadth of parametric situations to which waveguide formalism can be applied. Some of the case studies have met with considerable success (see e.g. Figures 4, 5 and 8) whereas some have met with complete failure (see e.g. Figures 12 and 14). It is believed that the failures are principally due to a lack of knowledge concerning the degree of lateral inhomogeneity of the layers studied. Theoretically there is much that can be done in implementing mode conversion methods (Cho and Wait, 1977) for such cases and this appears to be an area ripe for development. The need has been pointed out for developing approximate but quick methods (e.g. phase integral, ray hop, GTD or hybrid methods) appropriate to the microwave range. A reliable waveguide computer program, which has been the main issue of this paper, can, of course, be extremely useful in assessing the adequacy of such approximate methods.

ACKNOWLEDGEMENTS

Much of the work reported in this paper was performed under a contract with the Office of Naval Research. The authors are very grateful to Dr. H. Mullaney for his continued support.

REFERENCES

Barrick, D.E., 1971, Theory of HF and VHF Propagation Across a Rough Sea, Radio Science, 6, 517–533

Budden, K.G., 1961, The Waveguide Mode Theory of Wave Propagation, Logos, London

Brekhovskikh, L.M., 1960, Waves in Layered Media, Academic, New York

Cho, S.H., and J.R. Wait, 1977, EM Propagation in a Laterally Non Uniform Troposphere, Cooperative Institute for Research in Environmental Sciences (CIRES), University of Colorado, EM Report 1

Goodhart, C.L., and R.A. Pappert, 1977, Application of a Root Finding Method for Tropospheric Ducting Produced by Trilinear Refractivity Profiles, Naval Ocean Systems Center Technical Report 153

Hansen, P., 1977, Measurements of Basic Transmission Loss for HF Ground Wave Propagation in Sea Water, Radio Science, 12, 397–404

Hayes, M.G.W., 1973, The Transition from Locked to Leaky Modes in Tropospheric Radio Propagation, Journal of Physics A, 6, 177–191

Hitney, H.V., R.A. Pappert, C.P. Hattan and C.L. Goodhart, 1978, Evaporation Duct Influences on Beyond-the-Horizon High Altitude Signals, Radio Science, 13, 669–675

Kerr, D.E., 1951, Propagation of Short Radio Waves, MIT Rad. Ser., McGraw-Hill, New York

Morfitt, D.G., and C.H. Shellman, 1976, "Modesrch", An Improved Computer Program for Obtaining ELF/VLF/LF Mode Constants in an Earth-Ionosphere Waveguide, Naval Electronics Laboratory Center Interim Report 77T prepared for the Defense Nuclear Agency (DNA)

Pappert, R.A., 1974, Phase Integral Calculations for a Ducting Environment at VHF Through Microwaves, Naval Electronics Laboratory Center Technical Note 2845

Pappert, R.A., and C.L. Goodhart, 1977, Case Studies of Beyond-the-Horizon Propagation in Tropospheric Ducting Environments, Radio Science, 12, 75–87

Pappert, R.A., and C.L. Goodhart, 1978, Electromagnetic Propagation in Horizontally Stratified Ducting Environments, Naval Ocean Systems Center Technical Note 510

Pappert, R.A., and C.L. Goodhart, A Numerical Study of Tropospheric Ducting at HF, to be published in Radio Science

Richter, J.H. and H.V. Hitney, 1977: IREPS: A Refractive Effects Assessment System, Proc. 7th Technical Exchange Conference, El Paso, Tx. Published by ASL, WSMR, NM 88002, pp. 77–81

Wait, J. R., 1972, Electromagnetic Waves in Stratified Media, Pergamon, New York

MARITIME SURFACE DUCTING: UK MEASUREMENT AND THEORY

J F Sketchley

Admiralty Surface Weapons Establishment

Portsmouth, UK

ABSTRACT

The development of the UK's detailed model of surface evaporation ducting is summarised, together with its application to the preparation of a radiowave range prediction method for operational use at sea. The method's shortcomings include difficulty of use; alternative remedies are the provision of each ship with a book of curves giving the performance of its sensors in various conditions, or the implementation of the method on a programmable calculator. Initial evaluation data suggests that a significant improvement over earlier methods is to be expected, but that significant scatter remains. A further limitation is the breakdown of the model in certain conditions.

A year's measurement programme in West Cornwall (1976-7) is described in which regular samples were taken of I Band signal strengths over fixed over-water paths, both over-horizon and line of sight. The receiving station included antennas at several heights close to the sea surface. A wide variety of sea and air conditions, some representing open ocean, were covered. Results presented include details of height-gain curves, fading characteristics, and comparisons with the theoretical model.

The conclusions of the study include the following. The UK model is highly sensitive to met measurement accuracy, especially humidity. Simpler models may give as good an estimate of surface duct propagation as the full model (at least in this case). Current synoptic pictures could be useful for broad brush prediction. Not enough is known about the horizontal homogeneity of surface layers in coastal waters. Further work is required to determine the contributions of elevated layers and other types of surface refractive layer; it is not clear for what proportion of the time it is safe to make surface-to-surface predictions using a single surface ducting model.

1. INTRODUCTION

This paper covers more than one of the major topics of this conference: it is to some extent a position paper, rather than a detailed treatment of any one aspect of our work. It was felt that such an overview would be most appropriate in the circumstances.

The work described has been carried out by the Admiralty Surface Weapons Establishment and its contractors. This paper does not necessarily represent the position of other UK authorities.

The first part of this paper outlines the development of our surface duct model, and its application to prediction methods for use at sea. Our more recent propagation measurement programme is then described, together with the conclusions and outstanding problems.

1.1 Historical Background

Our work arose out of a requirement to be able to characterise and if possible predict the variable over-the-horizon propagation conditions we were encountering, which were previously dismissed as 'anomalous'. An initial trial, using aircraft range runs against a fixed site, demonstrated the wide variations of signal levels to be expected from refraction effects, and established a need for a fuller theoretical understanding of the surface duct, supported by a more extensive and controlled measurement programme.

2. MODELLING

A theoretical model of Surface Evaporation Ducting has been developed for us by S Rotheram at Marconi Research Laboratories, Chelmsford, England.

A model of the refractive index profile has been constructed, incorporating recent boundary-layer theory. The revised set of refractive index profiles has then been incorporated into a wave-guide mode model of the beyond horizon propagation through the duct.

The model has been applied retrospectively to data from the Hamburg University paths in the southern North Sea. Good agreement between theory and measurement was obtained.

A further development of the theoretical model has been made to cover line-of-sight propagation. A phase integral representation is used for the wave propagation in the layered refracting structure of the duct. Solutions to the differential equation are developed from Weber parabolic cylinder functions. Several different integrals are required to cover the different cases:

(a) Direct and reflected waves.

(b) Weak and strong ducting.

(c) Disposition of the terminal points with respect to the duct. Three different classes of path are identified.

The position of the interference lobes is shifted due to the phase shift introduced by different refraction effects on direct and reflected path lengths. The corresponding imbalance of amplitudes reduces the depths of the nulls, since complete cancellation depends upon equal amplitudes of direct and reflected waves.

The effect of sea roughness has been incorporated in the model, the incoherent reflected wave being treated statistically.

The effect of the rough sea is to decrease the coherently reflected wave, particularly at short ranges, and thus reduce the amplitude of the interference pattern. The 5% and 95% probability levels are also included. In the presence of a strong duct, the angle of incidence at reflection from the sea tends tc increase, which in turn leads to a larger value of the Rayleigh Parameter and to an increase in the magnitude of the incoherent reflected wave. This is another way of saying that we expect sea clutter to be enhanced under ducting conditions.

At the same time the coherent reflected wave is much reduced, thus reducing the amplitude of the interference pattern still further. The phase effect (ie the displacement of the lobes) is the same as for the smooth sea case.

3. APPLICATIONS

3.1 Engineers' Curves

The principal application of the Surface Duct Model is to assessments of the performance of existing and future sensor systems in ducting conditions. The model itself is available to our engineers in the form of a FORTRAN program suite. Additionally a book of Engineers' Curves has been prepared, which may be entered with the Duct Height, Atmospheric Stability, Sea State, and system parameters ie Antenna Heights, Radio Frequency. Curves of signal strength (with respect to free space) versus range are presented, together with curves of attenuation coefficients and height gain functions to enable other curves to be constructed, eg: signal strength vs height, or signal strength vs duct height. A full range of ducting conditions and radio frequencies is covered, for the beyond-horizon case only.

3.2 RSG-6 Prediction Method

Another important application of this work is to the on-board prediction of propagation conditions and their effects on sensors, using on-scene meteorological measurements. A manual prediction method has been prepared from Rotherams theoretical model, with funding from NATO Research Study Group RSG-6.

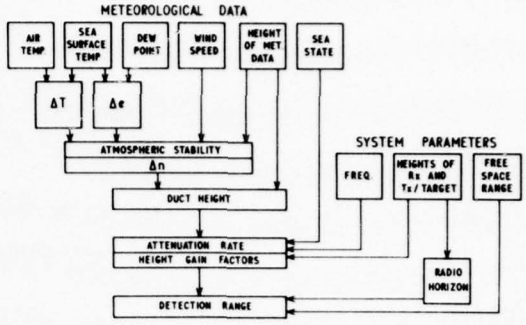

Figure 1. RSG-6 Prediction Method.

The form of the calculation is indicated in Figure 1. The usual single-point met data are used, namely air temperature, humidity and wind speed at a single known height above the sea, together with sea temperature. A correction for sea state is also available. The calculation proceeds via duct height and atmospheric stability. For each sensor system the radio frequency and receiver and transmitter or target heights are then brought in, together with the power factors such as e.r.p., receiver sensitivity, target cross-section; these power factors are incorporated into a once-and-for-all calculation of free space range.

If an assumption has been made, such as a standard target in the radar case or a standard emitter type in the ESM case, it is better that this should be explicit and not buried in the prediction method. I have therefore recommended that a warning note should accompany any prediction that depends on assumptions of this kind. It is important not to give the impression of precision where none exists.

The calculation is at present set out as approximately 30 steps, each of which is either a simple arithmetic calculation or a curve reading. It is assumed that a simple calculator will be available to assist with the arithmetic. The method is designed for use by qualified Met Officers, like its predecessor; it can be expected to take in excess of 15 minutes to perform, although the initial ten steps leading to duct height and atmospheric stability do not have to be repeated when considering additional sensors operating in the same environment.

A preliminary comparison has been made between the RSG-6 prediction method and an earlier method based on German work, using ship-to-ship data collected on a deployment in the Red Sea and South Pacific in 1975/6. The data sample is small, but includes UHF/VHF, E/F and I bands. Strong evaporation ducting was present throughout the sample.

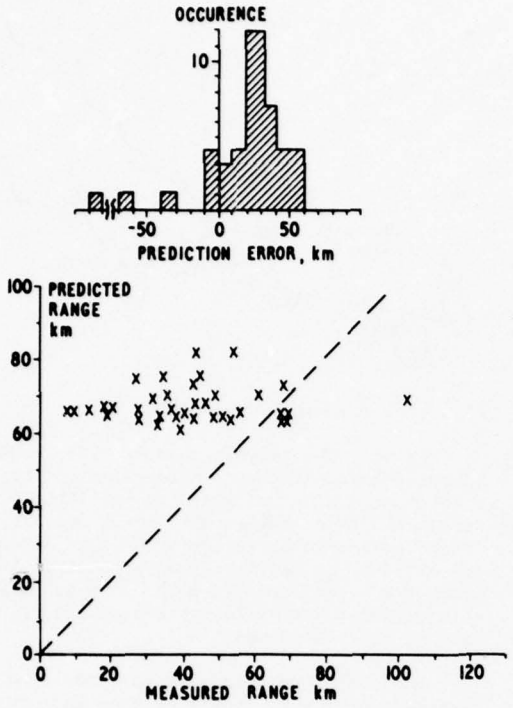

Figure 2. 'German' Prediction Method Performance.

Figure 2 indicates the performance of the older method. Predicted maximum range is plotted against measured maximum range. An error histogram is given above, error being defined as prediction minus measured signal. The method fails to account for the variation of the range enhancement with radio frequency (this is the main failing) and with terminal height and power factors.

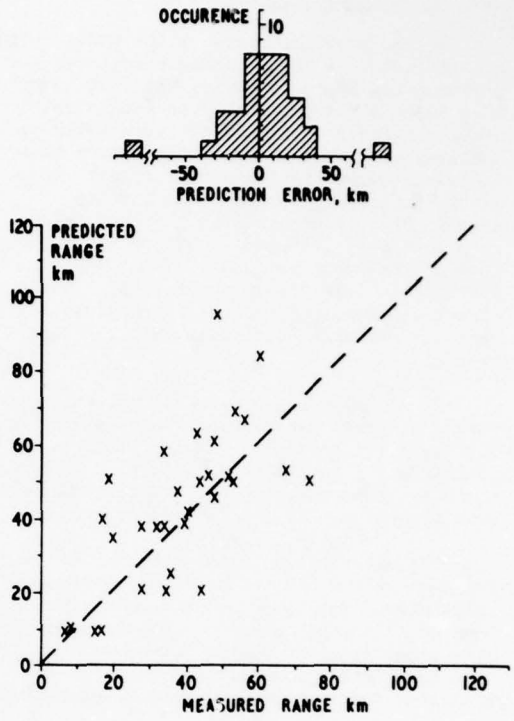

Figure 3. RSG-6 Prediction Method Performance.

Figure 3 shows the performance of the Marconi method against the same data. The variation with RF is much better modelled. A considerable scatter still remains, but is centred about zero error. ESM intercept ranges during the trial were particularly variable and difficult to predict. From this limited sample it can be said that the Marconi method shows promise. It does have limitations however:

(a) It only deals with surface evaporation ducting. Evidence is accumulating to the effect that in many cases it is not safe to ignore other forms of refraction effect, such as elevated layers and advection ducts.

(b) The duct model used breaks down under certain conditions; fortunately in a fairly obvious way. When the air temperature is much in excess of sea temperature, excessive duct heights are returned which lead to invalid predictions. We have found that the failure conditions are not common in temperate waters, but about a third of the data from the Red Sea and South Pacific led to failure. Further refinement of the duct model will be required if the method is to be fully useful world wide.

(c) In its present form the method is too slow and difficult to use. We have therefore studied methods for simplifying and/or automation of the method, especially for use on smaller ships.

3.3 'Fast Prediction Method'

In one possible solution the usual met data are collected; a programmable calculator then performs the steps to derive the duct height. This value might profitably be communicated to other platforms in the force, especially to those unable to make met measurements themselves. Another alternative is to include duct height in a more general forecast. This has the disadvantage of generality; the surface duct can be a localised phenomenon. There is no substitute for good on-scene met data. The climate around the British Isles is very variable, limiting the effectiveness of historical refractivity methods: short term changes tend to swamp long term trends.

The final stage of the method could use curves of performance versus duct height, prepared for the given ship's particular sensors, and thus incorporating the known antenna heights and power factors. Separate curves would be required for each frequency band and for each radar type.

The alternative to these curves is to implement the whole method on a programmable calculator. This has just been achieved (with some shuffling of cards) on a Hewlett Packard 67. Some simplification of the method was required. This Fast Prediction Method has now to be evaluated for accuracy and ease of operation.

4. WEST CORNWALL MEASUREMENT PROGRAMME 1976-7

To supplement the evaluation of Rotheram's model against German data from Helgoland, we have made an extended series of propagation measurements at Gunwalloe in West Cornwall, aimed particularly at covering a wide range of weather conditions, and collecting data for a range of receiver heights.

4.1 Sites and Conditions

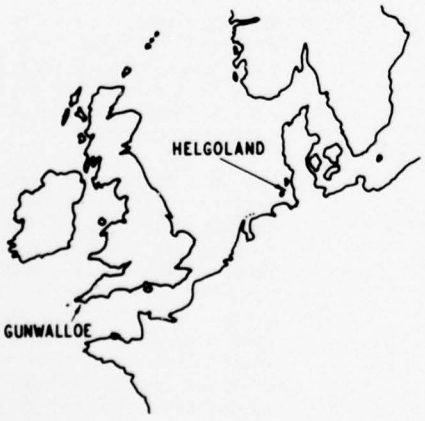

Figure 4. Location of Propagation Sites.

The West Cornwall location was chosen because it is reasonably open to N Atlantic weather and sea conditions in the prevailing SW air stream.

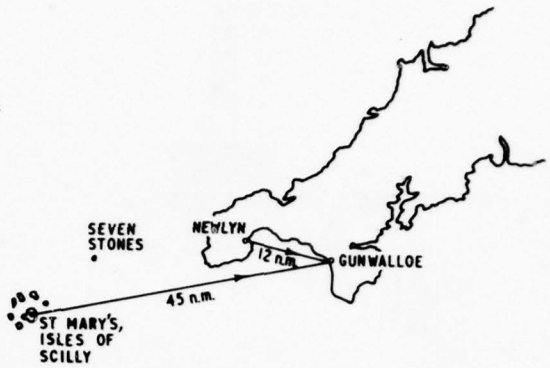

Figure 5. Cornwall Propagation Paths.

Fixed paths between coastal sites were used, to provide sampling over a long period, to provide a wider coverage than would be available from relatively short trials with ships and aircraft I band navigational radars with fixed antennas are sited at St Mary's, Isles of Scilly, to provide a beyond horizon path of 45 nautical miles, and at Newlyn to provide a line of sight path of nautical miles.

Horizontal polarisation is used. The 3.9 dB beamwidth of the St Mary's antenna is narrow enough to eliminate all but the lowest elevated ducts from effective contribution to the received signal at Gunwalloe. Similar J band transmitters have recently been commissioned on each site; but measurements are in progress. Met data for ducting calculations are collected at Seven Stones Light Vessel, adjacent to the long path, supplemented by measurements at the coast when appropriate.

The receiving site at Gunwalloe is equipped with antennas at 50 feet above low water and a stack of six horns between low water and 25 feet. These give us a fairly full set of measuring heights as the tide height varies. The sea bed shelves steeply in front of the mast, so wave steepening is only significant close in, and open sea conditions are maintained over most of the path in southerly weather.

The main measuring programme comprised one week's measurement each month for a year, thus sampling a variety of conditions. Signal levels on both paths and at all heights were recorded every four hours, at times coinciding with met data collection at Seven Stones. More frequent recordings were taken when signal behaviour required.

The climate sampled in the year included, as we had hoped, a very wide variety of weather and sea conditions, ranging from calm dry high pressure to the strong winds and rapidly changing conditions associated with the passage of depressions and frontal systems. Another important and fairly common weather type is relative calm with sea mist or fog. In these conditions no duct becomes established - poor visibility and poor over-the-horizon radar coverage being correlated in this case.

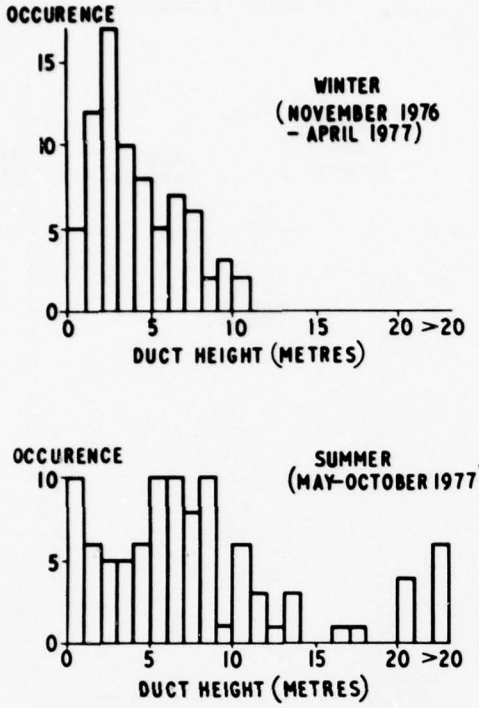

Figure 6. Occurrence of Duct Height (Seven Stones).

Figure 6 presents histograms of the calculated duct height for the summer and winter periods. The strongest ducts appeared only in the summer months, but significant ducting can occur year-round.

4.2 Signal Characteristics and Fading

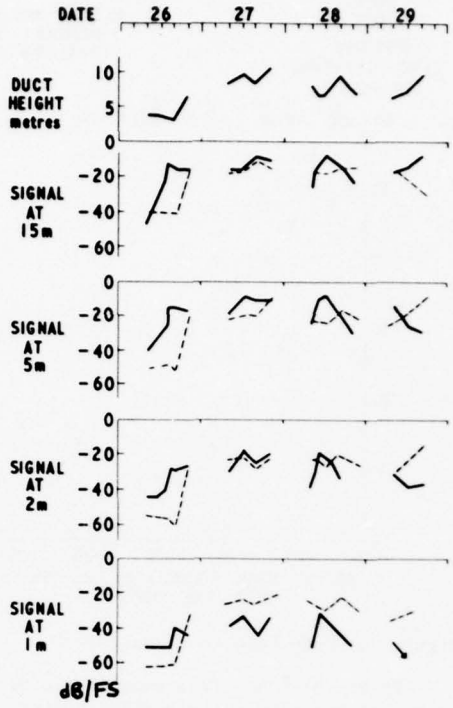

Figure 7. Beyond-horizon Signal, 26-29 April 1977.

Figure 7 shows a typical plot of four days over-the-horizon signal data. The dotted lines represent signal predictions. The following points are worth noting:

(a) The signals at different heights have similar time variation. An interesting exception is the first of the four days, where a sharp rise in signal level becomes established first at 15 metres, and subsequently in turn at 5 metres, 2 metres and 1 metre, over a period of hours. Large, sudden changes of signal level were often readily correlated with the passage of frontal weather systems.

(b) The prediction follows the measured signal's overall variation, on a time-scale of several days. It fails to keep in step with the sudden increase on the 26th however. This time lag between prediction and measured signal was observed on several occasions; it suggests the movement over the area of a horizontally inhomogeneous air mass.

A subset of the recorded signal data has been examined for fading characteristics. The subset derives entirely from summer measurements (April, May and June) but it includes the full range of signal levels and propagation conditions.

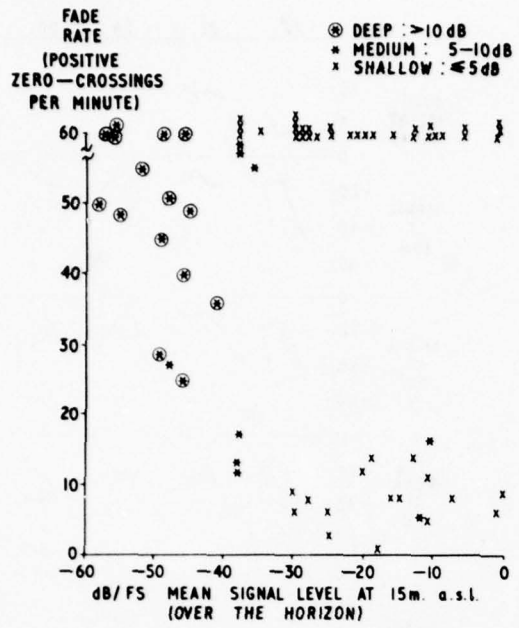

Figure 8. Fade Rate vs Signal Level.

In Figure 8 the fade rate (positive zero-crossings per minute) is plotted against signal level. Fading depth is also indicated by categorising the points, into shallow, medium and deep fading to help to distinguish fading types.

The compression at the top of the figure is due to limitations of the recording medium, which would not allow measurement of fade rates greater than 60 Hz, though they could still be resolved.

The following features were observed:

(a) Weak signals exhibit deep fast fading, the Rayleigh fading of a scatter signal.

(b) Stronger signals experience two principal types of fading:

(i) Shallow, fast scintillation, which was in fact observed in virtually all signals.

(ii) Slower variations in level, which in most cases are also shallow. With very strong signals, however, deep slow fading may sometimes occur.

The line of sight signal was almost always steady, but subject to scintillation. However, on one occasion deep slow fading was observed.

4.3 Height-Gain Curves

One of our principal concerns is the variation of signal strength with height close to the sea surface. Theoretical results suggested that in the strongest ducting a re-entrant in the height/gain relationship could occur, such that signal strength decreased with increasing height over part of the height range of interest. This would be tactically significant.

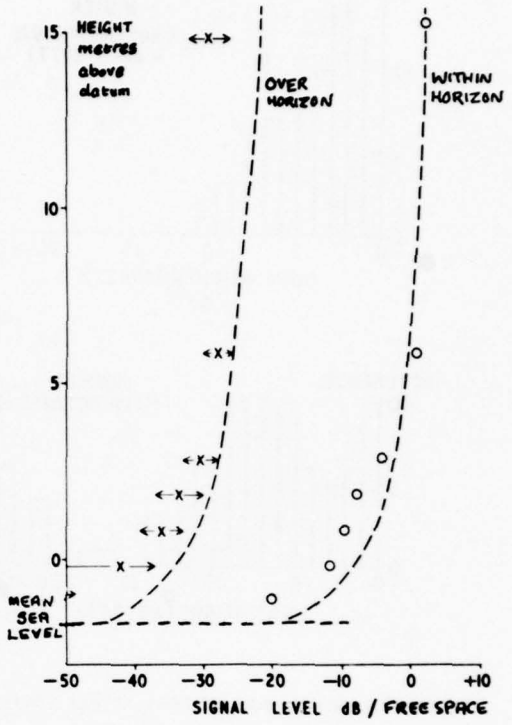

Figure 9. Typical Height-Gain Curves (30 May 1977).

Our measurement programme was therefore designed to provide signal strengths for a range of heights above sea level, which we conventionally plot as a height-gain curve of height versus signal strength. The left-hand curve is for the beyond-horizon link; the right-hand curve for the line of sight. Arrows about the measured points indicate fading range. The dotted lines are the theoretical curves. This is an example of a good fit between theory and measurement.

Despite some variation, the general shape of the measured height-gain surve is fairly constant, especially close to the sea. Variations in absolute level are much greater than variations in shape of the height-gain curve.

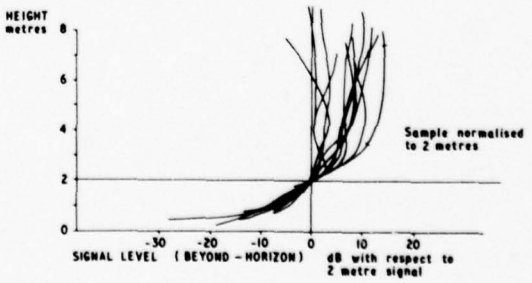

Figure 10. Measured Shape of Height-Gain Curves.

Figure 10 presents a sample of measured height-gain surves normalised about the signal level at 2 metres above sea level. It further demonstrates the fairly constant shape of the signal vs height relationship in a wide variety of duct strengths.

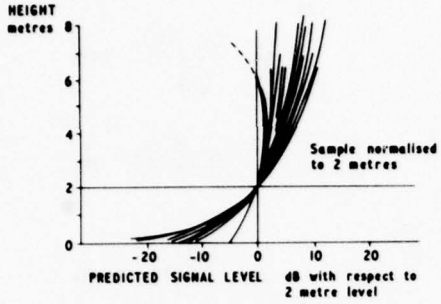

Figure 11. Predicted Shape of Height-Gain Curves.

Figure 11 shows the predictions for the same sample of height-gain curves, normalised at 2 metres as before. The shape of the height-gain curve is generally much better predicted than its absolute level. This led us to consider whether the use of a standard shape for all predictions would introduce significant additional error. It was found that overall the additional error would be small compared with the error already present. However, certain important special cases would no longer be predicted, notably the shallow re-entrants above 2 or 3 metres that sometimes occurs in strong ducting. More severe re-entrants were not found, nor any re-entrants below 3 metres.

4.4 Comparison with Prediction

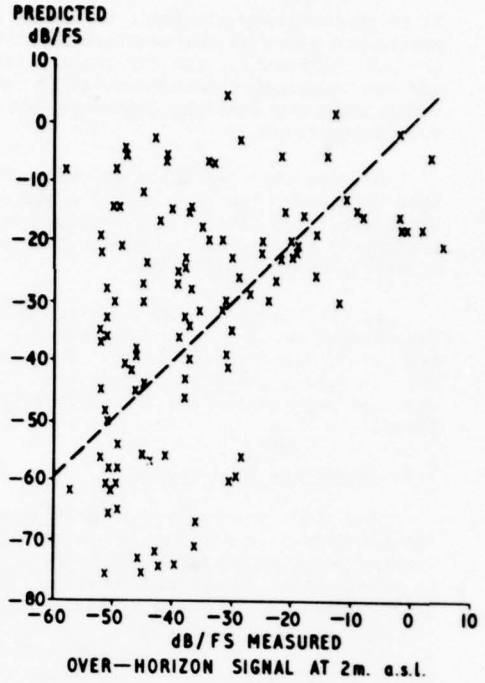

Figure 12. Scatter Diagram: Predicted vs Measured Signal.

Many workers have presented their results in the form of scatter diagrams of predicted signal against duct height or against measured signal. Figure 12 presents one of our scatter diagrams, for beyond-horizon signal strengths at 2 metres above sea level. A poor correlation is apparent. The signal levels at other heights are similarly scattered. The line-of-sight signal was much better predicted however, with rms error typically 7 dB, while the beyond-horizon rms prediction error was typically 20 dB. The correlation coefficients obtained from the beyond horizon scatter plots, while formally quite significant, indicated that a significant part of the variance of the measured signal was due to factors not correctly included in the prediction process.

5. SOURCES OF ERROR

5.1 Signal Measurement

Signal measurement error, including calibration inconsistencies etc, would only account for $\pm$ 4 dB error at worst (systematic and random error combined).

5.2 Sensitivity of the Model to Meteorological Measurement Accuracy

The model was found to be very sensitive to inaccuracies in certain met parameters. Wind speed and sea state, varied together over the likely range, gave variations up to 8 dB. Sensitivity to sea temperature and air temperature variation was roughly 16 dB/Deg C and 12 dB/Deg C respectively. Inaccuracies in wet bulb temperature are naturally the most serious of all, leading to changes of up to 50 dB/Deg C.

It is particularly important to use well calibrated pairs of thermometers for the wet and dry bulb hygrometry, and for the air temperature and sea temperature measurements, so that temperature and humidity gradients may be accurately found.

Despite this sentivity problem, wet and dry bulb hygrometry can be a sufficiently accurate technique, with temperature readings to 0.1 Deg C leading to an accuracy of about ± 1% relative humidity in ideal conditions.

In our case we estimated 0.15 °C as typical measurement error for wet bulb and sea temperature, and 0.1 °C for dry bulb error. This would contribute an r.m.s. prediction error of 3 dB. This will not account for the extreme prediction errors found.

5.3 Horizontal Inhomogeneity

The other meteorological consideration affecting the result is horizontal homogeneity. The ducting model characterises the propagation path by measurements of air and sea conditions at one point. This has produced useful results for open sea conditions, and studies of the decorrelation of duct height with time suggest that such characterisations can be expected to have validity of an average 3 to 4 hours.

This assumption of horizontal homogeneity must be questioned for coastal waters in the light of our results. Another look at the map (Figure 5) suggests that while our Seven Stones met data could well be representative of the beyond-horizon path in south to south west winds, it does not necessarily represent the inshore half of the path, especially in unsettled conditions and in winds with a northerly component. It is certainly open to question as a measure of the line of sight path.

Good horizontal homogeneity of the duct has been found in some areas by Richter and others. Our conditions differ in their tendency towards unsettled weather conditions, and the relatively mobile sea with strong tidal currents and irregular depth, which subjects the sea surface temperature to fairly abrupt fluctuations. Finally, there is the adjacent land mass, which may contribute an advection duct in north or north-east weather and in settled anticyclonic conditions.

6. SYNOPTIC APPROACHES

It was questioned whether a broader description of the current synoptic weather situation might be used to give a broad brush prediction. This would be of use where the full method could not be used, perhaps because detailed met data were not available.

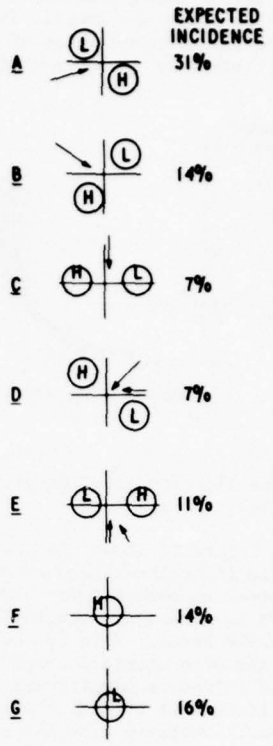

Figure 13. Simplified Weather Classifications.

A simplified classification of weather type by pressure patterns was derived from Bilham (1938). Similar classifications could be developed for other areas. The synoptic chart for noon of each observing day was examined and classified according to this scheme.

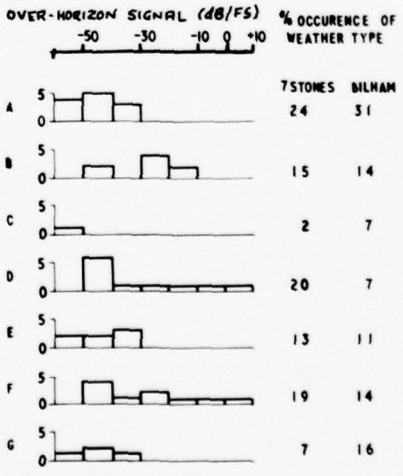

Figure 14. Beyond Horizon Signal vs Weather Type.

Figure 14 shows histograms of the noon 5 metre signal for each category. The ordinate is signal strength in dB with respect to free space. The percentage occurrence of each weather type in our sample is compared with Bilham's figures at the right.

The sample is small, but high signals only appear in weather Types D and F, and moderate signals in Type B. This is not unexpected, since Type B is the north-westerly air stream often associated with the relatively dry and clear weather following a cold front; Type D is the dry north-easterly continental air stream; and Type F is a static anticyclone. High signal levels might also have been expected in weather Type C, but our sample of this type is too small to be significant.

The median signal in each weather class has been used as a predictor, prediction errors using this synoptic method had a standard deviation of 15 dB as against the 21 dB using the full model. The synoptic method fails to predict the important highest signal levels as well as the full method however.

It should be noted that measured current synoptic pictures were used, rather than forecasts or historical data. Short term forecasts are not expected to introduce much additional error.

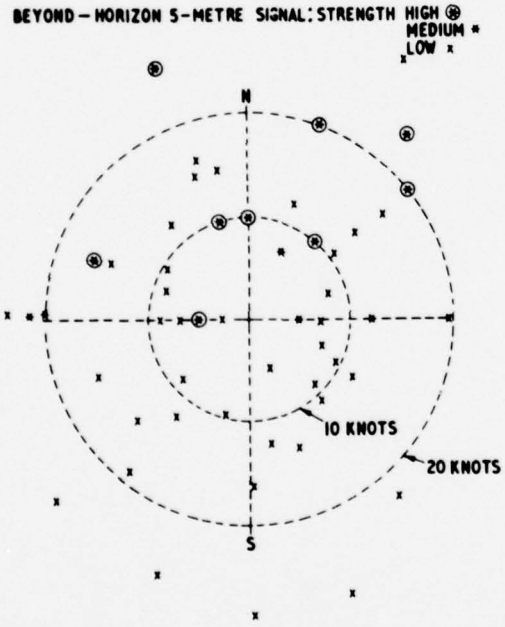

Figure 15. Signal vs Wind Vector.

The Bilham classification is based on pressure patterns, but it is reducable to wind direction without much loss of information. This suggested an even cruder prediction method, only applicable to a given location, using wind direction. In Figure 15 the position of the points represents wind direction and strength, the signal strength being classified by symbology as high, medium or low.

High and medium signals occur only in winds with a northerly component.

These correspond to the pressure Patterns B, D and F. A simple prediction classification by wind direction again gave 15 dB rms error.

In conclusion, simplifier and synoptic models would seem to offer some prediction capability, which may be useful when full surface ducting calculations are not possible or not applicable.

7. ALTERNATIVE PROPAGATION MECHANISMS

We conclude that in the test environment the propagation is not fully described by the surface duct model alone. A feature of the results is that a number of measured signals are strong while the prediction is quite low. It is likely that these under-predicted signals are due to alternative propagation mechanisms.

Jeske (1977) has drawn attention to the incidence and influence of elevated layers on 10 GHz surface-to-surface over-the-horizon paths. The results contained two classes of signal, of roughly equal occurrence. One type of signal, characterised by fast fading, was well predicted by an evaporation duct method. The other, characterised by slow fading, was usually badly under-predicted, and is associated by Jeske with elevated ducting.

We obtained retrospectively radio-sonde profiles for two subsets of our data, one corresponding to the severely under-predicted signals, the other a control. Unfortunately the nearest radio-sonde data was for a point some miles inland and therefore of limited applicability. Furthermore, the geometry of our over-the-horizon path was such as to limit effective elevated layer contributions to the lower and narrower ducting layers, and these tend to be so narrow that they are not registered by standard meteorological radio-sondes. Perhaps because of these two problems, no correlation could be found between our severe under-predictions and elevated layers.

More significantly, a comparison between those signals of slow fading and those of severe under-prediction yielded no correlation, unlike Jeske's very clear results. There is a need for further work to determine the extent to which elevated layers will affect surface paths. It is by no means clear that elevated layers can generally be ignored for surface to surface predictions, but it may well be that line-of-sight and short over-horizon paths will be unaffected, depending on antenna elevation beamwidths.

In anti-cyclonic conditions especially, dry air spreads out from the land over coastal waters, forming an advection duct whose thickness is much in excess of that of a pure evaporation duct. The strength moreover depends strongly on the distance from the coast. The advection duct will not necessarily conform to our model of the refractive index profile for the evaporation duct, and horizontal homogeneity is lost. A detailed

surface evaporation duct prediction on met data from a single off-shore point cannot be expected to cope with advection ducting.

Advection ducts are a problem. We know when and where they are generally likely to occur, but they are difficult to measure because they are not necessarily uniform over an area. This also makes them difficult to model. Ideally we should collect refractivity profiles all along the path and then integrate along it to find the resultant field. A generally applicable full theory cannot be prepared since the form of the duct will depend on local geography. A model for a straight flat coastline would be an interesting first step. Advection ducting remains a significant gap in our radiometeorology.

8. CONCLUSION

In summary, coastal waters are important to us, and coastal refractive effects are complex phenomena made up of more than one contributing mechanism. A detailed model of surface ducting will not describe signal conditions correctly on all occasions. The effects of elevated layers cannot always be neglected, and the formation and effect of advection ducts demands further study. As an interim measure, simple synoptic methods give some prediction capability.

References:

E C Bilham — The Climate of the British Isles. Macmillan 1938.

H Jeske et al — Final Report of Research Study Group RSG-6. NATO AC/243 (Panel III) D/160 1978.

RADAR CLUTTER UNDER ATMOSPHERIC DUCTING CONDITIONS

F. Perry Snyder

EM Propagation Division

Naval Ocean Systems Center

San Diego, CA 92152

ABSTRACT

Atmospheric ducting phenomena can seriously influence radar coverage, significantly extending radar ranges or causing radar "holes." Such atmospheric ducting conditions influence not only the radar target return signal, but also the signal returned from other objects i.e., radar clutter. Expected improvements in radar performance due to some ducting conditions can be seriously diminished, if not converted to degraded performance, due to clutter effects. An "on-board" capability to assess the effects of atmospheric ducting conditions on Navy sensor performance has been developed in the IREPS (Integrated Refractive Effects Prediction System) project at NOSC. Presently, the IREPS, or any other known general purpose performance assessment system, does not adequately consider clutter.

Radar clutter return has been investigated extensively, both theoretically and experimentally, and several empirical models for sea clutter have recently been developed. These sea clutter models have many features in common, particularly the consideration of only standard atmospheric conditions. A sea clutter effects model, capable of consideration of non-standard atmospheric conditions, has been developed for intended usage in the IREPS. The model, which couples a classical ray-optics propagation formulation with an empirical sea clutter cross-section model, is discussed. Also presented are predicted effects on radar coverage due to a variety of atmospheric ducting environments. The clutter effects model is most appropriate to a propagation environment resulting from an elevated refractive layer producing a ground based duct. For such ducting conditions, the clutter effects model predicts the occurrence of discretely spaced "clutter rings," in agreement with observations.

I. INTRODUCTION

Atmospheric ducting phenomena can seriously influence radar coverage conditions. For example, significantly extended radar ranges can occur due to ducting, and "holes" in radar coverage can result from refractive layers. Such atmospheric ducting conditions influence not only the radar target return signal, but also the signal returned from other objects; i.e., radar clutter.

Propagation models applicable to anomalous atmospheric conditions such as ducting have recently been developed at the Naval Ocean Systems Center (NOSC) in association with the development of the Integrated Refractive Effects Prediction System (IREPS) as discussed by Hitney in these proceedings. Recall that the purpose of IREPS is to provide an "onboard" capability to assess the effect of atmospheric refractive anomalies on sensor performance. The effort involves the development of models which express the effects of refractive anomalies in terms of equipment performance, the verification of these models, the software development of the models for shipboard implementation, and the inclusion of meteorological statistical data to estimate the probability of encountering refractive anomalies as a function of geographic area and season. The IREPS, however, does not presently consider clutter.

A very successful initial shipboard demonstration of IREPS aboard the USS ENTERPRISE was conducted during summer 1976. During this demonstration an excellent example of ducting effects on clutter was observed. A pictorial presentation of these observations is shown in Figure 1. Shown in the figure is a reproduction of a hand drawn tracing of a SPS-12 radar display for 16 June 1976 at about 2000 Z. Note that the normal radar horizon is about 17 Nmi in this case so that the occurrence of an elevated refractive layer producing a surface based duct is clearly indicated. Refractivity profiles, obtained during the time period the extended coverage was observed but not, unfortunately, at the time the clutter rings were most enhanced, indicated the presence of a surface based duct resulting from a thin refractive layer at about 300 metre altitude.

The sea clutter rings in the left central portion of the display were observed during some, but not all, of the time the coverage was extended due to the refractive layer. One description of the rings given by an observer was that they tended to "fade in and out" while remaining nearly fixed in position. A common feature of the clutter rings is depicted in the central rings shown. This is the splitting or separation into two narrow rings. Another common characteristic is the tendency of rings to form first in a narrow angular sector,

then growing in azimuthal extent until one or more concentric rings fully encircle the center of the radar display, then gradually disappearing, starting in the angular sector in which they first appeared and finishing in a sector in the opposite direction, all the while remaining at a nearly constant range.

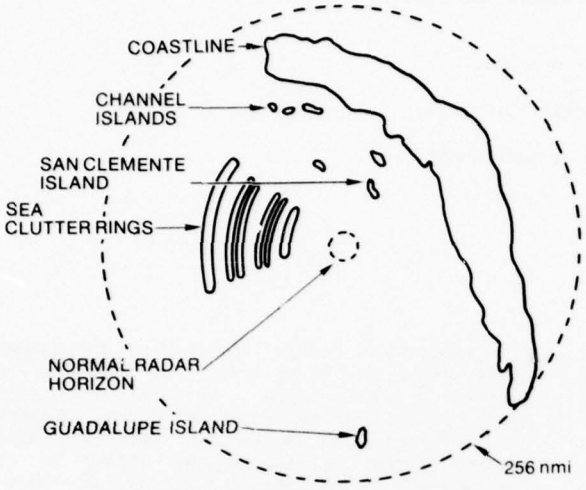

FIGURE 1. SIMULATED SPS-12 RADAR DISPLAY SHOWING OBSERVED CLUTTER RINGS (16 JUNE 76 2000 Z).

The theory of radar clutter return has been investigated extensively (e.g., Wright, 1968). Experimental observations of clutter have also been reported (e.g., Wiltse, et al, 1957 and Daley, et al, 1968). Several attempts have been made to combine the experimental and theoretical results into a working model for sea clutter cross-section. A notable example of such efforts is found in the empirical models recently developed for sea clutter (e.g., Daley, 1973; Sittrop, 1975). Most theoretical radar clutter models have two features in common. One is the essentially statistical description of the clutter sources, and the other is the consideration of only standard atmospheric conditions. The empirical models likewise are essentially based on the assumption of radar propagation under standard atmospheric conditions. No clutter model exists which is adequate under atmospheric ducting conditions.

Two types of atmospheric ducts occur which can be expected to greatly influence sea clutter. One is the surface-evaporation duct, which is formed essentially by the sea surface and the minimum in the near surface refractive-index profile, which is in turn determined by the vertical distribution of water vapor resulting from evaporation. The other is a ground based duct formed by an elevated refractive layer. Propagation in the two different environments can be best considered using two different formulations. Vertical dimensions for evaporation ducts are on the order of metres to very few tens of metres and a waveguide mode formulation would be appropriate for this type of duct. Vertical dimensions for ground based ducts formed by an elevated refractive layer are typically on the order of many tens of metres to a few hundred metres and ray-optical formulations would be appropriate here.

NOSC is currently involved in exploratory development of numerical models that assess the effects of the environment, particularly atmospheric ducting conditions, on radar sea clutter signals. This investigation is being made from two general viewpoints. The one viewpoint, most applicable to the elevated layer, ground based duct, considers ducting effects on sea clutter with a combination of an empirically derived normalized sea clutter cross-section (Dyer, 1978) coupled with a ray-optical propagation model. The other viewpoint is more applicable to general ducting-clutter problems and involves the consideration of scattering effects of a rough ground plane by using a waveguide mode propagation model combined with classical mode conversion concepts. In this formulation, the sea back scatter is modeled in terms of conversion of forward propagating modes into backward propagating modes.

Only the first model, using a ray-optical propagation formulation, will be further discussed in this report, and is considered in the next section. The empirical normalized sea clutter cross-section will also be considered in Section II. In Section III, implementation of the clutter effects model into the IREPS will be discussed. Further, some predicted effects of sea clutter on radar coverage for a variety of environmental conditions will be presented in Section III.

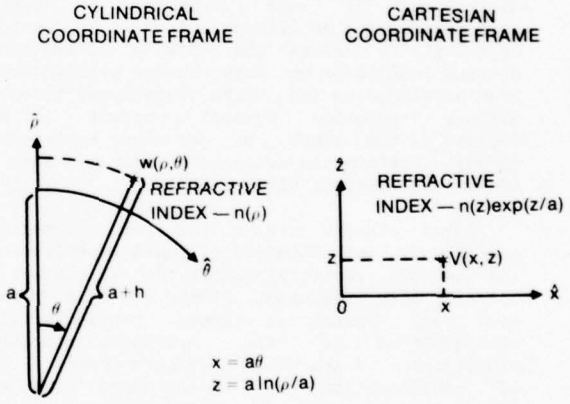

FIGURE 2. TRANSFORMATION FROM CYLINDRICAL COORDINATE FRAME TO CARTESIAN COORDINATE FRAME.

II. PROPAGATION AND CLUTTER CROSS-SECTION MODELS

The geometrical basis for the ray-optical propagation formulation is developed in the following way. The propagation environment is assumed to be two dimensional with the earth represented by a cylinder and propagation in a plane transverse to the cylinder axis. A classical conformal transformation to Maxwell's equations in cylindrical form is employed, converting the geometry from cylindrical to rectangular (Cartesian). This transformation has been discussed in the context of earth flattening by Richter (1966) and has been widely applied in radiowave and radar propagation problems when earth curvature in the direction of propagation is an important factor. The net effect of the

transformation is to change from the cylindrical geometry with refractive index given by n to the rectangular geometry with refractive index given by n multiplied by exp(z/a), where a is the radius of the earth and z is essentially the altitude above the earth (see Figure 2).

The formulation of a ray path trajectory in the clutter effects model is somewhat unconventional and is found in the following way. First it is assumed that the original refractive index is known or can be determined only at a limited number of altitudes. It is often assumed at this point that the refractive index is continuous and varies in some prescribed way between these altitude points, and some type of "ray trace" formulation is used to compute the ray path. Rather than doing this, it is here assumed that the refractive index is continuous with unknown variation between profile points and that the ray path in the transformed coordinate frame is parabolic between refractive index profile heights. Thus, if x, z represent the coordinates of a point on a ray path between two profile heights, then

$$z = \alpha x^2 + \gamma x \tag{1}$$

where, for convenience, the reference point $x = 0$, $z = 0$, is chosen at one profile height and $x = x_1$, $z = z_1$ will be chosen at the other (see Figure 3).

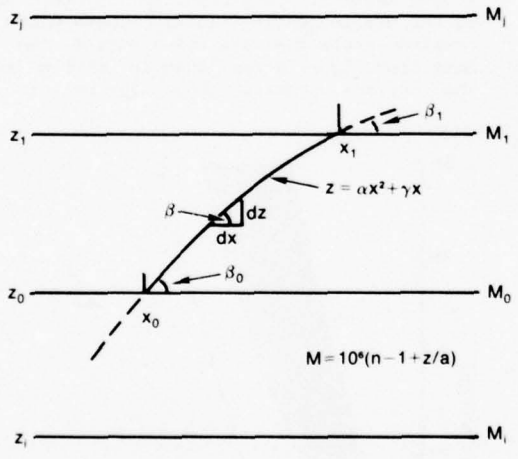

FIGURE 3. PARABOLIC RAY PATH TRAJECTORY.

Differentiating (1) with respect to x, recognizing that this slope is equal to $\tan\beta$, where β is the angle between the ray trajectory and the x axis, and calling the initial angle β_o (where $x = 0$) and the final angle β_1 (where $x = x_1$), yields, after some algebra

$$\gamma = \tan\beta_1$$

$$\alpha = \frac{\tan^2\beta_1 - \tan^2\beta_2}{4z_1} \tag{2}$$

At this point, recourse to Snell's law in the transformed coordinate frame is necessary. The refractive index in this frame, n_a, is given by

$$n_a = e^{z/a} \quad (z) \tag{3}$$

Because the atmospheric refractive index n(z) is only slightly greater than unity, it is convenient to write $n(z) = 1 + \delta n(z)$ where $\delta n \ll 1$. Typically, $\delta n \approx 10^{-4}$ so in order to have a number of more convenient magnitude, the "refractivity" N has been defined to be $N = (n - 1) \times 10^6 = \delta n \times 10^6$.

Expanding the exponential term in (3), using the modified refractivity, defined as $M = N + 10^6 z/a$, and retaining terms to first order in smallness, Snell's law in the rectangular frame is

$$n_a \cos\beta = \text{CONSTANT} = A_o$$

or

$$(1 + 10^{-6}M)\cos\beta = A_o \tag{4}$$

The constant A_o is conveniently determined at some height where M and β are both known. Using trigonometric identities in (2) along with Snell's law from (4) yields

$$\alpha = \frac{10^{-6}(M_1 - M_o)(2 + 10^{-6}(M_1 + M_o))}{4A_o^2 z_1} \tag{5}$$

If a small angle ($\beta < 10°$) approximation were valid, assuming a quadratic order to the variation between profile points for a ray trajectory would be equivalent to a linear variation in modified refractivity between profile points. Making such an assumption in general, and writing

$$M_1 - M_o = \left(\frac{\Delta M}{\Delta z}\right) z_1$$

where $\Delta M/\Delta Z$ is the slope of the modified refractivity, and using $\bar{M}$ as the average value of M, (5) becomes

$$\alpha = \frac{10^{-6}\left(\frac{\Delta M}{\Delta Z}\right)(1 + 10^{-6}\bar{M})}{2A_o^2}$$

or, within the spirit of the approximations

$$\alpha = \frac{10^{-6}\left(\frac{\Delta M}{\Delta Z}\right)}{2A_o^2} \tag{6}$$

The ray path between profile heights is thus essentially determined through knowledge of the path angle at one height and the change in M between the heights.

Some properties of ray paths which are important to the question of sea clutter under ducting conditions are shown in Figure 4. A surface based duct resulting from an elevated refractive layer is shown diagramatically in Figure 4 as a tri-linear M-profile. Assume that a ray source is located at some height, such as position A in the figure. From (1) and (6), a ray will be concave upward within the first linear segment of the profile and concave downward within the second. Further, from Snell's law (4), the magnitude of the slope of any ray trajectory will be the same at all points within the profile with the same M-value, provided of course, that the ray reaches the

particular point at all. For example, a ray launched horizontally (labelled Ⓐ in Figure 4) at A will be continually turned upward until reaching the first change in profile slope and will then begin turning downward. As the ray approaches the height A', where the M-value is the same as at A, the ray trajectory will again approach horizontal and continue turning downward, thus being "reflected" at height A'. The ray trajectory again changes concavity where the M-profile slope changes and is again horizontal at height A, being reflected upward at this height. The ray is thus "ducted" or "trapped" between A and A'.

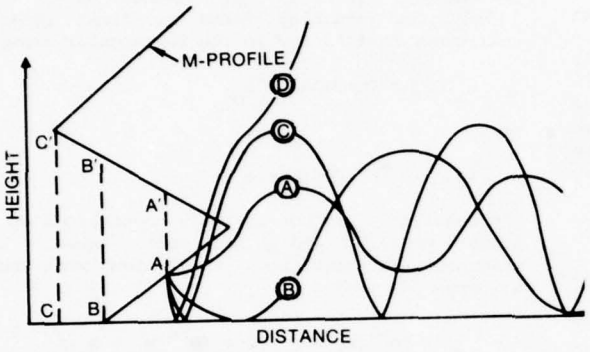

FIGURE 4. SAMPLE RAY PATHS WITH A SURFACE BASED DUCT.

Consider a ray launched downward at A with such an angle that the continual upward turning will result in a horizontal trajectory just above the surface. Such a ray, labeled Ⓑ in Figure 4, will be trapped between the heights of B and B' as shown in Figure 4. Any ray launched below this ray will reach the lower surface (which is necessary before the ray can contribute to sea clutter) and be reflected according to the usual laws of reflection at a plane interface. There is a launch angle for which a ray will just become horizontal as it approaches C' in Figure 4. Such a ray, labeled Ⓒ in Figure 4, will be reflected downward at C' and will thus be trapped between the surface and C'. Any ray launched below this ray (such as ray Ⓓ in Figure 4) will reach the height C' at a non-zero angle and continue upward, escaping through the top of the duct. There is thus a range of downward launch angles for which rays will be both trapped in the duct and reflected off the lower (sea) surface. By symmetry and reciprocity arguments, there is also a family of rays with upward launch angles which will be trapped in the duct as well as be reflected off the lower surface. It is these two families of rays which contribute to sea clutter enhancement under conditions when an elevated refractive layer produces a surface based duct.

This geometrical property is perhaps best seen by examining a series of ray trace trajectories for an actual profile. Shown in Figure 5 are two modified refractivity profiles, each typifying a thin refractive layer with top at about 1200 feet (366 metres). One of the profiles, designated M1, has a modified refractivity minimum at the top of the layer of approximately 10 M-units less than the surface value and the other profile, M2, has a minimum value of approximately 40 M-units less than the surface value.

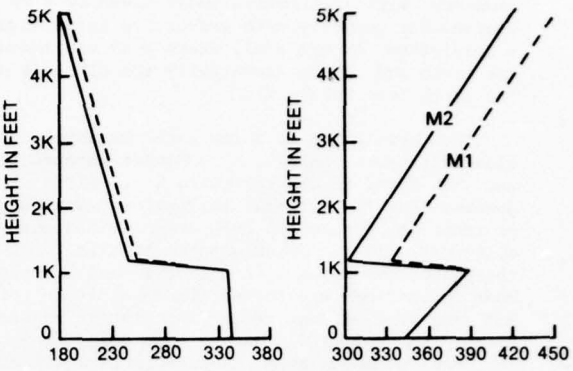

FIGURE 5. REFRACTIVITY PROFILES IN N-AND-M UNITS.
$(N=(n-1)\times 10^6 ; M=N+(h/a)\times 10^6)$
n = refractive index = c/v

Using these two refractivity profiles, the ray trace propagation model was exercised. The results are shown in Figure 6 for the weaker duct - M1, and in Figure 7 for the stronger duct - M2. Also shown in each figure is the grazing angle as a function of range. Note in Figure 6 that most of the trapped rays depicted never actually reach the surface. These rays could contribute to a significant radar return from elevated targets (e.g., land masses) but could not contribute to sea clutter return. This point is further emphasized by the grazing angle plots. These plots show the grazing angle for rays which strike the surface. Note from Figure 6 for example that no rays reach the surface between about 15 nmi to 50 nmi.

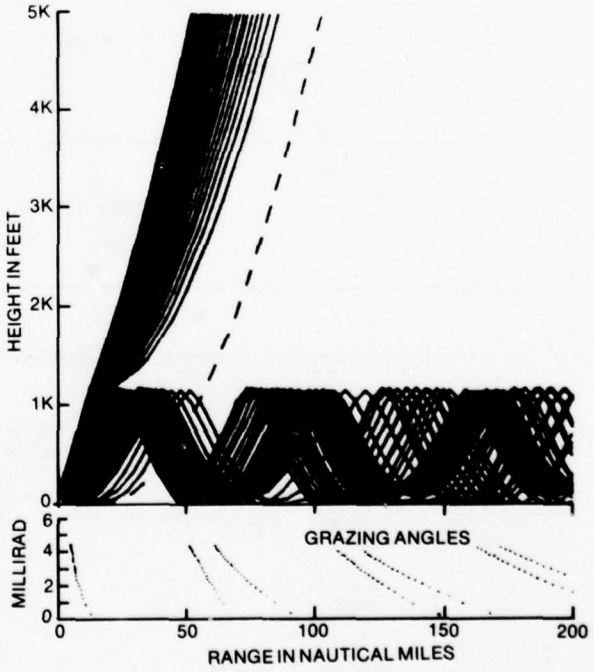

FIGURE 6. RAY TRACE DIAGRAM AND GRAZING ANGLES FOR MODIFIED REFRACTIVITY M1. RADAR HEIGHT 142 feet

Further, the maximum grazing angle for any ray reaching the surface is between four and five milliradians. From Figure 7, for the stronger duct, note that the range from about 15 nmi to 35 nmi is devoid of any rays reaching the surface. Also, the maximum grazing angle for the stronger duct is increased to about nine milliradians.

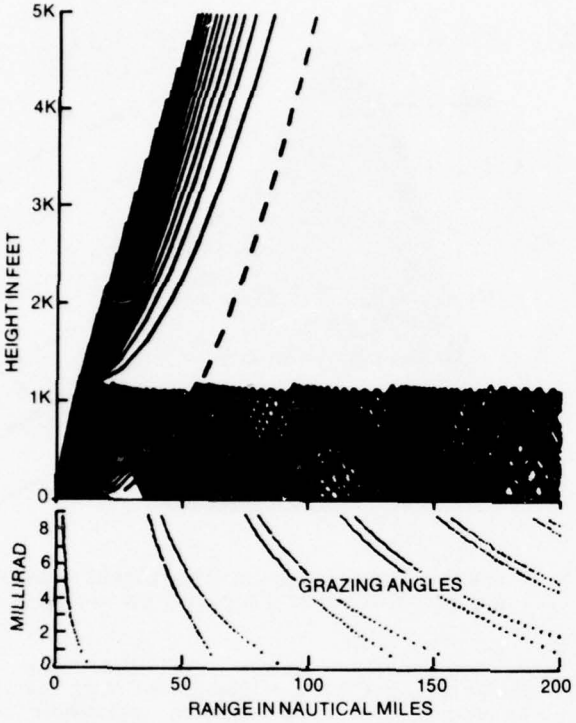

FIGURE 7. RAY TRACE DIAGRAM AND GRAZING ANGLES FOR MODIFIED REFRACTIVITY M2. RADAR HEIGHT 142 feet

The clutter cross-section model used with the ray path propagation model was obtained from Dyer (1978). The model is semi-empirical and calculates the normalized clutter cross-section as a product of three variables: sea direction, windspeed, and multipath. The model assumes a "fully arisen" sea for which wave height and wind speed are coupled under the assumption of equilibrium conditions. Both the wind/sea direction dependence and the wind speed dependence of the cross-section model are empirically derived. The multipath portion of the model has a theoretical basis.

The sea clutter cross-section per unit area is shown in Figure 8 for two radar frequencies (C-Band and L-Band) at several wind speeds. Both upwind and downwind values are shown for a 15 knot wind speed. Some properties of the sea clutter cross section per unit area are to be especially noted. For high wind speeds, the sea clutter cross-section for the C-Band increases very rapidly at very small grazing angles, reaching a nearly constant value between five and ten milliradians. This property is also exhibited at L-Band, although not so dramatically. For both bands, there is a large sensitivity to variations in wind speeds for moderate speeds. For example, there is as much as a 20 dB change in cross-section between 10 knot and 15 knot winds. There is a much decreased sensitivity to changes in wind speed at higher wind speeds although the clutter cross-sections are much larger for higher wind speeds. Note also that the directional dependence of clutter cross-section is insensitive to the actual windspeed and grazing angle although there is some sensitivity to the radar band, with the larger directional dependence at higher frequencies.

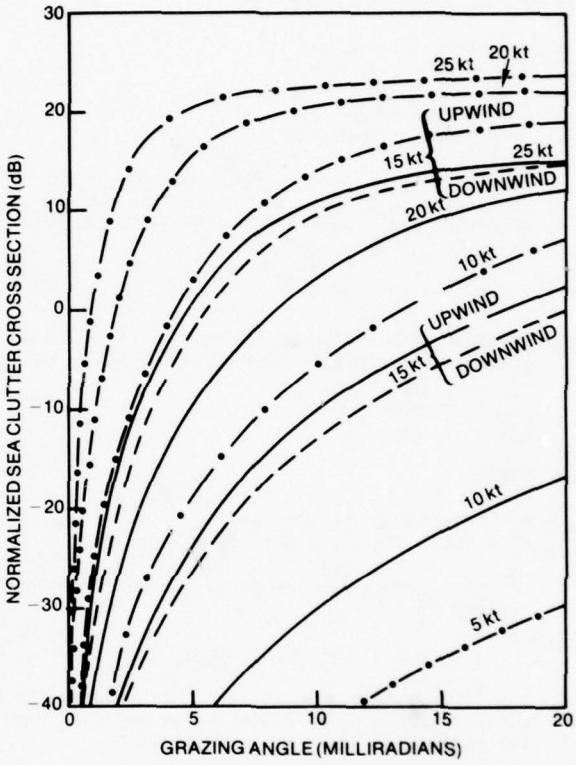

FIGURE 8. NORMALIZED SEA CLUTTER CROSS SECTION (RELATIVE dB) VS GRAZING ANGLE (— 1300 MHz; —•— 5600 MHz)

The operational implications of the combined ray path propagation model and normalized clutter cross-section model can be qualitatively inferred from the considerations of the individual aspects already discussed. It can be expected, for example, that at high wind speeds, even moderately strong surface based ducts will result in enhanced clutter effects. The clutter ring "splitting," mentioned previously in regards to the USS ENTERPRISE demonstrations of the IREPS, can be inferred from the existence of two sets of influential rays (the initially upgoing and downgoing launched sets). The existence of clutter rings in only a limited angular sector might be inferred by the directional dependence of the clutter cross-section, but horizontal inhomogeneity in the environment would seem a more likely cause.

III. IMPLEMENTATION INTO IREPS

The basic transmission equation for radar can be written (Kerr, 1951)

$$P_r = \frac{P_t G^2 \lambda^2}{(4\pi)^3 R^4} F^4 \sigma_t \qquad (7)$$

where

P_r = target power returned

P_t = transmitted power

G = antenna power gain
λ = radar wavelength
R = radar-to-target range
F = pattern-propagation factor
σ_t = target cross-section

If the range to target detection in free space is denoted R_{fs}, then the ranges at which target detection can occur under actual conditions are given by

$$R < F * R_{fs}$$

provided clutter is not present. If clutter is present, the clutter power can be written as

$$P_c = \frac{P_t G^2 \lambda^2}{(4\pi)^3 R^4} \sigma_c \qquad (8)$$

where

P_c = clutter power returned
σ_c = total clutter cross section

If clutter is present, target detection is assumed if

$$R < F * R_{fs} \ \underline{\text{AND}} \ P_t > P_c \qquad (9)$$

The second requirement can be related to the pattern-propagation factor by using (7) and (8). The equivalence is

$$F > \frac{\sigma_t}{\sigma_c}$$

The total clutter cross-section in (8) is related to the clutter cross-section per unit area of Section II as

$$\sigma^0 = \sigma_c / A$$

where σ^0 is the cross-section per unit area and A is the area of the clutter patch. The azimuthal portion of the area is determined by the antenna beam width and the range portion by the pulse length. The range to the clutter patch is assumed to be the surface range. A contribution to clutter from a given range may be made by both sets of ray families as discussed previously. These are assumed to sum noncoherently.

The clutter effects model has been coded and implemented into the IREPS. Typical results are presented in the "coverage diagrams" of Figures 9-11. A hypothetical C-Band radar with 100 nm free space detection range against a certain target is assumed located at 140 feet height. As a reference, the coverage diagram for a non ducted (standard) atmosphere with a 10 knot wind is shown in Figure 9. Recall that the darkened area of the diagram represents the range/height conditions where the radar would detect the target.

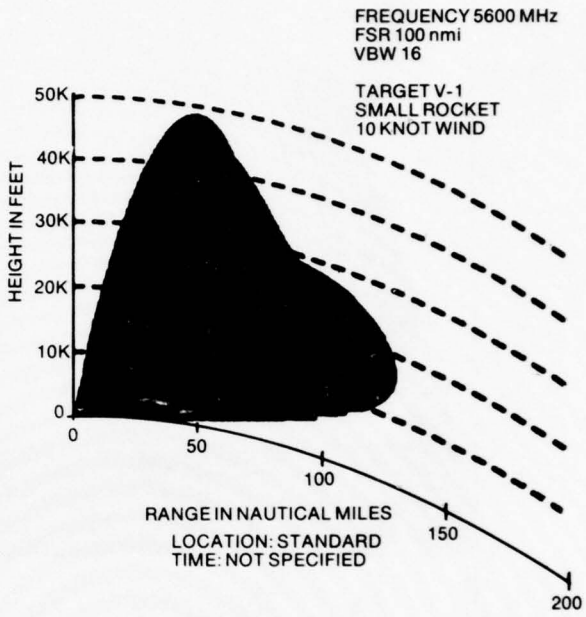

FIGURE 9. COVERAGE DIAGRAM FOR C-BAND RADAR AT 140 feet HEIGHT. STANDARD ATMOSPHERE WITH 10 KNOT WIND.

A coverage diagram for the same wind conditions, but for a surface based duct is shown in Figure 10. The elevated refractive layer causing this duct is located at about 300 metres

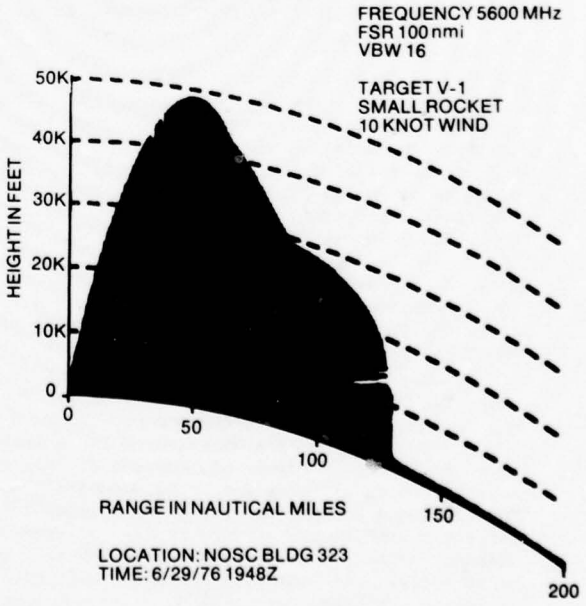

FIGURE 10. COVERAGE DIAGRAM FOR C-BAND RADAR AT 140 feet HEIGHT. ELEVATED LAYER, GROUND BASED DUCT WITH 10 KNOT WIND.

and is about 40 metres thick. The M-unit deficit between the surface and the layer minimum is about 40 M-units. Notice the enhanced coverage for low altitudes to longer ranges. For this case, any clutter effects are just barely observed. A coverage diagram for the same refractivity profile but for a 15 knot wind is shown in Figure 11. For this case, the predicted effects of clutter are quite dramatic. Within the darkened areas of the diagram, target detection would be expected.

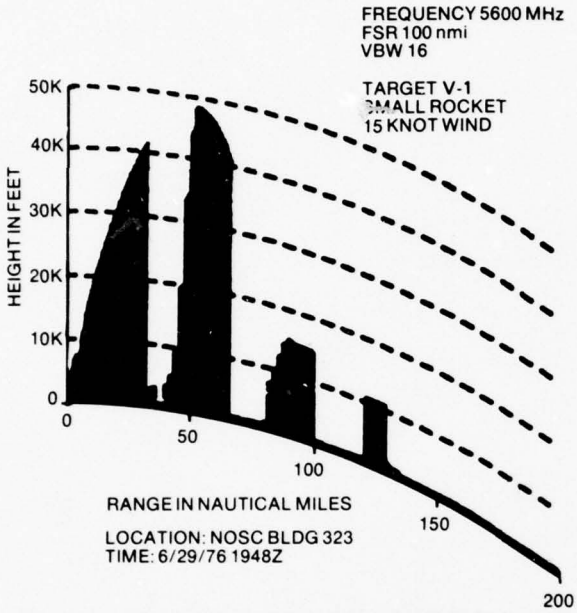

FIGURE 11. COVERAGE DIAGRAM FOR C-BAND RADAR AT 140 feet HEIGHT. ELEVATED LAYER, GROUND BASED DUCT WITH 15 KNOT WIND.

However, within the areas no longer darkened compared to Figure 10, the target would no longer be detectable compared to clutter. The presence of clutter in this case would appear on a PPI type display as bright rings, masking the target.

The ray-optical propagation model presented here appears to be adequate for the elevated layer, ground based duct propagation environment. Before the entire clutter effects model can be implemented for "in-fleet" usage however, quantitative evaluation is still required.

The work reported in this paper was performed under sponsorship by the Naval Air Systems Command. The author would like to thank J. W. Willis for his continued support.

References

Daley, J. C., An Empirical Sea Clutter Model, Naval Research Laboratory Memo Report 2668, Oct. 1973.

Daley, J. C., J. T. Ransone, J. A. Burkett and J. R. Duncan, Sea Clutter Measurements on Four Frequencies, Naval Research Laboratory Report 6806, Nov. 1968.

Dyer, F. B., Georgia Institute of Technology, Private Communications, 1978.

Kerr, D. E. (ed.): "Propagation of Short Radio Waves," MIT Radiation Laboratory Series, vol. 13, McGraw-Hill Book Company, New York, 1951.

Richter, J. H., "Application of Conformal Mapping to Earth-flattening Procedures in Radio Propagation Problems," Radio Science, vol. 1, no. 12, December 1966, pp. 1435-1438.

Sittrop, H. Ir., X and Ku-Band Radar Backscatter Characteristics of Sea-Clutter, Physics Laboratory, TNO, Report PHL 1975-08, April 1975.

Wiltse, J. C., S. P. Schleisinger, and C. M. Johnson, "Backscattering Characteristics of the Sea in the Region from 10 to 50 kMc, "Proc. IRE., Vol. 45, pp. 220-228, Feb. 1957.

Wright, J. W., "A New Model for Sea Clutter," IEEE Trans., Vol. AP-16, pp. 217-223, March 1968.

SURFACE DUCT EFFECTS ON RADAR/ESM DETECTION RANGE

LT Richard A. Paulus and Herbert V. Hitney

Naval Ocean Systems Center

San Diego, CA 92152

ABSTRACT

Anomalous propagation effects due to surface-based ducts are quantitatively examined for variation of (1) detection range for fleet radars versus destroyer-sized targets and (2) maximum ESM intercept range for various threat emitters. Both the surface-based duct from elevated refractive layers and the evaporation duct effects on surface to surface propagation paths are considered. Elevated refractive layers, created by rapid transitions between differing layers of air, may, depending upon height of the layer and its M deficit, form a surface-based duct. This situation can be assessed by units having access to radiosonde or refractometer data. Although relatively uncommon in most ocean areas, this ducting mechanism, when it does occur, nearly always results in greatly extended ranges. The evaporation duct, created by the rapid decrease of moisture just above the ocean surface, can be assessed by a simple graphical technique using standard meteorological measurements and an accurate sea surface temperature measurement. The resulting evaporation duct height is a parameter that indicates the strength of the evaporation duct. The effects of this type of duct are highly dependent upon frequency and, to a lesser extent, antenna heights.

1. INTRODUCTION

It has long been recognized that changes in the vertical distributions of the air temperature and humidity near the sea surface can have significant effects on the propagation of radio waves (Katzin, 1947 and Kerr, 1951). In particular, signals propagating between terminals reasonably close to the sea surface, such as characteristic of shipboard heights, will experience variation of signal strength of up to several tens of dB at ranges far in excess of the horizon. The impact of such propagation variations on the detection ranges of fleet radars and maximum intercept range of ESM (Electronic Warfare Support Measures) receivers can be dramatic, with maximum ranges varying between near-horizon ranges and 250 nautical miles or more. The propagation mechanisms responsible for the increased ranges are of two types: surface-based ducts created by elevated refractive layers and the surface evaporation duct created by the rapid decrease of moisture just above the sea surface. Recent developments in modeling of these propagation mechanisms (Hitney, 1975) as substantiated by propagation measurements (Richter and Hitney, 1975) now make it possible to quantitatively predict maximum radar detection and ESM intercept ranges for varying ducting conditions. The desire to make such quantitative predictions is in response to the fleet's need for passive/active detection and targeting of over-the-horizon contacts for the HARPOON missile system. However, all surface units and submarines should find this development useful in assessing search radar capabilities and in ESM utilization planning.

2. SURFACE-BASED DUCTS FROM ELEVATED REFRACTIVE LAYERS

Over ocean areas there often exists a cool, moist marine air mass extending vertically from the ocean surface to an altitude of up to a few hundred metres. The air mass above this altitude can be much warmer and drier than the marine air for a variety of reasons and creates a transition region in which the air warms up and dries out rapidly with increasing altitude. The rapid warming and drying of the air can cause the radio refractive index to decrease rapidly enough to refract radio waves at low incident angles downward and create a duct. If the M decrease through the transition layer is great enough, a surface-based duct is created (Figure 1). This type of duct will trap radar signals at all frequencies and will generally give greatly extended ranges for detection or interception of surface targets (Figure 2). The frequency of occurrence of surface-based ducts

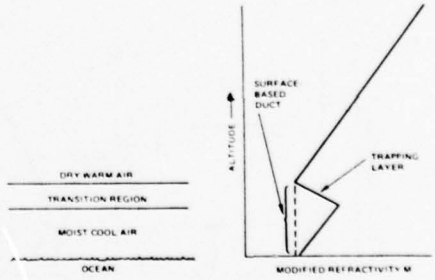

Figure 1. Air masses and transition region responsible for the trapping layer and resulting surface-based duct shown on the right.

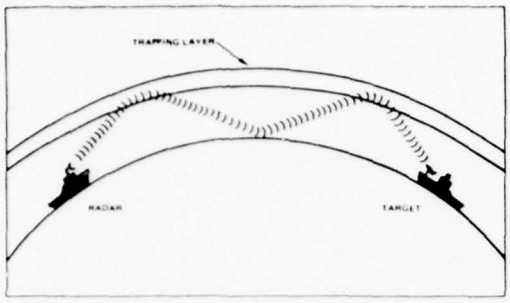

Figure 2. Radar wave path for a surface-based duct created by an elevated trapping layer.

varies with geographic location, season, and even time of day. They are relatively uncommon in most ocean areas but may occur as much as 20 to 40% of the time in such areas as the southern California operating area, the eastern Mediterranean, and the northern Indian Ocean.

A surface-based duct from an elevated refractive layer can be properly assessed only with information of the refractive index profile of the lowest part of the atmosphere. This information is presently derived in the fleet by meteorological personnel from balloon-borne radiosonde measurements.

3. EVAPORATION DUCTS

A very persistent ducting mechanism is created over ocean areas by the rapid decrease of moisture immediately above the ocean surface. For continuity reasons, the air adjacent to the ocean is saturated with water vapor and the relative humidity is thus 100%. This high relative humidity decreases rapidly in the first few metres to an ambient value which depends on varying meteorological conditions. The rapid decrease of humidity causes the modified refractivity M to decrease with height initially, but at greater heights the humidity distribution will cause M to reach a minimum and thereafter increase with height, as illustrated in Figure 3. The height at which M reaches a minimum value is called the evaporation duct height and is a measure of the strength of the evaporation duct. The evaporation duct, which extends from the surface up to the duct height, is much thinner and weaker than a surface-based duct from an elevated refractive layer. As a result, the effect that the

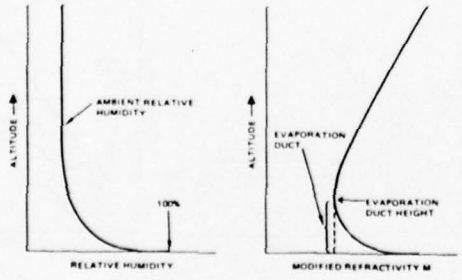

Figure 3. Relative humidity and modified refractivity M versus altitude for an evaporation duct.

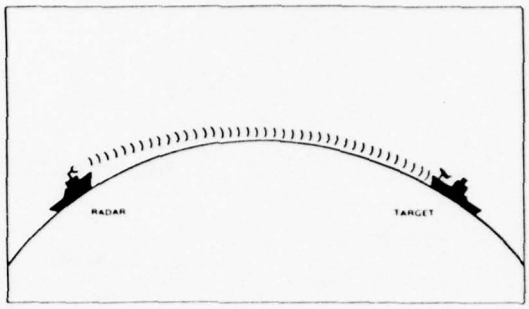

Figure 4. Radar wave path under evaporation ducting conditions resulting in beyond-the-horizon detection.

evaporation duct will have on detection and intercept range is very dependent on the particular radar frequency, and to a lesser extent, on the height above water of the antennas. It must be emphasized that the evaporation duct height is a measure of the strength of the duct only and is not a height below which a radar antenna must be to give extended detection ranges. For a given radar, detection and intercept range will generally increase as the duct height increases and, for duct heights sufficiently large, surface targets will be detected at ranges significantly beyond the horizon, as illustrated in Figure 4. The frequency of occurrence of duct heights sufficiently large to give beyond-the-horizon detection capability to a particular radar varies significantly according to geographic location, season, and time of day. Generally duct heights will be greater at latitudes nearer the equator, during the summer season, and during daylight hours.

The evaporation duct can be assessed from meteorological measurements of sea temperature, air temperature, humidity, and wind speed and use of the evaporation duct calculator developed within the EM Propagation Division of NOSC. A sample duct height calculation is presented in a later section.

4. DETERMINATION OF RANGE

Detection and intercept ranges are derived by calculating the range at which the path loss,

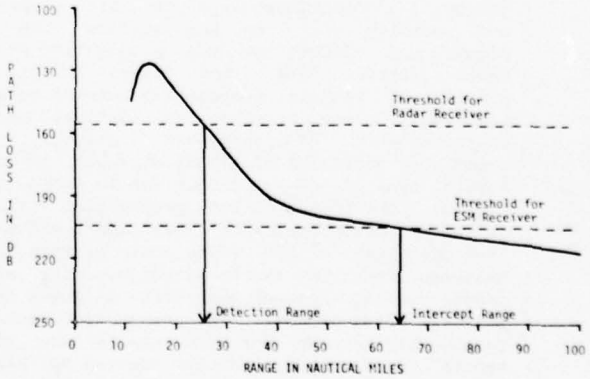

Figure 5. Path loss curve for SPS-10 surface search radar under standard atmospheric conditions.

determined by the environment and transmitter and receiver/target heights, exceeds a given threshold that is determined by system parameters. Figure 5 shows a sample path loss profile for the SPS-10 surface search radar. The range at which the one-way path loss threshold for the radar system intersects the path loss curve is defined as the detection range. Similarly, the threshold of the ESM receiver determines the intercept range.

5. EXTENDED RANGE ASSESSMENT

An assumption inherent in the propagation model is that the atmosphere is horizontally homogeneous. This assumption can lead to unrealistically large ranges. Thus, maximum ESM intercept range was arbitrarily constrained to be 200 nmi or less.

Since the meteorological conditions that lead to formation of the two types of surface ducts are different, a surface-based duct from an elevated refractive layer and the evaporation duct can exist at the same time. When this does occur, the effects of the surface-based duct are considered to dominate the effects of the evaporation duct and normal detection and intercept ranges are nearly always greatly extended.

Assessment of extended ranges caused by evaporation ducting is done utilizing the duct height calculator of Figure 6 and the meteorological measurements mentioned above. For

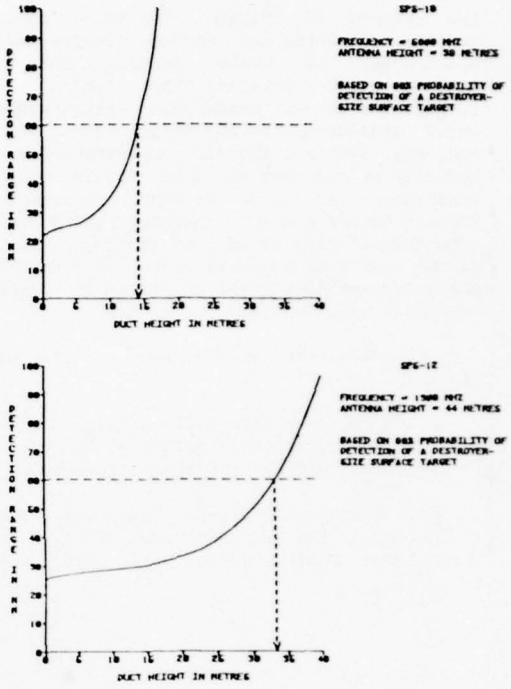

Figure 7. Radar detection range for a destroyer-sized surface target versus evaporation duct height.

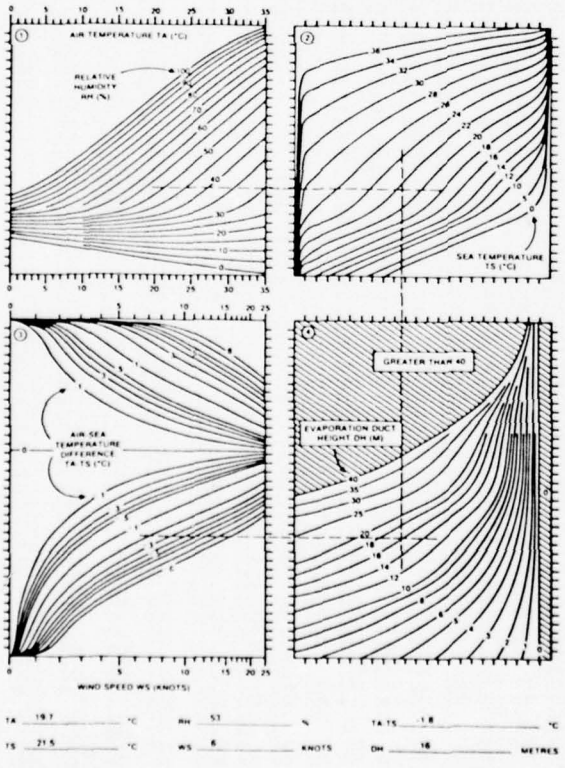

Figure 6. Duct height calculator and sample calculation.

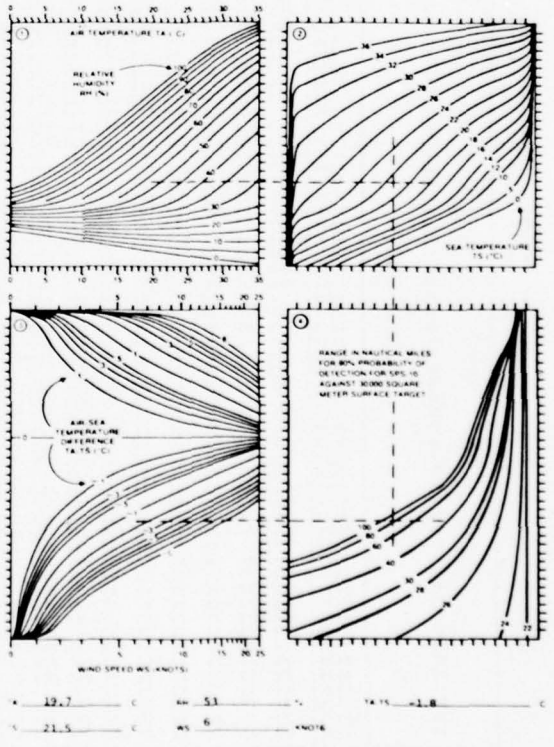

Figure 8. Detection range calculator and sample calculation.

the example in Figure 6, TS, 21.5°C, is a measurement of the sea surface temperature. This measurement is quite critical but can be satisfactorily obtained by taking a bucket temperature or an expendable bathythermograph in water undisturbed by the ship's wake. TA, 19.7°C, and RH, 53%, are the air temperature and relative humidity as commonly measured aboard ship. This measurement is taken at some convenient height above 6 metres and in a location that minimizes any ship-induced effects such as heating. WS, 6 knots, is the true wind speed as corrected from the ship's anemometer reading. The procedure to calculate the evaporation duct height, DH is then:

1. Find the intersection of TA and RH in graph 1.

2. Project a line horizontally into graph 2 until it intersects TS. Extend a line from this intersection vertically downward into graph 4.

3. Compute the air-sea temperature difference TA-TS. Find the intersection of TA-TS and WS on graph 3 and project a line horizontally into graph 4.

4. The intersection of lines from graphs 3 and 4 indicates the evaporation duct height.

The resultant duct height for the example in Figure 6 is 16 metres. This information can then be used in conjunction with graphs such as those in Figure 7. These graphs show the variation of detection range of a destroyer-sized target with duct height and can be prepared for any radar. Notice that detection ranges increase with duct height. And, although the performance characteristics of the two radars are not the same, the major difference between the two curves can be explained by the difference in frequency. Thus, the higher frequency is enhanced more than the lower frequency. Conversely a higher frequency radar requires a less strong duct for a given detection range than does the lower frequency radar.

Alternatively, the same information for a given radar can be displayed as in Figure 8, giving detection range directly.

Figures 9 and 10 show the variation of maximum ESM intercept range with duct height for an arbitrary receiver with two different antenna

Receiver at 3'

(INTERCEPT RANGE IN NAUTICAL MILES)

		EVAPORATION DUCT HEIGHT (METERS)																					SURFACE BASED DUCT HEIGHT (METERS)				
EMITTER	FREQ (MHZ)	0	2	4	6	8	10	12	14	16	18	20	22	24	26	28	30	32	34	36	38	40	150	225	300	375	450
1	215	200	200	200	200	200	200	200	200	200	200	200	200	200	200	200	200	200	200	200	200	200	200	200	200	200	200
2	220	200	200	200	200	200	200	200	200	200	200	200	200	200	200	200	200	200	200	200	200	200	200	200	200	200	200
3	220	181	181	181	181	181	181	181	181	181	181	181	181	181	181	181	181	181	181	181	181	181	200	200	200	200	200
4	220	200	200	200	200	200	200	200	200	200	200	200	200	200	200	200	200	200	200	200	200	200	200	200	200	200	200
5	220	200	200	200	200	200	200	200	200	200	200	200	200	200	200	200	200	200	200	200	200	200	200	200	200	200	200
6	425	79	79	79	79	79	80	80	80	81	81	82	82	83	83	84	85	86	87	88	90	91	200	200	200	200	200
7	896	73	73	73	73	73	73	74	74	74	75	76	77	79	82	85	88	93	98	104	112	121	200	200	200	200	200
8	1030	31	32	33	34	35	36	37	37	38	40	42	44	47	50	53	57	62	68	74	83	93	200	200	200	200	200
9	1150	24	25	26	27	28	28	29	29	30	31	33	35	37	40	43	46	51	56	62	70	80	200	200	200	200	200
10	3000	123	123	123	123	123	123	123	123	125	134	156	200	200	200	200	200	200	200	200	200	200	200	200	200	200	200
11	3000	117	117	117	117	117	117	117	117	120	130	153	197	200	200	200	200	200	200	200	200	200	200	200	200	200	200
12	3000	157	157	157	157	157	157	157	157	158	160	177	200	200	200	200	200	200	200	200	200	200	200	200	200	200	200
13	3000	133	133	133	133	133	133	133	134	135	141	162	200	200	200	200	200	200	200	200	200	200	200	200	200	200	200
14	3000	34	36	38	39	42	46	51	58	68	81	101	134	179	200	200	200	200	200	200	200	200	200	200	200	200	200
15	3005	115	115	115	115	115	115	115	116	119	129	153	197	200	200	200	200	200	200	200	200	200	200	200	200	200	200
16	3030	41	42	43	45	47	51	56	64	74	89	111	148	200	200	200	200	200	200	200	200	200	200	200	200	200	200
17	3080	198	198	198	199	198	198	198	198	198	198	200	200	200	200	200	200	200	200	200	200	200	200	200	200	200	200
18	3500	161	161	161	161	161	161	161	161	162	175	200	200	200	200	200	200	200	200	200	200	200	200	200	200	200	200
19	3600	97	97	97	97	97	97	98	102	116	143	191	200	200	200	200	200	200	200	200	200	200	200	200	200	200	200
20	3625	111	111	111	111	111	111	111	112	114	125	152	200	200	200	200	200	200	200	200	200	200	200	200	200	200	200
21	5533	70	70	70	70	72	78	95	130	200	200	200	200	200	200	200	200	200	200	200	200	200	200	200	200	200	200
22	5550	148	148	148	148	148	148	149	172	200	200	200	200	200	200	200	200	200	200	200	200	200	200	200	200	200	200
23	5662	200	200	200	200	200	200	200	200	200	200	200	200	200	200	200	200	200	200	200	200	200	200	200	200	200	200
24	9800	46	46	48	53	67	95	184	200	200	200	200	200	200	200	200	200	200	200	200	200	200	200	200	200	200	200
25	8815	17	19	22	29	41	66	146	200	200	200	200	200	200	200	200	200	200	200	200	200	200	200	200	200	200	200
26	8815	27	31	34	42	56	83	153	200	200	200	200	200	200	200	200	200	200	200	200	200	200	200	200	200	200	200
27	8815	23	26	29	35	47	69	125	200	200	200	200	200	200	200	200	200	200	200	200	200	200	200	200	200	200	200
28	8950	37	38	41	49	64	95	184	200	200	200	200	200	200	200	200	200	200	200	200	200	200	200	200	200	200	200
29	8950	37	38	41	49	64	95	184	200	200	200	200	200	200	200	200	200	200	200	200	200	200	200	200	200	200	200
30	8954	25	29	32	40	53	80	151	200	200	200	200	200	200	200	200	200	200	200	200	200	200	200	200	200	200	200
31	9050	25	29	32	40	53	81	156	200	200	200	200	200	200	200	200	200	200	200	200	200	200	200	200	200	200	200
32	9050	20	23	25	31	41	61	111	200	200	200	200	200	200	200	200	200	200	200	200	200	200	200	200	200	200	200
33	9050	36	38	41	49	64	97	191	200	200	200	200	200	200	200	200	200	200	200	200	200	200	200	200	200	200	200
34	9050	26	29	33	41	55	83	161	200	200	200	200	200	200	200	200	200	200	200	200	200	200	200	200	200	200	200
35	9050	25	29	32	40	54	82	158	200	200	200	200	200	200	200	200	200	200	200	200	200	200	200	200	200	200	200
36	9050	27	31	34	43	57	86	168	200	200	200	200	200	200	200	200	200	200	200	200	200	200	200	200	200	200	200
37	9050	27	30	34	42	56	86	167	200	200	200	200	200	200	200	200	200	200	200	200	200	200	200	200	200	200	200
38	9080	30	34	37	46	61	92	183	200	200	200	200	200	200	200	200	200	200	200	200	200	200	200	200	200	200	200
39	9375	19	21	23	29	39	58	111	200	200	200	200	200	200	200	200	200	200	200	200	200	200	200	200	200	200	200
40	9375	21	24	27	34	45	70	141	200	200	200	200	200	200	200	200	200	200	200	200	200	200	200	200	200	200	200
41	9375	19	21	23	29	39	58	111	200	200	200	200	200	200	200	200	200	200	200	200	200	200	200	200	200	200	200
42	9375	15	21	23	29	37	55	104	200	200	200	200	200	200	200	200	200	200	200	200	200	200	200	200	200	200	200
43	9375	19	22	24	30	40	61	118	200	200	200	200	200	200	200	200	200	200	200	200	200	200	200	200	200	200	200
44	9375	20	23	26	32	43	66	131	200	200	200	200	200	200	200	200	200	200	200	200	200	200	200	200	200	200	200
45	9375	20	23	26	32	43	67	132	200	200	200	200	200	200	200	200	200	200	200	200	200	200	200	200	200	200	200
46	9410	17	19	21	25	33	50	89	200	200	177	107	92	103	103	103	103	103	103	103	103	103	200	200	200	200	200
47	9445	17	19	21	25	33	50	91	200	200	174	106	93	103	103	103	103	103	103	103	103	103	200	200	200	200	200
48	9445	17	19	21	25	33	50	91	200	200	174	106	93	103	103	103	103	103	103	103	103	103	200	200	200	200	200
49	9445	20	23	26	32	44	68	137	200	200	200	200	200	200	200	200	200	200	200	200	200	200	200	200	200	200	200
50	9525	26	30	34	42	58	91	200	200	200	200	200	200	200	200	200	200	200	200	200	200	200	200	200	200	200	200
51	10125	11	12	13	15	19	29	34	20	16	15	14	14	14	14	14	14	14	14	14	14	14	200	200	200	200	200
52	10125	15	17	19	23	31	50	101	200	118	57	40	42	44	44	44	44	44	44	44	44	44	200	200	200	200	200
53	10375	21	25	28	36	50	87	200	200	200	200	200	200	200	200	200	200	200	200	200	200	200	200	200	200	200	200
54	15550	17	20	24	36	67	200	200	200	200	200	200	200	200	200	200	200	200	200	200	200	200	200	200	200	200	200

Figure 9. ESM intercept range versus duct height for a receiving antenna 3' above the sea surface

Receiver at 170'

(INTERCEPT RANGE IN NAUTICAL MILES)

EMITTER	FREQ (MHZ)	EVAPORATION DUCT HEIGHT (METERS)																					SURFACE BASED DUCT HEIGHT (METERS)				
		0	2	4	6	8	10	12	14	16	18	20	22	24	26	28	30	32	34	36	38	40	150	225	300	375	450
1	215	200	200	200	200	200	200	200	200	200	200	200	200	200	200	200	200	200	200	200	200	200	200	200	200	200	200
2	220	200	200	200	200	200	200	200	200	200	200	200	200	200	200	200	200	200	200	200	200	200	200	200	200	200	200
3	220	191	191	191	191	191	191	191	191	191	191	191	191	191	191	191	191	191	191	191	191	191	200	200	200	200	200
4	220	200	200	200	200	200	200	200	200	200	200	200	200	200	200	200	200	200	200	200	200	200	200	200	200	200	200
5	220	200	200	200	200	200	200	200	200	200	200	200	200	200	200	200	200	200	200	200	200	200	200	200	200	200	200
6	425	86	86	86	86	86	86	87	87	87	87	87	85	88	89	89	90	90	91	92	94	95	200	200	200	200	200
7	896	80	80	80	80	81	81	81	81	82	82	83	85	87	89	92	96	102	105	112	119	129	200	200	200	200	200
8	1030	40	40	41	42	42	43	44	45	46	47	49	52	54	58	61	65	70	76	83	91	101	200	200	200	200	200
9	1100	35	36	36	37	37	38	35	39	39	40	41	43	45	48	51	55	59	65	71	79	88	200	200	200	200	200
10	1000	132	132	132	132	132	132	132	133	136	147	172	200	200	200	200	200	200	200	200	200	200	200	200	200	200	200
11	1030	126	126	126	126	126	126	126	126	131	143	168	200	200	200	200	200	200	200	200	200	200	200	200	200	200	200
12	1000	167	167	167	167	167	167	167	167	165	172	191	200	200	200	200	200	200	200	200	200	200	200	200	200	200	200
13	1000	143	143	143	143	143	143	143	143	145	154	177	200	200	200	200	200	200	200	200	200	200	200	200	200	200	200
14	1000	44	47	49	52	54	59	65	72	83	97	117	151	184	200	200	200	200	200	200	200	192	200	200	200	200	200
15	1005	124	124	124	124	124	124	124	125	130	143	168	200	200	200	200	200	200	200	200	200	200	200	200	200	200	200
16	1030	49	51	54	56	59	64	70	78	89	104	127	165	200	200	200	200	200	200	200	200	200	200	200	200	200	200
17	1030	200	200	200	200	200	200	200	200	200	200	200	200	200	200	200	200	200	200	200	200	200	200	200	200	200	200
18	1500	170	170	170	170	170	170	170	170	172	189	200	200	200	200	200	200	200	200	200	200	200	200	200	200	200	200
19	3600	105	105	105	105	105	105	107	115	131	160	200	200	200	200	200	200	200	200	200	200	200	200	200	200	200	200
20	3625	120	120	120	120	120	120	121	125	139	169	200	200	200	200	200	200	200	200	200	200	200	200	200	200	200	200
21	5533	77	77	79	78	82	92	112	150	200	200	200	200	200	200	200	200	200	200	200	200	200	200	200	200	200	200
22	5550	158	158	158	158	158	158	159	160	190	200	200	200	200	200	200	200	200	200	200	200	200	200	200	200	200	200
23	5662	200	200	200	200	200	200	200	200	200	200	200	200	200	200	200	200	200	200	200	200	200	200	200	200	200	200
24	9800	52	55	59	65	85	120	195	200	200	200	200	200	200	200	200	200	200	200	200	200	200	200	200	200	200	200
25	9815	30	34	38	46	59	88	157	200	200	200	200	200	200	200	200	200	200	200	200	200	200	200	200	200	200	200
26	9815	40	45	50	59	74	105	166	200	200	200	200	96	73	72	72	72	72	72	72	72	72	200	200	200	200	200
27	9815	37	41	45	52	65	92	136	200	200	149	61	37	37	37	37	37	37	37	37	37	37	200	200	200	200	200
28	9950	45	50	55	65	82	118	193	200	200	200	200	200	200	200	200	200	200	200	200	200	200	200	200	200	200	200
29	9950	45	50	55	65	82	118	193	200	200	200	200	200	200	200	200	200	200	200	200	200	200	200	200	200	200	200
30	9954	39	44	49	57	71	102	160	200	200	200	106	56	46	46	46	46	46	46	46	46	46	200	200	200	200	200
31	9050	39	44	49	57	72	104	166	200	200	200	95	54	45	45	45	45	45	45	45	45	45	200	200	200	200	200
32	9050	34	38	41	48	60	84	119	200	175	35	34	34	34	34	34	34	34	34	34	34	34	200	200	200	200	200
33	9050	45	50	55	65	82	119	199	200	200	200	200	200	200	200	200	200	200	200	200	200	200	200	200	200	200	200
34	9050	39	44	49	58	73	106	169	200	200	200	130	65	56	56	56	56	56	56	56	56	56	200	200	200	200	200
35	9050	39	44	49	57	72	104	166	200	200	200	108	55	49	49	49	49	49	49	49	49	49	200	200	200	200	200
36	9050	40	45	50	59	75	109	176	200	200	200	192	93	75	75	75	75	75	75	75	75	75	200	200	200	200	200
37	9050	40	45	50	59	75	108	175	200	200	200	177	87	71	71	71	71	71	71	71	71	71	200	200	200	200	200
38	9080	42	48	53	62	79	115	191	200	200	200	200	172	134	134	134	134	134	134	134	134	134	200	200	200	200	200
39	9375	33	37	40	46	57	82	115	200	54	33	33	33	33	33	33	33	33	33	33	33	33	200	200	200	200	200
40	9375	35	40	44	51	64	94	145	200	200	43	35	35	35	35	35	35	35	35	35	35	35	200	200	200	200	200
41	9375	33	37	40	46	57	82	115	200	54	33	33	33	33	33	33	33	33	33	33	33	33	200	200	200	200	200
42	9375	32	37	39	45	56	79	107	200	35	33	32	32	32	32	32	32	32	32	32	32	32	200	200	200	200	200
43	9375	34	38	41	47	59	85	121	200	77	34	34	34	34	34	34	34	34	34	34	34	34	200	200	200	200	200
44	9375	35	39	42	49	62	90	135	200	156	35	35	35	35	35	35	35	35	35	35	35	35	200	200	200	200	200
45	9375	35	39	42	50	62	90	136	200	170	35	35	35	35	35	35	35	35	35	35	35	35	200	200	200	200	200
46	9610	31	35	37	43	52	73	92	188	33	31	31	31	31	31	31	31	31	31	31	31	31	200	200	200	200	200
47	9665	31	35	37	43	52	73	93	179	33	31	31	31	31	31	31	31	31	31	31	31	31	200	200	200	200	200
48	9665	31	35	37	43	52	73	93	179	33	31	31	31	31	31	31	31	31	31	31	31	31	200	200	200	200	200
49	9665	35	39	43	50	63	92	140	200	160	35	35	35	35	35	35	35	35	35	35	35	35	200	200	200	200	200
50	9525	39	45	50	59	77	116	200	200	200	200	117	71	65	65	65	65	65	65	65	65	65	200	200	200	200	200
51	10125	26	28	30	33	38	47	33	29	27	26	26	26	26	26	26	26	26	26	26	26	26	200	200	200	200	200
52	10125	30	34	36	41	51	70	88	35	31	30	30	30	30	30	30	30	30	30	30	30	30	200	200	200	200	200
53	10375	35	40	45	53	70	106	200	200	118	35	35	35	35	35	35	35	35	35	35	35	35	200	200	200	200	200
54	15550	31	35	40	52	76	200	32	31	31	31	31	31	31	31	31	31	31	31	31	31	31	200	200	200	200	200

Figure 10. ESM intercept range versus duct height for a receiving antenna 170' above the sea surface

heights versus various radars. It is seen that a surface-based duct traps all frequencies and gives greatly extended ranges (200 nmi or greater). It is also obvious that the evaporation duct effects are highly frequency dependent. Low frequencies, less than approximately 500 MHz, do not experience great variation in range as duct height varies whereas the higher frequencies do. Intercept range generally increases with duct height. However, in some cases, an optimum duct height is reached above which the receiver and emitter antenna heights become the dominant factor and the intercept range decreases with increasing duct height (higher frequencies in Figure 10). Also note that the higher frequencies do not require as strong a duct for the same range enhancement as the lower frequencies. Comparing Figures 9 and 10 shows the effect of antenna height on intercept range under standard atmospheric conditions (0 duct height). Under weak ducting conditions (low duct heights), the high antenna gives longer intercept ranges. However, under strong ducting conditions (high duct heights), the low antenna gives longer intercept ranges at the higher frequencies.

6. REFERENCES

Hitney, H. V., 1975: Propagation Modeling in the Evaporation Duct, NELC TR 1947.

Katzin, M., R. W. Bauchman, and W. Binnian, 1947: 3- and 9-Centimeter Propagation in Low Ocean Ducts, Proc. IEEE, 35, 891-905.

Kerr, D. E., 1951: Propagation of Short Radio Waves, McGraw-Hill, New York.

Richter, J. H. and H. V. Hitney, 1975: The Effect of the Evaporation Duct on Microwave Propagation, NELC TR 1949.

METEOROLOGICAL MEASURING SYSTEM (MMS) - DROPSONDE AND MINI-REFRACTIONSONDE

Edward T. Schmidt

Naval Air Development Center
Warminster, Pennsylvania 18974

ABSTRACT

This paper is intended to present an overview of a program currently under development at the Naval Air Development Center. The program, which is sponsored by the Naval Air Systems Command (AIR-370), is intended to provide meteorological sensors and processors which will allow for the tactical exploitation of refractive anomalies by the Fleet. The first section of the paper will briefly review the environmental conditions which can affect electro-magnetic propagation. These effects will then be treated relative to mission impact for an ASW aircraft. The mechanism by which fleet ASW forces can utilize refraction data will be discussed followed by a description of an air launchable dropsonde system currently under development. A brief description of a shipboard launched mini-refractionsonde, also under development, will be presented and finally status summaries and developmental schedules for each system will be discussed.

DISCUSSION

I. Electromagnetic Refraction and the Environment.

Environmental effects on the propagation of electro-magnetic radiation near the surface of the earth cause two primary anomalous effects: a low-loss surface propagation duct and a related high-loss "shadow zone" above the surface duct. The parameters that are most influential in controlling propagation anomalies (temperature, pressure, and humidity) are also most variable near the earth surface and are thus more likely to cause a surface duct than an elevated duct. The surface duct is defined as a region which causes some upward traveling rays from a surface-based emitter to bend toward the earth which, after becoming downward rays, either bounce from the earth surface or are subsequently refracted upward. These totally refracted or refracted-reflected rays stay trapped within the dimension of the duct while other rays emitted at more acute angles penetrate and escape the duct. The emission ray angle closest to the vertical which becomes trapped in the duct is called the limiting ray angle. The emission angle closest to the emission angle just beyond the limiting ray does not become trapped, but penetrates and escapes the duct. After penetration of the duct, the acute rays typically become upward refractive, forming an energy void between the limiting ray path and the top of the surface duct. This region is known as a shadow zone and contains no direct path emission energy. An example of this is depicted in Figure 1. Since the proximity of the emitter to the top of the duct influences the limiting ray angle, the vertical dimension of the duct will influence the amount of energy trapped.

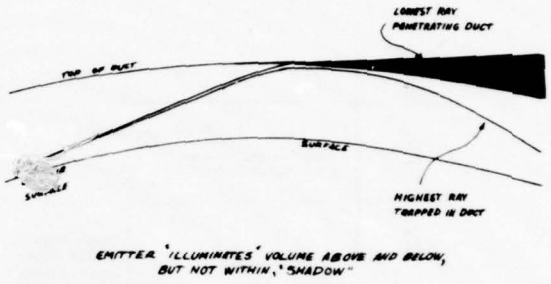

Figure 1. "Shadow" caused by emitter in surface-based duct

Under normal conditions, electro-magnetic radiation propagates to a line of sight horizon which can be calculated from linear geometric principles. These values are typically used to predict effective radar ranges. Surface duct propagation effects however can trap energy and produce a low-loss propagation condition which can effectively extend radar ranges. This condition is sometimes referred to as an extended horizon since it effectively produces electromagnetic propagation paths which follow the earth curvature and extend well beyond straight line horizons. Since the altitude of radar contacts is usually based on straight line ray path assumptions and antenna elevation angles, a surface-based duct which refracts emissions may result in erroneous estimates of the altitude of radar detected aircraft. Examples of distortion of straight line horizons and elevation errors of detected aircraft for surface based ducts are depicted in Figure 2. The effect of a surface-based duct on the performance of radar emissions for targets and emitters at the sea surface, within, and above the duct, are summarized in Table I.

The surface duct is present in many geographical areas and is often very dynamic over time; i.e., some locations exhibit these ducts only under certain weather conditions which change dramatically over time. In addition, some weather conditions cause

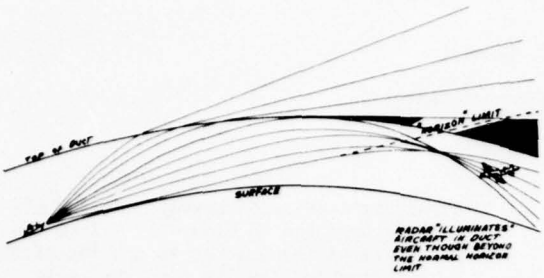

Figure 2. Range extension and elevation errors caused by trapped rays

Radar Position \ Target Position	Surface	In Duct	Above Duct
Above Duct	Extended horizon, elevation errors near horizontal	Reduced range in shadow	
In Duct	Enhanced ranges, elevation errors, signature distortion		Reduced ranges in and near shadow, elevation errors near horizontal, extended range
Surface			

Table I. Surface-based duct -- expected radar performance effects

propagation ducts at altitudes well above the earth surface. These phenomena, referred to as elevated ducts, influence the propagation of electro-magnetic emissions in much the same fashion as surface ducts for emitters within the duct. However for elevated ducts, there are conditions which place emitters below or above the duct. It is of some instructional value to review these conditions and their effect on propagation. For the conditions of an elevated duct with an emitter below the duct, rays penetrating the duct at low elevation angles, remain within the duct for a considerable range, are refracted, and then escape through the top of the duct. This condition results in a false target elevation for a radar tracking an aircraft. For the case of an emitter above the duct, there is a limiting ray for penetration of the duct and a resultant shadow zone above the duct at a distant range. In addition, there is a false horizon for the ray slightly elevated from the ray that would calculate to the horizon. This ray will produce a propagation extension beyond the true horizon. These conditions are depicted in Figure 3 and show that false ranges are derived from radar detections of surface targets, and detections are lost by shadow zones at very achievable ranges for aircraft targets. The radar performance effects for combinations of emitters and targets at the sea surface, immediately below, in, and above these elevated ducts, are summarized in Table II.

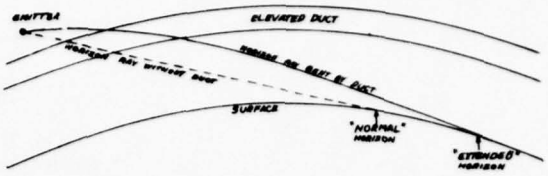

DUCT BENDS RAYS.
BEND RADIUS IS LESS THAN CONCENTRIC.
SURFACE IS ILLUMINATED BEYOND NORMAL HORIZON.

(a)

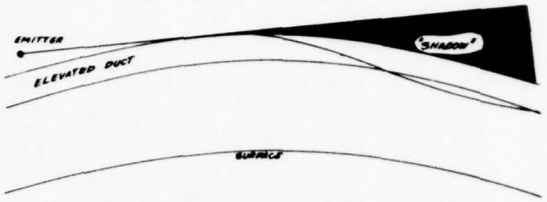

RAYS TANGENT TO TOP OF DUCT ARE CRITICAL.
RAYS BELOW CRITICAL ARE BENT BY DUCT.
RAYS ABOVE CRITICAL ARE UNAFFECTED BY DUCT.
VOLUME NOT ILLUMINATED IS SHOWN AS "SHADOW."

(b)

Figure 3. Extended radar ranges (a), "shadow" (b) caused by emitter above elevated duct

Radar Position \ Target Position	Surface	Below Duct	In Duct	Above Duct
Above Duct	Extended horizon, elevation errors near horizontal		Reduced range in shadow	
In Duct	Elevation errors near horizontal	No duct effect	Enhanced range, signature distortion	Reduced range in and near shadow
Below Duct			Elevation errors near horizontal	Extended ranges, elevation errors near horizontal
Surface				

Table II. Elevated duct -- expected radar performance effects

II. Refraction Impact on ASW Missions

The refraction anomalies discussed earlier can combine with the ASW mission parameters to cause both desirable and undesirable situations. ASW aircraft flying at altitudes without knowledge of refraction anomalies can produce situations which cause loss of sonobuoy RF data during operations, loss of communication links with friendly surface vessels or task force and more subtly, a false security from distant enemy detection and attack. If refraction conditions are known, proper altitude selection can optimize the successful completion of the mission and return of deployed aircraft. An optimum flying condition for all these concerns is depicted in Figure 4.

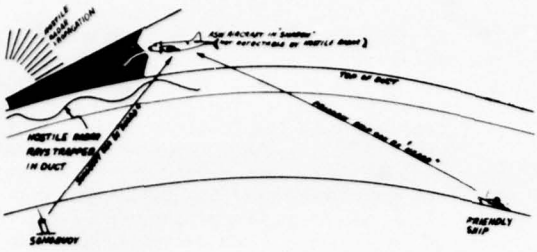

Figure 4. Optimum flying position for monitoring sonobuoys

Presently, ASW forces have available during pre-flight the historical data files from FNWC (Fleet Numerical Weather Central) for areas of operations. Generally because of the dynamics of these environmental conditions, historical data are not relied upon. The sole source of these kinds of data for today's ASW fleet operations becomes local radiosonde data obtained at a carrier for S-3 type aircraft. These data are rarely used by patrol aircraft for mission tactical planning and only occasionally used by carrier-based aircraft. However, the meteorological unit on board carriers continuously updates their information by launching radiosondes. The recently developed IREPS (Index of Refraction Effects Prediction System) is intended for use in both VP (Patrol) and CV (Carrier) TSC (Tactical Support Center). This functional capability has a most desirable product and ideally could be utilized to impact both ASW and other aircraft mission plans. If the input data are current and related to the locale of the mission, the utilization of these data will increase.

The dropsonde system is being developed so that these data are used by both land-based and carrier-based aircraft. Incidentally, the dropsonde utilization will assist in answering the nagging unknown about horizontal homogeneity while at the same time supplying large quantities of data for confidence building of the statistics over season, weather conditions, and location. The dropsonde is a system which includes both the sensor and the processor. This system will be utilized aboard P-3 aircraft for TECHEVAL testing and data will be collected, processed, and displayed aboard the aircraft via the dedicated carry-on processor. In addition, the raw data from the ASW aircraft receiver will be recorded on magnetic tape and processed at the TSC.

The ultimate utilization of this system could include on-board processing and display of refraction data for both P-3 and S-3 aircraft without the addition of hardware to the avionics suite. Each aircraft could then use these data for survivability to and from mission sites, maximizing mission success by full reception of all sonobuoy telemetry and communication with task forces, and even for maximum effectiveness of a missile strike. Each aircraft could also telemeter these data to other forces in air, on land, or sea for more broad-based utilization and could record (on magnetic tape currently used for acoustics and Bathythermograph data) these data for post mission reproduction and analysis at a TSC or equivalent.

III. Dropsonde Characteristics

The dropsonde system under development consists of a sensor and a processor. The intent is to utilize the dropsonde system with currently used ASW aircraft receivers, much in the same manner as a sonobuoy and its processor. The dropsonde sensor is contained within the form factor of an "A" size sonobuoy (4.785" diameter x 36" length cylinder). With this design, the sensor can be loaded aboard and launched from ASW aircraft in exactly the same fashion as sonobuoys. The sensor weighs 11 pounds and is retarded in the air stream after launch by a two-stage parachute system which is initiated by a wind flap mechanism. Once deployed into the airstream, the sensor orients and stabilizes in-air flow within six seconds, while descending at a rate of 1700 feet/minute. This descent rate combines with the commutation rate of 0.8 seconds/cycle and sensor sample interval of 0.4 second/sample for temperature, pressure, and humidity to yield a data profile resolution of 12 feet. The output data format of the sensor is depicted in Figure 5. The data are multiplexed into the LOFAR (Low Frequency Analysis and Recording) sonobuoy acoustic passband and telemetered to the aircraft on one of three VHF sonobuoy channels used by the AXBT (Aircraft Expendable Bathythermograph) sonobuoy. This format enables the present avionics aboard ASW aircraft to receive this data and record the data on magnetic tape units normally used for acoustic data from sonobuoys. The details of the dropsonde sensor are listed in Table III.

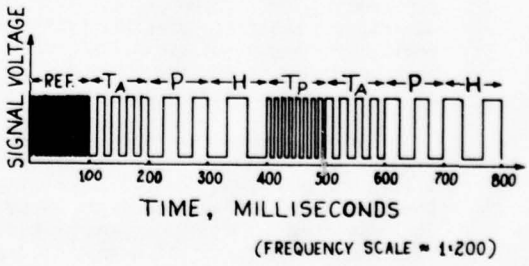

Figure 5. Refraction dropsonde output data format

The processor under development for use aboard ASW aircraft is designed to decommutate, digitize, and smooth data that is inputted from the ASW receiver. The processor will then convert the environmental data to engineering units, select significant values, and display the output. One output format will provide a 40 character-wide printed

Parameters	Description/Parameter Range & Accuracy
Package	'A' Size Sonobuoy - 11 lbs. - 2 stage chute
Transmitter	UHF - Sonobuoy Chs. 12-14-15
Modulation	FM
Data Frequency	225 to 2254 Hz (2500 Hz reference)
Data Waveform	Squarewave - 50% duty cycle
Commutation Rate	0.8 sec/cycle - 0.1 sec/sample
Sensor Sample Interval	0.4 seconds
Launch	Min.: 3500 ft @ 300 knots, Max.: 36,000 ft @ 300 knots
Battery	Lithium (SO_2) - 12C min. operating - 5yr. shelf (90%)
Temperature	Rod Thermistor - YSI #1152-236 (-65°C to +50°C) ± 0.5°C
Humidity	Carbon Hygristor - YSI #1153-56 (0 to 100% R.H.) ± 5% R.H.
Pressure	Solid State - Honeywell (100 to 1050mb) ± 2mb

Table III. Refraction dropsonde details

report of the real time refractive layer, including the altitude (in feet) at the top of a duct, the strength of a duct (in "M" units), and the altitude (in feet) at the bottom of the duct. It will also indicate date, time, latitude, longitude, and miscellaneous labeling information. Another output format will provide a refractivity report that will be available within minutes after the cessation of telemetered data. Finally, it will provide a meteorological report in WMO (World Meteorological Organization) format.

The real time refractive layer report can be compared on-site with the mission environment prediction received prior to flight and adjustments and refinements in the mission plan can be made when required. In addition, a message can be sent back to the meteorological center or TSC indicating differences between the predicted information and the on-site measurements.

The refractivity profile report will be used as an input to the IREPS. These data can be used to construct and revise refractivity prediction information used to develop tactical mission plans. This report will also include pertinent header information for identification and the data entry will list pressure in feet, geopotential altitude in meters, and modified refractivity in "M"-units. The number of significant data points in this report is limited to 29 for compatibility with the IREPS input format.

The meteorological report option will provide data at significant and mandatory levels for WMO format weather reporting. These data collectively form the input to a local weather prediction by the meteorological unit aboard carriers. It also provides FNWC data to facilitate global weather assessments and as a byproduct provides archival data for the research and development community. This report contains listings of mandatory levels of pressure (mb), altitude (meters), temperature (^{o}C), and dew point depression (^{o}C) and listings of significant levels of pressure (mb), temperature (^{o}C) and dew point depression (^{o}C).

IV. Improved Refraction Sensor for Shipboard Use

In addition to the dropsonde sensor/processor system development which can be used by ASW aircraft, an improved shipboard refractivity measuring system is also under development by the Naval Air Development Center. This system, referred to as the MRS (Mini-Refractionsonde System), is designed so that the entire activity associated with the launch reception and processing of the data can be handled by one person aboard ship. In addition, the filling of the balloon and associated handling can all be accomplished below deck. This system receiver has an automatic signal acquisition feature which tracks a communication frequency, preventing loss of data. The system also requires no baseline check because of a plug-in calibration scheme and the processor functions are automated providing outputs without operation interaction. This entire system is the subject of the next paper to be presented. It is only mentioned here for introductory purposes.

V. Status and Development Schedules for Improved Refraction Sensor Systems

The dropsonde system is presently in the advanced development phase of the product acquisition cycle. The feasibility of this system has been demonstrated and presently initial acceptance evaluations are ongoing. This phase is expected to be completed by late FY-79. By sometime in early FY-80, a formal TECHEVAL of 100 dropsondes and two processors will be initiated. This evaluation is expected to require about nine months. If the TECHEVAL is successful, ASU (Approval for Service Use) is expected by the end of FY80. Production contracts for this system would be issued in FY-81 and fleet introduction would occur by FY-82. A layout of the principle events of this development schedule are shown in Figure 6.

The MRS system is basically similar to the dropsonde in nature, but is about three months later in achieving the ASU action. However, fleet introduction should be about the same time due to the simplicity of design and the less severe environmental justifications of the sensor in this system.

Because the dropsonde system has an environmental sensor of the form of a sonobuoy, it has led the community to consider combining the AXBT, another environmental sensor of this form, with the dropsonde. The AXBT is used in acoustic ASW in a manner analogous to the refractionsonde. The AXBT data are used to input to ray tracing programs to derive underwater acoustic propagation layers and their dimensions, limiting rays to the surface, and general propagation loss from source to receiver. It is entirely feasible, considering the volume available in an "A" size sonobuoy container, to combine these two functions into one overall environmental sensor. The critical issues of this marriage are the sensor and mission cost impact and the basic

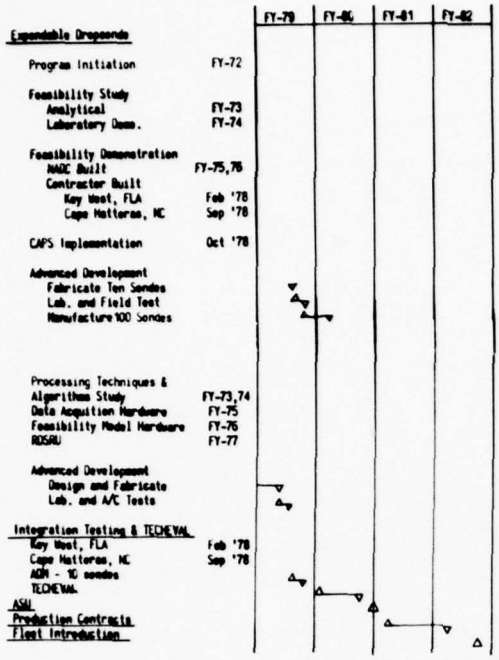

Figure 6. Refraction dropsonde system development schedule

sensor conflicts; e.g., a slow in-air descent for refraction vs a desire to rapidly obtain BT data to begin an ASW contact prosecution. Some of these issues are under investigation at present. Any resolution of these issues that would encourage sensor development will be scheduled into future plans.

Another growth potential for the dropsonde sensor for ASW impact has been studied and evaluated in the past but never pursued. The inclusion of wind into the sensor capability, by the reception and retransmission of Omega navigation data, is a desirable ASW parameter. These data would enable much more accurate sonobuoy location estimates to be made so that higher altitude target localization can be achieved. This improvement is also being considered for future plans, but for now the schedule shown earlier will be followed for the basic dropsonde system.

THE MINI-REFRACTIONSONDE SYSTEM (MRS) FOR MEASURING REFRACTIVE INDEX

Curtis D. Motchenbacher

Honeywell, Inc.

Hopkins, Minnesota 55343

1. INTRODUCTION

The Navy has a requirement to measure the vertical profile of index-of-refraction from sea level to above 15,000 feet. It is necessary to make these measurements from many classes of ships under typical operating conditions. To fill this need, a light-weight balloon sonde and processor (mini-refractionsonde system) is being developed by Honeywell under contract from Naval Air Development Center and sponsored by Naval Air Systems Command (AIR-370).

This paper discusses the mini-refractionsonde program plan and status. The development of the sonde, ground station, balloon filling and handling equipment are described. Discussions on utilization of the sonde are included.

2. BACKGROUND

The principal purpose of the mini-refractionsonde program is to develop a system for measuring the altitude and strength of atmospheric inversion layers. Near a land mass, these layers will create cells of atmosphere that are homogeneous over a distance of 10 to 20 miles. These cells create holes or ducts for radar signals. For shipboard radars this can greatly extend the range of radar detection along the surface, but can create elevated holes in the radar coverage. Communications signals are also affected by the inversion layers. This is particularly a problem when trying to communicate from surface ships to aircraft aloft.

There are three difficulties in measuring atmospheric refractivity from a shipboard environment. First it is desirable to measure refractivity in localized areas of 10 to 20 miles. Second it is necessary to make the measurements while operating in a confined shipboard space. Third, it is necessary to operate in a high radar and RF interference environment.

A solution to the problem of measuring atmospheric refractivity from a shipboard environment is to develop a small light-weight miniature balloon sonde that can be launched with small 30 gram or 100 gram pibal balloons. Because of the smaller balloon it is possible to launch the sondes from ships such as destroyers and frigates where conventional sonde launching capabilities are not available. For ease of handling, the equipment is made semi-automated for one man operation. The system is one-man portable for transfer from ship to ship. This way data can be obtained over a wide area as the ship is deployed. The telemetry system is being made RF tolerant so it will operate in an EMI and radar environment.

3. DESCRIPTION OF DEVELOPMENT

3.1 Mini-Refractionsonde

The function of the sonde is to measure temperature and humidity versus altitude so refractive index can be calculated.

A VIZ premium rod thermistor is used for temperature measurement over the range of -95°C to +55°C. A VIZ premium carbon hygristor is used for humidity measurement over the range of 0 to 100 percent RH.

For pressure measurement, a Honeywell silicon diaphragm barometer is used. This device was originally developed for measuring altitude in commercial aircraft. The miniature pressure sensor consists of a 0.1 inch square silicon chip with strain sensitive resistors diffused into the surface of a one mil thick diaphragm. The back of the sensor is mounted on an evacuated tube to measure absolute pressure. The diaphragm is normally deflected by atmospheric pressure on the front of the diaphragm. As the pressure changes the diaphragm deflection decreases giving a change in reading on the diffused piezoresistive sensors. The altitude and pressure change is read out as a varying DC voltage. The pressure sensor has a basic accuracy of 5 millibars and has a reproducible accuracy of much better than one millibar. The resolution and hysteresis are much better than 0.1 millibar. The barometers are calibrated to one millibar and an overall accuracy of approximately 1.5 millibar over the pressure range of 0 to 1,050 millibars is expected. The barometer is capable of operating to greater than 10 atmospheres. This light-weight low cost barometer is the technological breakthrough that allowed the development of a light-weight mini-sonde.

A cut-away view of the mini-refractionsonde is shown in Figure 1. The sensors are mounted at the top in an air duct. Inside the case are located the meteorological electronics, the NAVAID receiver for wind sensing, the battery power supply, and telemetry transmitter. The antenna projects from the bottom of the case.

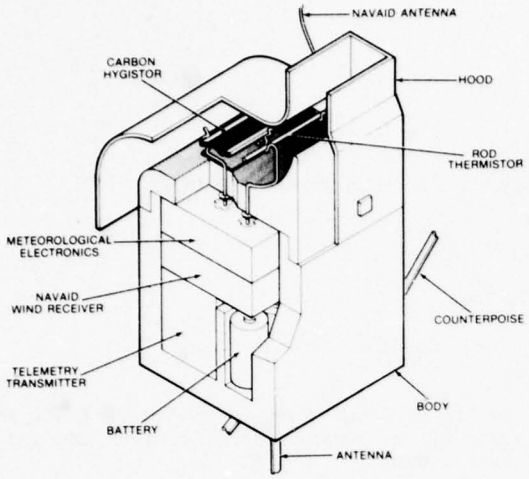

Figure 1. Mini-Refractionsonde, Cutaway

The sensor signals are commutated by an integrated electronics package which commutates at a 10 cycle per second rate. This gives an output of a high reference and all three sensor signals every 0.4 second. At a vertical ascent rate of 700 feet per minute, this gives a complete data frame every five feet of vertical ascent. The sensor voltage signals are converted to audio frequencies in the range of 200 to 2500 hertz by a linear voltage-to-frequency converter. These frequencies are telemetered to the ground station processor by an FM telemetry transmitter. The transmitter operates with 1/2 watt of power in the 400 to 406 megahertz meteorological telemetry band. Frequency modulation minimizes interference from other radio frequency sources. The telemetry transmitter antenna is a quarter wave ground plane antenna to give omni-directional signal radiation.

Power for the mini-sonde is provided by three lithium/sulfur dioxide cells. These cells each weigh 12 grams and will power the sonde for approximately two hours of operation. This is sufficient time for an ascent to 90,000 feet using a 300 gram balloon or to 20,000 feet using a 30 gram balloon. The cells are available either from PR Mallory & Company or from Honeywell's Power Sources Center. The development of high energy light-weight cells that can operate at 0°C has been a real boon to the mini-refractionsonde program.

The case for the sonde is made of molded styrofoam for light-weight and insulation. The upper hood shown in Figure 1 can be removed for insertion of the carbon hygristor. When the hood is placed on top of the sonde it forms a duct that increases the air flow past the hygristor to 1.8 times the vertical ascent velocity. This improves the carbon hygristor time-constant. The hood is metallized to eliminate solar effects on the carbon hygristor.

3.2 Ground Station

A drawing of the intended ground station is shown in Figure 2. The ground station consists of an antenna, preamplifier, telemetry receiver, microprocessor and printer. The present shipboard 400 megahertz dipole ground plane antennas will be used for the mini-refractionsonde system. A preamplifier and filter will be mounted at the antenna to improve telemetry range and interference signal rejection.

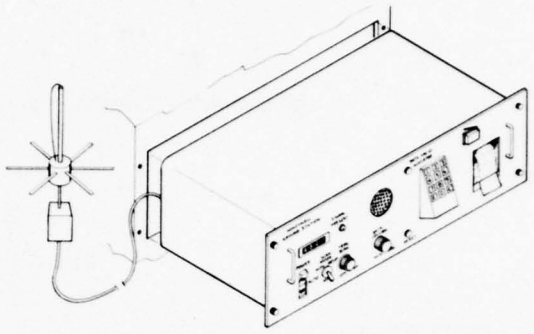

Figure 2. Ground Station

A special telemetry receiver has been developed to receive the meteorological signals in the presence of a high EMI environment. The receiver has high skirt rejection for out-of-band signals and a high intermodulation intercept point to reject in-band signal interference. Large radar pulses that overload the receiver are automatically blanked for the duration of the interference pulse. The receiver has automatic track-and-lock so that it will search for the sonde telemetry signal, lock-on and track the signal if the transmitter frequency drifts.

When the receiver is operated in the automatic mode it will scan for a signal until a sonde is acquired. If no signal is detected it will continue scanning until one is found. If the signal detected is not from a sonde, the processor will inform the receiver to continue scanning for a sonde signal.

The data processor consists of three microprocessor chips. The first microprocessor is concerned with telemetry receiver control and data reception. This first processor reads the sonde signal during each 0.1 second commutation, and passes the frequency on to the second processor. The second processor calculates the temperature, pressure and humidity using a dedicated arithmetic microprocessor. This second processor automatically analyzes the data, looking for inflection points in the temperature and humidity profiles. The output consists of a report of all of the significant levels as well as the mandatory levels required by the WMO format. A complete dump of all the sonde data is available on-line as the signals are being received.

The data is outputed on a 40 character wide ruggedized printer. The output is either in refractivity format or WMO format.

The mini-sonde does not require baselining. The sonde comes with lock-in values for the thermistor, hygristor and barometer stored in a PROM. Prior to launch, the PROM is inserted in the ground station processor. This automatically inputs all of the calibration data for the sonde into the calculation algorithms. If the PROM is lost or damaged, a set of nominal values are stored in the processor memory so the sonde can be used with

slightly degraded accuracy. A 12 button keyboard inputs launch altitude and launch location.

The ground station will be made for permanent mount or portable operation. The unit will be mountable in a standard 19-inch rack or in a water-proof carrying case. For ease of maintainability, the same units are used for permanent and mobile operation so they can be interchanged in case of breakdown.

The telemetry receiver can be operated in a manual mode with the front panel controls. A speaker is provided for monitoring the sonde telemetry signal. This may prove useful in accessing possible interference sources. A digital frequency display is provided.

3.3 Balloon Filling and Handling Equipment

To ease the task of balloon filling and insure inflation accuracy, an automatic balloon inflation device was constructed. The automatic filling mechanism is shown in Figure 3. The balloon is attached to a cup and hooked to a lever arm. As the balloon fills, it raises the lever arm and rotates the cam turning off the helium supply. If a greater free-lift is desired, the balloon is moved to a shorter lever arm. This requires a greater lifting force to turn off the helium. Either 300 or 100 gram balloons can be inflated by using their respective holes.

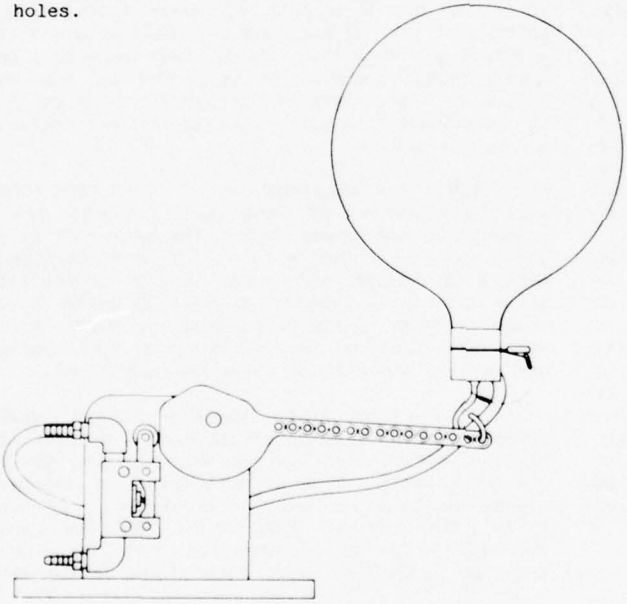

Figure 3. Balloon Filling Mechanism

For ease of handling a nylon shroud is placed over the balloon. Since the balloon is approximately 30 inch diameter it will pass through a standard hatchway door. The nylon shroud minimizes damage due to brushing against the door or overhead pipes. A covering shroud will be provided with each case of sondes.

After the balloon has been filled, the neck is tied using the cable tie strip shown in Figure 4. The sonde is supported by a harness line. The line is wrapped around a light-weight disposable train regulator. On the end of the line is a connector that inserts into the balloon tie strap, attaching the sonde to the balloon without making any knots.

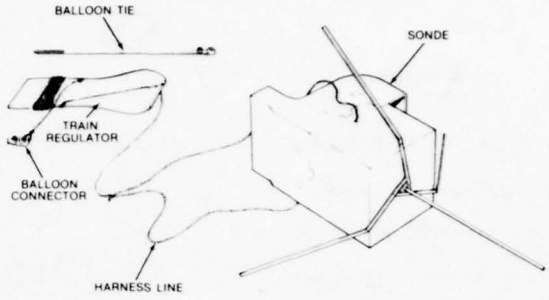

Figure 4. Launch Assembly

4. OPERATION WITH THE MINI-REFRACTIONSONDE SYSTEM

A typical operational sequence for a mini-refractionsonde launch is listed in Table 1. Except for the balloon filling and sonde launch, the operation is totally automatic. There is no baselining of the sonde, only the launch altitude must be entered. As the sonde is activated the receiver will automatically acquire and track the telemetry frequency. As the sonde is launched, the processor will detect the rise in altitude and begin the data processing. As the sonde ascends the refractive profile will be calculated and reported as each significant level is reached. When the balloon bursts and the sonde begins to descend, the processor will terminate the message.

TABLE 1. OPERATIONAL SEQUENCE

- o TURN "ON" GROUND STATION POWER
- o UNWRAP SONDE & BALLOON
- o INSERT ROM IN PROCESSOR
- o ENTER LAUNCH ALTITUDE
- o FILL & TIE BALLOON
- o PLACE COVER ON BALLOON
- o OPEN HYGRISTOR CAN & INSERT IN SONDE
- o CHECK FOR "DATA RECEIVED" LIGHT
- o ATTACH SONDE TO BALLOON
- o CARRY BALLOON & SONDE ON DECK
- o RELEASE BALLOON & SONDE
- o REFRACTIVITY MESSAGE BEGINS IMMEDIATELY
- o COMPLETE MESSAGE IN 15 to 30 MINUTES

Some of the advantages of the mini-refraction-sonde system compared to the present system are tabulated in Table 2. These advantages are primarily in the ease of operation and the reduction of the number of personnel required for launch. The amount of helium required for a typical operation is also significantly reduced.

TABLE 2. MRS ADVANTAGES

	PRESENT SYSTEM	MRS
LAUNCH PERSONNEL REQUIRED	3	1
TIME FOR A SOUNDING	3 HRS.	45 MINS.
BASELINE OF SONDE	YES	NO
AUTOMATIC DATA REDUCTION	NO	YES
BALLOONS FILLED/TANK	2-1/2	40

There is a cost savings in making a sounding only to the altitude required for the operation. A lower level sounding uses both a less expensive balloon and less helium. For soundings to 20,000 feet a 30 gram balloon can be used. A 100 gram balloon will carry the mini-sonde to 35,000 feet. A 300 gram balloon will provide a sounding to 90,000 feet.

Since most refractive anomalies occur below 10,000 feet, it is anticipated that the 30 gram balloon will be the primary ascent vehicle. If higher altitude soundings are desired, a larger balloon can then be selected.

5. WIND SENSING CAPABILITY

The Mini-Refractionsonde System does not presently measure winds aloft. There is a strong interest in incorporating wind sensing into the sonde. The sonde could be made into a wind sonde without the use of a tracking antenna by using the Omega NAVAID station signals. The use of Omega for wind sensing was demonstrated by Honeywell for NADC using the AMT-22 dropsonde. This wind sensing system consists of an Omega receiver in the sonde that receives and retransmits the Omega signals to the ground processor. The addition of wind sensing to the sonde would increase the weight and cost of the sonde by less than 10 percent. There is no formal plan to incorporate wind sensing in the Mini-Refractionsonde System; however, wind sensing Omega receivers are being added to some of the sondes for demonstration purposes. It is hoped that wind sensing capabilities can be added to the mini-refractionsonde within this year's program.

6. MRS PROGRAM PLAN AND STATUS

A copy of the Mini-Refractionsonde System program plan is shown in Figure 5. The program is proceeding in two stages. The first stage to be completed in mid-1979, will cover the advanced development of the mini-sonde, ground station and launch support equipment. The mini-sonde has previously gone through two development cycles and this is the third iteration. During the first project, the feasibility of a 100 gram sonde was demonstrated. During the second step, lab tests and flight tests at Wallops Island demonstrated the capabilities of the sonde. This advanced development phase is directed at making a producible sonde.

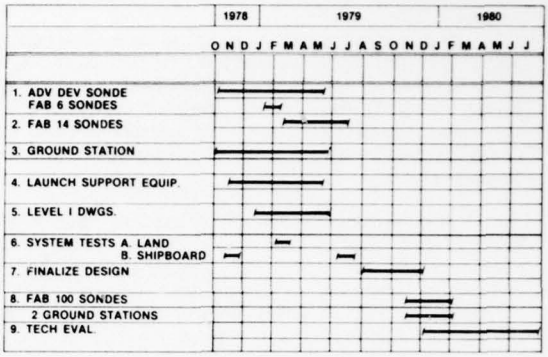

Figure 5. Mini-Refractionsonde System Program Plan

A ground station is being developed to automatically receive and process the telemetry signals from the sonde. A special RF telemetry receiver has been developed to receive the meteorological signals in the presence of radar interference. A microprocessor based ground station is being developed to provide on-line real-time data reduction and display. A ruggedized paper printer will output the data. The breadboard model of this ground station has been constructed and tested.

The launch support equipment consists of a method for filling and handling small balloons in a confined environment. The filling mechanism is a semi-automatic system to fill the balloon with helium to a predetermined nozzle lift. A model of the launch and fill mechanisms have been constructed and lab tested.

After the construction of 20 sondes, there will be a series of land tests in mid-1979 to demonstrate the operation of the mini-refractionsonde system. These tests will be conducted in an area with a high refractive anomaly probability. After successful completion of land tests of the sonde, further tests onboard an aircraft carrier will be conducted to demonstrate the system's operability under field operating conditions.

After successful demonstration of system operation under land and shipboard conditions, the Mini-Refractionsonde System will go through the final preproduction design phase in which any operational difficulties will be corrected. An additional quantity of 100 sondes and two ground stations will be constructed for use during TECHEVAL. TECHEVAL will take place during early 1980.

7. ACKNOWLEDGEMENTS

We would like to acknowledge the support of our sponsor, Mr. Ted Czuba of Naval Air Systems Command (AIR-370) and the contracting agent, Mr. Ed Schmidt of Naval Air Development Center. Thanks are also due to Lt. Commander Dan Gleavy for his support of our tests aboard the USS Ranger.

E-2C REFRACTOMETER

William A. Heile

Naval Avionics Center

Indianapolis, Indiana

ABSTRACT

In-flight display of measured refractive conditions has presented a problem to effective refractometer utilization. Previous developmental models utilized X-Y plotters and strip chart recorders to display refractivity as a function of altitude or time. These displays proved difficult to interpret in the operational environment. Recent effort has centered on the development of an improved microprocessor controlled display to provide the refractometer operator with a meaningful in-flight assessment of ducting layers encountered during climbout. Measurement technique, accuracy requirements and principles of operation of the AN/AMH-3(XAN-5) Airborne Microwave Refractometer (AMR) are presented.

1. INTRODUCTION

The AMR is being developed by Naval Air Systems Command to provide E-2C (Airborne Early Warning Aircraft) sensor and communications equipment operators with a propagation assessment immediately after climbout. A second purpose is to provide refractivity data to the carrier based Environmental/Weapons Effects Prediction System.

Previous models of the AMR underwent initial technical and operational testing on E-2B aircraft during 1976. As a result of this testing a decision was made to develop an improved (operationally effective) display and to retest the AMR in E-2C aircraft prior to a production decision.

2. REFRACTOMETER DESCRIPTION

The three units of the AMR are shown in Figure 1. The air sensor unit consisting of a fairing, microwave cavity and thermistor probe is pictured disassembled. This sensor unit is mounted atop the aircraft forward of the prop line. The ½ ATR sized processor unit is shock mounted in the avionics equipment bay. The new Light Emitting Diode (LED) display unit is mounted in the copilots console. The equipment is powered by 28 volts dc at 1.25 amps and weighs 28 pounds.

During flight, sensor data is digitized and recorded on standard 300 foot Phillips cassette tapes by the processor unit pictured in Figure 2. Sensor data consists of atmospheric pressure (from aircraft static system), ram refractivity, ram air temperature and total pressure (from aircraft pitot system). These quantities are recorded every two seconds. Twelve hours of data can be recorded on a single cassette. An 1802 CMOS microprocessor is utilized within the processor unit to correct displayed data for ram heating effects, to calculate and store altitudes of ducting layers and to perform built in test functions. An erasable programable read only memory is also utilized which will permit later growth in the refractive assessment programming to include display of additional anomalies such as subrefractive layers.

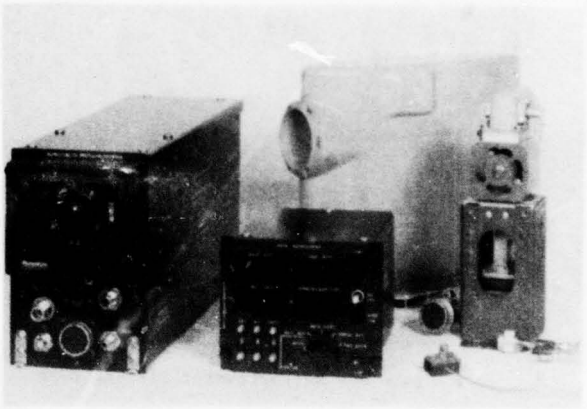

Figure 1. Airborne Microwave Refractometer AN/AMH-3(XAN-5)

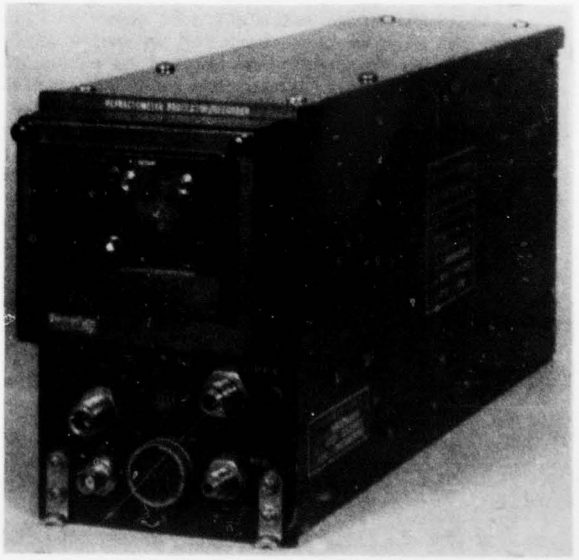

Figure 2. Refractometer Processor Unit

The display unit is pictured in Figure 3. After climbout to station altitude, the operator (copilot) can select any of the measured atmospheric ducting layers for display. Only layers greater than 200 feet thick are displayed at present. Analysis of all previous cassette data has resulted in a maximum of seven ducting layers displayed. The display is limited to nine layers. Typically between 0 and 2 layers are detected. The highest ducting layer to date was measured at 18,000 feet.

Figure 3. Refractometer Display Unit

In addition to ducting layers, the display unit also indicates current aircraft altitude, proposed aircraft altitude, built in test status (IFPM digit) and horizontal range to the expected propagation anomaly. Horizontal homogeneity of the atmosphere is assumed. If the aircraft descends below the base of a displayed ducting layer, that layer no longer causes a significant anomaly and no range calculation can be displayed. If the aircraft descends into a duct, the symbol "DDD" is displayed to alert the operator to over-the-horizon propagation in that layer. A physical representation of the range calculation is shown in Figure 4. The AMR uses measured data for ΔN (refractivity changes to the layer) and ΔH (height change to the layer). The calculation assumes the N-gradient is linear. If the operator selects a proposed altitude for display, the range calculation assumes a -8 N-unit/1000 feet gradient from the layer top. If no ducting layers are displayed (or the 0 layer is selected) the range calculation represents the radio horizon

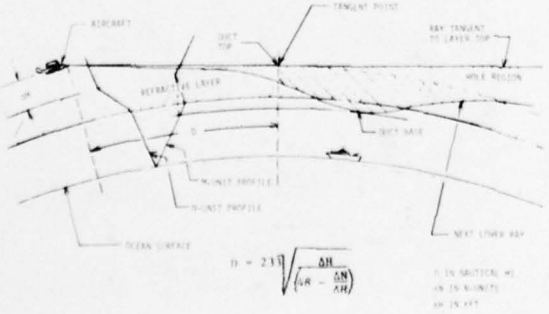

Figure 4. Refractometer Range Calculation

3. MEASUREMENT TECHNIQUE

Measurement requirements for the AMR are shown in Table 1. The ranges of the sensors are consistent with those expected in the lower 30,000 feet of the atmosphere. Raw data with ram air and thermal lag effects are recorded on magnetic tape and later corrected by computer. Air temperature and pitot pressure measurements provide the corrections. Typically these corrections add from one to 10 N-units to measured refractivity values.

Quantity Measured	Range	Resolution	Accuracy Thresholds
Absolute Atmospheric Pressure (From Aircraft Static System)	300-1050 millibars	0.75 millibars	± 5 millibars
Absolute Total Pressure (From Aircraft Pitot System)	318-1068 millibars	0.75 millibars	± 5 millibars
Relative RAM Refractivity	0-500 N-Units	0.5 N-Units	± 2 N-Units
Corrected Refractivity (Postflight)	0-500 N-Units	0.5 N-Units	± 2 N-Units
RAM Air Temperature	-50° to +50° Celsius	0.1° Celsius	± 2° Celsius
Corrected Air Temperature (Postflight)	-50° to +50° Celsius	0.1° Celsius	± 2° Celsius

Table 1. Refractometer Measurement Requirements

A block diagram of the refractivity measurement technique is shown in Figure 5. Air flowing through the invar sampling cavity varies its resonant frequency by one part per million per N-unit of refractivity change. A harmonic of a swept Voltage Controlled Oscillator (VCO) is phase locked to the cavity. The average frequency of the VCO therefore varies directly with the refractivity of the air. The gate time of the VCO counter was diliberately made rather long (0.27 sec) to cause some smoothing of the measured data. Rainfall can cause loss of cavity lock. This is detected by monitoring counter overflow which sets a test point to warn the operator and post-flight data analyst. Lock is automatically restored when the cavity dries.

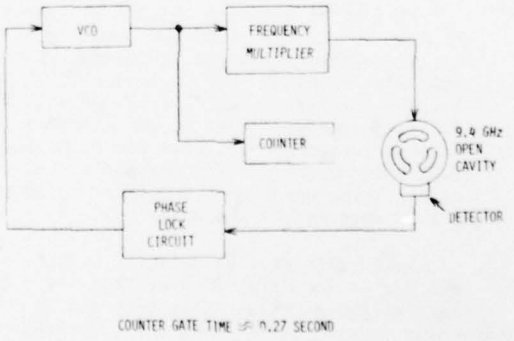

Figure 5. Refractometer Measurement Technique

4. TEST AND EVALUATION/PRODUCTION PLANS

Currently two developmental models of the AMR have been built. The planned evaluation and production schedule is shown in Table 2. The schedule is subject to change pending receipt of approval for service use.

DEVELOPMENTAL TEST & EVALUATION (NAVAL AIR TEST CENTER, PATUXENT RIVER)	FEB-APR 1979
OPERATION TEST & EVALUATION (EAST COAST SQUADRON)	MAY-JUL 1979
APPROVAL FOR SERVICE USE	SEP-NOV 1979
AIRCRAFT INSTALLATIONS	1981 - 1984

Table 2. Refractometer T&E/Production Plans

PASSIVE REFRACTIVE INDEX BY SATELLITE MONITORING (PRISM)

Kenneth D. Anderson
Herbert V. Hitney
EM Propagation Division
Naval Ocean Systems Center
San Diego, CA 92152

ABSTRACT

A dual channel, high performance receiver has been developed to validate a technique that infers the tropospheric refractive index structure from measurements of the optical interference pattern created by a satellite-borne radio frequency transmitter as the satellite moves through low elevation angles. Presented here are the preliminary results of the observations; the salient points include the following. First, the analytical models predicting the null locations from known refractive index structure agree remarkably well with observations of the optical interference pattern. Second, the null number ambiguity associated with surface based ducting conditions can readily be resolved by monitoring two suitable radio frequency signals simultaneously.

1. INTRODUCTION

NOSC is developing a passive technique to determine the refractive structure of the lower atmosphere by monitoring radio frequency signals from a satellite (Figure 1). The technique, known as Passive Refractive Index by Satellite Monitoring (PRISM), provides several advantages over current methods of determining the refractivity structure. First, the technique is completely passive since only the satellite radiates. Second, the receiver needs no high calibration since the relative amplitude of the signals is the only requirement. Third, since the dominant refractivity effects occur in the first two degrees above the horizon, there is no need to track the satellite. Finally, no complex logistics support is required as compared with radiosonde or refractometer operations.

2. OBJECTIVE

The objective of the PRISM project is to develop and validate a technique to provide the refractive index structure of the lower atmosphere by monitoring radio frequency signals from a satellite as the satellite moves through low elevation angles. The specific objective of this paper is to describe the technique, summarize the work that has been completed to date and outline future plans.

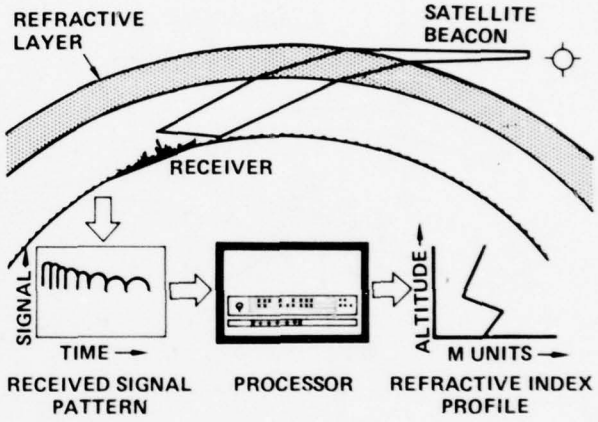

Figure 1. Schematic diagram illustrating PRISM concept.

3. METHOD

The technique utilizes observed differences between the direct and sea-reflected path-lengths to accurately infer the true elevation angles at the ground station. The refractive structure is inferred by assuming a wide variety of refractive profiles and computing the null locations for each assumed profile based on knowledge of the true elevation angles. The modeled null locations are fit to the observed, and the profile yielding the "best-fit" will be representative of the true refractive structure.

Figure 2 illustrates the geometry of the direct and reflected path. It is assumed that both paths are parallel and equally affected by the presence of an elevated refractive layer. Once the path length difference δ is established and the corresponding ground ranges noted, a wide variety of refractive index profiles are assumed. For each assumed profile, the true elevation angle α at the ground station (associated with a particular δ) can be calculated by a numerical solution of the following formulas.

$$\gamma = \sqrt{(\alpha/3)^2 + 2h/3a_e} - \alpha/3 \qquad (1)$$

$$\delta = 2\sqrt{(h^2 + a_e(a_e + h)\gamma^2}\ (\alpha+\gamma)^2 \qquad (2)$$

where γ = earth central angle
h = height of ground station antenna
a_e = effective earth radius factor based on lowest segment of assumed refractivity profile, and
δ = path length difference = $d_2 - d_1$

Equations (1) and (2) are valid if it can be assumed that the direct and reflected rays are parallel. This is certainly a good assumption on a satellite-to-ground path. Also note, there will be no effect on the path length difference from any elevated refractive layers, since both the direct and reflected rays traverse parallel paths and any effect on one is cancelled by an equal effect on the other.

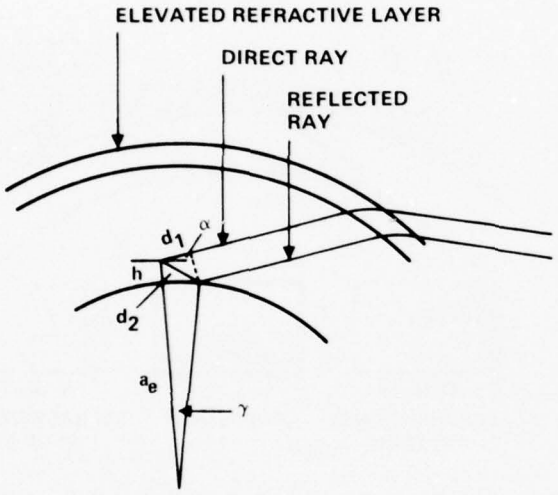

Figure 2. Geometry used for relating path length difference to elevation angle under the assumption of parallel direct and reflected rays.

After the elevation angle is calculated, the ground range to the satellite is determined by numerical solution of the following formula.

$$R = C \int_h^s \frac{dz}{(1 + z/a)\sqrt{((1 + a/a)n)^2 - c^2}} \qquad (3)$$

where

R is the sub-orbital range to the satellite,
n is the refractive index at height z,
C is the ray characteristic, $n_o \cos(\alpha)$,
h is the height of the ground station antenna,
n_o is the refractive index at height h,
s is the height of the satellite and,
a is the true radius of the earth.

The computed ranges are compared to the observed ranges and the assumed profile which yields the "best fit" will be representative of the actual profile.

The only serious complication in this technique is the assignment of the path-length difference to each null in the observed pattern. For example, since a surface based duct will trap low elevation angle rays, the first null observed may not correspond to a difference of one wavelength. However, this complication can be eliminated by using frequency or height diversity methods.

4. EQUIPMENT

To implement the technique, a dual channel, computer controlled receiver was designed to process two independent signals (one in the 1 to 2 GHZ band, the other in the 2 to 3 GHZ band) with a typical sensitivity of -143 dBm. The antenna is a 2.4 metre circular parabolic dish providing beamwidths of 8.7 and 5.8 degrees for 1.2 GHz and 2.8 GHz respectively. Figure 3 is a block diagram of the PRISM receiver and illustrates the major components.

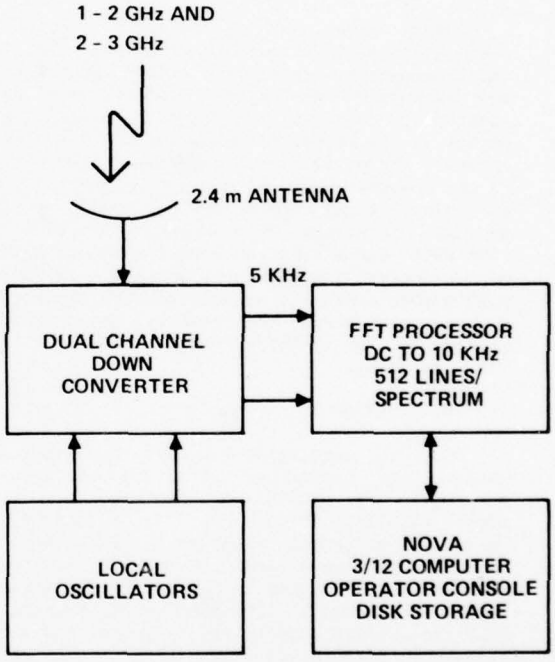

Figure 3. Block diagram of the PRISM receiver.

The primary transmitter used during the measurement periods is satellite P76-5 (Wideband) developed by the Stanford Research Institute for the Defense Nuclear Agency to characterize transionospheric communications channels. The satellite transmits ten coherent CW signals, one in VHF, seven in UHF and two in SHF bands. The two highest frequencies are the only frequencies monitored by the PRISM receiver and are located at 1239 MHz and 2891 MHz. The lower frequencies are not monitored since, for low elevation angles, the number of nulls received at the ground station are too few to be used in inferring the refractive index structure.

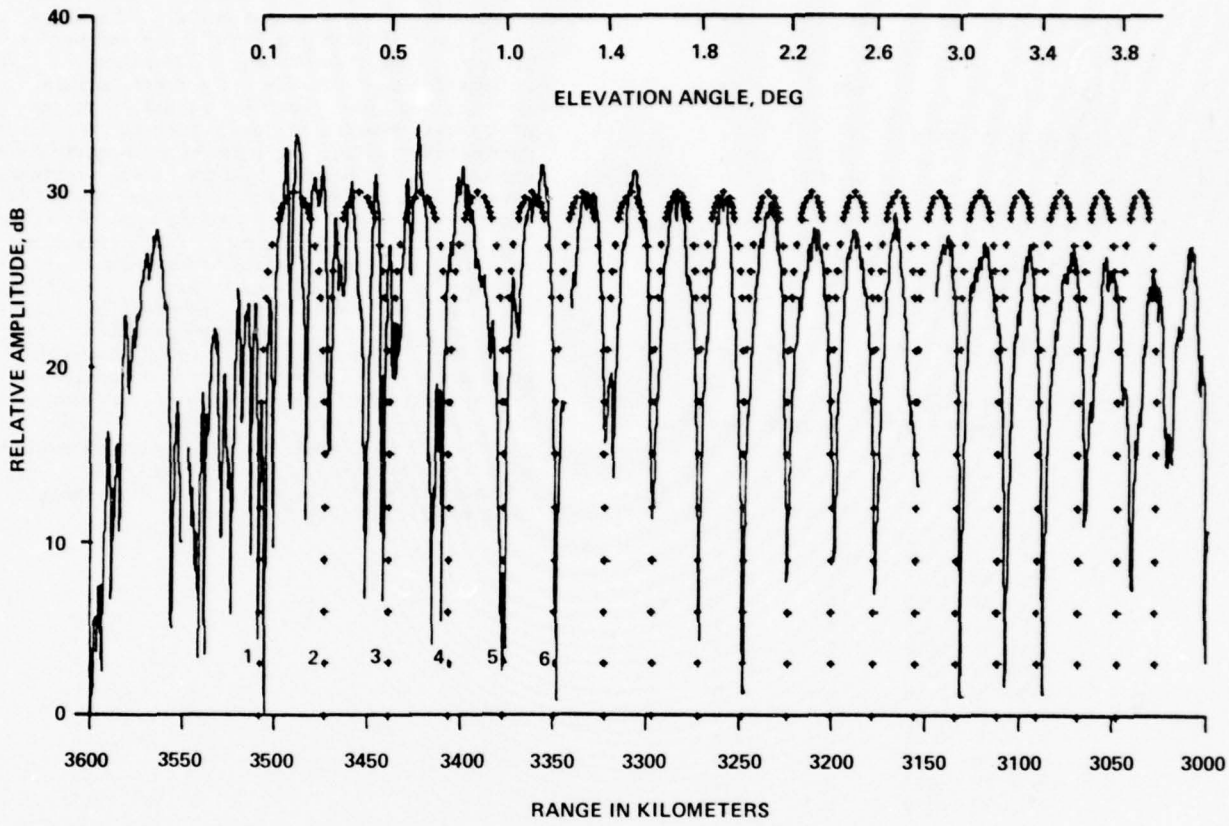

Figure 4. Comparison of the modeled and observed interference pattern at 1239 MHz for 14 August 1978.

Table 1 lists the power budget parameters for the Wideband/ground station equipment. The free space signal levels are approximately 17 dB above the receiver noise threshold. Since the peak amplitude of the interference pattern is 6 dB above the free space level there is approximately 23 dB dynamic range available for detecting the nulls.

5. RESULTS

The orbit of the Wideband satellite and the location of the ground station normally allow measurement of the null patterns as the satellite ascends and descends over the horizon during one orbit. Measurements of the interference pattern are made for orbits where the transmitter-to-receiver path is entirely over water (useable orbits occur twice daily at noon and midnight). Supporting meteorological measurements are made in between the ascent and descent of the satellite by a balloon-borne radiosonde.

Table 2 provides a summary of the measurement periods made during 1978. The table lists the dates of the measurement period, the height of the satellite, and indicates whether the satellite was ascending or descending at the horizon. The column labeled Offset describes the absolute range difference between the modeled null pattern and the observed pattern. The largest absolute range difference of -24.5 km corresponds to a time difference of 4.2 seconds between the location of the satellite predicted from orbital parameters and its location modeled by the PRISM technique. Since the accuracy of the ground station timing is ±1 second and the orbital prediction program is ± 4 km, this leaves a residual of approximately 14 km (worst case) in the absolute PRISM technique. This means that the technique, by itself, cannot reliably determine the path length difference at high elevation angles which are not affected by the refractivity structure.

Figure 4 is a plot of the interference pattern observed on 14 Aug 1978 at 2051 GMT. The figure shows the 1239 MHz signal plotted as relative amplitude in dB versus sub-orbital range to the satellite. Superimposed on the received signal curve is the pattern modeled from the measured refractive index profile. The numbers 1 to 6 locate the first 6 optical interference nulls. Also shown is the true elevation angle reference. Inspection of Figure 4 shows remarkable agreement between the observed and modeled interference patterns and validates the algorithms currently used.

Frequency	1239 MHz	2891 MHz
ERP (dBm)	+22	+19
Free Space Path Loss (dB)	-166	-173
Antenna Gain	+20	+32
Polarization Loss (dB)	-3	-3
Received Signal Level (dBm)	-127	-125
Receiver Noise Level (dBm)	-144	-143
S/N Radio (dB)	+17	+18

Table 1. Power budget calculation for Wideband Satellite and PRISM receiving station.

Date	Height (km)	Ascent or Descent	Offset (km)
7/20/78	1001	A	-5.5
7/20/78	1022	D	+2.5
7/28/78	1009	A	-9.0
7/28/78	1032	D	+12.5
8/02/78	1039	D	-24.5
8/03/78	1019	A	-9.0
8/03/78	1038	D	-10.5
8/14/78	1036	A	-3.0
8/14/78	1048	D	+12.0
8/16/78	1037	A	-5.0
8/16/78	1050	D	-5.5

Table 2. Summary of PRISM measurement periods for 1978 showing offset between modeled and observed null patterns.

6. FUTURE PLANS

It is recognized that a major problem with the PRISM technique is the positive identification and numbering of the received nulls. Therefore, the next step in developing PRISM is to refine the null location and numbering algorithms. These refinements may consist of a cross-correlation of segments of the received signal patterns with analytical models of the pattern to reject extraneous fading or other post-reception signal processing techniques. After these refinements have been made, a program will be developed to infer the best-fit refractivity profile from the observed null locations using a least-squares fit routine. Following the development of this program, there will be a set of measurements performed to verify the program by comparing best-fit profiles with measured profiles. Finally, a report documenting the PRISM technique and programs will be prepared with recommendations for future work and possible shipboard implementations.

The work reported in this paper was performed under sponsorship of the Naval Sea Systems Command. The authors would like to thank C. E. Jedrey for his continued support.

EXPERIMENTAL STUDY OF ELEVATED DUCTS

John L. Skillman and Douglas R. Woods

Department of Defense

Fort George G. Meade, Maryland

ABSTRACT

The results of a study of elevated ducts in the Hawaiian Islands are discussed. Signal strengths and the refractive index have been measured as a function of altitude and range, and compared with calculations.

The duct altitudes were typically between 1000 meters and 2000 meters. Measurements were performed at frequencies of 150 MHz, 450 MHz, and 2200 MHz, at ranges from 100 km to 800 km and at altitudes up to 3000 meters.

A number of aircraft and ground sites were used to measure the signal strengths and meteorological parameters. Two transmitters (150 MHz and 450 MHz) were on the ground while three additional transmitters (150 MHz, 450 MHz, and 2200 MHz) were placed in a helicopter which typically flew at the altitude of the duct. Calibrated receivers located over-the-horizon on the ground, in a helicopter, and in an airplane were used for simultaneous measurements. The receiving helicopter typically performed measurements as a function of altitude at ranges of 400 km to 500 km. The airplane was used to measure the signal strengths as a function of range and to characterize the path between the transmitters and the receiving helicopter. On one occasion, however, the plane flew the other direction from the receiving helicopter to a range 800 km from the transmitters.

The refractive index height profile along the measurement path has been reconstructed. Calculations based on this profile are presented and compared with the measured data.

1. INTRODUCTION

VHF and UHF radio signals normally travel in a straight line and, because of the earth's curvature, efficient propagation is usually limited to ranges no greater than the distance to the horizon. Normal atmospheric refraction extends the radio horizon somewhat beyond the visual horizon. Tropospheric ducting, however, when present provides a mechanism for strong VHF/UHF signals to be transmitted far beyond the radio horizon. A tropospheric duct is a layered condition of the atmosphere where there is a sharp drop in humidity between a lower layer of moist air and a higher layer of dry air. This sharp drop is often associated with a temperature inversion. The sharp decrease in humidity with height produces a sharp refractivity index gradient which can cause VHF/UHF radio waves to bend sharply and follow the humidity boundary far over the horizon.

There are a number of different kinds of ducts. The evaporation duct is the type which commonly occurs in the first few meters above a body of water. There is another type of surface duct with typical heights of 100 meters, and there are low elevated ducts with typical heights up to 1000 meters, and high elevated ducts with typical heights up to 2000 meters.

This study is directed at characterizing the high type elevated ducts which are typical of lower latitudes in the central and western Pacific and Atlantic Oceans, and of the Caribbean Sea.

2. MEASUREMENTS

2.1 Overview

Radio meteorological measurements were performed in the Hawaiian Islands from 16 May 1977 through 24 June 1977. Signal strengths were measured as a function of altitude and range. Height profiles of the atmospheric pressure, temperature, and humidity (and hence refractivity) were measured along the propagation path.

Figure 1 presents a schematic representation of the experimental arrangement. Beacon transmitters operating at 149.1 MHz and 449.0 MHz were located on the ground near South Point on the island of Hawaii. The antennas were on a telephone pole 18 meters (60') above the 98 meter (320') elevation of the site. Three more transmitters were mounted in a UH-1 helicopter which orbited over the island near South Point. These transmitters operated at frequencies of 149.3 MHz, 449.2 MHz, and 2201.7 MHz, slightly offset from the ground transmitter frequencies.

A UH-3 helicopter equipped with beacon receivers was used to make measurements off the coast of Kauai, and a U-21 airplane equipped with beacon receivers was used to make measurements along the 500 km path between the islands of Kauai and Hawaii. These two aircraft along with the transmitting helicopter were also equipped with meteorological instrumentation to measure atmospheric temperature, humidity, and pressure. The UH-3 helicopter had receivers for all the ground and airborne transmitters. The U-21 airplane had receivers for both the air and ground 149 MHz transmitters. For the final three flights, an

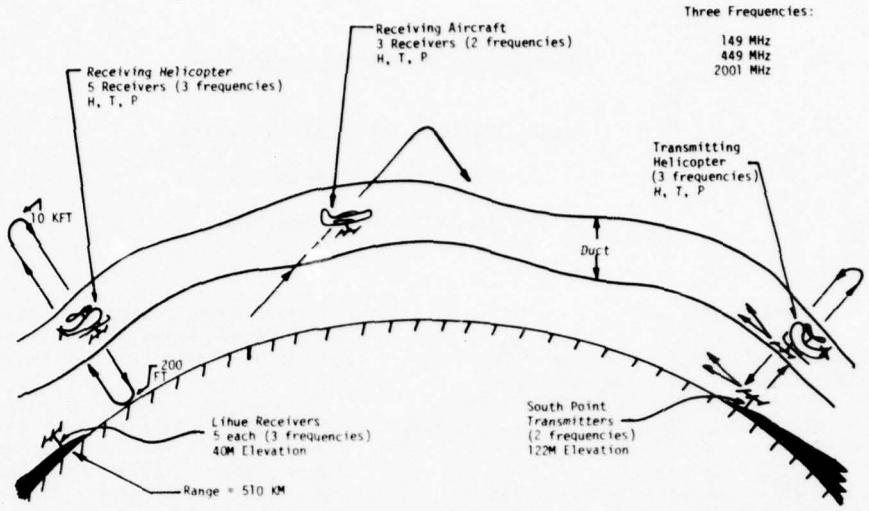

Figure 1. Schematic representation of experimental plan (May-June 1977)

additional receiver was installed in the U-21 to measure either the air or ground 449 MHz signal. A ground site located at Lihue Airport on the island of Kauai measured the signals from the helicopter transmitters.

2.2 Propagation Geometry

The propagation zones for the path between the transmitter site at South Point and the Kauai receiver site are summarized in Figure 2. The transmitter is assumed to be at an altitude of 1500 m (4920') and the flat earth representation is used. The maximum line-of-sight path to a receiving aircraft at a typical duct height of 1500 m is 320 km. Free space signals can be expected to within 40 km of this limit. The diffraction zone provides a transition between the free space zone and the tropospheric scatter zone which follows. Beyond a range of 360 km (at an altitude of 1500 m) the normal propagation mechanism is tropospheric scatter. In this zone $\Gamma \approx 40$ to 60 dB, where Γ indicates the propagation loss in excess of free space.

2.3 Typical Measurements Flight

Typically the U-21 airplane would make a series of ascents and descents on an outward flight from the island of Kauai to the island of Hawaii (see Figure 3). These soundings from 60 to 3000 meters (200' to 10,000') were used to determine the altitude of the sharp humidity drop. Then the U-21 would fly the return trip just below the sharp humidity drop and measure the radio signal strengths and meteorological conditions as a function of range. The transmitting helicopter would take off just before the U-21 arrived at the Hawaii end of its flight, make a sounding, and then orbit in the duct just below the sharp humidity drop. Simultaneously with the level return flight of the U-21 airplane, the UH-3 receiver helicopter would make vertical soundings off the coast of Kauai.

2.4 Summary of Ducting Conditions During Measurements Period

The ducting conditions that occurred during the measurements period are summarized in Figure 4. This figure is based on the Lihue Airport radiosonde. Each vertical line represents the height and thickness of the duct as indicated by the radiosonde. The strength of the duct is indicated by the width of the line. The data collection flights are indicated by the flight number and corresponding arrows. A refractivity slope greater than -100 N/km was taken as the threshold for ducting. The -100 N/km value, rather than the theoretical threshold of -157 N/km, was used because this procedure has been found in practice to provide a nominal compensation for the sluggish humidity response of the radiosonde.

The figure indicates that during the setup and shakedown period of the first few days there were strong ducting conditions. During the middle of the test, the ducting conditions were nearly nonexistent allowing a number of reference flights

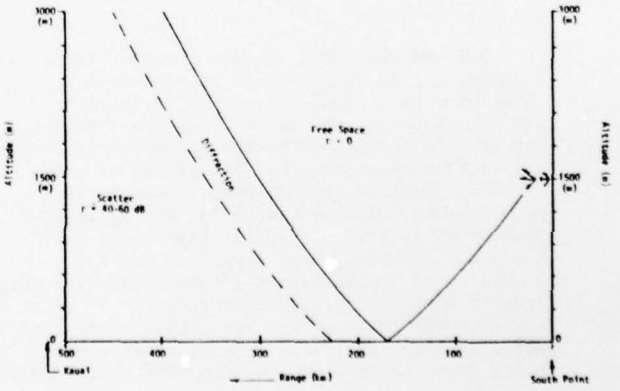

Figure 2. Propagation zones for beacon at 1500 m

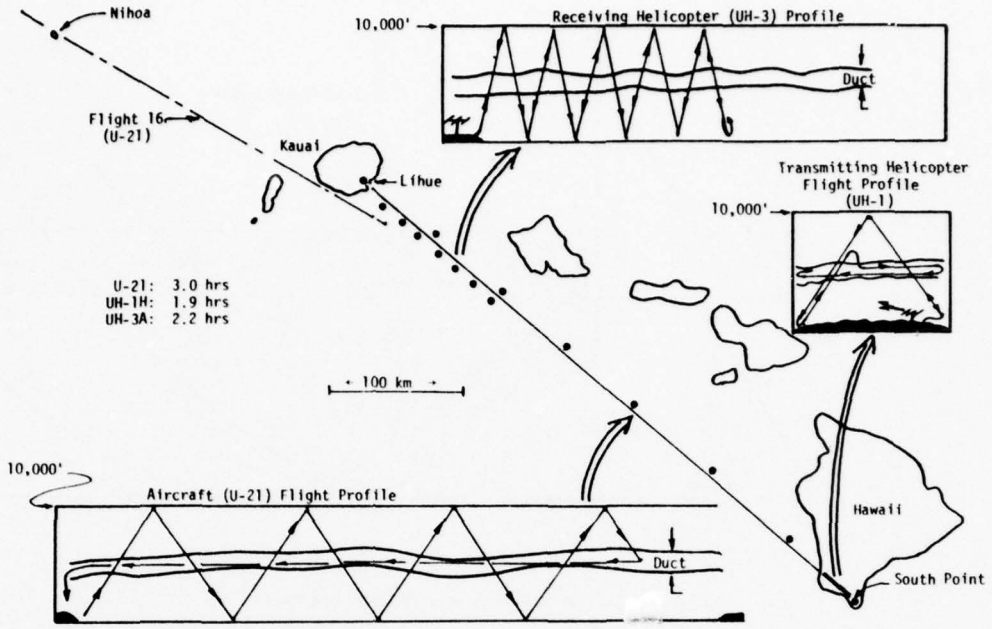

Figure 3. Flight profiles.

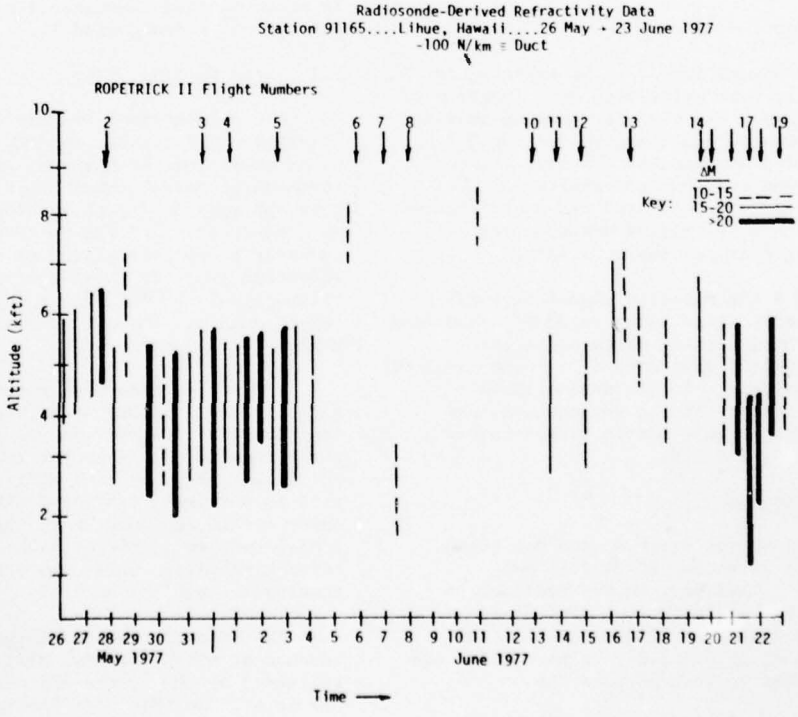

Figure 4. Summary of ducting conditions during measurements period.

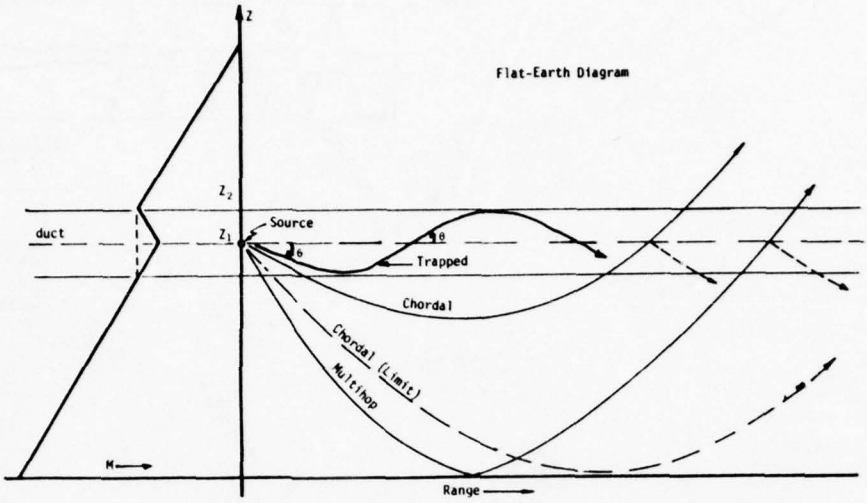

Figure 5. Trilinear refractivity model and flat-earth diagram.

to be flown. Fortunately, the good ducting conditions returned during the last week of the test and this is when most of the good data was taken. The data to be discussed in this report was taken on Flights 16 and 18.

3. THEORY

3.1 Introduction

The ducted signal levels to be expected on Flights 16 and 18 were calculated as a function of altitude and range. The computer program used for these calculations is discussed in Section 3.2. Frequencies of 149 MHz and 449 MHz were treated for the ground and airborne transmitters. The refractivity profile models used for each flight were based on the refractivity measurements* performed during that particular flight.

In Section 4 the measured signal strength profiles are analyzed and interpreted by comparison with theory. Three ducting cases and their characteristic height-gain curves form the basis of much of this analysis. These three classes of ducting, their characteristic attenuation, and their typical height-gain curves are discussed in Sections 3.3, 3.4, and 3.5.

3.2 Computer Program

The basic computer program used for these calculations was developed by Pappert and Goodhart (1977). This program was modified to increase its input and output capabilities. In particular, routines were written to plot the output in a number of different formats which are intuitively useful in interpreting the calculations.

The program is based on a planar waveguide analysis and obtains solutions to the modal equation. It treats a horizontally stratified three-segment refractivity model in the flat earth representation where M is the modified refractivity Kerr (1951). The M profile used is shown on the left side of Figure 5. The first inflection point is at an altitude designated Z_1, and the second inflection is designated Z_2.

3.3 Three Ducting Cases

Over-the-horizon propagation induced by elevated ducts can be conceptually separated into three cases and the physical interpretation of these three cases is represented by the three types of rays in Figure 5; trapped, chordal, and multihop rays. For the purpose of visualization, consider a ray propagating at altitude Z_1 with an elevation angle θ. Note that Z_1 is the source altitude which would trap a ray with the largest launch angle†. Thus, it is logical to specify angles at this altitude.

For angles less than a critical elevation angle, a ray launched at Z_1 will be totally contained or "trapped" in the duct. For angles whose magnitude is somewhat larger than this critical angle, the rays will not be trapped, but will be partially reflected off the refractive layer within the duct, with the reflected portion propagating in a chordal fashion under the refractive layer, while the transmitted portion continues above the duct.

As the angle becomes larger, a point is reached at which the rays will alternately be reflected by the ground and partially reflected by the layer. In this case the ray propagates in a multiple hop fashion under the duct, with

*Actually the refractivity was determined from the aircraft measurements of temperature, pressure, and humidity.

†The large launch angle required to escape the duct might be interpreted as meaning Z_1 is the optimum height to couple energy into the duct.

transmitted portions of the ray continuing above the duct at each partial reflection point.

3.4 Mode Attenuation Characteristics

Figure 6 shows the mode attenuation rates versus the real part of the eigenangle as calculated by the Pappert/Goodhart computer program for an M profile typical of Flight 18. The plot is separated into three segments corresponding to the three mode types. The three segments can be understood if we consider the expected loss per unit-length characteristics of each mode type.

From simple geometry and ray tracing considerations one finds that for Flight 18, rays with an angle less than 7.7 mr (milliradian) at Z_1 (1313 m) are trapped in the duct, and thus would be expected to have low losses. This angle corresponds to the eigenangle transition between the trapped and chordal cases, with the low-loss trapped modes having eigenangles less than or equal to 7.7 mr.

For the chordal rays which have angles larger than 7.7 mr, the amount of partial reflection depends on the amount and the abruptness of the decrease in refractivity at the ducting layer, and on the angle of incidence at Z_1. If the angle of incidence is near the critical angle the partial reflection approaches 100%. However, as the angle increases above the critical angle, two things happen: the reflection loss increases, and the path length between the reflection points also

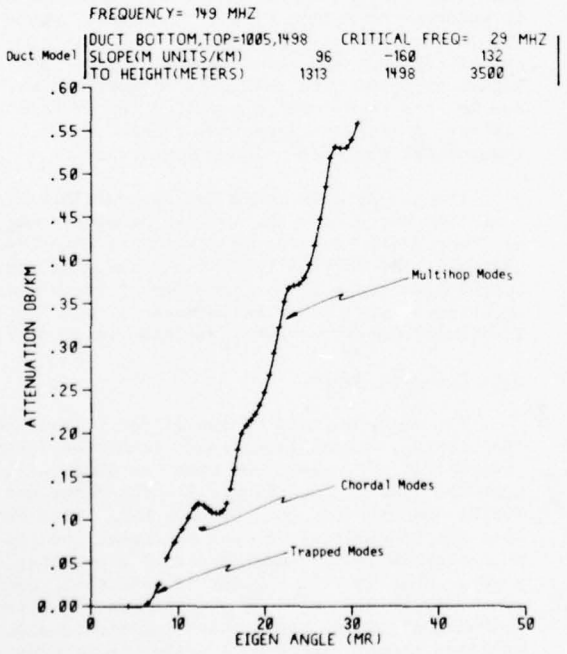

Figure 6. Mode attenuation as a function of eigenangle (149 MHz).

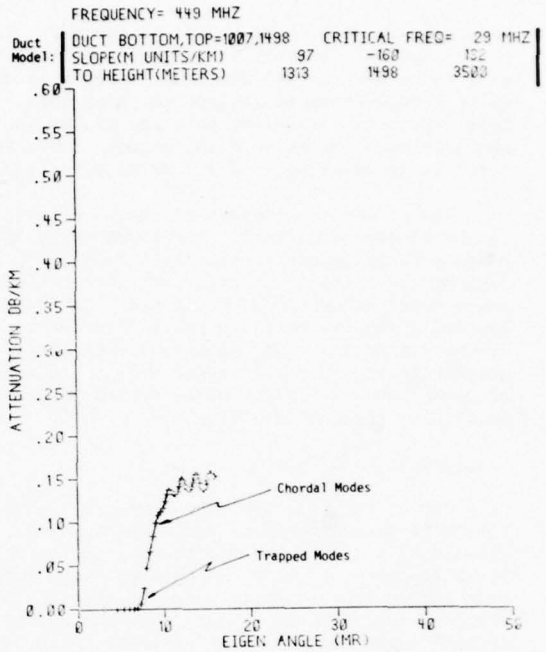

Figure 7. Mode attenuation as a function of eigenangle (449 MHz).

increases. When the loss per unit-length is calculated these two effects generally offset each other, although initially the increase in reflection loss dominates, resulting in a sharp increase in per unit-length attenuation at the transition between the trapped and chordal cases. This is exactly what is seen in Figure 6. At larger angles, the path distance factor is slightly stronger and the per unit-length attenuation actually decreases slowly. Figures 6 and 7 do not show chordal modes with eigenangles large enough for this effect to become apparent, because rays with these large angles hit the ground.

The transition between the chordal and multihop cases is defined by the ray that just grazes the earth's surface. For the Flight 18 refractivity profile, this ray has an angle of 15.9 mr at Z_1 (1313 m). At this point additional increases in the angle at Z_1 shorten the distance between reflection points and increase the partial reflection angle. These two loss effects add instead of cancel, resulting in a dramatic increase in the mode attenuation shown in Figure 6 at the transition between the chordal and multihop modes. This transition occurs at 16 mr, exactly where the ray interpretation would have it.

In Figure 7 the mode attenuation is plotted for the first 50 modes and a frequency of 449 MHz. The first seven modes are the low-loss trapped modes, and the remaining modes are the partial reflection modes. Note that the attenuation curve is relatively flat after the first few of the partial reflected modes. The curve does not

appear to go back up as it did at 149 MHz. The reason for this is that at 449 MHz there are many more modes than at 149 MHz, and 50 modes is not quite enough modes to include the high-loss multihop modes. However, note the transition angle between the trapped and chordal modes is still at an eigenangle of 7.7 mr as expected.

The attenuation values of the three mode types can be simply summarized. The low-loss trapped modes have attenuations of only a few dB/100 km, medium-loss multiple partial reflection chordal modes have attenuations on the order of 10 dB/100 km, and high-loss multiple partial reflection, ground reflection modes have substantially greater attenuations. Note that these values are "rules of thumb" and the exact values depend on the particular case being considered.

3.5 Height Gain Curves

One of the principal means used to relate theory to measurements is by comparing the calculated and measured height-gain curves. Thus it is important to know the nature of the height-gain curves for the three cases of trapped, chordal, and multihop modes. Figure 8 gives typical height-gain curves for these three cases. Note that in the case of the trapped mode, the signal is fairly well confined in the duct, dropping off dramatically below the duct and moderately above the duct. These features become more pronounced at higher frequencies. At lower frequencies or for higher order trapped modes (which approach the partial reflection case), the features are less pronounced. In fact, the highest order trapped modes give signals above the duct which are almost as strong as those in the duct.

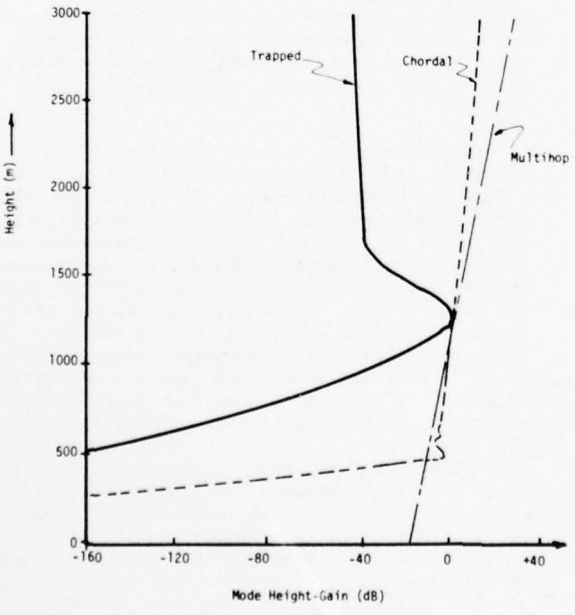

Figure 8. Typical mode height-gain profiles.

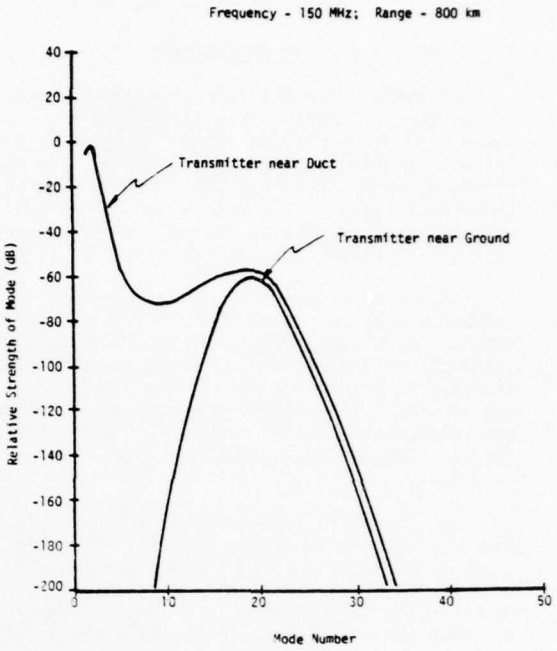

Figure 9. Relative strength of different modes for a transmitter near the duct and for a transmitter near the ground.

The typical height-gain curve for a partial reflection chordal mode has a sharp drop in the curve as the altitude is reduced below some minimum value. The height of this minimum decreases for the higher order chordal modes until it reaches the ground at the transition between the chordal and multihop modes. The curve is relatively constant above this altitude. The slow signal increase with height is interpreted as being due to rays which have penetrated the partial reflecting layer at locations closer to the transmitter where the signal was stronger.

The height-gain curve for the multihop case is flat from the ground up, increasing slowly with altitude. The increase is due to the same reasons given for the partial reflection case, but somewhat accentuated since the attenuation of these modes is greater, and hence the increase of the signal at locations closer to the transmitter is greater.

3.6 Dominant Modes

The contributions of the different modes to the received signal level were calculated for two transmitter altitudes, one near the duct and one near the ground. See Figure 9. The range was 800 km and the frequency was 149 MHz. Note that when the transmitter is near the duct, the low-loss well-trapped modes contain most of the signal power. When the transmitter is near the ground, the power is concentrated in a few modes at the transition between the partial reflection and multihop cases. In this case the higher order modes are eliminated by their high attenuation rate, while the lower order modes, including the well-trapped modes are not excited by the ground transmitter.

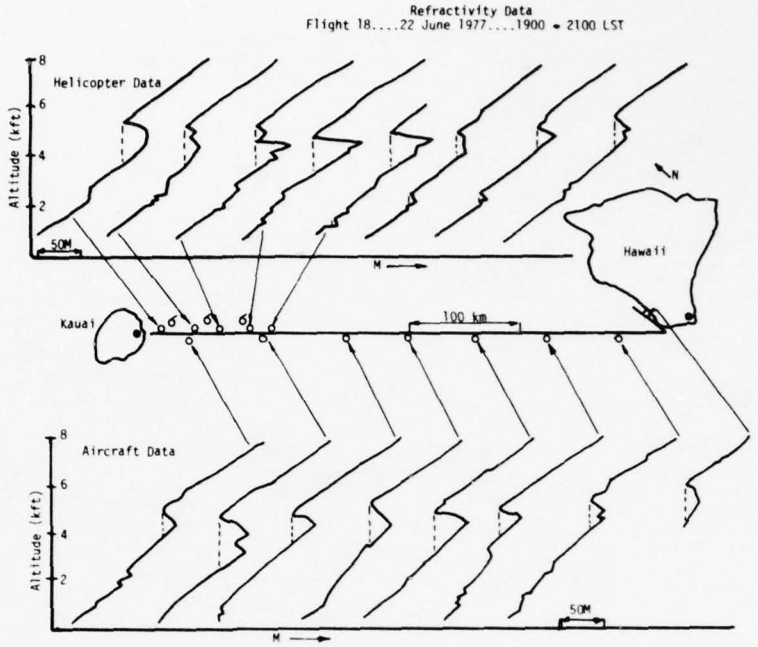

Figure 10. Refractivity data summary for Flight 18.

Thus one would expect the sharply peaked height-gain curve, which is characteristic of well-trapped modes, when the transmitter is near the duct. The relatively flat height-gain curve characteristic of higher order chordal and multihop modes would be expected when the transmitter is near the ground. These effects were observed in the data and will be discussed in the following section.

4. EXPERIMENTAL RESULTS AND DISCUSSION

4.1 Introduction

Samples of the measured data from Flights 16 and 18 are presented in this section, and their comparison with theoretical calculations is discussed. Height-gain curves for the ground transmitter and the airborne transmitter at 149 MHz, 449 MHz, and 2200 MHz are presented for a 500 km range. An additional 149 MHz height-gain curve and a "range-gain" curve are given for ranges to 800 km. All cases presented in this section are for the receiver far over the radio horizon, beyond the diffraction region, where the normal troposcatter propagation mode can not account for the measured signal levels.

4.2 Flight 18 Refractivity Data

The refractivity along the entire propagation path was measured by the U-21 airplane. In addition the UH-3 helicopter performed more concentrated measurements at the Kauai end of the path. The results of these measurements are presented in Figure 10. It can be seen that at an altitude of 1000 to 1500 meters (3300 to 5000 feet) there is a consistent ducting pattern along the entire path. Based on these measurements the following tri-linear refractivity model was selected for the Flight 18 calculations.

Z_1 = 1313 m
Z_2 = 1498 m
Slope from ground to Z_1 = 96 M units/km
Slope from Z_1 to Z_2 = -160 M units/km
Slope above Z_2 = 132 M units/km

4.3 Flight 18 Signal Strength Data

A typical set of 149.3 MHz height-gain curves is given in Figure 11. These curves were measured with the UH-3 helicopter at ranges between 450 km and 500 km. The beacon transmitter, indicated by the "B", was just above the top of the duct at an altitude of 1554 meters (5100 feet).

The signal strength peaks near the free space level in the upper portion of the duct, drops off sharply below the duct and remains within approximately 10 dB of the peak level far above the duct.

The signal level envelopes show good repeatability from sounding to sounding while the interference nulls under the envelopes grow, decay, and shift in altitude. The path length is on the order of 0.25×10^6 wavelengths and a 2 M unit change in the average refractivity, integrated over the path for a particular mode, will result in a 180° phase shift. Thus, considering that 2 M units is a small change in atmospheric refractivity, and that the transmitting helicopter does not remain in exactly the same location, it is not surprising that the nulls under the signal envelope change from sounding to sounding.

AD-A071 781 NAVAL OCEAN SYSTEMS CENTER SAN DIEGO CA F/G 4/1
PROCEEDINGS OF CONFERENCE ON ATMOSPHERIC REFRACTIVE EFFECTS ASS--ETC(U)
JUN 79 J H RICHTER

UNCLASSIFIED NOSC-TD-260 NL

2 OF 2
AD
A071781

END
DATE
FILMED
8-79
DDC

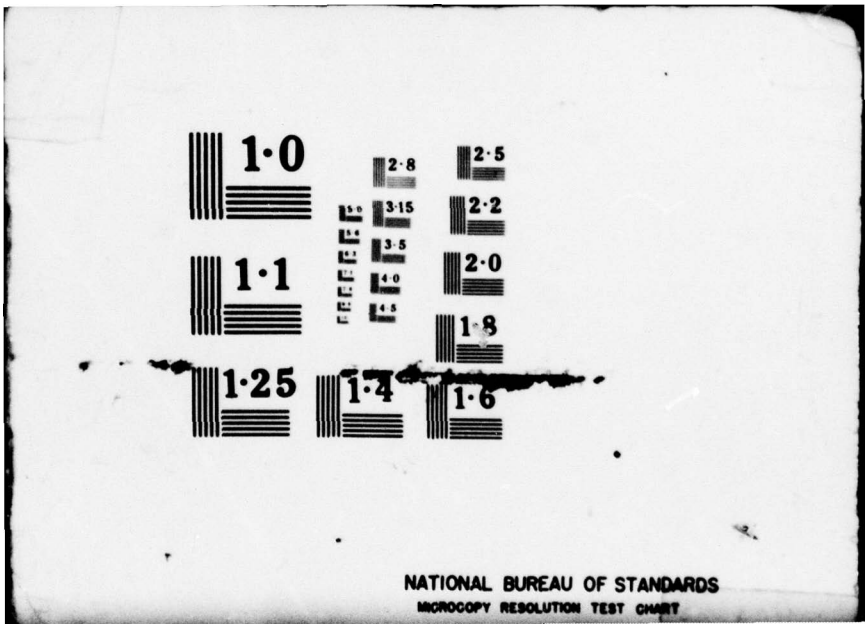
1·0
1·1
1·25
2·8
3·15
3·5
4·0
4·5
1·4
2·5
2·2
2·0
1·8
1·6
NATIONAL BUREAU OF STANDARDS
MICROCOPY RESOLUTION TEST CHART

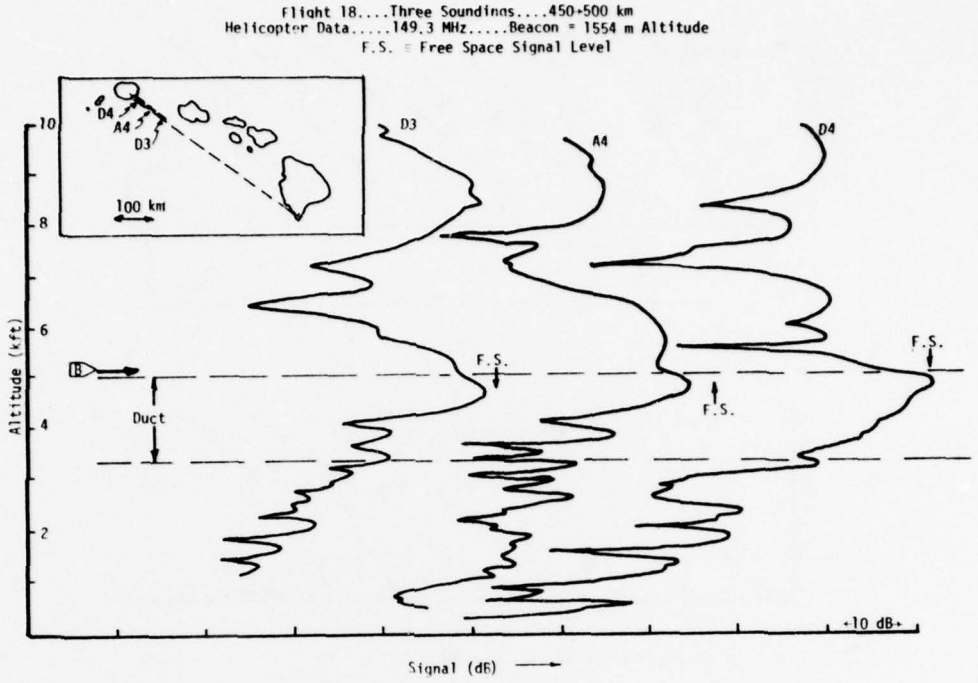

Figure 11. Measured height-gain profiles for the 149 MHz transmitter near the duct (Flight 18).

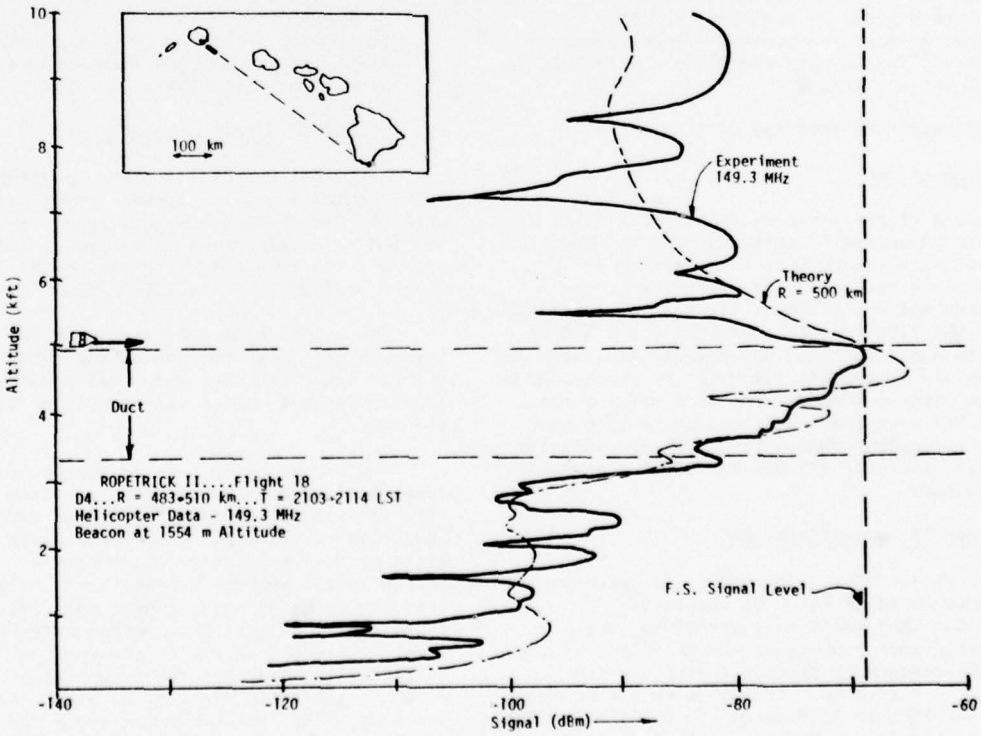

Figure 12. Comparisons of calculated and measured height-gain profiles for a 149 MHz transmitter near the duct (Flight 18).

Flight 18....Descent 4....449.2 MHz
Range 483-510 km....Beacon Altitude = 1554 m

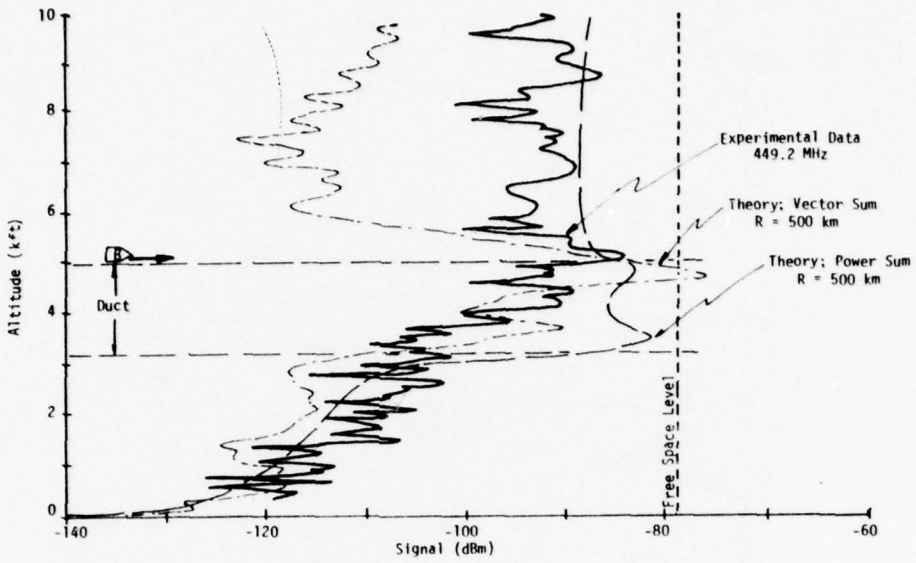

Figure 13. Comparison of calculated and measured height-gain profiles for a 449 MHz transmitter in the duct (Flight 18).

Flight 18....Descent 4....Range = 483-510 km
UH-3 Helicopter Data....Beacon = 1554 m Altitude

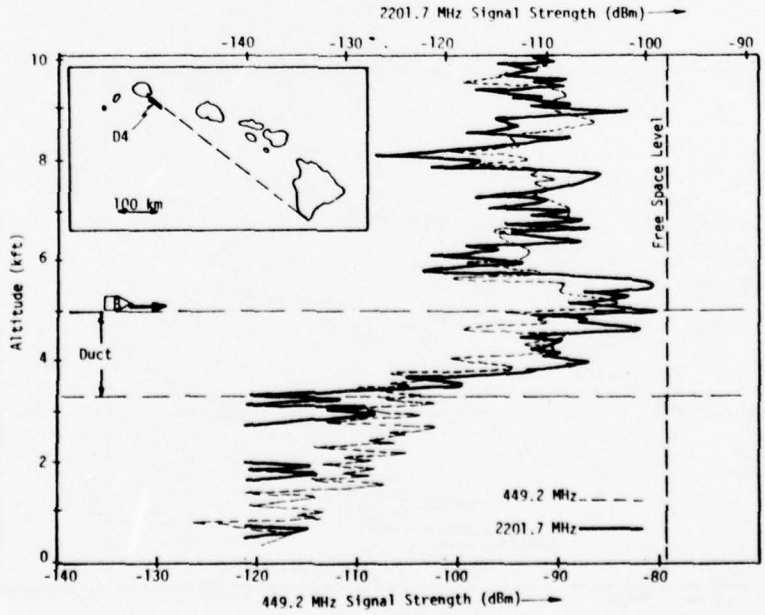

Figure 14. Comparison of the measured height-gain profiles for 449 MHz and 2 GHz transmitters in the duct (Flight 18).

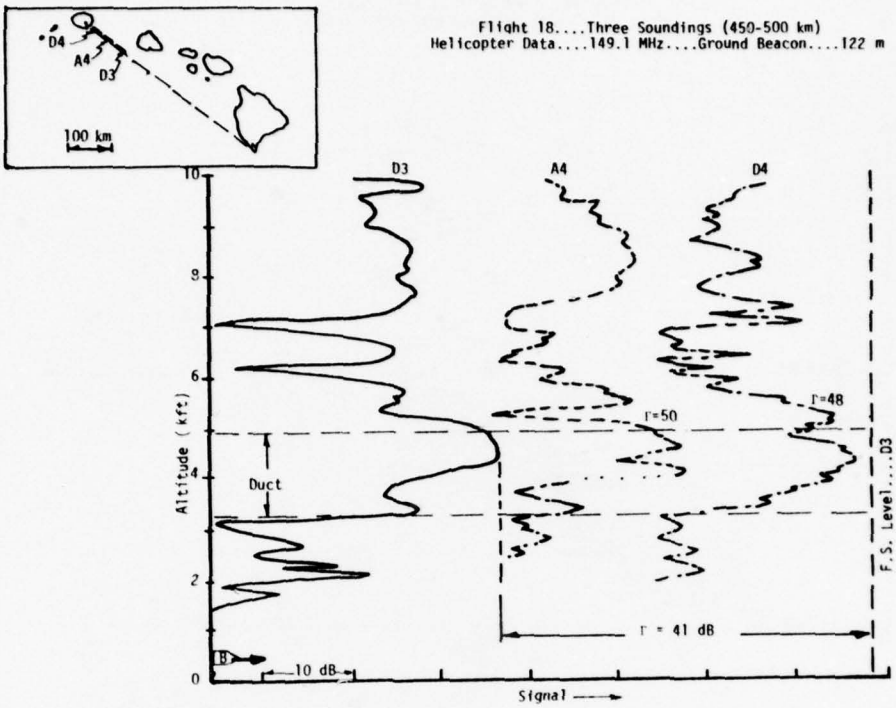

Figure 15. Measured height-gain profiles for the 149 MHz transmitter on the ground (Flight 18).

Flight 18....Descent 4....Range 483-510 km
Helicopter Data....149 MHz
Dotted Lines: Beacon at 122 m Altitude
Solid Lines: Beacon at 1554 m Altitude

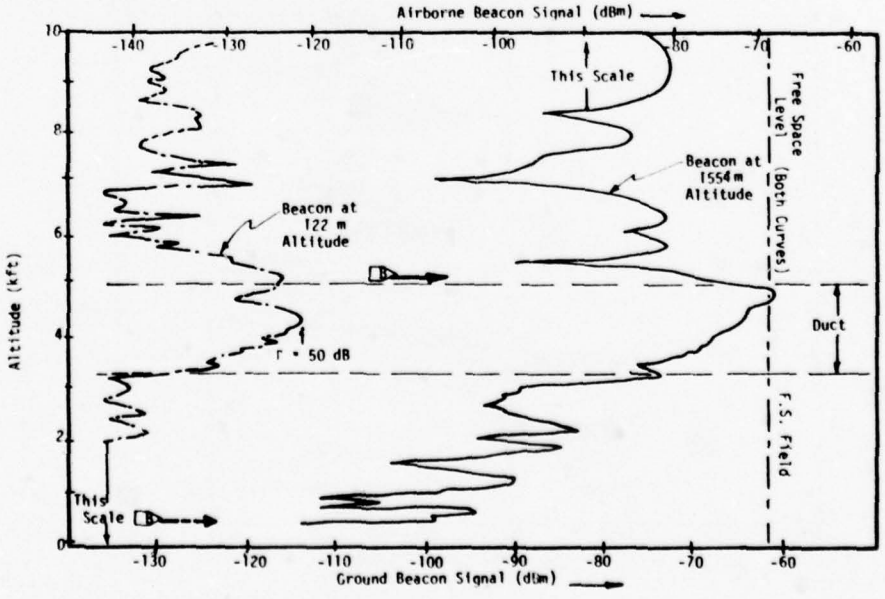

Figure 16. Comparison of simultaneous height-gain profiles for transmitters on the ground and near the duct (Flight 18).

The signal strength was calculated for comparison with the third measured profile (D4) given in Figure 11. It can be seen in Figure 12 that the measured and calculated profiles both peak in the duct as would be expected from the discussion in Section 3.5. The envelopes of the calculated and measured signals are in fairly good agreement. However, the measured signal level is somewhat weaker in the duct and stronger outside the duct, particularly at the higher altitudes. This suggests that there may be some leakage out of the duct in addition to what would be expected theoretically for the horizontally homogeneous three-segment refractivity model used here. In terms of a modal analysis this would be expressed as a conversion of energy from low-loss, well-trapped modes to high-loss chordal modes caused by some perturbation. Horizontal refractivity inhomogenuities provide a likely source of the perturbation.

There is no better agreement between the measured signal nulls and the calculated signal profile than was found comparing the null structure of different measured soundings. Thus it appears that the relative phase of different modes may become random for long paths in the atmosphere.

The apparent loss of definite phase relationships between the various modes is dramatically illustrated by the 449 MHz data for the same sounding, as shown in (D4) Figure 13. In this case the calculation shows the modes canceling above the duct, resulting in a 20 dB to 30 dB reduction in the calculated signal strength (thin dashed line). However, if the modes are assumed to have a random phase relationship and mode powers are added (broken line) instead of the usual vector addition of mode voltages used in the other calculations, the calculated signal strength profile is found to be in good agreement with the measured profile (thick line).

The 2200 MHz signal strength profile measurements are particularly interesting because they tend to mimic the 449 MHz measurements. This can be seen in Figure 14 where the 2200 MHz height profile is compared with the 449 MHz profile given in the previous figure. The close agreement between these two profiles is encouraging since it suggests that measurements and calculations at 449 MHz can be used to infer the general nature of duct propagation at much higher frequencies, where mode calculations require many modes and are therefore more difficult.

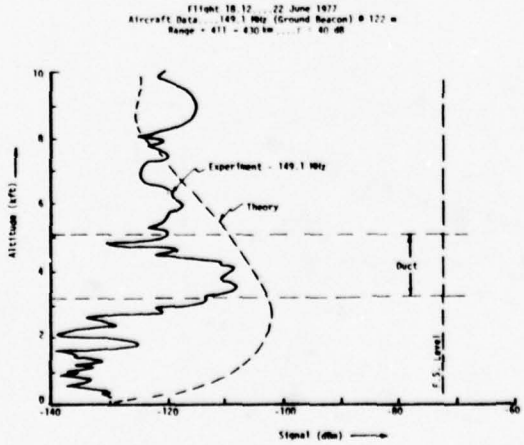

Figure 17. Comparison of the calculated and measured height-gain profiles for a 149 MHz transmitter on the ground (Flight 18).

Height-gain curves for the ground beacon transmitter are given in Figure 15. These curves are for the same soundings used to measure the curves previously presented for the airborne beacon. The three curves for the ground beacon are reasonably consistent having the characteristic sharp drop in signal below the duct, a peak in the duct and a modest reduction of the signal level above the duct. However, in this case the peak signal level is quite weak being 40 dB to 50 dB below free space.

The duct coupling loss (or excitation factor) from the ground can be inferred by comparing the signal levels received from a transmitter in the duct with those from a transmitter on the ground, as shown in Figure 16. In this case the coupling loss can be seen to be on the order of 40 dB to 50 dB.

The theoretical height-gain profile was calculated for the ground transmitter and is compared with the measured profile in Figure 17. The predicted height-gain curve is quite broad as would be expected for partial reflection modes, while the observed height-gain curve shows a sharp peak at the duct height. This sharp peak indicates that the signal is primarily due to the well-trapped modes and not the partial reflection modes.

The lack of partial reflection modes can be explained by the fact that for the ground transmitter the theoretical assumption does not correspond to reality. The calculations assume a transmitter 116 meters above a spherical surface, while in reality the transmitter was at 116 meters with a 131 meter hill between it and the assumed spherical surface (the ocean). This hill should block all the chordal modes and lower order multihop modes. The attenuation of the remaining high order modes is so great that they could not be detected beyond 100 km. This explains the weak signal below the duct but does not explain the observation of a height-gain curve characteristic of well-trapped modes. According to the theory used here, these modes should not be significantly excited by a ground transmitter.

It appears that the explanation must be that in the case of a ground transmitter, the well-trapped modes are excited by mode conversion from higher order modes which are subsequently attenuated leaving only the low-loss trapped modes.

4.4 Flight 16 Measurements and Discussions

Flight 16 is unique in that the receiving airplane flew out to a range of 800 km from the beacon transmitters allowing ducted 149 MHz signals to be measured at long ranges. The ducting conditions during Flight 16 were quite ordinary as indicated by the refractivity data given in Figure 18. While ducting refractivity profiles were

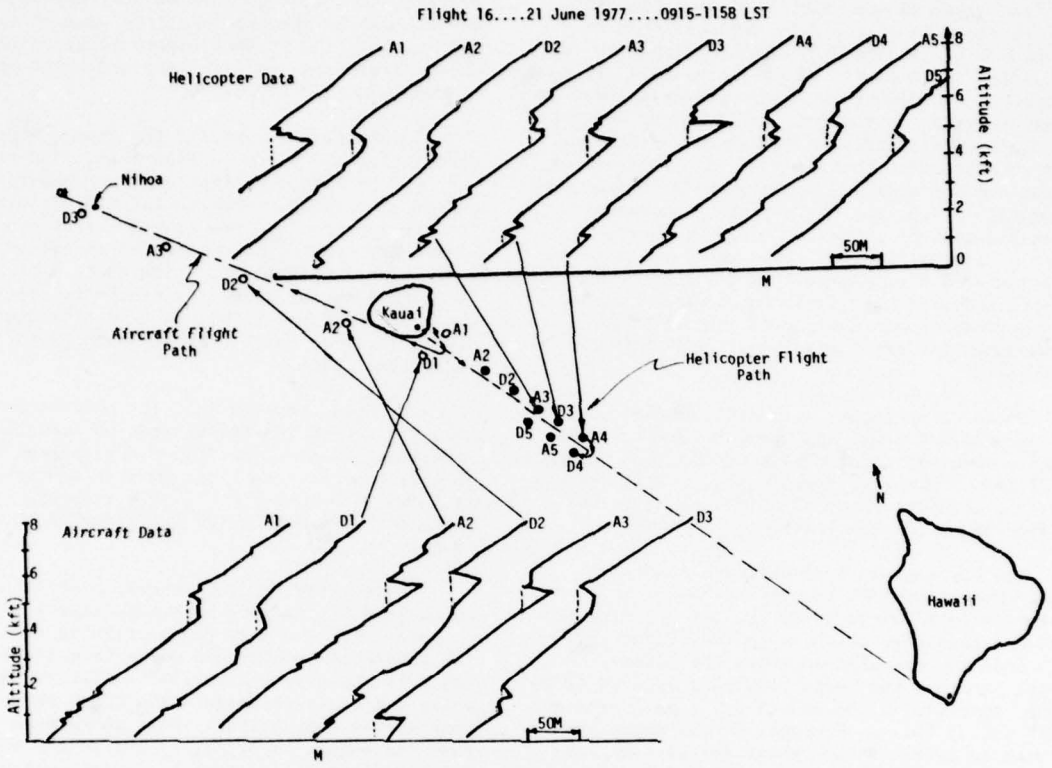

Figure 18. Refractivity data summary for Flight 16.

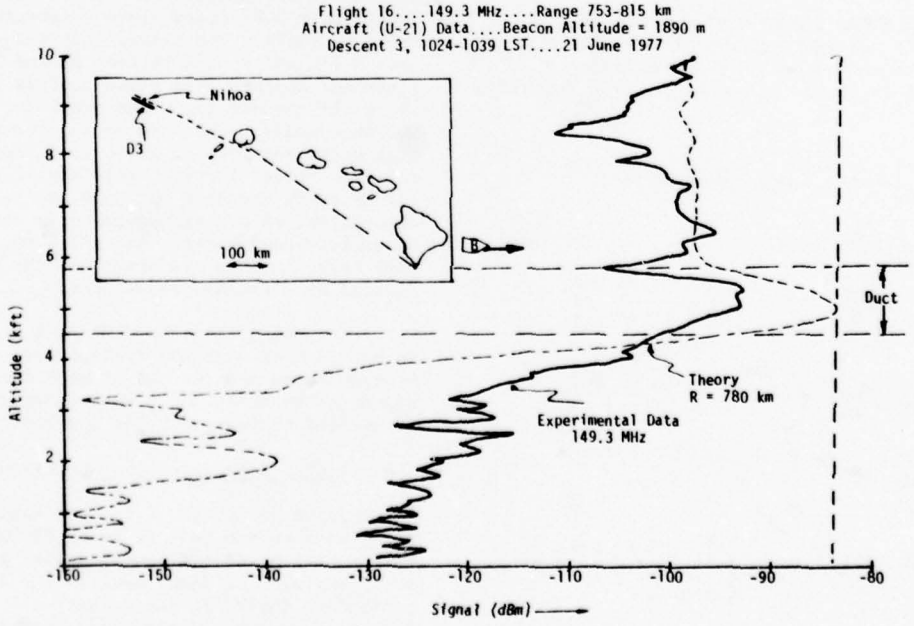

Figure 19. Comparison of the calculated and measured height-gain profiles for a 149 MHz transmitter just above the duct and a range of 800 km (Flight 16).

clearly present, they were not as consistent as the Flight 18 profiles.

4.4.1 Signal Strength Above the Duct

The measured and calculated height-gain curves for the 149 MHz airborne transmitter at a range of 800 km are compared in Figure 19. The measured signal has a broad null above the duct which is not present in the calculated signal. Aside from this null, the envelope of the calculated and measured signals are in excellent agreement above and below the null. The null appears to indicate that the calculated mode phases above the duct are not accurate, while the agreement of the signal levels outside the null indicate that the mode strengths are being correctly calculated.

4.4.2 Signal Strength Below the Duct

Below the duct the measured signal is much stronger than the calculated signal. In Section 3.5 it was shown that the height-gain curve for chordal modes allows for significant signal levels below the duct while the height-gain curve for well-trapped modes drops dramatically below the duct. However, chordal modes which are directly excited by the transmitter are attenuated below detectability before they reach the receiver. Thus the stronger measured signal strengths are interpreted as resulting from the excitation of high-loss chordal modes by the interaction of well-trapped modes with irregularities in the atmospheric refractivity along the propagation path.

4.4.3 Signal Strength in the Duct

The measured signal strength inside the duct is much less than calculated for the particular sounding presented in Figure 19. However, it will become apparent in the following paragraphs that this large difference gives a misleadingly pessimistic view of the comparison of theory with measurements.

The difference between the measured and calculated signals in the duct is thought to be the result of the calculated modal phase relationships being slightly different than the actual phase relationships. The reduction in the measured signal strength is too great to represent the trapped mode power that was converted to chordal modes. Only a small fraction of the abundant trapped power is required to account for all of the weak signal power observed below the duct (.1% of the ducted signal).

While a large number of modes contribute significantly to the signal level above and below the duct, only the two lowest order modes contribute significantly to the signal in the duct at these long ranges. The signal levels of the third, fourth, and fifth modes are down 25 dB, 40 dB, and 50 dB, respectively. This is because of the increased leakage losses of the higher order modes. At 800 km even a low-loss mode with an attenuation of 0.03 dB/km will be attenuated 24 dB.

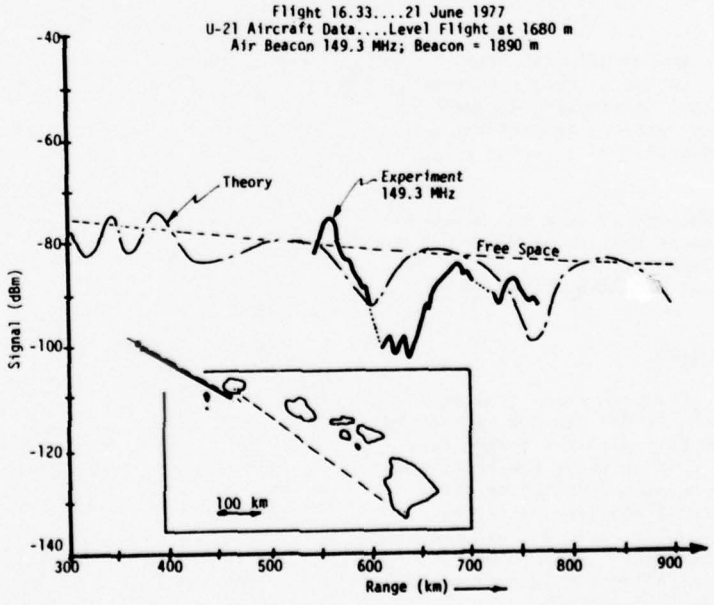

Figure 20. Comparison of calculated and measured signal strength as a function of range for a 149 MHz transmitter just above the duct.

The two calculated modes have slightly different phase velocities resulting in a 360° relative phase shift and a maximum in the signal strength every 160 km. This can be seen in Figure 20 where the measured and calculated signal strengths are compared as a function of range. The measured maxima are offset 30 km in range from the calculated maxima, and are spaced by 130 km instead of 160 km. It is this offset that results in the difference between the measured and calculated signal levels observed at the duct altitude in the previous height-gain profile. The difference in the locations of the calculated and measured maxima indicate that the relative phase of the actual modes is somewhat different than the calculated phase. This difference could be due to any one of three factors: experimental uncertainty in the measured range, experimental uncertainty in the refractivity model parameters, or a basic inadequacy of the refractivity model itself.

The uncertainty in the measured range is on the order of 30 km. The location of the airborne transmitter was taken to be exactly over the ground transmitter. The instantaneous range from the airborne transmitter varies from 10 km greater, to 40 km less than this nominal range. There may also be comparable errors in the location of the receiving aircraft which for this flight was essentially determined by dead reckoning techniques with fixed locations at Kauai and Nihoa.

The choice of parameters for the three segment refractivity model may not have been optimum to represent the irregular refractivity conditions present during Flight 16. The 30 km difference in the distance between measured and calculated maxima represents only a 2 M unit change in the average refractivity of one of the modes relative to the other.

The third possible factor affecting the locations of the signal maxima is that the three segment refractivity model is simply inadequate to properly account for the vertical irregularities and horizontal inhomogeneities encountered in the real atmosphere.

Thus the 130 km distance between the measured maximum signal locations is felt to be in excellent agreement with the theoretical value of 160 km as is the agreement of their absolute locations to within 30 km.

5. SUMMARY AND CONCLUSIONS

Elevated ducts at altitudes above 1 km can result in the propagation of VHF and UHF signals to ranges greater than 800 km. When the transmitter and receiver are located in or above the duct, the signal strengths approach normal operating (free space) levels. When either the transmitter or receiver is located below the elevated duct the signals are greatly attenuated. Radiosonde measurements can be used to identify the presence of elevated ducts and develop ducting climatological data.

VHF and UHF signal strengths were measured as a function of height and range for elevated ducting conditions, and beacon transmitters were located on the ground, and at the elevated duct altitude. The refractivity height profiles were measured along the entire propagation path. Theoretical signal strength calculations based on this refractivity data were compared with the measurements.

A direct examination of the measurements revealed 149 MHz signals near the free space level at ranges to 800 km when the transmitter was located at the duct altitude and the receiver was in or above the duct. The measured 449 MHz ducted signal profiles were found to closely correspond to the measured 2200 MHz signal profiles. This may be a useful result for those interested in developing simplified duct propagation models.

Comparisons of the measured signal strengths with theoretically calculated values resulted in a number of revealing insights into the phenomena of elevated ducting. A number of cases were observed which suggest the presence of mode conversion between low-loss trapped modes and the higher loss leaky modes. This is thought to arise from vertical irregularities and horizontal inhomogeneities in the atmospheric refractivity. Calculated interference effects of the two lowest order modes were found to be in agreement with the measurements, while the actual phase relationships of high order modes appear to become somewhat random at long ranges in the real atmosphere.

Kerr, Donald E., (1951) Propagation of Short Radio Waves, p. 12, Dover Publications Inc., New York

Pappert, R.A., and C.L. Goodhart, (1977) Case studies of beyond-the-horizon propagation in tropospheric ducting environments, Radio Sci., 12, 75-87.

DISCUSSION CONTRIBUTION

A PROPOSAL TO INVESTIGATE THE INCIDENCE OF ANOMALOUS PROPAGATION IN THE NORTH-WESTERN ATLANTIC

John Clarke

Royal Signals and Radar Establishment

Great Malvern, U.K.

Several papers in this conference have already drawn attention to lack of knowledge regarding horizontal uniformity in the atmosphere. A statement has been made that the atmosphere appears to be uniform for 85% of all time; also that substantial super-refraction (or ducting) occurs for 20% of the time in some parts of the world. Therefore the question of the extent of horizontal uniformity in super-refracting atmospheres is of major importance. It may be noted propagation prediction programs, such as IREPS, assume the same vertical profile of refractive index at all locations.

It is proposed that an experimental investigation be made in the maritime environment of the north-western Atlantic off the coast of Scotland, to indirectly explore horizontal uniformity of super-refracting atmospheres. A path of operational importance will be used as shown in Fig 1, for which one terminal is at medium altitude (ie an aircraft equipment) and the other is near to the surface of the sea (ie a shipborne equipment or a coastal defence site). The operational equipment at either terminal might be a communication set, jammer, radar, passive detection system, or identification system.

The experiment will comprise an SSR site (secondary surveillance radar) on the Hebrides, see Fig 2, observing trans-Atlantic aircraft traffic over a two year period. For the SSR equipment selected, a path loss of up to 155 dBi can be accommodated and this allows aircraft to be tracked beyond the normal horizon in the presence of super-refraction. Fig 3 shows path loss versus range curve for various uniform super-refracting atmospheres: thus by correlating the occurrence of long range SSR performance with local vertical refractivity soundings, a check can be made on the validity of assumed horizontal uniformity. The experiment will also provide directly statistics of the incidence of anomalous propagation over this type of path in the maritime environment.

Thus, in summary, a proposal has been made to investigate the incidence and uniformity of super-refracting atmospheres in the north-western Atlantic. The results will be of particular interest because the propagation path passes over the Gulf Stream.

TRANS - HORIZON AIR-GROUND PATH IN A REFRACTING ATMOSPHERE

FIG. 1

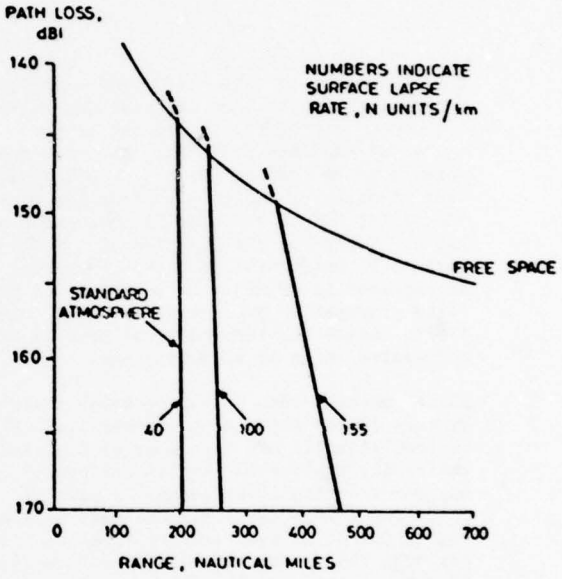

PATH LOSS v RANGE FOR DIFFERENT ATMOSPHERES

FIG. 3

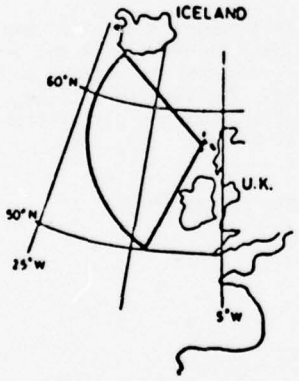

EXPERIMENTAL SEA AREA SHOWING 500 NAUT. MILES CLEAR SEA ARC

FIG. 2

REFRACTIVE INDEX PROFILE EVOLUTION: A NUMERICAL MODEL STUDY

Stephen D. Burk

Naval Environmental Prediction Research Facility

Monterey, California 93940

ABSTRACT

Forecasts of the modified refractive index field are presented in three case studies that use a one-dimensional boundary layer model. In the first experiment, stratus clouds exert a strong influence on the development of an elevated duct. In the second experiment, observational data from CEWCOM-76 are used to initialize the model; the predicted boundary layer behavior in this experiment is quite realistic when compared with detailed observations. In the third experiment, a surface duct disappears near the time of fog formation; however, this duct dissipation is found to have no direct cause and effect relationship with the fog formation.

1. INTRODUCTION

High resolution numerical models of the marine planetary boundary layer (MPBL) have the potential for forecasting the detailed evolution of the refractive index field. This paper discusses the capacity of such a model to forecast the time-dependent behavior of the modified refractive index field in two typical MPBL situations and in one overland case. The model is a second-moment turbulence closure model which has a complexity of "Level 3" (Mellor and Yamada, 1974).

The model is one-dimensional; the grid points may be thought of as an "instrumented tower." Given initial information on the wind, temperature, pressure, and moisture fields, one solves the model equations in an iterative fashion to forecast new values for these quantities. Hence, one is forecasting wind, temperature, pressure, and humidity at each level of the tower. The evolution of the modified refractive index field is then diagnostically calculated from these forecast fields.

The turbulence closure model also forecasts the evolution of important statistical quantities that describe the turbulence field, such as variances of temperature and moisture. By this approach, the intensity of refractive index fluctuations caused by turbulence (as measured by the structure parameter, C_n^2) can be forecast (Burk, 1978). This paper, however, presents the time-dependent behavior of mean rather than turbulence quantities. Particular attention is paid to the modified refractive index, M.

We recognize the danger of making overenthusiastic claims for a one-dimensional model. Grid points for computing horizontal gradients are absent; the time-dependent behavior of advection and subsidence cannot be calculated. These terms, however, can be externally specified. That is, if information concerning subsidence and advection is available from analyzed charts or from a larger-scale model, then this information can be added to the prognostic equations of the one-dimensional model.

2. MODEL EXPERIMENTS

Rather typical situations are discussed in the two MPBL model experiments presented here. The first experiment (Case A) represents a situation in which an initially cloud-free boundary layer develops into a stratus-capped boundary layer during the period of the model forecast. The second experiment (Case B) is based upon data from the Cooperative Experiment in West Coast Oceanography and Meteorology (CEWCOM-76). The behavior of the MPBL on 3 October 1976, as discussed by Noonkester (1978a; 1978b), provides the focus of the Case B experiment. Case C addresses results from an overland simulation.

2.1 Case A

This experiment is based upon the work of Sommeria (1976), who used the three-dimensional Deardorff model to simulate an undisturbed MPBL situation. The boundary layer is well mixed, initially, to a height of 500 m. Between 500 and 1425 m there is a conditionally unstable layer that is capped aloft by the dry, stable, free atmosphere. The air-sea temperature difference is 1°C and the surface specific humidity is taken at the saturation value for the given sea surface temperature. Initially, the boundary layer is cloud-free; the relative humidity within the conditionally unstable layer is near 95%. A subsidence of 2 cm s^{-1} is specified at the grid top (2.5 km) and this subsidence decreases linearly to zero at the surface. Shown in

Fig. 1 are the initial profiles of potential temperature and specific humidity.

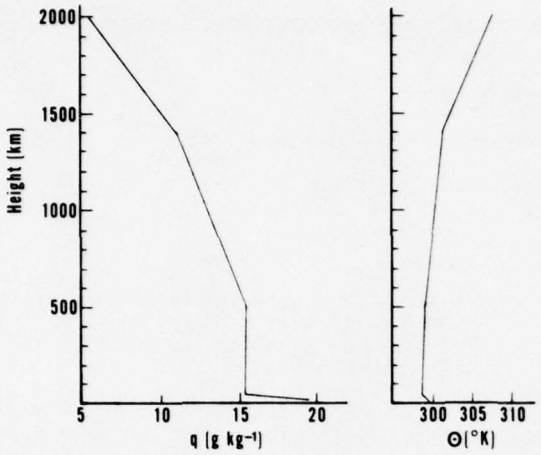

Fig. 1. Initial profiles of specific humidity and potential temperature used in Case A.

During the first three hours of integration, the overlying stable region lowers about 130 m due to the subsidence. The moisture within the mixed layer increases due to the upward moisture flux from the surface. This lowering of the inversion and moisture increase appear in Fig. 2, which shows the evolution of the potential temperature and specific humidity fields.

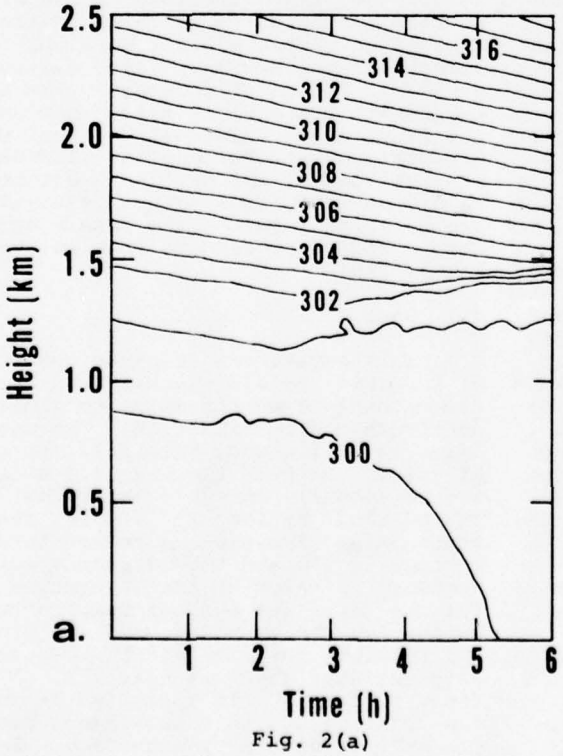

Fig. 2(a)

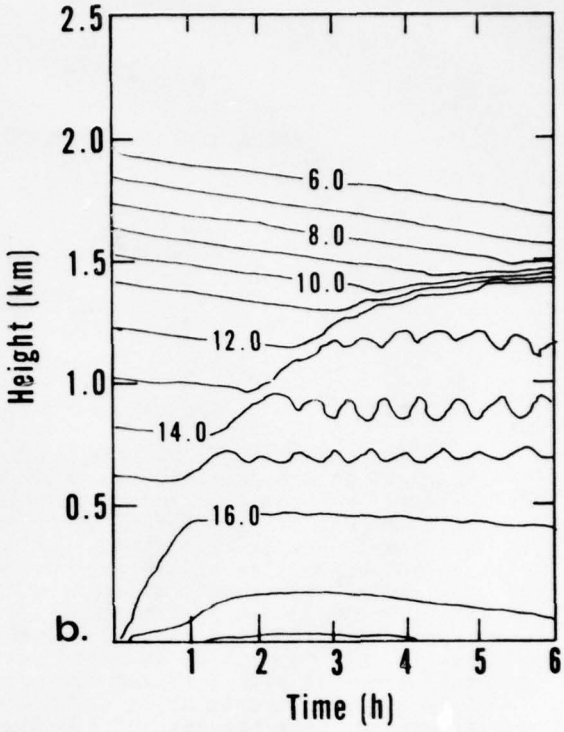

Fig. 2. (a) Model-predicted evolution of the potential temperature (°K) field in Case A; (b) Specific humidity field (gm kg^{-1}).

Clouds begin to form two hours into the integration and a well-defined stratus layer is present during the final three hours of the forecast. Radiative cooling at stratus top creates an unstable lapse rate within the cloud layer. This thermal instability causes the turbulent intensity to increase and thereby increases the rate at which the stable overlying air is entrained into the MPBL. Thus, enhancement of turbulence by radiative transfer is a mechanism by which a stratus-capped boundary layer can grow in depth. As an indication of this stratus effect, note in Fig. 2 that beyond three hours into the forecast, the mixed-layer depth increases slightly despite the continued presence of subsidence. The liquid water content of these clouds is shown in Fig. 3. A more complete discussion concerning the dynamics of stratus-capped boundary layers is presented by Oliver et al. (1978).

We now turn to the evolution of the M field during the integration period. The sharp moisture gradient near the surface (Fig. 1) creates a 20-m deep evaporation duct. Above this surface duct, the modified refractive index has a monotonic increase, initially. The initial temperature inversion and moisture decrease present near 1.4 km in Fig. 1 are not intense enough to produce a trapping layer, although these gradients do create a region in which the M field is rather flat. Once the stratus layer develops, however, the combination of radiative cooling at cloud top and

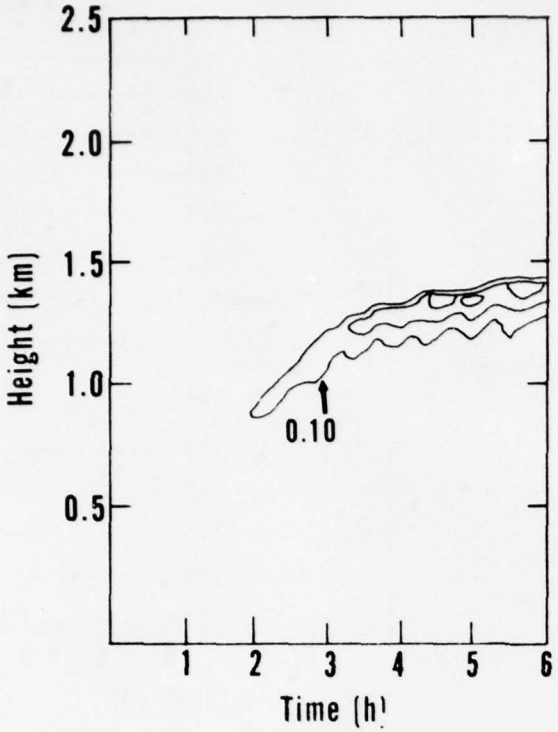

Fig. 3. Liquid water content (gm kg^{-1}) showing stratus development in Case A, contour interval 0.1 gm kg^{-1}.

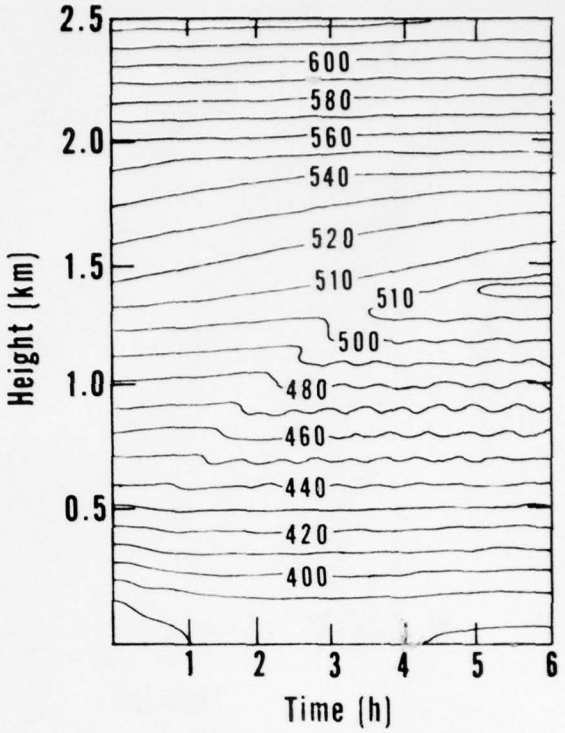

Fig. 4. Evolution of the modified refractive index field as forecast by the model in Case A.

subsidence heating aloft acts to intensify the capping inversion and moisture lapse across the inversion. The stratus development creates a trapping layer in a short time. Similarly, this trapping layer could be eradicated rather quickly if the stratus layer were to dissipate.

With the exception of the evaporation duct, which is too thin to be resolved by the depicted contours, the features of the M field are shown in Fig. 4.

2.2 Case B

Case B examines a MPBL situation similar to that described for Case A, except that real data from CEWCOM-76 are used. Noonkester (1978a) presents detailed acoustic sounder and FM-CW radar data for 3 October 1976 taken near San Diego as part of CEWCOM-76. Shipboard and radiosonde data are available for this date. Fig. 5 in Noonkester, 1978a, indicates that the depth of the MPBL is about 325 m at 1200 LT. The boundary layer grows to a depth of about 600 m at 1500 LT and then is suppressed to a depth of about 500 m at 1800 LT. Noonkester points out that the descent of an elevated inversion indicates the presence of subsidence. Radiosondes showed this elevated inversion descending from 2 km to 830 m between 0500 and 1700 LT on this date. This information was used to specify the magnitude of subsidence for this model run.

The model was initialized with conditions representative of 1200 LT. The inversion initially present near 325 m rises to about 575 m at 1800 LT, in reasonable agreement with the CEWCOM data. However, there is no indication, as there was in the CEWCOM data, of suppression of the boundary layer depth between 1500 and 1800 LT. Perhaps this disagreement results from lack of detailed information concerning the time-dependent behavior of the subsidence. The growth of the boundary layer is apparent in Fig. 5, which shows the potential temperature and specific humidity fields. The model-predicted boundary layer levels off beyond 1800 LT (not shown) at about 600 m.

Case B develops only a very thin stratus layer that has an insignificant liquid water content. The inversion does strengthen somewhat during the period of the forecast. This strengthening, as illustrated in Fig. 5, results from the subsidence aloft and the turbulent mixing at low levels. If the stratus layer had developed more fully, then a significant elevated duct very likely would also have developed. Instead, the M field has only a weak trapping layer near the inversion. As in Case A, there is a surface duct in this experiment. Fig. 6 shows the behavior of the M field in Case B. The evaporation duct, as in Case A, is not resolved by the contours.

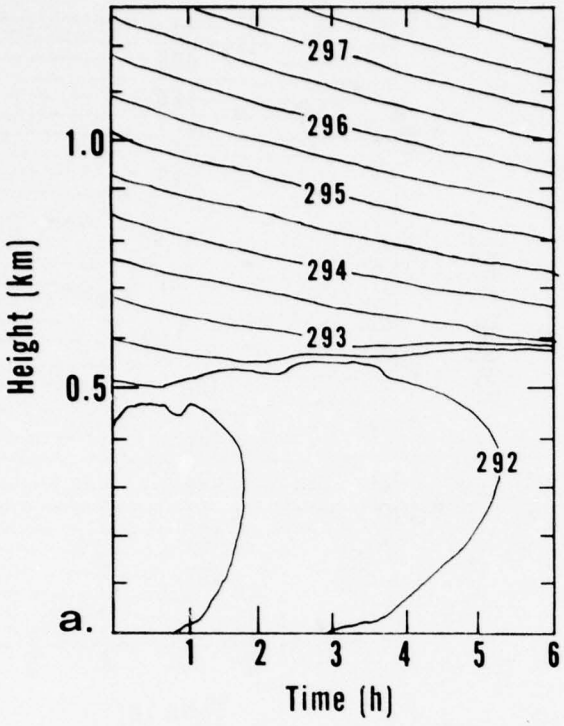

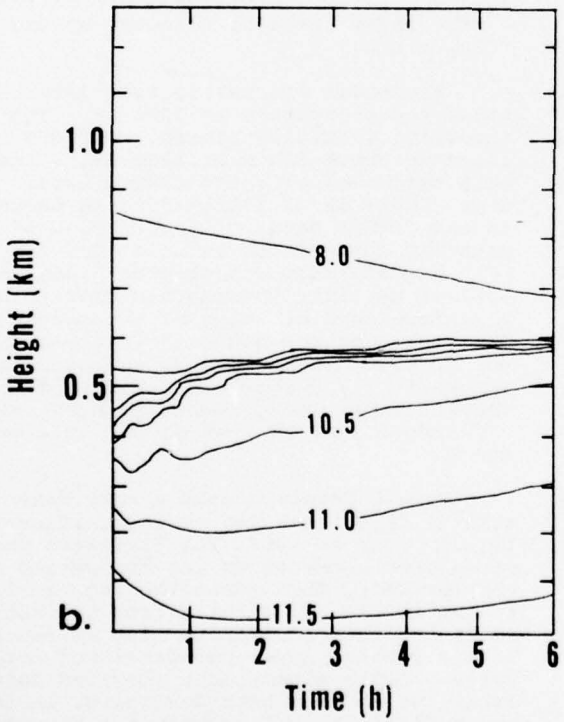

Fig. 5. (a) Model-calculated evolution of potential temperature (°K) field in Case B; (b) Specific humidity field (gm kg^{-1}).

2.3 Case C

Case C is a simulation of the diurnal PBL behavior over land. Some aspects of this numerical experiment are presented in Burk (1977). An Ekman-type wind profile and stable boundary layer are present initially as shown in Fig. 7. The surface temperature is specified to undergo the diurnal wave shown in Fig. 8. The surface specific humidity undergoes a similar wave as a simulation of evapotranspiration effects.

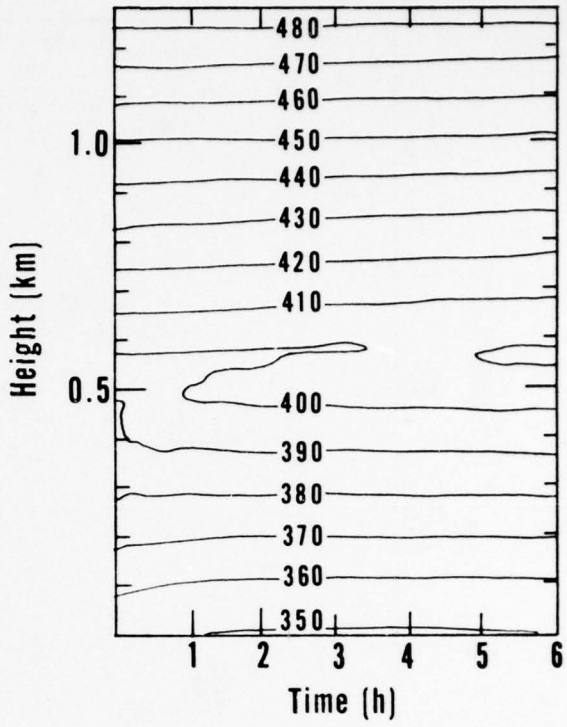

Fig 6. Evolution of the modified refractive index field as forecast by the model in Case B.

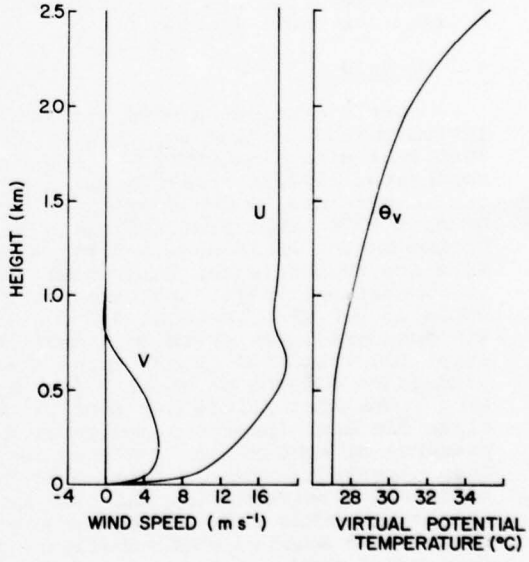

Fig. 7. Initial wind and virtual potential temperature profiles used in Case C.

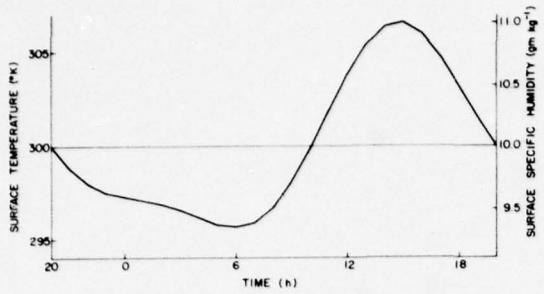

Fig. 8. Specified diurnal variation of surface temperature and surface specific humidity used in Case C.

No clouds develop in this case. A nocturnal inversion about 500 m deep develops, while during the day the large convective activity associated with the surface heating causes the PBL depth to increase to about 1.7 km (Figs. 3 and 4 in Burk, 1977). This lifting of the inversion during the day manifests itself in the M field. The "wrinkle" in the contours in Fig. 9 locates the position of the rising inversion. It is evident, however, that no trapping is present in this case even though the contours do tend to fold back near the inversion.

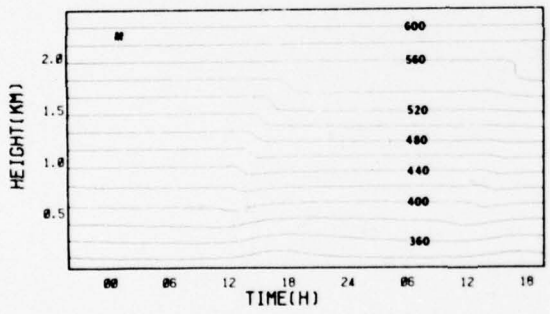

Fig. 9. Evolution of the modified refractive index field as forecast by the model over a two-day period in Case C.

This experiment recently was repeated with a slight modification. In the modified version, the specified surface specific humidity is increased. This humidity increase leads to development of a nocturnal ground fog. Such nocturnal "radiation" fogs are relatively common over wet agricultural fields. Interestingly, a surface duct develops early in the evening in this numerical experiment and dissipates when the fog forms later in the evening. Battan (1973, p. 26) notes that disappearance of surface ducts is quite common when fog forms. In this experiment, however, no direct cause and effect relationship exists between the fog and the surface duct dissipation. Rather, the conditions conducive to fog development are also conducive to dissipation of the surface duct. To explain this last statement more fully, the sequence of events should be outlined.

During the day, the near surface specific humidity decreases due to entrainment of dry air from aloft. As evening approaches, a substantial moisture lapse exists near the wet surface. This moisture lapse, in conjunction with the development of the nocturnal temperature inversion at the surface, creates a surface duct. As the evening progresses, the air adjacent to the surface moistens. There is little downward entrainment of dry air from aloft because the turbulence is weak. Fog formation occurs when the near surface air has cooled and moistened to the dew point. Concurrently, the moistening of this layer adjacent to the surface acts to decrease the moisture lapse and, therefore, to reduce the likelihood of a surface duct.

3. CONCLUDING REMARKS

This paper addresses several typical MPBL cases and one overland experiment. The behavior of the M field at altitudes near the inversion has been particularly emphasized. If desired, however, surface duct behavior could easily be emphasized by expanding the grid display near the surface.

Second-moment turbulence closure models are complex numerically. One solves not only time-dependent equations for the mean quantities, but also solves equations for the ensemble-averaged turbulence variables. However, when restricted to one dimension, numerical computations with such closure models run quite quickly and efficiently.

A multi-dimensional model can deal more realistically with the three-dimensional nature of the atmosphere than can a one-dimensional model. In the operational marine environment, however, one rarely has the detailed three-dimensional data necessary to specify initial and boundary conditions for a multi-dimensional MPBL model. Typically, only isolated soundings are available in conjunction with bulk air-sea data. This type of limited information is compatible with the initialization and boundary condition requirements of a one-dimensional model.

Although the model results presented here are encouraging, further detailed comparisons with atmospheric data are needed. For such model testing, research experiments such as CEWCOM offer a very useful data base. A model must be verified by an abundance of detailed atmospheric observations before the model can be confidently applied to a data sparse environment.

4. REFERENCES

Battan, L.J., 1973: Radar observation of the atmosphere. The University of Chicago Press, 324 pp.

Burk, S.D., 1977: The moist boundary layer with a higher order turbulence closure model. J. Atmos. Sci., 34, 629-638.

Burk, S.D., 1978: Use of a second-moment turbulence closure model for computation of refractive index structure coefficients. NEPRF Tech. Rept., TR 78-04, 58 pp.

Mellor, G.L., and T. Yamada, 1974: A hierarchy of turbulence closure models for planetary boundary layers. J. Atmos. Sci., 31, 1791-1806.

Noonkester, V.R., 1978a: Multi-sensor measurements of ocean based convective activity. Proc. 18th Conf. Radar Meteor., Amer. Meteor. Soc., 55-64.

Noonkester, V.R., 1978b: Acoustic echo-sounder, acoustic bistatic wind and FM-CW radar measurements during west coast foehn winds. Fourth Sympos. on Meteor. Observations and Instrumentation, Amer. Meteor. Soc., 447-454.

Oliver, D.A., W.S. Lewellen, and G.G. Williamson, 1978: The interaction between turbulent and radiative transport in the development of fog and low-level stratus. J. Atmos. Sci., 35, 301-316.

Sommeria, G., 1976: Three-dimensional simulation of turbulent processes in an undisturbed trade wind boundary layer. J. Atmos. Sci., 33, 216-241.

Acknowledgements: The author gratefully acknowledges the assistance of Drs. K. Davidson, C. Fairall, and G. Schacher of the Naval Postgraduate School, who provided shipboard data taken during CEWCOM-76.

CLIMATOLOGY OF EVAPORATION DUCT PROBABILITIES

Paul R. Lowe

Naval Environmental Prediction Research Facility

Monterey, California 93940

ABSTRACT

This report outlines a procedure for generating a probabilistic climatology of the effect of the presence of an evaporation duct on radar range. Examples of the probability of range enhancement (success) are presented as a demonstration of the utility of such a climatology for short term forecasting.

1. INTRODUCTION

Climatologies of atmospheric events have generally been required as inputs into the process of long term strategic planning. Climatologies for such purposes are usually limited to monthly or seasonal histograms, some measures of central tendency, and some measures of dispersion. Measures of central tendency might include the algebraic mean (average), the median (50% value), or the mode (the most typical value). Measures of dispersion might include the variance, the interquartile range, or the interdecile range. Such climatologies have little use for short term (day-to-day, hour-to-hour) decision making.

It is possible to compile climatologies which do provide input into the short term decision making process. Such climatologies are probabilistic (stochastic) in nature and address the behavior of the atmospheric event under consideration as a function of time. In this type of compilation the probability of persistence or change of the event under consideration is determined. Such probabilities are conditional in nature, i.e., given the state of an event at the present time, the future state may be predicted in a probabilistic fashion. In contrast to the classical approach, the stochastic approach has forecasting utility as well as utility for long term planning.

The purpose of this presentation is to demonstrate the type of operationally significant information provided by a stochastic analysis of historical data. The demonstration takes the form of a probabilistic analysis of the influence of the strength of evaporation ducts on the range of radar systems.

The presentation is organized in a developmental fashion. Section 2 discusses the nature of evaporation ducts, the determination of duct intensity, and the effect of duct intensity on range. Section 3 defines the analysis procedure and events studied, and describes the data analyzed. Section 4 describes the analysis results in terms of estimates of unconditional and conditional probabilities, and describes models derived from the analysis. Sections 5 and 6 summarize the presentation and offer recommendations for further study, respectively.

2. THE EVAPORATION DUCT

In maritime regions, there is almost continual evaporation of water from the ocean surface. This evaporation generates a rather steep moisture gradient in the lower few tens of meters of the atmosphere. This moisture gradient leads to ducting of microwave propagation which, in turn, leads to extended radar ranges. The intensity of the duct is dependent on the moisture gradient.

Jeske (1971) derived a relationship for assessing duct intensity as a function of readily observable environmental parameters. Hitney (1975) subsequently modified and improved this relationship. The relationship is

$$\delta = f(T_a, T_s, T_d, U) ,$$

where δ is duct intensity; T_a is air temperature; T_s is sea surface temperature; T_d is dew point temperature; and U is wind speed. This relationship is based on bulk parameters and stability considerations. Details of the computational procedure are found in Hitney (1975).

Hitney (1978) has shown that the existence of an evaporation duct can influence the range of a radar system in one of two ways. The range is either enhanced or not enhanced (even inhibited) depending on the intensity of the duct and the type of radar system. Each radar system has its own critical duct intensity. If actual intensity exceeds this critical value, the range of the system is enhanced. If actual intensity is less than or equal to the system critical intensity, radar range will

not be enhanced and may even be inhibited. Hereafter, enhancement will be referred to as "success"; and nonenhancement will be referred to as a "failure."

3. ANALYSIS AND DATA

The analysis procedure followed in this study is similar to that used by Grantham and Lund (1977) in a study of the persistence and recurrence of cloud cover categories. The term persistence (E_x) is defined as having the event (success, S; or failure, F; as defined in Section 2) occur at x consecutive observations. x may take on any value from 1 through 12. Thus S_3 indicates the occurrence of success conditions at 3 consecutive (contiguous) observations, 3 hours apart, i.e., SSS. F_4, in the same fashion, indicated the occurrence of failure conditions at 4 consecutive observations. The term recurrence is defined as the event where a success (or failure) condition exists now and also L hours from now. S_0S_L symbolically indicates the existence of a success condition now and also L hours from now. F_0F_L indicates a similar event for failure conditions.

The actual analysis determined frequencies of success or failure for each set of x consecutive observations where x took on the values 1 through 12. That is, each individual observation was classified as a success or a failure and frequencies were established. Next, each pair of (consecutive - contiguous) observations were examined and frequencies of 2 successes or 2 failures were established. This procedure was continued until all possible sets of 12 contiguous observations were examined and frequencies were established for S_{12} and F_{12}. At the same time, frequencies were established for the recurrent events E_0E_L where E could take on the value S or F and L varied from 3 to 33 hours.

The frequencies thus determined were used to estimate the probabilities for the occurrence of particular events. For example, the probability of the occurrence of 3 consecutive observations of success conditions is estimated by

$$\hat{P}(S_3) = \frac{n(S_3)}{N_3} , \qquad (1)$$

where $n(S_3)$ is the number of events of 3 consecutive observations that showed all successes; and N_3 is the total number of consecutive triplets. Similarly the probability of the occurrence of 4 consecutive observations of failure conditions is estimated by

$$\hat{P}(F_4) = \frac{n(F_4)}{N_4} . \qquad (2)$$

It should be noted here that $\hat{P}(F_4) + \hat{P}(S_4) \neq 1$. This situation holds because the events F_4 and S_4 are not exhaustive. Other situations such as FSFS are possible. In general the estimate of the probability of an event of interest is given by

$$P(E_x) = \frac{n(E_x)}{N_x} , \qquad (3)$$

where the symbols have a meaning similar to those used in the foregoing examples. Frequencies of recurrence were derived in a similar fashion and used to estimate probabilities. The probability for a recurrent event is given by

$$P(E_0E_L) = \frac{n(E_0E_L)}{N_x} , \qquad (4)$$

where L is the number of hours from the current time.

The data analyzed in this study consisted of surface observations taken at ocean weather station ECHO (35N, 48W) for five years 1951-55. The sampling density was three hourly observations. The analysis was applied to each month of the year.

4. ANALYSIS RESULTS

4.1 Persistence

The basic results of the analysis consist of estimates of the unconditional probabilities for persistent events. The probability of having a success condition at any observation chosen randomly is ~.66. Probabilities of success for longer sequence observations decay in an exponential manner. The longest sequence analyzed was one of 12 observations for which the probability was found to be ~.18.

A negative exponential model (function) was derived for these probability values. This model fits the analysis (observed) values very closely and is given by

$$P(S_x) = P(S_1) \exp \{-a(x-1)^b\} \qquad (5)$$

where $P(S_x)$ is the probability of having the success condition for a sequence of x observations. x may take on any integer value from 1 to 12. $P(S_1)$ is the probability that any randomly selected single observation shows the success condition. The value for this probability is 0.6578. The parameters 'a' and 'b' vary for different months. For January for the success condition, 'a' and 'b' take on the values 0.1368 and 0.9210 respectively. The parameter 'a' is largely a function of the climatic frequency of the event in question, while the parameter 'b' is a function of the decay rate for the probability of longer sequences.

The goodness of fit of the model to the observed unconditional probabilities was examined by determining the upper and lower bounds of the 95% confidence limits for each observed probability. This interval is the region within which probabilities determined from different samples of the same population can be expected to lie 95% of the time. If a model value lies between these limits, that value is acceptable as a representative estimate of the underlying population. Fig. 1 illustrates the analyzed unconditional probability

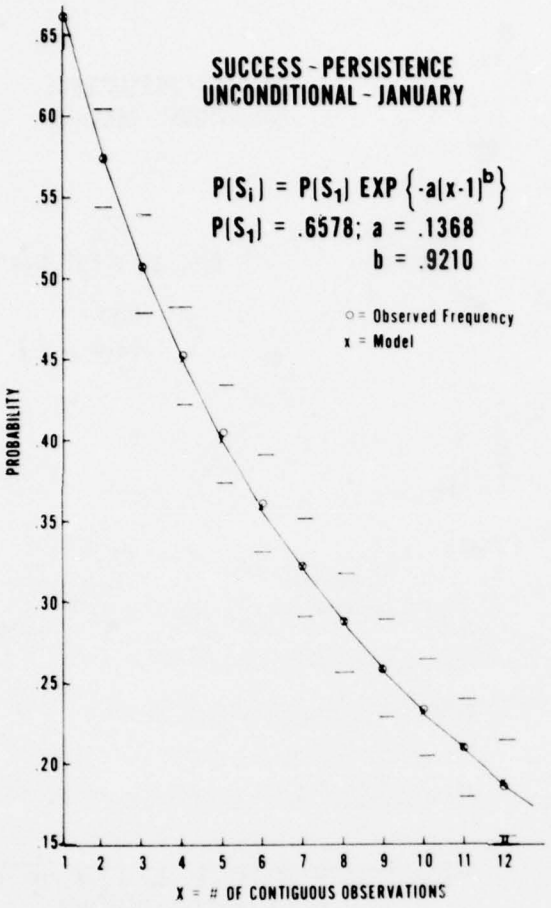

Fig 1. Unconditional probability $P(S_x)$ (Success-January). The points marked with o's represent analysis outputs. The x's indicate model values. The short horizontal lines indicate the upper and lower bounds of the 95% confidence interval.

structure and also the values produced by the model.

Conditional probabilities can be derived by application of the calculus of probability to the unconditional probabilities just described. Conditional probabilities take the form

$$P(A|B) = \frac{P(A,B)}{P(B)}\ , \qquad (6)$$

i.e., the probability that event A will occur, given that event B has occurred. This probability is determined by dividing the joint unconditional probability of A and B by the unconditional probability of B. For example, the probability of a success occurring at the next observation given that x successes have been experienced up to now is given by

$$P(S_1|S_x) = \frac{P(S_{x+1})}{P(S_x)}\ . \qquad (7)$$

Probabilities of this type were calculated for values of x = 2,...,11. The probabilities change very little as x takes on larger values. For x = 2, the probability is ~.87 and for x = 11, the probability is ~.89. The highest probability is .905 and is found at x = 9. These values show significant contrast with the unconditional probability that a given observation shows a success condition.

These conditional probabilities can be expressed in terms of the model established for the unconditional probabilities. The result is given by

$$P(S_1|S_x) = \exp\{a[(x-1)^b - x^b]\}\ . \qquad (8)$$

This result was obtained by substituting the appropriate unconditional model expressions for the factors on the right side of of Eq. (7). The parameters 'a' and 'b' have the values indicated above. As before, the model very closely approximates the values derived from the unconditional probabilities. All values lie well within the 95% confidence interval. Fig. 2 illustrates

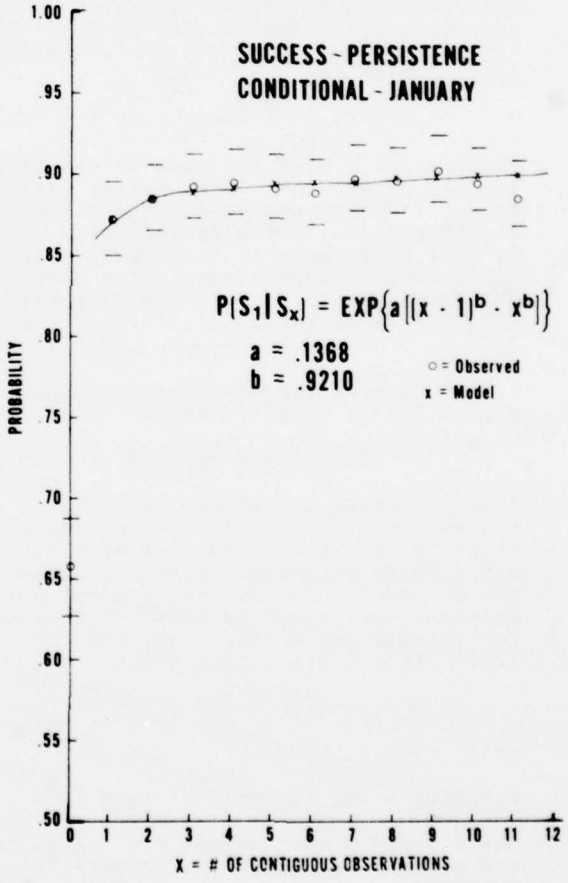

Fig. 2. Conditional probability $P(S_1|S_x)$ (Success-January). The points marked with o's represent analysis outputs. The x's indicate model values. The short horizontal lines indicate the upper and lower bounds of the 95% confidence interval.

the derived probabilities as a function of sequence size, the model values, and the confidence limits.

In addition to the conditional probabilities just discussed, probabilities of the form $P(S_x|S_1)$ were also derived (from the unconditional data). $P(S_x|S_1)$ signifies the probability that a sequence of x successes will occur given that a success condition exists at the present. These probabilities are determined by

$$P(S_x|S_1) = \frac{P(S_{x+1})}{P(S_1)} . \qquad (9)$$

As with the unconditional values, these probabilities decay as a negative exponential, but they have rather higher values (e.g., $P(S_2|S_1) \simeq .77$ while $P(S_2) = .575$). The rate of decay is about 50% steeper than that for unconditionals. Thus, again, information relevant to the present or recent past more clearly defines the probability of the event in the near future.

Again, the basic model was applied to approximate the derived probabilities. This was accomplished by substituting model expressions for the factors on the right hand side of Eq. (9). The result of this substitution is

$$P(S_x|S_1) = \exp\{-ax^b\} , \qquad (10)$$

where a and b have the same values as previously shown. All model values fall within the confidence intervals, thus making an acceptable fit to the derived data. The largest difference is found at x = 3. This difference is approximately two percentage points on the low side. The discussion of $P(S_x|S_1)$ is graphically illustrated by Fig. 3.

A general expression for unconditional probabilities is given by

$$P(S_x|S_y) = \frac{P(S_{x+y})}{P(S_y)} . \qquad (11)$$

This indicates the probability that a sequence of x consecutive successes will occur, given that a sequence of y successes has already occurred. Such probabilities can be modeled by substituting appropriate unconditional model expressions (Eq. (5)) for the factors on the right side of Eq. (11). This substitution gives

$$P(S_x|S_y) = \frac{P(S_1)\exp\{-a(x+y-1)^b\}}{P(S_1)\exp\{-a(y-1)^b\}} , \qquad (12)$$

which reduces to

$$P(S_x|S_y) = \exp\{a[(y-1)^b - (x+y-1)^b\} , \qquad (13)$$

where a and b have values previously shown, and x and y may take any positive integer values.

4.2 Recurrence

A recurrent event is defined as the event in which a condition exists both now and and also L hours from now with no consideration of the intervening time.

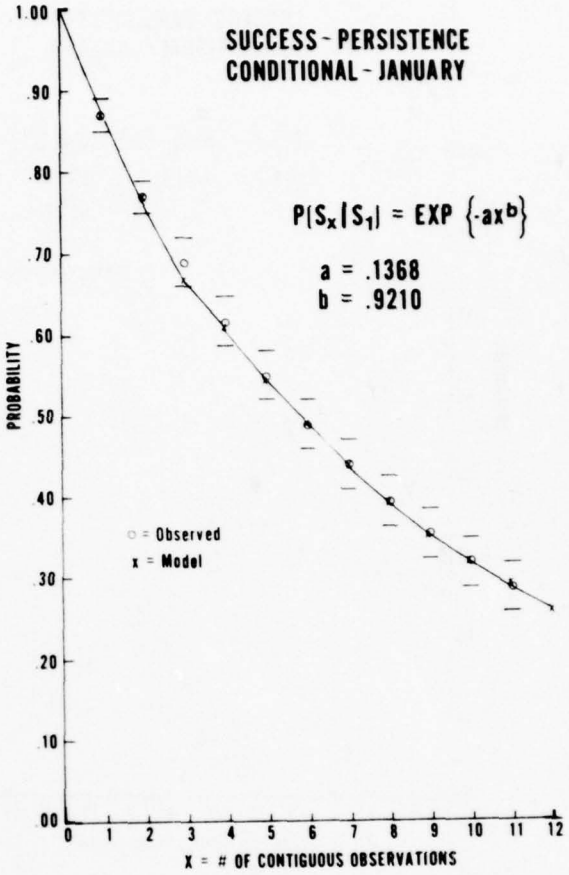

Fig. 3. Conditional probability $P(S_x|S_1)$ (Success-January). The points marked with o's represent analysis outputs. The x's indicate model values. The short horizontal lines indicate the upper and lower bounds of the 95% confidence interval.

Estimates of the conditional probabilities $P(S_L|S_0)$ were produced by the basic analysis. The probability $P(S_3|S_0)$ is ~.87 and that for $P(S_{33}|S_0)$ is ~.69. In general there is, again, an exponential-like decay with increasing time and the decay becomes assymtotic to the value of $P(S_1)$, the basic climatological frequency. The decay curve, however, is not as regular as that shown for the events discussed in Para. 4.1. There is the hint of some cyclic periodicity where L = 21 and 30 hr. This irregularity might be indicative of some kind of diurnal effect or it might be a result of data sampling chance effects. Grantham and Lund (1977) did observe periodicities in the probability of the recurrence of cloud cover with land observations. One would not expect to find significant diurnal variations in the maritime atmosphere. In modelling the recurrence probabilities, no effort was made to fit the possible periodicity.

The model form used was again an exponential form. This was different in that it consisted of two terms in order that the function values assymtotically approach the basic climatic value. The functional form for the model is

$$P(S_L|S_O) = P(S) + P(F) \exp\{-aL^b\} , \quad (14)$$

where a and b have the values .2176 and .6964 respectively. P(S), the climatic probability, is .6578 and P(F) = 1-P(S). All model values fell within the 95% confidence interval for the derived probabilities. While the fit here is not quite as good as in those models previously discussed, this model does give acceptable probability values. The largest difference occurs at L = 24 hr and is approximately 1 1/2 percentage points. This discussion of recurrence probabilities is illustrated in Fig. 4.

In order to attempt modelling the possible periodicity, it would be necessary to conduct an analysis stratified by time of day. Grantham and Lund (1977) conducted such an analysis and were able to fit the periodicity for cloud cover quite well. Before this can be done for evaporation ducts, the reality of the periodicity must be confirmed.

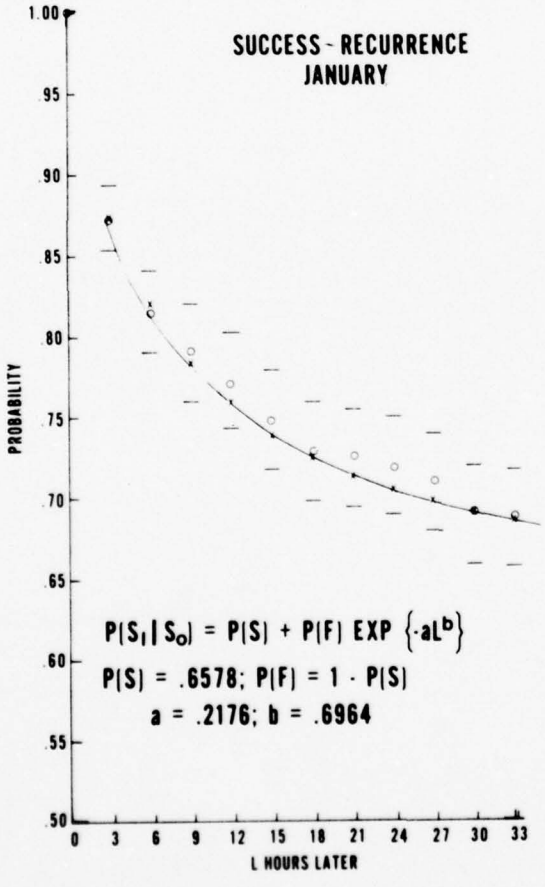

Fig. 4. Recurrence probability $P(S_L|S_O)$ (Success-January). The points marked with o's represent analysis outputs. The x's indicate model values. The short horizontal lines indicate the upper and lower bounds of the 95% confidence interval.

5. SUMMARY AND CONCLUSIONS

It has been demonstrated that it is possible to develop a probabilistic climatology that has a forecasting utility. Even though the basic data consists of observations that are separated by 3 hr, it seems possible to interpolate probability between observation times. This is so because of the very high degree of persistence for both the "success" and "failure" conditions.

The information derived from this study proved to be amenable to curve fitting. Such models have a number of advantages. They are quite economical in that they obviate the need for the storage of large arrays of numbers (e.g., a climatology of this nature, for all ocean weather stations in the North Atlantic, can be stored in a single solid-state module of a hand calculator). The 'a' and 'b' parameters make it rather easy to compare the probability structure at different stations, or at the same station for different months of the year.

The approach used here is not limited to studies of evaporation duct behavior. This approach may be applied to any environmental parameter or phenomenon which can be characterized as a binary (go or no-go) variable with regard to some particular weather-dependent operation.

Finally, the analysis method described above has been applied to each month of the year for both success and failure conditions. The models for the failure condition take the same form as for the success condition. However, the a and b parameters take different values.

6. RECOMMENDATIONS

There are a number of tasks to be done in order to complete the stochastic climatology. First, the models derived must be tested and verified on an independent data sample. Next, the analysis must be applied to all ocean weather stations (OWS). Then, a comparative analysis of all OWS, each one against the others, will be required. To make the climatologies more useful as a forecasting aid, it will be necessary to condition the success and failure conditions on such basic data as temperature. Finally it will be necessary to define probability distribution that accounts for all combinations of success or failure in a given sequence x hours long.

REFERENCES

Hitney, H.V., 1975: Propagation modeling in the evaporation duct. NELC TR-1947, Naval Electronics Laboratory Center (now Naval Ocean Systems Center), San Diego, CA 92152.

Hitney, H.V., 1978: Available to qualified requestors.

Jeske, H., 1971: The state of radar range prediction over sea. Tropospheric Radio Wave Propagation, Part II, NATO-AGARD.

Lund, I.A., and Donald D. Grantham, 1977: Persistence, runs and recurrence of sky cover. AFGL-TR-77-0308, Air Force Geophysics Laboratory, Hanscom, AFB, MA 01731.

ASSESSMENT OF MICROWAVE PROPAGATION IN THE LOWER TROPOSPHERE FROM LARGE SCALE MODEL OUTPUT

Wayne Sweet

Naval Environmental Prediction Research Facility

Monterey, California 93940

1. INTRODUCTION

Anomalous microwave propagation is not currently assessed or forecasted routinely because the necessary radiosonde data are not available for most ocean regions. Such assessment and forecasting will become a reality, however, when valid methods are developed to acquire the necessary input data from large scale numerical models. One such procedure, developed by Gjessing and Moene (1967), has been found to yield good results in determining whether the region from the surface to the 850 mb level is characterized by anomalous or normal propagation.

The Gjessing and Moene procedure uses an 850 mb parameter to forecast anomalous propagation over oceanic regions. The parameter is an indication of dry air aloft (at the 850 mb level) over a moist marine layer. This combination of dry air over moist air typically leads to strong vertical gradients in water vapor, hence anomalous propagation.

The procedure was developed using received signal intensity data to classify days as being characterized by either normal or anomalous propagation. These classified days were then compared to the assessed classification based on the 850 mb parameter. Both an L-band radar and a 1 GHz radio band were used to examine the correlation between received signal intensity and the 850 mb parameter.

2. REVIEW OF GJESSING AND MOENE (1967) PROCEDURE

Gjessing and Moene related a parameter determined from 850 mb data, referred to here as ΔN, to microwave propagation in the lower troposphere. They measured signal intensity at the ground level by positioning remote signal recorders beyond the normal radar horizon. The signal intensity recordings were used to classify days as exhibiting either normal or anomalous propagation. These event days were then related to the ΔN parameter, defined as

$$\Delta N = Nw(Ta) - Nw(Td),$$

where

$Nw(T) = Be(T)/T^2$

Ta = air temperature

Td = dew point

$B = 3.8 \times 10^5$ and

e = water vapor pressure.

These points are illustrated in Fig. 1.

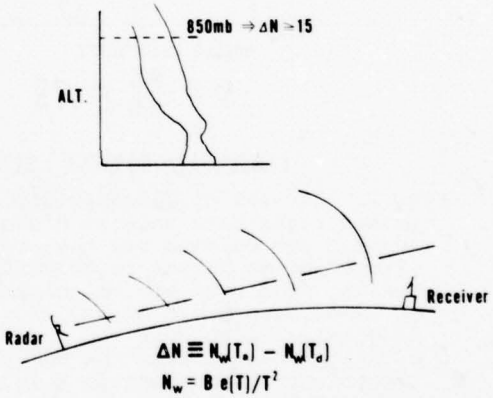

Fig. 1. Gjessing and Moene (1967) related ΔN to received signal intensity. The definition of ΔN uses the wet term of the N equation which relates ΔN to the dryness of the air at 850 mb. A signal receiver was placed beyond the normal radar horizon and was used to classify days as normal or anomalous propagation. The value of ΔN was then correlated to the classification of propagation.

The value of ΔN is linearly related to vapor pressure depression

$$\Delta e = e(T) - e\ (Td)\ .$$

Therefore ΔN is simply a measure of the dryness of the air at 850 mb. Dry air at 850 mb over oceanic regions implies a strong marine inversion and an accompanying anomalous propagation.

The results of the L-band radar data analysis are presented in the form of a contingency table in Fig. 2. The columns are observed days, classified as either anomalous propagation (AP) or normal. The rows are the assessed (calculated) classifications which use $\Delta N \geq 15$ to indicate AP and $\Delta N < 15$ as indicating normal propagation. Fig. 2 shows that of the 134 days assessed as AP, 118 were observed to be so. The diagonals are the correctly assessed days: the off-diagonals are the incorrect assessments. The total ratio correctly assessed is simply the sum of the diagonals divided by the total (443).

OBSERVED

CALCULATED ($\Delta N \geq 15$)	ANOMALOUS PROPAGATION	NORMAL	TOTAL
ANOMALOUS PROPAGATION	118	16	134
NORMAL	24	285	309
TOTAL	143	301	443

Heidke Skill Score

$$S = \frac{R \cdot C}{T \cdot C} = .79$$

PERCENTAGE CORRECT - 91%

Fig. 2. Results of Gjessing and Moene L-band radar data showing high skill score. The columns are the observed days classified as normal or anomalous propagation. The rows are the classification of those days based on the ΔN value. The diagonal elements are the correct number of days assessed from the ΔN parameter; the percentage correct is a relatively high value of 91%.

The Heidke skill score (Panofsky and Brier, 1958) was used to compare the procedure to a standard. The expression for the skill score involves a quantity C, which is the sum of the expected values of the diagonal elements. This sum has traditionally been determined by taking the marginal distributions to compute the probability of an event being on the diagonal. For example, the expected value, based on chance, for the L-band radar data is simply the probability of an event being assessed as AP and observed as AP, plus the probability of the event being assessed and observed as normal, times the total number of events. To demonstrate, the table derived from Fig. 2 would appear as:

		Observed AP	Observed N	Total
Calculated	AP	a_{11}	a_{12}	134
	N	a_{21}	a_{22}	309
Total		143	301	443

Then if the a_{ij}'s are the expected values based on the observed and assessed distributions,

$$C = a_{11} + a_{22}$$
$$= \left(\frac{134}{443}\right)\left(\frac{143}{443}\right) + \left(\frac{309}{443}\right)\left(\frac{301}{443}\right) \quad 443$$
$$= 253.2 \quad .$$

Thus

$$S = \frac{403-253}{443-253} = .79 \quad .$$

Notice that since the observed distribution is used in the computation of C, climatology enters into the chance skill score. Therefore, it is not surprising that computation of the climatological skill score relative to chance shows virtually zero skill. In a real sense then, at least for a dichotomous variable, skill relative to chance also implies relative to climatology.

The range of the skill score is -1 to +1; zero implying no skill, -1 meaning perfect negative skill. To get a feeling for how good a skill score of .79 is, compare the score to scores of normal weather forecasts of precipitation which fall in the 0.5 to 0.6 range (Pierce, 1976).

3. STUDY OBJECTIVE

The apparent skill of the Gjessing and Moene procedure encourages examination to determine

a. the skill of the procedure in another ocean region;

b. independently, the critical value of ΔN; and

c. if the procedure has better skill in some limited region in the vertical.

It was decided to evaluate the procedure in a region noted for frequent AP and from which good radiosonde data were available. Such a region was found in the Eastern Pacific off the west coast of the United States; here, radar picket ships had been on station for about six years and had launched radiosondes twice daily. More than 1,500 soundings were analyzed to cover a region bounded by 34°N, 40°N, 127°W, and 135°W.

4. ANALYSIS

Ideally, received signal data should

be correlated to the ΔN at 850 mb; however, this requires extensive field measurements and years of effort. It was decided to evaluate the refractive structure using radiosonde data, and using the same data to calculate the 850 mb value of ΔN. The method of analysis was first to chose arbitrarily a ΔNc value, then calculate ΔN at 850 mb. If ΔN ≥ ΔNc, the a priori assessment was AP; otherwise, it was assessed as normal. In the region of assessment, the refracting structure was determined and classified as normal, superrefractive and/or ducting. Then a contingency table was generated and a skill score was calculated. The process was then iterated on ΔNc by increasing ΔNc by 2 N units, and repeated until a peak in the value of S was noted; the value of ΔNc was then defined as the optimum ΔNc. Fig. 3 illustrates the analysis procedure.

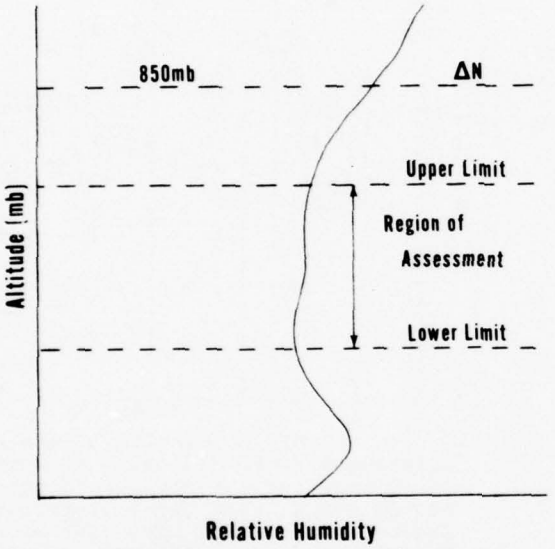

Fig. 3. Procedure for generating 2x2 contingency tables to evaluate the critical value of ΔN using radiosonde data. For each sounding, the value of ΔN (at the 850 mb level) is calculated and the refractive structure in the region of assessment is determined. The skill score is then calculated based on an arbitrary starting value of ΔNc. The procedure is then iterated on ΔNc + 2 and the iteration continues until a maximum in the skill score is obtained.

The seven regions of assessment are separated into two groups: pressure surface limits, and constant thicknesses (Fig. 4). The regions have a maximum upper limit of the 850 mb level, since this is the level of ΔN determination. Limiting the region at a lower level than 850 mb examines the effect of the refractive structure nearest the level of the predictor; limiting the bottom of the region at some level above the surface examines its surface-based AP assessment skill. The constant thickness regions are included to determine if the procedure has improved skill when assessing a region which is independent of surface pressure.

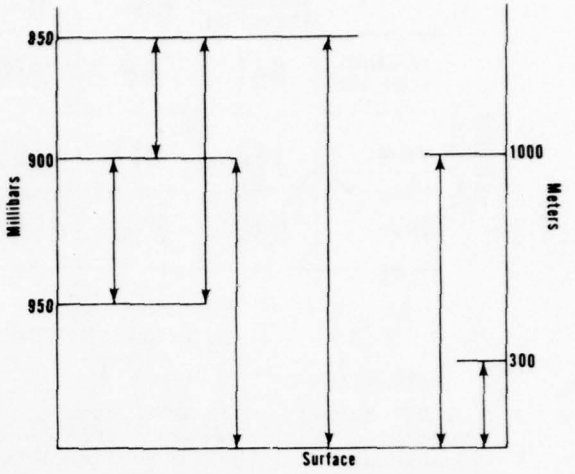

Fig. 4. The regions of assessment were bounded by upper and lower limits, giving a total of seven regions. The regions of assessment were chosen to establish the region of greatest skill. The partial regions (850 mb to 900 mb, 900 mb to 950 mb and 900 mb to the surface) evaluate the assumption that elevated refractive structure resided in some preferred region.

5. RESULTS

For each assessment region an optimum ΔNc was found, its contingency table was generated and a skill score (relative to chance) was calculated. An example of the resulting tables is shown in Fig. 5 for the region 850 mb to the surface. This region shows good skill (S=.67) and also shows considerable advantage over simple climatology (84% versus 67%). Note that the optimum ΔNc is only 3 N units greater than the Gjessing and Moene value of 15 N.

The summary of the skills and optimum ΔNc for ducting or superrefraction are given in Fig. 6. The region of greatest apparent skill is 850 mb to 950 mb, with the 850 mb-to-surface region a close second. Notice that these two are well above the others in skill, but below that of Gjessing and Moene. There seem to be two factors which would account for these differences. The radiosonde is notoriously misleading for near-surface data, so elimination of this region's data improves the skill; the very low skill of the 300 m-to-surface region supports this point. Secondly, the procedure itself is designed to evaluate AP associated with marine inversion phenomena and hence any skill at regions close to the surface would be coincidental.

The other three pressure-surface-limited regions show similar skills. This implies that no real preference exists for any of the three regions, hence no altitude resolution is indicated.

OBSERVED

CALCULATED ($\Delta N > \Delta N_c$)	ANOMALOUS PROPAGATION	NORMAL	TOTAL
ANOMALOUS PROPAGATION	841	89	930
NORMAL	148	447	595
TOTAL	989	536	1525

ΔN_c = 18 REGION: 850 TO SURFACE

S = .67 DUCTING/SUPERREFRACTION

CORRECT · 84% CLIMATOLOGY · 67%

Fig. 5. Example of a contingency table generated in this study. This contingency table is for the region from the 850 mb level to the surface, and includes both ducting and superrefraction as types of anomalous propagation. The skill score, critical ΔN and assessment region are nearly the identical to those of Gjessing and Moene's study.

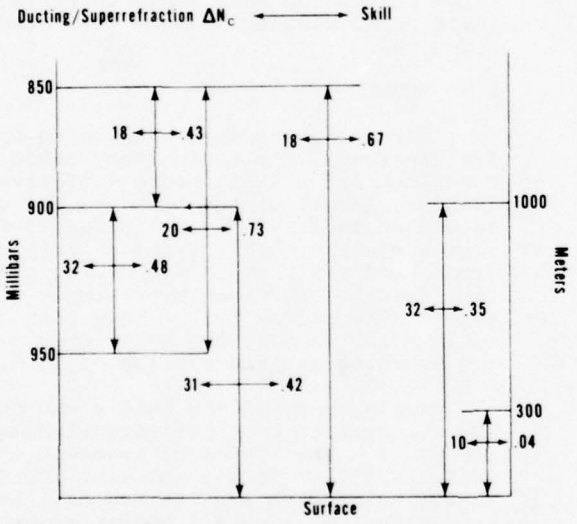

Fig. 6. Summary of the results of the seven assessment regions showing the critical ΔNc values and the corresponding skill scores for ducting/superrefraction. The highest skill score is for the 850 mb-to-950 mb region, since the region near the surface where the radiosonde does a poor job in determining refractive structure has been deleted. The 300 m-to-surface region shows virtually no skill over climatology.

The values of optimum ΔNc vary little for the upper limit of the 850 mb level. For the 900 mb upper limit, much larger ΔNc values result. This is reasonable since this optimum ΔNc must be best at assessing AP some distance below its level; therefore, considerably drier air at 850 mb is needed to indicate a strong gradient some distance below.

Examination of the results for ducting only (Fig. 7) shows that the 850 mb-to-surface region has the highest skill; note that the 900 mb-to-surface region has almost identical numbers, both in skill and in ΔNc. This implies that the top of the marine inversion in this area is normally found at or below the 900 mb level, since this is the most likely region for ducting conditions. The generally higher optimum values of ΔNc (see Fig. 8) reflect the fact that for ducts alone, drier air aloft at 850 mb is needed to skillfully predict such AP.

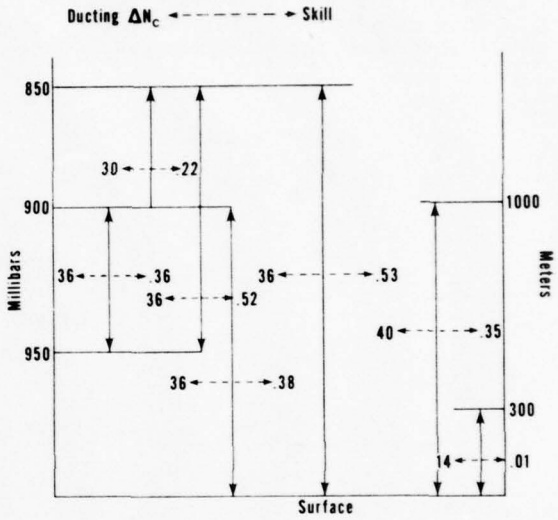

Fig. 7. Summary of results of the seven assessment regions showing the critical ΔNc values and the corresponding skill scores for ducting. The highest two regions are the 850 mb-to-950 mb regions. The region of 300 m to the surface shows virtually no skill over climatology.

6. SUMMARY

The Gjessing and Moene procedure shows definite skill over chance and climatology and is comparable (slightly better) to operational weather forecasts. The assessment skill of the ΔN procedure is better for elevated anomalous propagation than for surface conditions. It has no apparent skill for altitude resolution. The optimum value of ΔNc is a function of the type of AP: ducting alone, or ducting and/or superrefraction.

7. FUTURE TASKS

Two primary tasks should be accomplished to implement this procedure and generate operational analyses and forecasts of anomalous microwave propagation from numerical model fields. First, in the EASTPAC region and using the optimum ΔNc found in this work, contingency tables and skill scores should be generated using an independent data set and compared to the

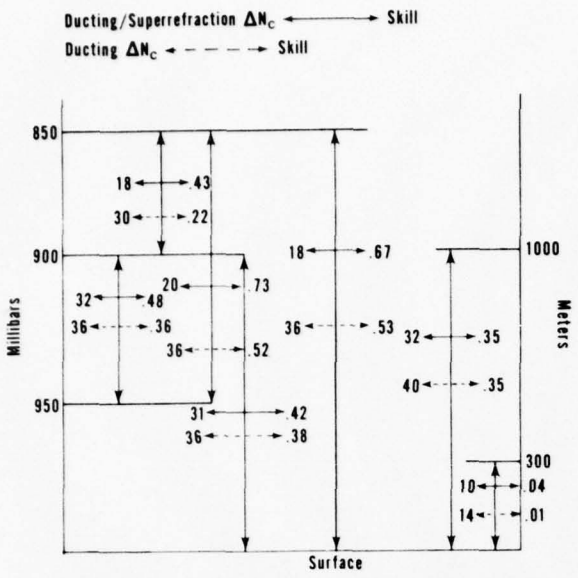

Fig. 8. Summary of results for the seven regions of assessment comparing ducting to ducting/superrefraction. The ΔNc values for ducts alone are almost twice as large as those values for ducting/superrefraction for those regions whose upper limit is the 850 mb level. Regions of assessment whose upper limits are 400 mb (or 1000 m) show less change in ΔNc between the two types of anomalous propagation.

results of this study. Second, other oceanic regions should be examined for skill and optimum ΔNc.

The procedure could also be improved by refinement by season of the regional ΔNc's wherever reliable data exists. The ΔN (850) parameter could be combined with other synoptic scale parameters such as surface pressure. In doing so, perhaps some skill in general altitude resolution, as well as improvement in overall skill, could be attained.

REFERENCES

Gjessing, D., and A. Moene, 1967: On the influence of the meteorological conditions on the radiation properties of long range radars and on the field strength from a distant radio transmitter. Norwegian Defense Research Establishment, Int. Rep. E-112.

Panofsky, H., and G. Brier, 1958: Some applications of statistics to meteorology. Pennsylvania State University, 200 pp.

Pierce, C., 1976: Are weather forecasts improving?. Weatherwise, June 1976.

DIAGNOSIS OF ELEVATED DUCTS BY MEANS OF EQUIVALENT ALTITUDE

Roger A. Helvey

Pacific Missile Test Center

Point Mugu, California

1. INTRODUCTION

An elevated duct is often found in the lower atmosphere over much of the world's ocean surface, associated with an extensive and persistent subsidence inversion separating a relatively cool and moist marine layer from an overlying warmer and drier air mass. This situation is particularly prevalent in temperate latitudes, in connection with the tradewind inversion. The topography and other characteristics of the elevated duct and inversion affect determination of environmental effects on performance of Fleet surveillance, communications, and weapons systems. Because direct measurements of atmospheric properties aloft are so scarce over the open ocean, indirect techniques are often necessary for estimation of these characteristics. In this report a description and preliminary evaluation of an objective method for inferring probability and altitude of occurrence of elevated ducts is presented. The method applies the hydrostatic relationship to data from two reference levels to estimate the altitude of an intervening inversion layer by calculating a parameter, "Equivalent-Altitude", determined from standard-level meteorological analyses. This height index and another parameter indicating overall stability of the atmospheric layer of interest are easily computed from numerical analyses of meteorological fields in the form of grid point data. Together they permit estimation of duct occurrence and altitude with a potentially substantial improvement in accuracy over climatology, although limitations to application of the method exist which are not yet completely explored.

2. THE EQUIVALENT-ALTITUDE TECHNIQUE

The pressure at some level in the atmosphere can be regarded as the sum of the pressure at some higher altitude plus the weight of the intervening atmosphere. Because density is inversely proportional to temperature, an increase (decrease) in mean temperature of the intervening layer will tend to produce a corresponding decrease (increase) in pressure at the lower level. When an inversion is present between the two levels, changes in the altitude of the inversion will have a direct effect on the mean temperature of the layer, and thus on the difference in pressure between the two levels. For example, if the upper pressure is constant, and if the upper and lower temperatures are also constant, an increase in altitude of the inversion will result in a decrease in the mean temperature of the whole layer, and cause an increase in pressure at the lower level. This suggests a method by which altitude of an inversion (and accompanying elevated duct) may be estimated at some location where sounding data is unavailable, given only data from two reference levels, one above and one below the altitude region of interest.

A typical temperature profile through an inversion in the lower atmosphere (such as found in trade-wind areas) is shown in Figure 1 as a solid line. A relatively cool marine layer with approximately adiabatic lapse rate occurs at the base of the inversion. An abrupt change in lapse rate occurs at the base of the inversion, followed by a more gradual change to more nearly adiabatic lapse rates again at higher altitudes. A rough but useful two-layer approximation of the temperature structure of the lower atmosphere in such a situation is shown by the dashed line, with constant potential temperature (adiabatic lapse rates) assumed in both the lower and upper layers, equal to actual potential temperatures at the lower and upper levels, respectively. The altitude of the model interface can be determined so that actual and model pressures are in agreement, giving an "Equivalent-Altitude" which, we will demonstrate later, can be empirically related to the altitude of the inversion (and duct) in the real atmosphere.

The difference in potential temperature between the upper and lower layers provides an index of the maximum possible strength of the intervening inversion, and also the likelihood of occurrence and strength of the associated duct. In addition, this "Strength Index" determines the sensitivity of changes in the interface altitude to changes in pressure/height at the reference levels, and vice versa. It should be apparent that both likelihood and strength of inversions and their associated ducts will tend to increase as the Strength Index increases, whereas as this index approaches zero, near-adiabatic conditions and lack of inversions will prevail throughout the entire altitude range between the two reference levels, in which case elevated ducts will be very unlikely in that same region.

Derivation of an expression for Equivalent-Altitude is shown in Figure 1. Note that if relative humidity at the reference levels is not available, then potential temperature can be used instead of virtual potential temperature, although with some decrease in accuracy in calculated values of Equivalent-Altitude.

EQUIVALENT – ALTITUDE

FROM THE HYDROSTATIC EQUATION, WE HAVE:

$$Z_2 - Z_1 = k \int_1^2 T^* d(\ln p) \qquad (1)$$

WHERE

$Z_2 \equiv$ ALTITUDE OF UPPER REFERENCE LEVEL

$Z_1 \equiv$ ALTITUDE OF LOWER REFERENCE LEVEL

$k \equiv 96.09494$ (FOR p IN MB, Z IN FT., T^* IN DEG. K)

$T^* \equiv$ VIRTUAL TEMPERATURE

$p \equiv$ PRESSURE

FROM THE DEFINITION OF POTENTIAL TEMPERATURE:

$$T^* = \theta^* \left(\frac{p}{1000}\right)^{\kappa} \qquad (2)$$

WHERE

$\theta^* \equiv$ VIRTUAL POTENTIAL TEMPERATURE

$\kappa \equiv R/C_p \quad 0.286$

SUBSTITUTING (2) IN (1), HOLDING θ^* CONSTANT, AND INTEGRATING:

$$Z_2 - Z_1 = C\theta^*(p_1^{\kappa} - p_2^{\kappa}) \qquad (3)$$

WHERE

$$C \equiv \frac{k}{\kappa \cdot 1000^{\kappa}}$$

NOTING THAT PRESSURES FOR BOTH LAYERS ARE IDENTICAL AT THE INTERFACE, FOR THE UPPER LAYER WE WRITE:

$$Z_i - Z_t = C\theta_t^*(P_i - P_t) \qquad (4)$$

AND FOR THE LOWER LAYER:

$$Z_i - Z_b = C\theta_b^*(P_b - P_i) \qquad (5)$$

WHERE $Z_i \equiv$ ALTITUDE OF INTERFACE

$Z_t \equiv$ ALTITUDE OF TOP OF UPPER LAYER (UPPER REFERENCE LEVEL)

$Z_b \equiv$ ALTITUDE OF BOTTOM OF LOWER LAYER (LOWER REFERENCE LEVEL)

$\theta_t^* \equiv$ VIRTUAL POTENTIAL TEMPERATURE IN UPPER LAYER

$\theta_b^* \equiv$ VIRTUAL POTENTIAL TEMPERATURE IN LOWER LAYER

$P_i \equiv p_i^{\kappa}$, κ TH POWER OF PRESSURE AT INTERFACE

$P_t \equiv p_t^{\kappa}$, κ TH POWER OF PRESSURE AT TOP OF UPPER LAYER

$P_b \equiv p_b^{\kappa}$, κ TH POWER OF PRESSURE AT BOTTOM OF LOWER LAYER

BY ELIMINATING P_i BETWEEN (4) AND (5) WE OBTAIN AN EXPRESSION FOR THE INTERFACE ALTITUDE IN TERMS OF VALUES OF TEMPERATURE AND PRESSURE AT THE TWO REFERENCE LEVELS:

$$Z_i = \frac{C\theta_b^*\theta_t^*(P_b - P_t) + Z_b\theta_t^* - Z_t\theta_b^*}{\theta_t^* - \theta_b^*} \qquad (6)$$

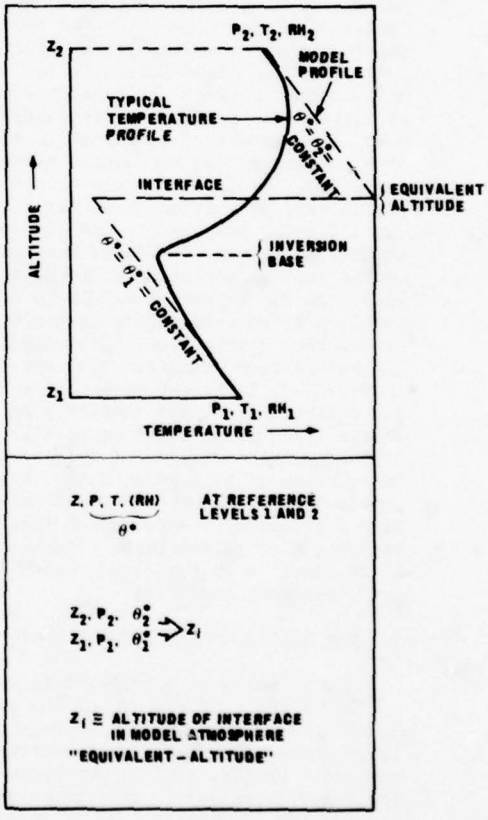

Figure 1. Derivation of Equivalent-Altitude

3. APPLICATION OF TECHNIQUE

Application of the Equivalent-Altitude technique depends on two factors: (1) availability of pressure, height, temperature, and relative humidity (optional) data at reference levels above and below the altitude range of interest; and (2) a knowledge of the relationship between the calculated Equivalent-Altitude and Strength-Index parameters, and actual inversion/duct behavior. The reference data required for operational calculation of these parameters can be obtained from numerical analyses of meteorological fields at two standard levels, while the relationship between actual duct or inversion likelihood and altitude and the Equivalent-Altitude parameters can be empirically ascertained by using radiosonde data. It can be anticipated that this relationship will vary somewhat with geographical location and season, because of systematic differences in temperature and refractive profiles with these factors. Thus, the relationship must be evaluated for a number of widely separated locations. Ideally for this purpose one would calculate the Equivalent-Altitude parameters for a given site from the numerical analyses of the required fields, but computer processing of the numerical data (in the form of large arrays of values at grid points) is relatively cumbersome, and necessarily limited with respect to the number of individual cases included because of the massive amount of data involved. Thus, it is advantageous to compute the Equivalent-Altitude parameters on the basis of reference level data from the same soundings used to determine duct presence and altitude. Results will be presented in this report using both sources of reference level data.

4. RADIOSONDE EQUIVALENT-ALTITUDES

Point Mugu Data. Radiosonde data from two different sources have been examined in terms of Equivalent-Altitude/Duct relationships. The first set of data is from Point Mugu (NTD) for the period January 1967 through December 1976, comprising a total of 7025 soundings. An Equivalent-Altitude and Strength Index were computed for each sounding using the surface as the lower reference level, and either 850 or 700 mb as the upper reference level. The presence and altitude coverage of ducts between the surface and the upper reference level was noted. (Because of a spurious bias in surface-based ducts due to temperature-induced radiosonde humidity errors, ducts due to apparent trapping gradients appearing solely in the surface layer of a sounding were not counted.) The soundings were categorized according to Strength Index, and relative frequencies (in percent) of duct occurrence were computed at a number of altitude levels, for a number of Equivalent-Altitude categories. The results are presented as tabulations of these relative frequencies for each Strength Index category, by altitude and Equivalent-Altitude. Results for the total set of Point Mugu soundings are shown in the upper half of Table 1, where 850 mb was used as the upper reference level. Altitude is the vertical coordinate or rows in all of these tabulations. In this case data are given at 250-foot intervals from the surface up to 6,000 feet. Equivalent-Altitude is the horizontal coordinate or columns in these tabulations. In this case each column represents a separate 250-foot thick category, increasing from left to right: the leftmost column gives data for soundings with Equivalent-Altitudes of 0 to 250 feet, the next 250 to 500 feet, and so on up to 6,000 to 6,250 feet. The far right column gives relative frequencies of ducts without respect to Equivalent-Altitude, and thus indicates duct coverage with altitude according to climatology. Note that the individual frequencies in general do not add to 100% in each column; this is because a duct is often thick enough to cover more than one 250-foot altitude interval, and more than one duct may occur in any sounding. Total duct relative frequency of occurrence (of at least one duct) without respect to altitude is given at the lower left.

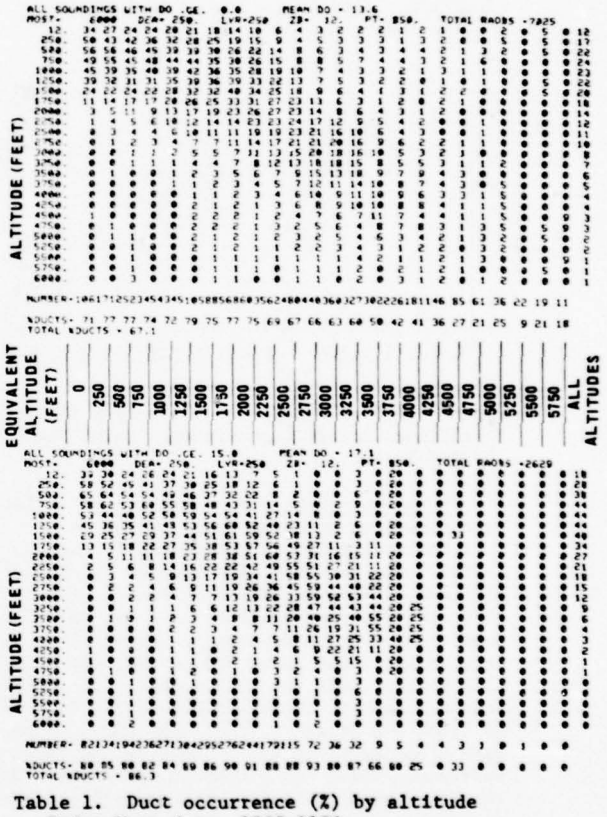

Table 1. Duct occurrence (%) by altitude
Point Mugu data, 1967-1976.
Upper: All data
Lower: Strength Index ≥15C

It is apparent that the altitude of maximum duct probability lies near 750-1,000 feet according to climatology, with a maximum occurrence of about 25% at that level, but with an overall occurrence of about 67%. A strong association between Equivalent-Altitude and actual duct altitude is readily apparent, and although the frequencies are not large, consideration of Equivalent-Altitude clearly results in a substantial improvement over climatological frequencies.

A considerable improvement in specification of duct altitude and occurrence results from

consideration of the Strength Index. Statistics for all cases with potential temperature difference of at least +15 deg C between 850 mb and the surface are shown in the lower half of Table 1. For these soundings the frequency of duct occurrence at specific altitudes becomes greater than 50% when Equivalent-Altitude is considered, and overall duct expectancy rises to about 86%.

A more detailed breakdown of the joint effects of Equivalent-Altitude and Strength Index on duct occurrence (without regard to altitude) is displayed in Figure 2. The upper reference level was at 700 mb. A high expectancy of duct occurrence is indicated when Equivalent-Altitude is low and vice versa, while a general increase in duct occurrence is associated with larger Strength Index. Depending on values of these two parameters, expected duct occurrence could range from frequencies exceeding 80% or 90%, to less than 20%.

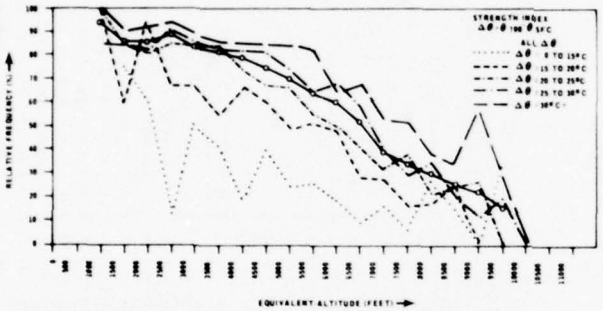

Figure 2. Duct occurrence (%) versus Equivalent-Altitude and Strength Index. Point Mugu data, 1967-1976.

Picket Ship Data. A second set of radiosonde data, provided by Wayne Sweet of the Naval Environmental Prediction Research Facility (NEPRF), was examined with respect to Equivalent-Altitude effects on duct occurrence. The picket ship data provided consists of a set of 6,090 soundings obtained during the period 1956-1965, between latitudes about 35N to 50N, and longitudes 125W to 135W, off the west coast of the United States. As with the Point Mugu data, Equivalent-Altitude and Strength Index were computed for each sounding using the surface as the lower reference level, and 850 mb as the upper. In the upper half of Table 2 the overall frequency of duct occurrence for these data is given at less than 27%, and the frequencies noted at individual altitudes for the various Equivalent-Altitude categories are correspondingly small, but the correlation between actual duct altitude and Equivalent-Altitude is still apparent. When we consider only soundings where the Strength Index was at least 15 C, shown in the lower half of Table 2, this relationship becomes much more distinct, and the overall duct occurrence increases to almost 56%. A marked difference in duct occurrence with latitude is shown by the next two Tables. In the upper half of Table 3 only data north of latitude 41 degrees has been included. The overall duct occurrence drops to about 19%, and Equivalent-Altitude does not appear to provide as good an indication of duct altitude. In the lower half of Table 3 only data south of 36N latitude is included. The overall duct occurrence is almost 43%, and there is a commensurate improvement in the dependence of duct altitude on Equivalent-Altitude.

DUCT OCCURRENCE (%) BY ALTITUDE
PICKET SHIP 1956-1965 RADB EQUIVALENT ALTITUDES
UPPER REFERENCE LEVEL AT 850mb

$\nabla\theta \geq 0°C$

NEPRF PICKET SHIP DATA
DO .GE. 0. MEAN DO = 10.50
MOST= 6000 DEA= 250. LVD=250 ZD= 0. PT= 850. TOTAL RADBS =6090

ALTITUDE (FEET)

	0	250	500	750	1000	1250	1500	1750	2000	2250	2500	2750	3000	3250	3500	3750	4000	4250	4500	4750	5000	5250	5500	5750	6000
NUMBER =	22	17	29	41	70	100	150	218	288	410	462	556	515	598	648	562	815	665	1035	819	592	157	67	16	5	2	1
%DUCTS =	22	11	31	24	29	24	30	29	29	30	33	30	31	29	26	24	29	18	13	28	37	40	0	0	0	0	0

TOTAL %DUCTS = 26.9
PAUSE

EQUIVALENT ALTITUDE (FEET)

$\nabla\theta \geq 15°C$

NEPRF PICKET SHIP DATA
DO .GE. 15. MEAN DO = 15.00
MOST= 6000 DEA= 250. LVD=250 ZD= 0. PT= 850. TOTAL RADBS = 659

ALTITUDE (FEET)

	0	250	500	750	1000	1250	1500	1750	2000	2250	2500	2750	3000	3250	3500	3750	4000	4250	4500	4750	5000	5250	5500	5750	6000
NUMBER =	0	0	4	1	8	17	31	38	54	77	64	79	57	61	61	38	31	19	14	4	0	0	0	0	0
%DUCTS =	0	0	50	100	75	58	64	68	61	61	67	55	58	52	58	42	32	31	35	25	0	0	0	0	0

TOTAL %DUCTS = 55.8
PAUSE

EQUIVALENT ALTITUDE (FEET)

Table 2. Duct occurrence (%) by altitude.
Picket Ship data, 1956-1965.
Upper: All data
Lower: Strength Index ≥15C

5. GRID EQUIVALENT-ALTITUDES

Although the use of reference level data from actual soundings to compute Equivalent-Altitudes and Strength Indexes is valuable for determining the basic nature of the effect of these parameters on duct occurrence and altitude, for operational applications the soundings are presumed to be unavailable. The basic premise of this effort is that significant information on probable duct behavior can be established using reference data from numerical analyses (or forecasts) of meteorological fields. Thus, a set of such fields for the year 1974 was obtained from Fleet Numerical Weather Central (FNWC), in the form of arrays of values for a 63 x 63 grid over the Northern Hemisphere. This considerable amount of data was processed on the Pacific Missile Test Center (PACMISTESTCEN) CYBER 175 computer to obtain values of Equivalent-Altitude and Strength Index over the entire array or at particular grid points as required.

DUCT OCCURRENCE (%) BY ALTITUDE
PICKET SHIP 1956–1965 RADB EQUIVALENT ALTITUDES
UPPER REFERENCE LEVEL AT 850mb
LATITUDE > 41°N

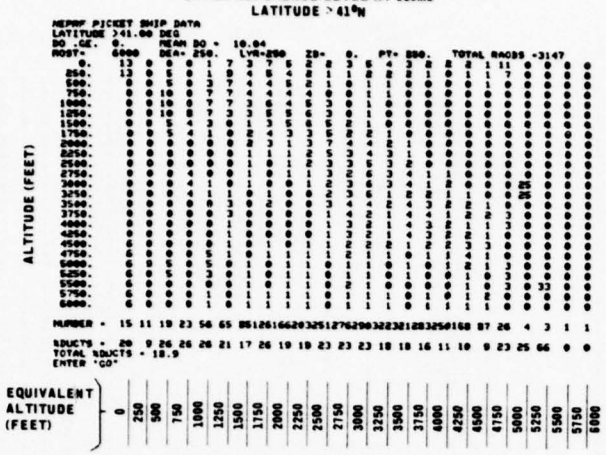

LATITUDE < 36°N

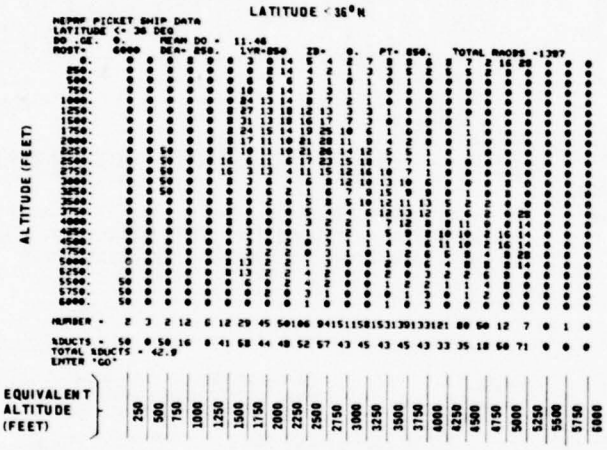

Table 3. Duct occurrence (%) by altitude. Picket Ship data, 1956-1965.
Upper: North of 41°N
Lower: South of 36°N

The year 1974 was chosen because of the availability of soundings at PACMISTESTCEN for January, April, July, and October of that year for a number of radiosonde stations in the Northern Hemisphere. These stations had been selected for the Refractive Effects Guidebook (REG) work unit in an attempt to obtain refractive information representative of oceanic regions around the globe. There are 14 of these stations in the Northern Hemisphere in all: Ship 4YN ("NAN"), Ship 4YH, Midway, Adak, Pt. Barrow, Ponape, Yap, Clark AFB, Thule, Keflavik, Bermuda, Balboa, Barbados, and Terceira. Their positions are shown in Figure 3, together with the 63 x 63 FNWC grid. For Ships 4YN and 4YH only data for January and a part of April were available.

Upon compilation of tables of duct occurrence versus Equivalent-Altitude and Strength Index, it was noted that at most tropical and polar sites duct occurrences were apparently either too infrequent or relationship with Equivalent-Altitude too weak to merit application of the technique. But the temperate-

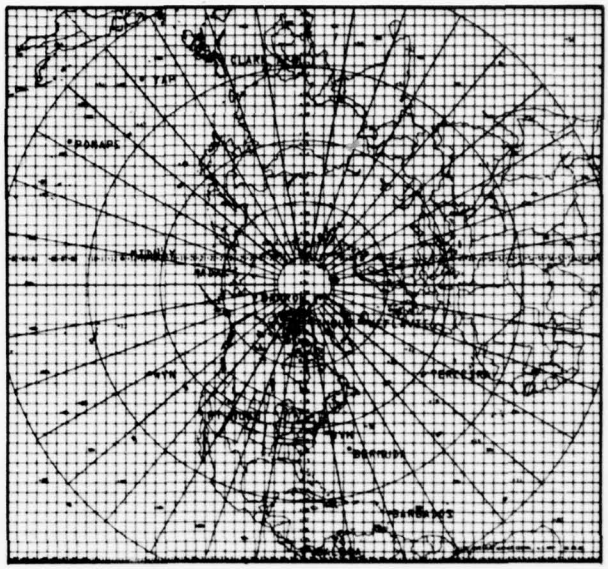

Figure 3. FNWC 63x63 grid, and locations of radiosonde stations for 1974 data base.

latitude stations did yield favorable results, as represented in Tables 4-8 for 4YN, Midway, 4YH, Bermuda, and Terceira. In these Tables only soundings for a Strength Index of at least 15 deg C were included, with the upper reference level at 700 mb. The overall duct occurrence for each station without considering Strength Index (not shown) for the four months of 1974 used was 60% for 4YN, 28% for Midway, 42% for 4YH, 50% for Bermuda, and 42% for Terceira. The overall frequencies for each station generally increased substantially with Strength Index, as given in the Tables, with an improvement of over 30% at Bermuda. Although sample sizes were not large, the association between duct altitude and Equivalent-Altitude is generally evident for each of these sites. The joint effect of Equivalent-Altitude and Strength Index is shown in Figure 4, prepared from a composite of data for all five stations. A great increase in duct occurrences occurs with increasing stability. But here, unlike the situation for Point Mugu (Figure 2) where duct occurrences were greatest for the lowest Equivalent-Altitudes, a distinct maximum occurs for Equivalent-Altitudes near 6,000 feet.

6. SYNOPTIC DISTRIBUTION OF EQUIVALENT-ALTITUDE

If the numerical analyses prove to be sufficiently accurate to permit reasonably reliable computations of Equivalent-Altitude, synoptic maps of the distribution of Equivalent-Altitude and Strength Index can be constructed which should provide valuable information on behavior of the elevated duct in time and space. Examples of such maps are given in Figure 4, for 12Z 3 April 1974, over a portion of the northeastern Pacific. Surface frontal positions and sea-level isobars are drawn in the conventional analysis in Figure 4a. Fields of Equivalent-Altitude in Figure 4b, and Strength Index in Figure 4c seem reasonably smooth and spatially coherent, without wild

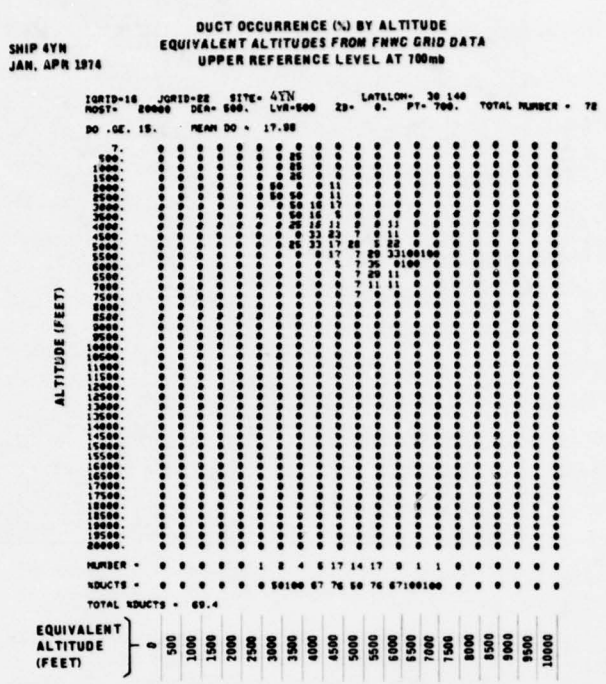

Table 4. Ship 4YN duct occurrence (%) by altitude. Equivalent-Altitude from FNWC grid data. Upper reference level at 700 mb. Strength Index ≥ 15C

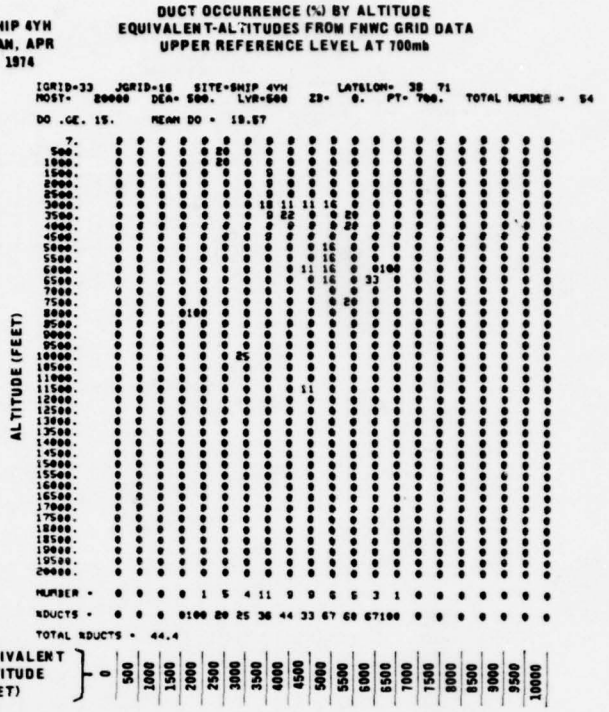

Table 6. Ship 4YH duct occurrence (%) by altitude. Equivalent-Altitude from FNWC grid data. Upper reference level at 700 mb. Strength Index ≥ 15C

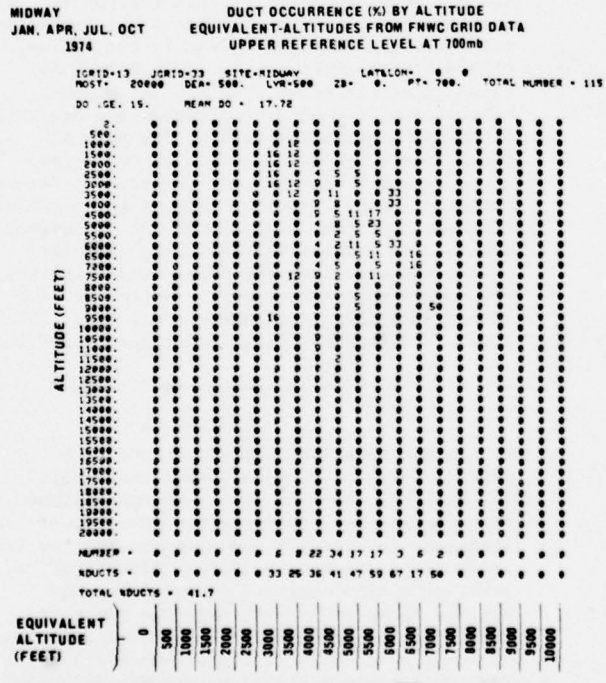

Table 5. Midway duct occurrence (%) by altitude. Equivalent-Altitude from FNWC grid data. Upper reference level at 700 mb. Strength Index ≥ 15C

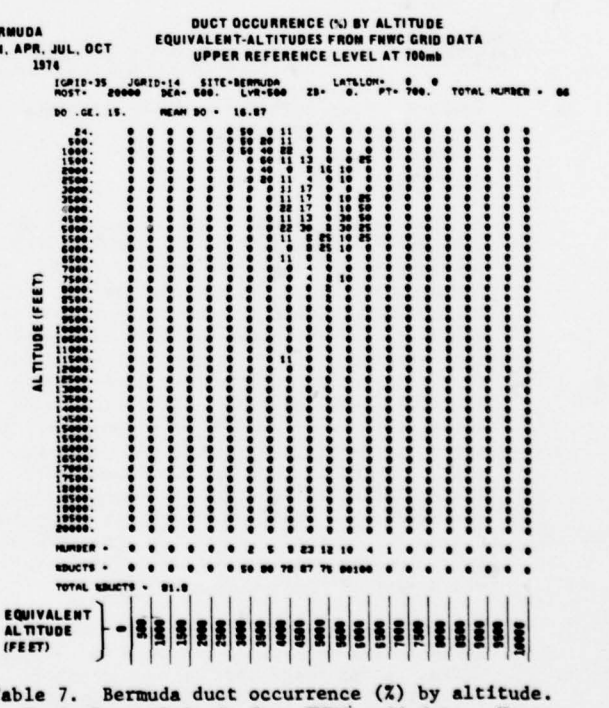

Table 7. Bermuda duct occurrence (%) by altitude. Equivalent-Altitude from FNWC grid data. Upper reference level at 700 mb. Strength Index ≥ 15C

TERCEIRA
JAN, APR, JUL, OCT
1974

DUCT OCCURRENCE (%) BY ALTITUDE
EQUIVALENT-ALTITUDES FROM FNWC GRID DATA
UPPER REFERENCE LEVEL AT 700mb

IGRID=43 JGRID=22 SITE=TERCEIRA LAT&LON= 0 0
MOST= 20000 DEA= 500. LVR=500 ZB= 0. PT= 700. TOTAL NUMBER = 127

DO .GE. 15. MEAN DO = 17.77

ALTITUDE (FEET)	EQUIVALENT ALTITUDE (FEET) 0	500	1000	1500	2000	2500	3000	3500	4000	4500	5000	5500	6000	6500	7000	7500	8000	8500	9000	9500	10000
111.	0	0	0	0	0	0	0	0	0	0	0	0	0	0	0	0	0	0	0	0	0
500.	0	0	0	0	0	0	0	0	0	0	0	0	0	0	0	0	0	0	0	0	0
1000.	0	0	0	0	0	0	0	0	0	0	0	0	0	0	0	0	0	0	0	0	0
1500.	0	0	0	0	0	0	0	0	5	0	0	0	0	0	0	0	0	0	0	0	0
2000.	0	0	0	0	0	0	0	0	16	0	0	0	0	0	0	0	0	0	0	0	0
2500.	0	0	0	0	0	0	0	0	22	3	3	0	0	0	0	0	0	0	0	0	0
3000.	0	0	0	0	0	0	0	14	5	7	7	0	0	16	0	0	0	0	0	0	0
3500.	0	0	0	0	0	0	0	28	5	14	19	7	0	16	0	0	0100	0	0	0	0
4000.	0	0	0	0	0	0	0	14	5	25	23	11	0	16	0	0	0	0	0	0	0
4500.	0	0	0	0	0	0	0	0	11	25	11	18	9	0	0	0	0	0	0	0	0
5000.	0	0	0	0	0	0	0	0	5	10	11	22	18	0	0	0	0	0	0	0	0
5500.	0	0	0	0	0	0	0	0	0	3	11	14	27	0	0	0	0	0	0	0	0
6000.	0	0	0	0	0	0	0	0	11	0	3	7	9	16	0	0	0	0	0	0	0
6500.	0	0	0	0	0	0	0	0	5	0	0	11	0	0	0	0	0	0	0	0	0
7000.	0	0	0	0	0	0	0	0	0	0	7	3	0	0	0	0	0	0	0	0	0
7500.	0	0	0	0	0	0	0	0	0	0	3	0	0	0	0	0	0	0	0	0	0
8000.	0	0	0	0	0	0	0	0	0	0	0	0	0	16	0	0	0	0	0	0	0
8500.	0	0	0	0	0	0	0	0	0	3	0	0	0	0	0	0	0	0	0	0	0
9000.	0	0	0	0	0	0	0	0	0	0	0	0	0	0	0	0	0	0	0	0	0
9500.	0	0	0	0	0	0	0	0	0	0	0	0	0	0	0	0	0	0	0	0	0
10000.	0	0	0	0	0	0	0	0	0	0	0	0	0	0	0	0	0	0	0	0	0
10500.	0	0	0	0	0	0	0	0	0	0	0	0	0	0	0	0	0	0	0	0	0
11000.	0	0	0	0	0	0	0	0	0	0	0	0	0	0	0	0	0	0	0	0	0
11500.	0	0	0	0	0	0	0	0	0	0	0	0	0	0	0	0	0	0	0	0	0
12000.	0	0	0	0	0	0	0	0	0	0	0	0	0	0	0	0	0	0	0	0	0
12500.	0	0	0	0	0	0	0	0	0	0	0	0	0	0	0	0	0	0	0	0	0
13000.	0	0	0	0	0	0	0	0	0	0	0	0	0	0	0	0	0	0	0	0	0
13500.	0	0	0	0	0	0	0	0	0	0	0	0	0	0	0	0	0	0	0	0	0
14000.	0	0	0	0	0	0	0	0	0	0	0	0	0	0	0	0	0	0	0	0	0
14500.	0	0	0	0	0	0	0	0	0	0	0	0	0	0	0	0	0	0	0	0	0
15000.	0	0	0	0	0	0	0	0	0	0	0	0	0	0	0	0	0	0	0	0	0
15500.	0	0	0	0	0	0	0	0	0	0	0	0	0	0	0	0	0	0	0	0	0
16000.	0	0	0	0	0	0	0	0	0	0	0	0	0	0	0	0	0	0	0	0	0
16500.	0	0	0	0	0	0	0	0	0	0	0	0	0	0	0	0	0	0	0	0	0
17000.	0	0	0	0	0	0	0	0	0	0	0	0	0	0	0	0	0	0	0	0	0
17500.	0	0	0	0	0	0	0	0	0	0	0	0	0	0	0	0	0	0	0	0	0
18000.	0	0	0	0	0	0	0	0	0100	0	0	0	0	0	0	0	0	0	0	0	0
18500.	0	0	0	0	0	0	0	0	0	0	0	0	0	0	0	0	0	0	0	0	0
19000.	0	0	0	0	0	0	0	0	0	0	0	0	0	0	0	0	0	0	0	0	0
19500.	0	0	0	0	0	0	0	0	0	0	0	0	0	0	0	0	0	0	0	0	0
20000.	0	0	0	0	0	0	0	0	0	0	0	0	0	0	0	0	0	0	0	0	0
NUMBER =	0	0	0	0	0	1	1	7	18	28	26	27	11	6	1	0	1	0	0	0	0
%DUCTS =	0	0	0	0	0	0100	0	29	56	57	62	67	64	50	0	0	0100	0	0	0	0

TOTAL %DUCTS = 58.3

Table 8. Terceira duct occurrence (%) by altitude Equivalent-Altitude from FNWC grid data. Upper reference level at 700 mb. Strength Index ≥ 15C

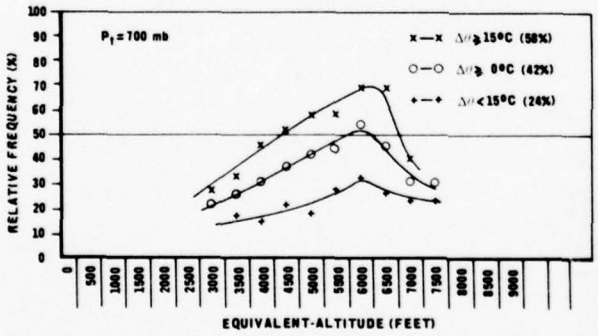

Figure 4. Composite 4YN + Midway + 4YN + Bermuda + Terceira duct occurrence by Equivalent-Altitude and Strength Index.

fluctuations between neighboring grid points which would indicate intolerable sensitivity to small deviations in the input data fields at the two reference levels (surface and 700 mb in this case). For operational use, these fields would be converted and displayed as probability of duct occurrence and expected altitude using empirical relationships established from a study of numerous individual stations.

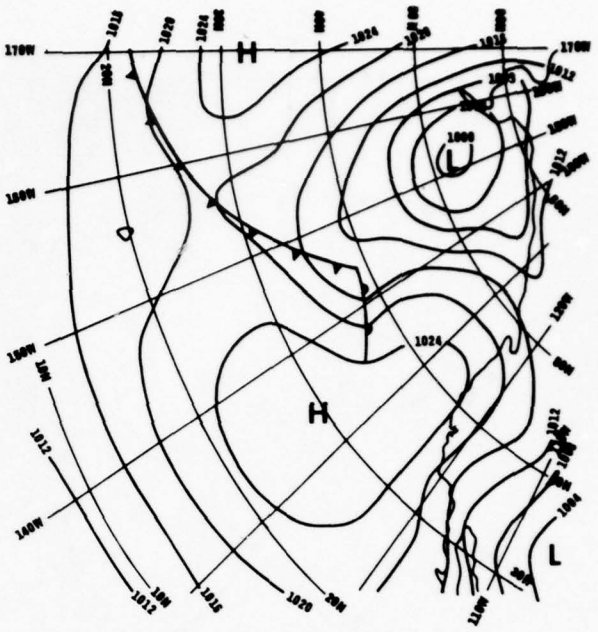

Figure 4a. Surface Chart, 12Z 3 April 1974

7. CONCLUDING REMARKS

From the data presented here, it is apparent that a significant relationship exists at temperate latitude stations between duct occurrence and altitude, and Equivalent-Altitude and Strength Index. This relationship is evident when either the sounding data itself, or data from numerical analyses are used to compute these parameters. The degree of relationship seems to vary geographically in the same manner as the overall frequency of duct occurrence itself, with the best results indicated at Point Mugu and Bermuda of the sites considered. While the frequencies of occurrence are generally rather small with respect to diagnosis or forecasting the presence of an elevated duct at specific altitudes, these frequencies will increase significantly if determined instead for a given altitude range within which frequency of duct occurrence is desired.

Because of scatter in the data, the frequency tabulations given in this report are not presently suitable for practical application. Additional data must be obtained to increase the reliability of the ducting statistics when computed for a number of simultaneous categories of Equivalent-Altitude and Strength Index. Rather than finding duct occurrence for individual altitudes, determination of frequency of occurrence over various altitude ranges may be a preferable mode of presentation for actual use.

Although clearly a relationship is evident, further work is desirable to determine if results can be improved by accounting for effects of additional synoptic-scale parameters. In this regard, while obviously there is an increasing likelihood of an inversion with

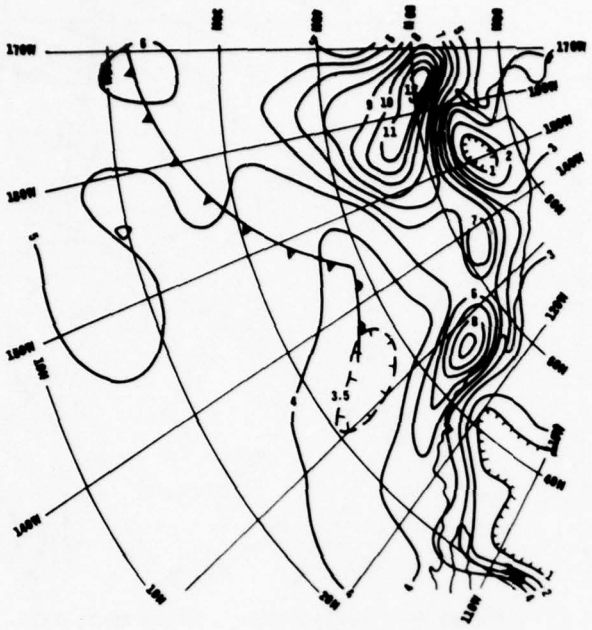

Figure 4b. Map of Equivalent-Altitude (calculated from FNWC numerical analyses at surface and 700 mb) in thousands of feet

increasing overall thermal stability of the region between the two reference levels, this may not always imply a greater probability of elevated duct occurrence. The tacit assumption is that in the presence of an inversion the upper air mass is relatively dry. But in certain weather conditions this may not be the case, as when the inversion is associated with advection of warm but also moist air aloft. These situations may be detectable by consideration of winds at various altitudes, for example.

Additional analyses of the spatial distribution of Equivalent-Altitude and Strength Index will be carried out in conjunction with conventional meteorological analyses to determine if these parameters behave in a systematic and reasonable manner in relationship to accepted synoptic models of air mass structure.

Statistics of distributions of estimated duct occurrrece with location and altitude based on the Equivalent-Altitude technique will be undertaken for a large number of grid point locations, to determine if it can be used to generate a duct climatology for regions where sounding data is sparse or unavailable.

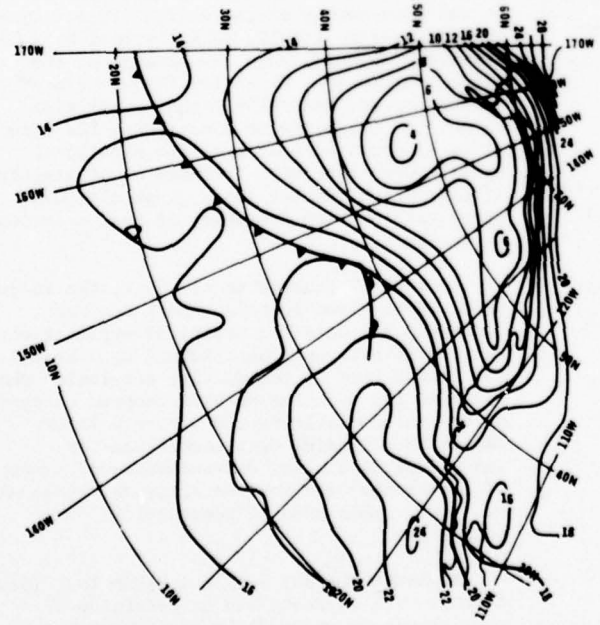

Figure 4c. Map of Strength Index (calculated from FNWC numerical analyses at surface and 700 mb) in degrees C

SOME SYNOPTIC CONSIDERATIONS RELATIVE TO THE REFRACTIVE EFFECTS GUIDEBOOK (REG)

Jay Rosenthal and Roger Helvey

Pacific Missile Test Center

Point Mugu, California

SUMMARY

A Refractive Effects Guidebook (REG) was developed for relating routine synoptic weather information to probable radio-frequency (RF) systems coverage conditions and was used operationally in the Fleet during 1977 and 1978. The REG employed simple procedures for estimating present or future refractive conditions (and hence systems coverage) from information supplied by synoptic charts, transmitted WEAX messages, or direct measurements. While the technique has been found to be procedurally feasible and attractive, objective evaluations of REG performance indicated significant discrepancies in verification, particularly for surface-based ducts. These can be explained by incomplete knowledge of the inter-relationship of synoptic and mesoscale conditions with refractive structure, by overly detailed attempts at profile-type specification, and by significant deficiencies in radiosonde data when used for refractive purposes. As a result of these evaluations and other Fleet recommendations, the physical and meteorological basis for a synoptic-refractivity relationship has been studied and comparisons made with independent sources of climatological statistics. Objective studies have been conducted to develop a statistical basis for relating refractivity conditions to preferred quadrants of synoptic features. Ducting has been found to be most likely over the southeast quadrants of anticyclones and to be positively correlated with sea level pressure and temperature differences between the surface and 700 mb. Other correlation parameters are being investigated. Based on a working model, revised REG charts have been developed for the North Pacific and North Atlantic areas. Modifications to the REG technique have been suggested which allow for a less detailed selection of refractive structure based on profile simplifications and their relationship to representative weather features. The meteorological and operational basis for developing the technique is discussed. Plans for meteorological and operational evaluation of the technique are also discussed.

1. INTRODUCTION

The influence of atmospheric layers in causing radar holes, ducting and other examples of anomalous propagation through the process of refraction has been recognized by Naval operating forces as a major cause of distorted or unexpected radar coverage in the Fleet. A number of specific operational, measurement and meteorological problem areas were discussed in the proceedings of a Navy refractivity conference published by the Naval Weather Service Command (1973). In order to exploit the effects of atmospheric refraction to tactical advantage, an Advisory Committee on Refractive Index Measurement and Forecasting composed of technical and operational representatives from throughout the Navy was formed under the management of the Naval Air Systems Command (AIR-370). A major achievement of this program has been the development by Naval Ocean Systems Center (NOSC) of the Integrated Refractive Effects Prediction System (IREPS), and is described in detail by Hitney and Richter (1976). The IREPS is a shipboard interactive computer system which produces quantitative assessments and graphical depictions of refractive effects on specific sensor systems in near real-time.

Since the atmospheric layers responsible for refractive effects are in turn a reflection of large scale air mass conditions, a requirement exists within the Navy program for a prediction capability which will allow conversion of routine synoptic weather information to an assessment of refractive structure. At the request of Commander, THIRD Fleet an attempt to develop a synoptic refractive prediction capability was initiated by Rosenthal (1976) at the Pacific Missile Test Center (PMTC) with assistance from the Naval Environmental Prediction Research Facility (NEPRF) resulting in the development of the REG.

2. REG DESCRIPTION

2.1 Basic Concepts

The REG was developed through a combined subjective/objective effort based on a study of climatology, the dynamic structure of anticyclones and a year's worth (mid-season months) of world-wide radiosonde data and surface and upper-air charts for 1974 obtained from the National Climatic Center (NCC). Using actual charts, characteristic synoptic patterns were selected for each season for each ocean operating area to serve as representative REG maps. The adiabatic charts for 16 coastal and island radiosonde stations were then studied to derive 11 standard profile types to be designated in different synoptic zones on the REG maps. The basic premise of the REG approach is the assumption that refractive conditions responsible for anomalous propagation and such specific features as radar holes and ducts can be related to the large scale weather patterns portrayed on routine

weather maps such as are available in the Fleet. Using this routine weather information the REG presents guidelines for planning the employment of radar, sensor and communication systems according to existing and predicted refractive conditions that frequently cause anomalous propagation.

The REG procedure was selected for simplicity; to use it effectively it is not necessary to be a weather or refractive expert. Given available weather information, the user merely matches these known or predicted conditions to one of the typical atmospheric cases described in the REG. Examination of the selected case reveals the typical coverage pattern appropriate to the specified conditions. Each case provides a typical refractivity profile and several ray trace diagrams which schematically illustrate the coverage that can be expected at different altitudes between the surface and 20,000 feet. The REG profiles and ray traces were produced on the IREPS systems and are accompanied by brief descriptive notes that interpret the diagrams and indicate the nature of surface-to-surface, surface-to-air, and air-to-air coverage that can be anticipated for each profile case. Hypothetical transmitters were located at altitudes of interest based on the refractivity profile.

2.2 Procedures

The appropriate profile is selected by the REG user according to one of three types of available weather information: (1) message, (2) facsimile chart, or (3) actual measurements.

In the simplest procedure, a WEAX message received aboard ship prescribes by letter the profile to be used.

The second technique requires onboard synoptic weather charts for the ship's area of interest. (Satellite photographs may ultimately add to the store of available data.) The meteorologist or aerographer's mate (AG) compares the charts to the indexed REG charts and determines which one most closely resembles the current synoptic situation for ocean area and time of year. Once the chart is identified as typifying existing or forecast conditions, he locates the ship's position with respect to dominant weather features (e.g., proximity to the center of a high, ahead of or behind a front, etc.). Letters superimposed on the chart tell which profiles are to be used in the various operational areas of interest.

The third technique is used by Fleet units having the capability to measure refractivity values in the lower atmosphere by means of radiosondes or refractometers. Using an actual refractivity profile derived from these soundings, the meteorologist/AG determines the REG profile that most closely resembles the actual conditions. This matching determines profile letter, and the information presented may then be applied for operational guidance.

Figures 1 through 3 schematically illustrate how each of the three techniques are employed in the REG.

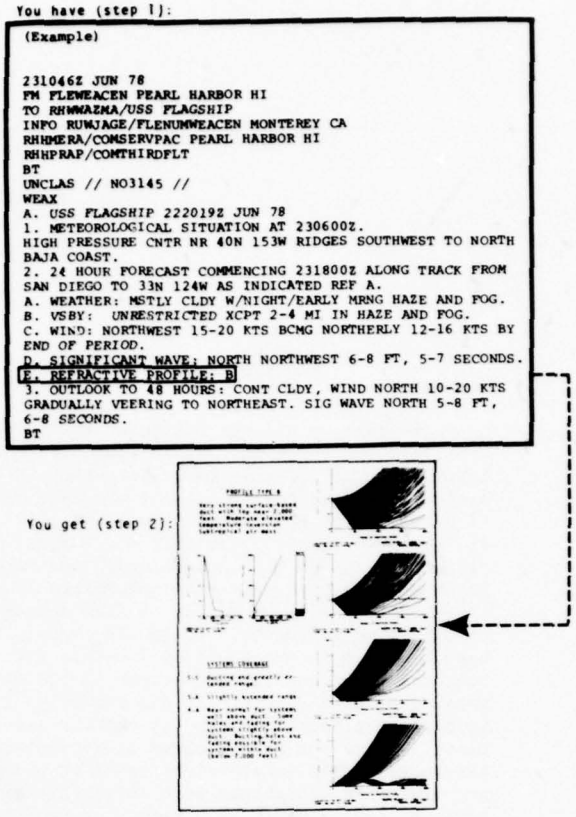

Figure 1. Example, REG Technique 1

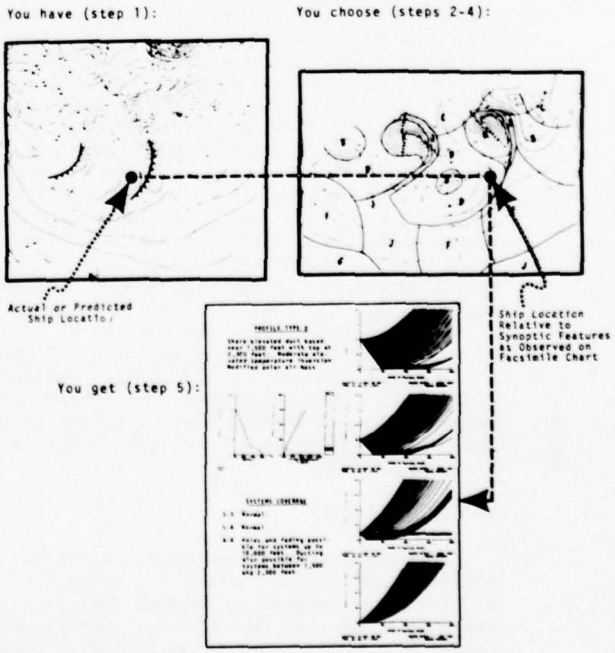

Figure 2. Example, REG Technique 2

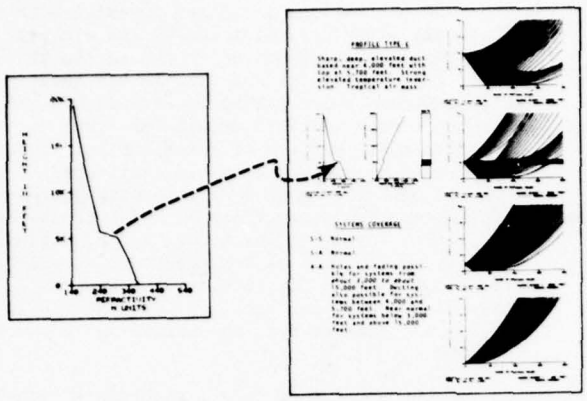

Figure 3. Example, REG Technique 3

2.3 Assumptions

Development of the REG required a number of assumptions. Among these are that refractivity conditions can be considered characteristic of air mass types and large scale weather conditions, that coastal and island radiosonde data used in development of the REG did in fact apply to the open sea, that REG solutions applied regardless of geographical location (although some geographical influence was implicitly incorporated in REG charts), that ray trace techniques were sufficient to describe coverage conditions, and that changes in profile type could be predicted more from a knowledge of proximity to synoptic features than to changes in shape or characteristics of synoptic features. Because of these constraints as well as the inhomogenieties of the atmosphere itself, it is obviously not possible to develop predictions and conclusions that are absolutely valid in all situations. It was believed, however, that the REG approach addressed the essential considerations and expected systems coverage, and that it provided valuable new guidance in a critical area where little information existed.

3. REG EVALUATION AND PERFORMANCE

The initial REG was promulgated as THIRD Fleet TACMEMO 280-1-76 in September 1976 and remained in effect till June 1978 when it was withdrawn from operational use pending modification and further development of the technique. It was put into operational use following an evaluation by Fleet Weather Central, Pearl Harbor which established the feasibility of REG implementation and the finding that useful guidance for radar operators could be provided through REG use based on a study involving six ships in the Pacific Ocean. In a related informal, semi-objective evaluation of the REG performed by Hargrave (1976) aboard USS ENTERPRISE, the REG produced promising results when seasonal transitions were considered and many helpful suggestions were offered for improving the technique. What still remained to be done was a thoroughly objective evaluation of the technique in terms of its verification in predicting coverage conditions in certain categories important to Fleet operations. Such an evaluation was performed by Glevy and Logue (1976). This NOSC (formerly NELC) study employed a data base similar to that used in the development of the REG and indicated disappointing REG performance in a number of important areas. Foremost of the REG shortcomings noted were its poor verification in predicting surface-based ducts, sub-refractive and standard conditions. The verification rates for predicting elevated ducts were much better. (Relatively good verification for elevated ducts was noted in a later informal test of REG predictions in the Hawaiian area during the reconstruction of Fleet data from RIMPAC-77.)

Because of the importance of surface-based ducts to the surface Fleet, REG deficiencies in this area (as well as in the area of sub-refractive and standard conditions) addressed by Glevy and Logue have been given serious consideration. It appears that these deficiencies can be attributed partially to an incomplete understanding of synoptic-refractive relationships and also to an overly detailed attempt to specify predicted profile types. A considerable part of REG shortcomings in predicting surface-based ducts can also be attributed, however, to deficiencies in radiosonde data when applied to open ocean conditions for refractive purposes. Unfortunately, the only radiosonde data available for evaluation and comparison with the REG are from islands, ships, and coastal locations. The REG itself assumes that such radiosonde data are representative of open sea conditions. There is little question but that radiosonde measurements currently provide the best and cheapest method of determining the general variation of basic atmospheric parameters with height. However, due to a tendency for radiosonde humidity sensors such as those used in American sondes to be warmer than the ambient air, particularly at the time of balloon releases over heated platforms (mainland or islands but also ships), the relative humidity reported for the first free-air and also subsequent data points may be too "dry" during daytime. When considered with surface-point data determined from standard psychrometer readings, this effect leads to a tendency for an erroneously high frequency of surface-based ducts during the daytime heating hours as discussed in detail by Helvey (1979).

The relevance of this problem is that while radiosonde data is virtually the only source of refractive data over the world's maritime areas and must be relied on either directly or indirectly as input to the REG or other refractive assessment systems, radiosonde data may nevertheless be responsible for spurious surface-based ducts which make it difficult to properly evaluate REG performance or that of other refractive prediction techniques for surface-based duct conditions. The problem also has serious implications for world-wide refractive climatologies in Naval planning and operations. Efforts are continuing at PMTC to determine the magnitude of the problem and to determine the feasibility of applying corrections to existing or future data.

In 1978, two other independent outside evaluations of REG performance were initiated. One is being conducted by Brookes (1978-79) based on input from questionnaires distributed to

Cruiser, Carrier, Destroyer, Frigate, Support Ships, Squadrons and other Fleet units. Two hundred twenty usable questionnaires were returned which addressed the questions of synoptic typing, profile selection, verification of profile type and indications of radarscope conditions. When asked if the "REG assessment of conditions was essentially correct," 48% responded "Yes", 32% responded "No" with the remainder undetermined. The second informal evaluation was conducted by Glevy (1978) as a follow-up to his earlier study. In this study, REG predictions were made for refractivity conditions in the SOCAL operating area and verifications of these predictions were based on radiosonde data from PMTC's San Nicolas Island (SNI). Based on a summary of the results the study concluded that the REG offered no improvement over random procedures. However, since a large number of soundings taken from SNI were launched from atop the island station at 570 feet mean sea level (MSL), the data can not be directly used in verifying surface-based ducts over the ocean.

An overall summary of REG performance would thus seem to be varied. In terms of its feasibility as a procedure, it performs well because of its simplicity. As a planning guide, as a predictive tool in regions where elevated ducts are frequent, under Electro-Magnetic Control (EMCON) conditions, and as an educational tool, the REG approach has the potential to be an asset. On the other hand, it is apparent from the NOSC evaluations and Fleet experience that there are major discrepancies in the synoptic-refractive relationship portrayed in the initial REG. The fundamental question is how quantitative can this relationship be established and can it be made reliable enough for Fleet use. Thus the basic premise of quantitatively inferring sub-synoptic considerations is challenged. Meteorologically, such a relationship must exist consistent with current capabilities of weather prediction for other parameters and conditions associated with air mass properties. The degree to which this can be reliably done however depends on continued detailed research and data evaluation such as that encouraged and supported by NOSC.

4. THE PHYSICAL BASIS FOR A SYNOPTIC REFRACTIVE RELATIONSHIP

The justification for an investment of effort in developing refractive prediction techniques from synoptic considerations must be based not only on the experience or knowledge of individual radio-meteorologists but also on well-established, fundamental principles reflected either in long term statistics or in a descriptive model with a physical basis. Supporting meteorological and physical evidence of this nature is discussed in the following sections.

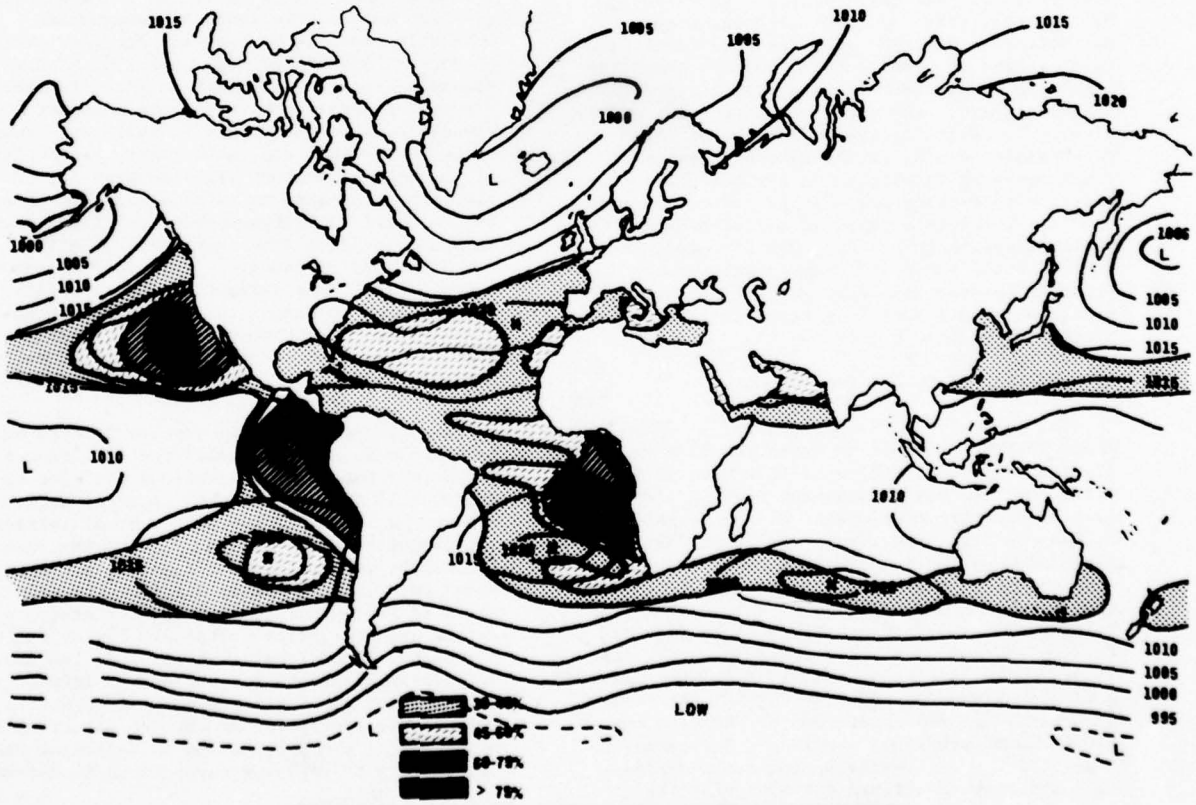

Figure 4a. Winter Sea Level Pressure and Duct Climatology (Purves)

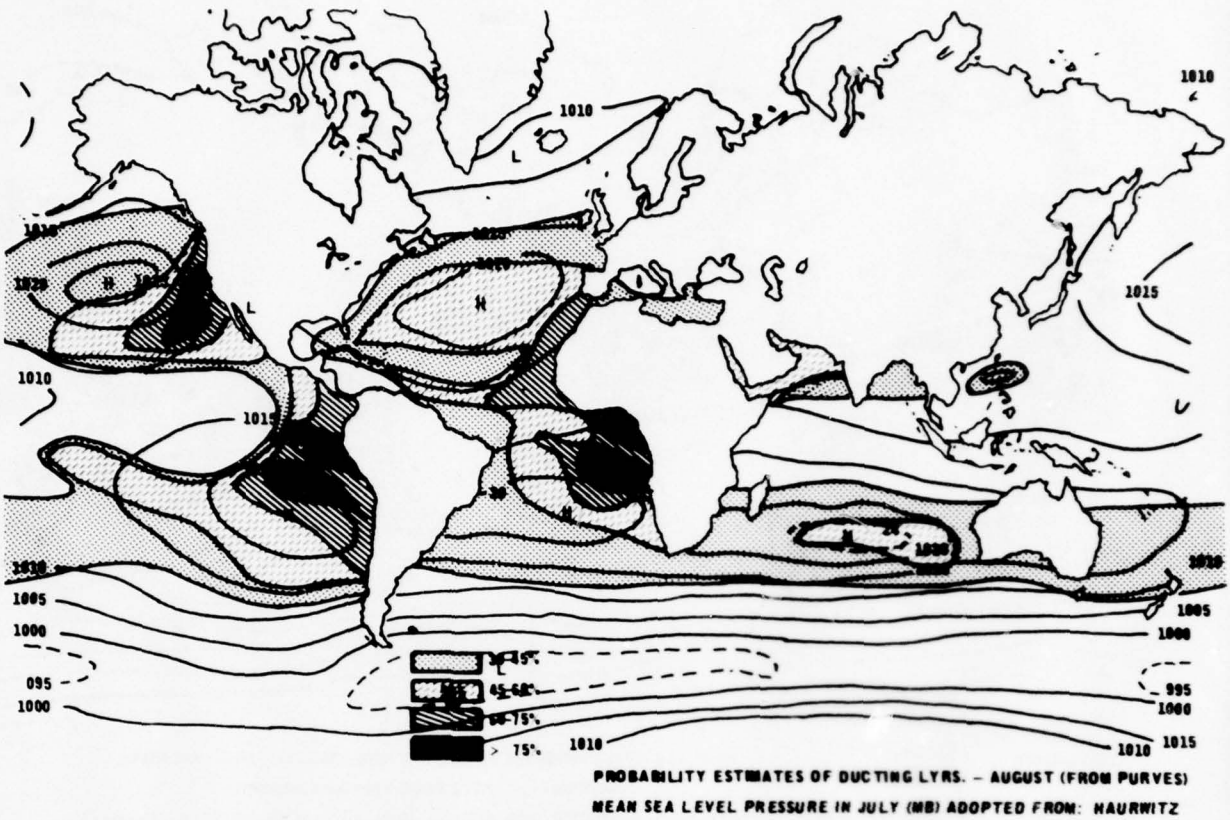

Figure 4b. Summer Sea Level Pressure and Duct Climatology (Purves)

4.1 Climatology

If a synoptic-refractive relationship exists, it is reasonable to expect that this will be reflected in climatological or time-averaged depictions of surface weather conditions. Maps of mean surface pressure patterns (MSL pressure) are shown in Figures 4a and 4b for the months of January and July (mid-winter and summer months) from standard references on climatology by Haurwitz and Austin (1944). These maps show mean strong high pressure regions over subtropical oceans in both hemispheres, especially in the Atlantic and Pacific Oceans. Superimposed on the pressure patterns are similar time-averaged maps developed by Purves (1974) for probability of encountering ducting layers. It is apparent that the regions depicting ducting probabilities of 45-60% and greater coincide with the subtropical high pressure areas in both hemispheres. Moreover, there is a strong tendency for the highest ducting probabilities as determined by Purves to be located within the eastern and equatorward sectors of the anticyclones where subsidence is normally greatest and inversions typically strong and low.

To lend more credence to the climatological agreement, comparisons were also made between the over-ocean pressure patterns adapted from Haurwitz with independent duct statistics derived from a world-wide study by Ortenburger (1973) using extensive radiosonde measurements and computer analysis. When the annual ducting frequencies from the latter (Figures 5a and 5b) are compared with surface pressure patterns, the same correlation is noted as earlier with the regions of greatest ducting frequencies (≥60%) coinciding with the most part with the eastern and equatorward sectors of the subtropical anticyclones.

4.2 Meteorological Structure and Models

If a synoptic-refractive relationship can be observed through climatological statistics, it does not seem overly optimistic to expect this relationship to be exhibited in individual case studies based on physical, dynamical and air mass considerations. A great deal of past work in both synoptic meteorology and radiometeorology is supportive in building a case for such a synoptic-refractive relationship. Noonkester and Hitney (1974) provided an excellent overview and chronology of radiometeorological work from the late 40's through early 70's when much of the pioneering work was done. A significant point in their discussion is the sensitivity of refractivity conditions to the distribution of moisture associated with air masses and other synoptic features, as well as the vertical motion field which affects the profile of both moisture and temperature. A three-dimensional view of meteorological conditions is therefore essential to describing and predicting refractivity conditions even though for the most critical applications results may be best demonstrated or applied near the surface.

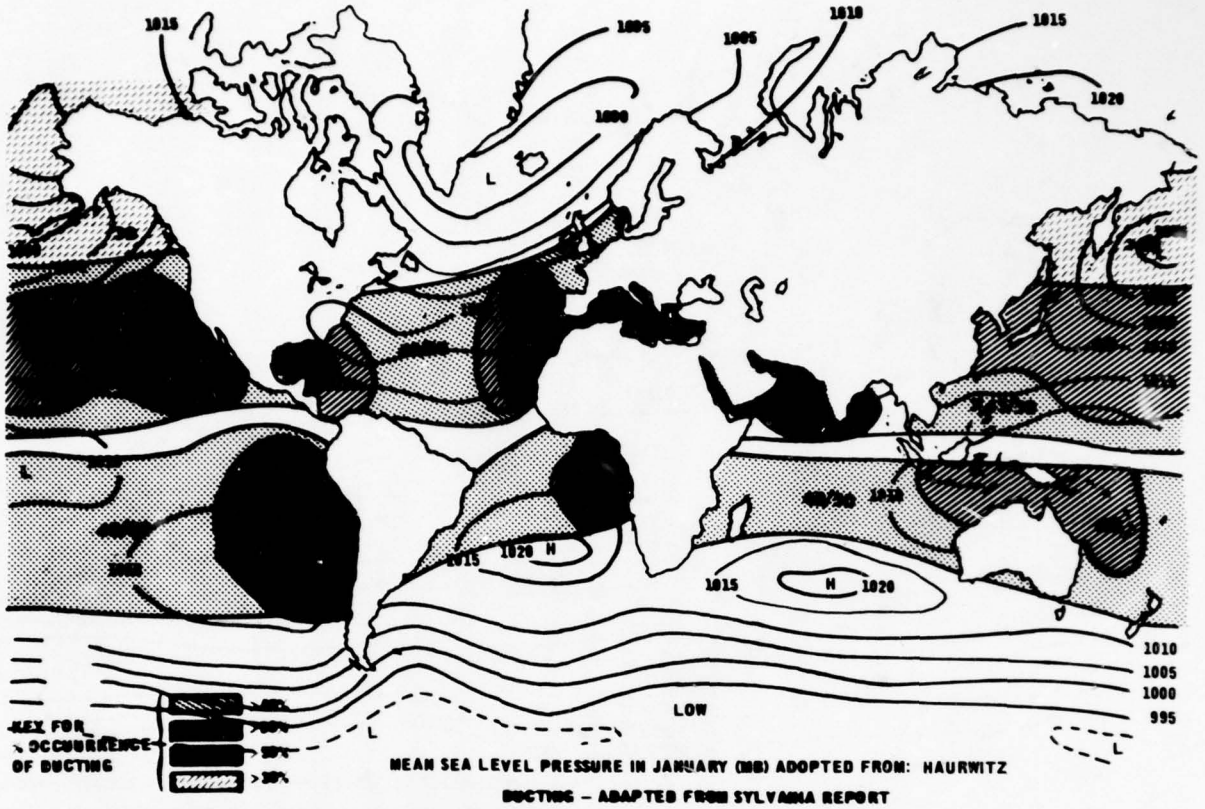

Figure 5a. Winter Sea Level Pressure and Annual Duct Climatology (Ortenburger)

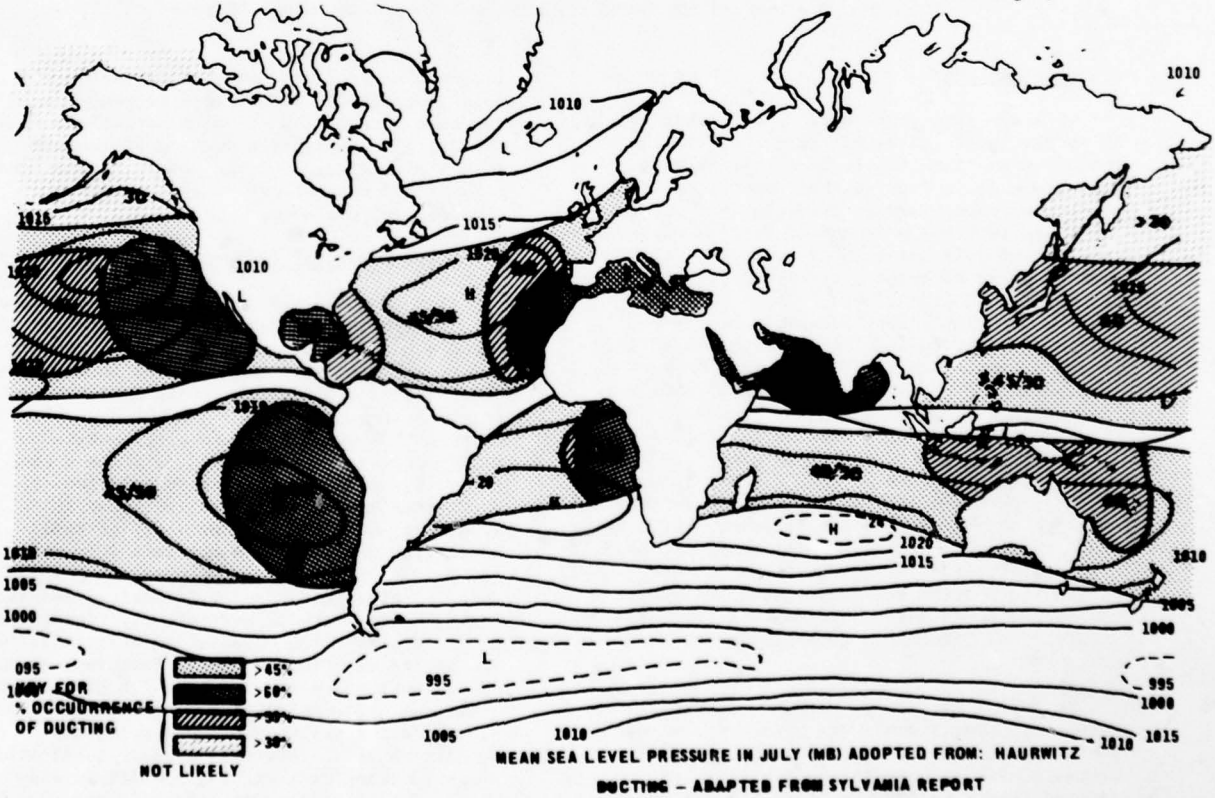

Figure 5b. Summer Sea Level Pressure and Annual Duct Climatology (Ortenburger)

4.2.1 Three-Dimensional Structure

Some of the earliest work in synoptic meteorology analyzed in detail the three-dimensional structure of cyclones and anticyclones. Pettersen and Namias (1940) described subtropical anticyclones separated by cols into cells on the order of 4,000 to 9,000 kilometers (km) in dimension. They also showed that due to the nature of the anticyclones circulation, air in the eastern parts of the cells will be more stable than in the western parts. This agrees with the climatological distributions shown in Figures 4 and 5 where duct frequency was greatest over the eastern parts of the subtropical highs. From a discussion of the hydrostatic equation it was also shown that the subtropical anticyclone tilts westward and equatorward with height and that subsidence occurs within the cell to compensate for frictional outflow near the surface. Thus the air aloft in anticyclones is typically dry and characteristic of a Superior air mass. Poleward of the subtropical highs are cyclones and fronts separating contrasting air masses. Figure 6 schematically illustrates the moisture field typically associated with a mid-latitude disturbance following the discussions of Namias and Petterssen (1940). A moist tongue is observed to flow poleward along and ahead of the cold front, spreading along the warm front to the east and around the low center to the west. As the moist air moves poleward, it also ascends so that humidity may increase with height near the warm front (resulting in sub-refractive conditions). Nearer the western half of the anticyclone in the warm air, a dry tongue may ascend so that humidity decreases with height (resulting in super-refractive conditions).

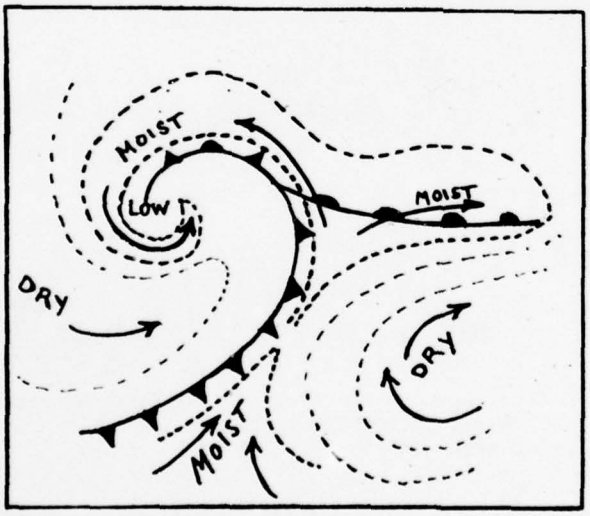

Figure 6. Moisture Distribution Associated with Typical Frontal and Cyclonic System (adapted from Namias)

Godske, Bergeron, Bjerknes and Bundgaard (1957) and Wexler and Bjerknes (1957) continued development of the three-dimensional structure of anticyclones and cyclones. They described air flow and compensating covergence/divergence patterns associated with highs and lows as shown schematically in Figure 7. The low and high centers tilt westward with height with the trough lines remaining within a region of convergence and the ridge line remaining within a region of divergence. In general low level

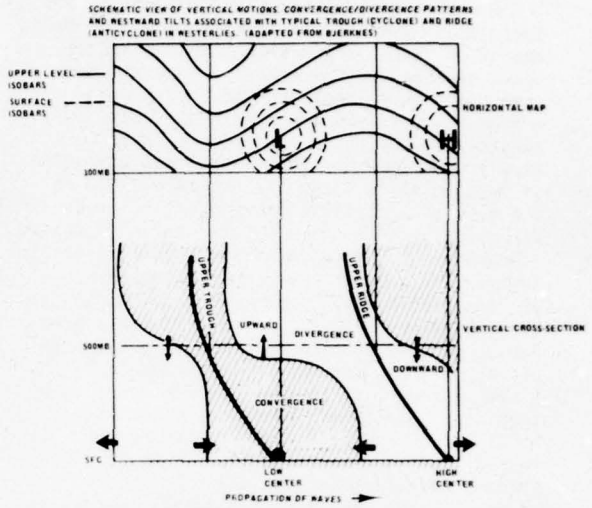

Figure 7. Vertical Motion and Divergence Patterns Associated with Typical Waves in the Westerlies (adapted from Godske, Bjerknes et al)

covergence is capped by a divergent flow of air aloft and low level divergence is capped by convergence of air aloft. To prevent air from piling up or being depleted, rising currents of air precede troughs and subsiding currents follow troughs (or precede ridges). While rising currents tend to destroy refractive stratifications, subsiding currents produce inversions, super-refractive conditions and ducts, particularly over the eastern sides of the subtropical highs as was shown on a statistical basis in Figures 4 and 5. Well-defined inversions are common in the eastern parts of subtropical highs, becoming weaker and higher toward the west. This leads to higher and weaker elevated ducts in the western region of the high cells. As the marine air beneath the inversion moves towards warmer waters south and west of the high cells, it is heated from below at the same time that radiational cooling occurs from cloud tops at the inversion base. This results in a well-mixed, increasingly deep marine layer which favors near standard refractivity conditions in the lowest region.

4.2.2 Airmass Considerations

Due to the vertical motion field associated with anticyclones, horizontal spreading of air occurs at low levels resulting in air masses with nearly uniform air characteristics over appreciable distances in the horizontal. Air mass properties are highly influenced by the nature of the surface over which they formed or move, being usually characterized as continental (c), maritime (m), polar (P), or tropical (T) in nature. Thus, maritime tropical air (designated mT) is warm and moist, continental polar air (designated cP) is cold and dry. Dry, subsiding air such as that found above the inversion within anticyclones is often designated as Superior (S) air. Due to the widely varying moisture, temperature and stability characteristics

of different air masses, refractivity conditions generally differ markedly from air mass to air mass depending on its origin and the surface over which it moves.

A number of investigators have examined individual synoptic air mass features for their impact on radio propagation. Nearly all of these earlier studies however, involve cases over continental regions rather than over maritime areas. In one such study based on conditions over the U. S. Midwest, Arvola (1957) observed that when horizontal advection of well modified polar air occurs such as to the rear of an anticyclone capped by a subsidence inversion, conditions are very conducive to the production of strong, elevated super-refractive layers. In general, he found that warm highs, or "dynamic" highs (highs that are cold at the surface and warm aloft) are best for elevated ducts. The subtropical highs, being warm are therefore ideal air masses for producing elevated ducts, particularly since subsidence inversions are common above the mixed layer. Arvola also found that even following many squall lines and for some rapidly moving cold fronts, subsidence of air may also produce elevated ducts, although conditions near these features are on the average probably well-mixed and near standard. In a review of anticyclones, Wexler (1957) discusses how the more pronounced cases of subsidence (and therefore super-refractive conditions) are thought to occur with the transformation of polar anticyclones to warm or dynamic anticyclones. As they warm, they tend to move slower than would shallow cold (polar) anticyclones. When capped by subsidence inversions, the top of the inversion layer generally marks the top of the true cP air mass. Extensive compilations of statistics relating surface and low-level refractivity conditions to air mass types for regions around the world have been prepared by Bean, Cahoon, Samson and Thayer (1966) and by Samson (1976).

4.2.3 Spatial Extent and Horizontal Homogeneity

The notion of air mass uniformity is a source of constant concern and needs to be put into perspective for its impact on refractivity considerations. On the one hand, there are a variety of small scale perturbations or wave motions, some of which are highly significant to radio propagation, which are superimposed on the basic air flow at various times and locations. They are detectable by aircraft and conventional atmospheric sampling methods such as by Edinger and Wurtele (1971); by special remote sensing systems such as the FM-CW radar developed and described by Richter (1969) and discussed by Gossard, Richter and Atlas (1970); and on a much larger scale by satellite sensing as described by Rosenthal and Posson (1977) and Noonkester and Hitney (1974). Carr (1960) and Glevy (1976) also studied the horizontal uniformity of meteorological features significant to radio propagation. The latter concluded as did most of the other investigators that mesoscale features such as eddies, squalls and other perturbations are most frequently observed near coastlines and topographic influences. Over the open sea, such features are apparently comparatively rare, so that synoptic-refractive relationships may be expected to work better over the open ocean than near land.

A great deal of data have been compiled which show that air mass characteristics and meteorological features do have an appreciable horizontal extent. For instance, Noonkester and Hitney (1974) and Hitney (1975) describe cross sections of radio-meteorological aircraft measurements made off the coast of California between San Diego and Guadalupe Island in 1948 in which refractive features extended more than 200 miles to sea from the mainland. Neiburger (1961) did a pioneering study in which he showed the subtropical inversion to extend in the average from the coast of California to the Hawaiian area. While average conditions do not reflect the interruptions and variations associated with individual moving weather patterns, the persistency of this feature during summer in the North Pacific is so great that it may closely approximate the average picture at any particular time.

The persistence of the subtropical inversion in time at a single location is also high. Rosenthal (1965, 1972) described the continuity of the inversion at San Nicolas Island (Figure 8) and described how large scale adiabatic ascent of air can explain relatively subtle inversion height fluctuations which correspond to the influence of transient synoptic troughs and ridges. The persistence of the inversion over the Eastern Pacific during the warmer months is also indicated by time-averaged statistics for Point Mugu compiled by Lea (1968) and de Violini (1967) of marine stratus behavior which is closely related to the subtropical inversion.

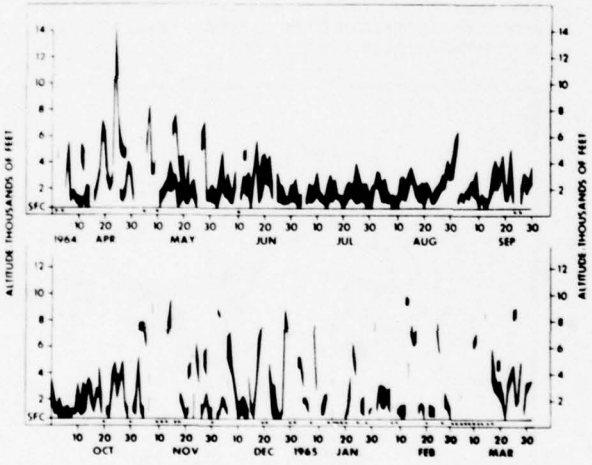

Figure 8. Daily Inversion Heights at San Nicolas Island for 0000Z, 1 April 1964 through 1 April 1965.

While meteorological features of concern to radio propagation are thus observed to exhibit considerable spatial and temporal uniformity, it is important to note that their extent is not completely horizontal. For instance, abrupt slopes are frequently observed near frontal boundaries, land features and near sharp gradients in sea surface temperature as was noted earlier for eddies and squalls. Subtle slopes are common within large air masses and within oceanic subtropical high pressure cells.

Not uncommonly, both small scale variability and large scale uniformity may occur simultaneously so that the question of horizontal homogeneity is often a matter of degree. For instance, in the satellite picture shown in Figure 9, the array of cloud cells suggests some fluctuation in marine layer depth. This occurs, however, in a regular manner over a vast region marked by inversion-capped marine layer conditions. The importance of this variability or lack of it, depends on the specific application. Thus, for refractivity assessments or predictions over regions covering several hundred miles across, the cellular variability may constitute only minor, operationally unimportant embellishment to a region describable by a single refractivity profile. For other purposes, the cellular detail may be operationally important. Studies are being conducted at PMTC to quantitatively determine the extent of horizontal homogeneity over the oceans using satellite imagery.

Figure 9. GOES SA1 Picture of California and Offshore Region for 1915Z, 21 May 1978.

From studies conducted so far, it appears that over the ocean, particularly away from land masses and frontal boundaries, the assumption of refractive horizontal homogeneity is generally acceptable for distances on the order of a few hundred miles in radius from a given atmospheric profile measurement. This means that propagation assessments under such conditions can probably be made from a single refractivity profile in agreement with Glevy's (1976) conclusion. For distances involving several hundreds of miles or more, or in instances with clear synoptic or mesoscale influence, different refractive structures must be used for different air mass segments based on additional direct measurements, climatology or synoptic solutions such as are employed in the REG concept.

4.2.4 Meteorological and Refractive Models

Interest by radio meteorologists in developing a descriptive model relating synoptic to refractive conditions followed from recognition that refractive conditions vary with air mass properties. Since the latter are predictable using established meteorological principles, it follows that there is a basis for expecting refractive conditions to also be predictable. Bean and Dutton (1966) provided much of the basic foundation in radio meteorology and emphasized the refractive significance of migratory cyclones and anticyclones in middle latitudes. They noted how certain surface patterns and vertical refractivity profiles occur frequently with particular types of synoptic systems in accordance with the three-dimensional structure of dynamic systems discussed earlier. Reducing the station-to-station variability of refractivity by converting values from conventional N units to sea level conditions, Bean formed a basis for mapping refractivity on a synoptic scale. To emphasize air mass contrast, a new refractive index 'A' unit was defined which modifies the height dependence of refractivity to indicate the departure of refractive index from the mean value at a given level. Synoptic mapping was then attempted by Bean for an actual case study for a strong polar outbreak over the U. S. in February 1952 accompanied by a surge of warm, moist tropical air from the Gulf of Mexico. Sharp contrast in refractivity conditions was observed between different air masses with strong horizontal gradients in the vicinity of transition zones (fronts). Based on these case studies, idealized vertical profile diagrams of cold and warm fronts were then constructed in A units to typify refractive-synoptic events. These are reproduced here from a U. S. Navy publication (1960) for the idealized cold front as Figures 10a and 10b. In Figure 10b the high A unit values correspond to the warm tongue near the surface ahead of the cold front. The strong horizontal gradient of A takes place in a narrow zone behind the cold front corresponding to the typical sharp decrease of humidity and temperature usually noted there. Bean's models included a tongue of high A values along the idealized warm frontal surface skewed towards the warm side to reflect the gentle ungliding of moist air along the frontal surface commonly observed with warm fronts.

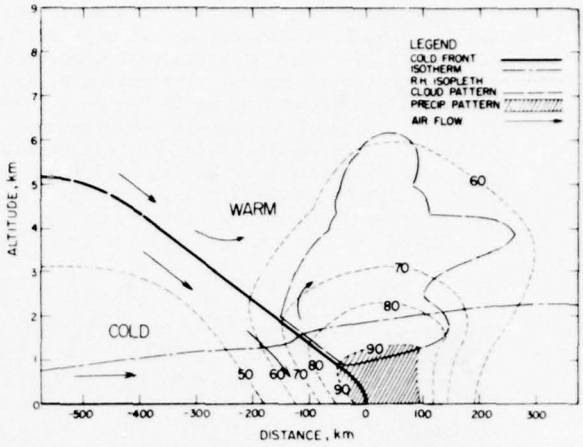

Figure 10a. Idealized Diagram of a Fast-Moving Cold Front (from U.S. Navy Weather Research Facility and Bean).

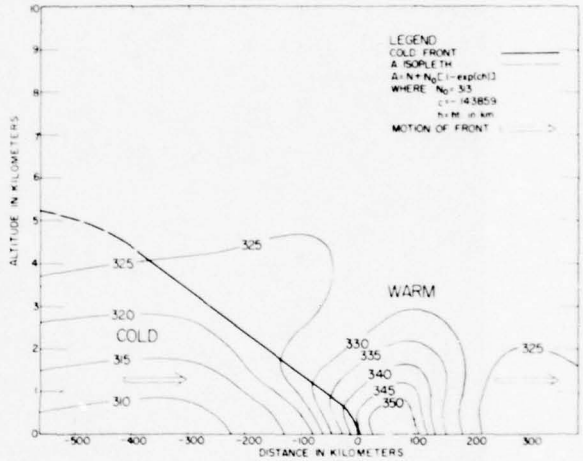

Figure 10b. Idealized Cold Front in A Units (from U.S. Navy Weather Research Facility and Bean).

The concept of potential refractivity employed by Bean was further developed by Jehn (1960) who defined a new potential refractive index K in terms of potential vapor pressure which refers N values to a reference pressure level of 1,000 millibars (mb). This parameter is also very useful in illustrating refractivity contrast across air mass boundaries.

While the attempts of Bean, Jehn, and others to describe synoptic-refractive relationships and derive meaningful models are illuminating and an essential stepping-stone, they all suffer from one drawback with respect to their application to the REG, - all the cases considered were for over-land situations. What is needed is a model that includes over-ocean conditions.

One of the most useful sources of descriptive models of synoptic features, though not directly applied to refractivity, was the work of Elliott and Thompson (1965). Their models were derived by a combination of objective and subjective information including statistical summaries based on an examination of over 300 ship or coastal soundings and near simultaneous Tiros satellite coverage from regions surrounding the

radiosonde stations. Figure 11 is an idealized surface synoptic pattern developed by Elliott and Thompson. Air masses are divided into different sectors according to the relationship of the air mass to its source region or other synoptic features. In general, the surface air mass regions are categorized into combinations of cyclonic, anticyclonic, polar, subtropical, pre- and post-frontal factors. A total of 10 sectors was defined for the surface model. In many respects, these sectors closely resemble the REG charts which were constructed for each season and ocean without prior knowledge of the Elliott-Thompson models.

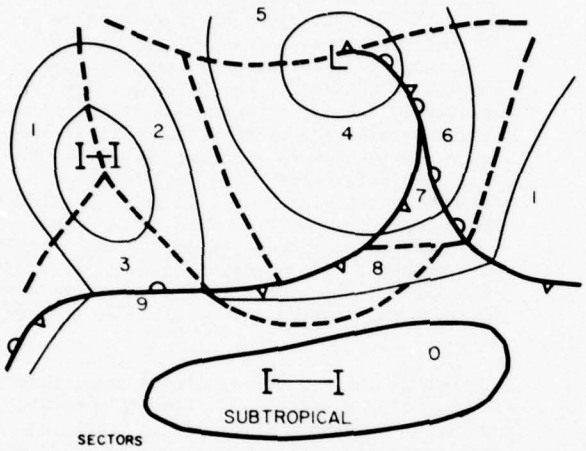

SECTORS

1. Anticyclonic, Returning Polar, Pre Frontal
2. Anticyclonic, Fresh Polar, Post Frontal
3. Anticyclonic, Returning Polar, Stationary Front to South
4. Cyclonic, Fresh Polar, Post Frontal
5. Cyclonic, Polar, North of Low Center
6. Cyclonic, Pre Frontal, Occluded or Warm Fronts
7. Cyclonic, Warm Sector
8. Cyclonic, or Anticyclonic, Pre Cold Frontal (Not Warm Sector)
9. Anticyclonic, Stationary Front to North
0. Anticyclonic, Sub Tropical, Any Sector

Figure 11. Idealized Surface Synoptic Pattern and Air Mass Sectors (from Elliott and Thompson).

A somewhat related depiction is shown in Figure 12 from a study by Serebreny and Blackmer (1974). This effort involved correlating data from the meteorological Application Technology Satellites with radio signal data for a 13-month period in the Philippine-Taiwan-Okinawa area. Based on the data collected and observations made, a descriptive model was developed which shows higher than average signal levels both between cells of the subtropical high (in warm moist air) as well as in moist pre-frontal air. Mean signal levels are depicted somewhat lower than the long term average in the vicinity of cold fronts, and in the cold air behind fronts.

In an earlier study by Clarke (1967) using radiosonde data from Argentia, Newfoundland, attempts were made to relate the heights of super-refractive layers to migratory polar (cP) highs moving into the Western Atlantic area between latitude 55° and 60°N. A tentative model was developed (Figure 13) which shows the topography of the main super-refractive layer in thousands of feet with greatest confidence assigned to heights within the high pressure regions.

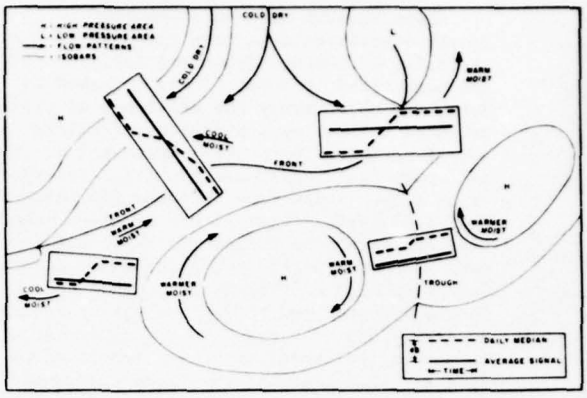

Figure 12. Qualitative Model of Changes in Daily Median Signal Levels Associated with Synoptic Features (from Serebreny and Blackmer).

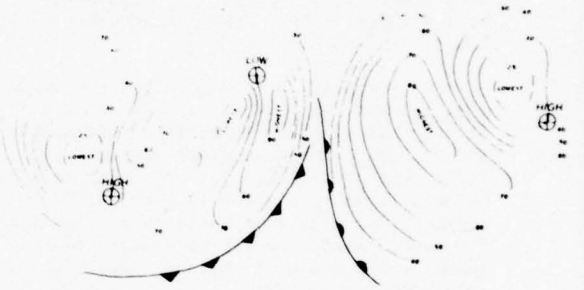

Figure 13. Topography of Main Super-Refractive Layers Associated with Synoptic Features Off Argentia, Newfoundland (from Clarke).

Of particular interest is that the lowest layer altitudes found were located within the northwest sectors of the highs rather than over the eastern sides as has been described or deduced from other studies. Possible explanations for this include a more complicated or random relationship than assumed, or a different structure for continental polar air masses in the Western Atlantic than for warmer tropical and subtropical highs. A third explanation might be a possible bias due to location such that high centers at these latitudes most frequently passed south of the radiosonde station affording few chances for sampling in the eastern and southern quadrants. Layer heights in the vicinity of cold fronts and low centers are relatively high (and presumably weak) in good agreement with earlier considerations. A region of high layer heights between the high center and an advancing warm front is unexplained.

Synoptic-refractive relationships have been investigated in other regions of the world and correlations noted. For instance, Gjessing (1967) found that radio signal strength over the North Sea was related to the temperature-dewpoint difference at 850 mb. Higher signal strengths were correlated with larger temperature differences, presumably reflecting a likelihood of a super-refractive layer between the relatively moist surface and the 850 mb level when the latter is dry.

Mixed results were noted however in a recent statistical/ pattern recognition study performed by Cuming, Caton and Kalinyak (1977) and summarized by Sweet (1979). Tasked to determine objectively the existence of typical patterns reflecting a synoptic-refractive relationship, efforts were unproductive. Data used were 6,922 upper-air soundings recorded by radar picket ships from October 1956 through June 1965 matched against the archived records of pressure height fields for three different wave component scales using the Rapid Analogue Selection System. The authors cited deficiencies in the synoptic and refractive data bases used as likely explanations. On the other hand, climatological statistics compiled from the data revealed clear correlations that would infer a likely synoptic-refractive relationship. For instance, in the southernmost zone studied, high 500 mb heights were associated with a trapping probability of 75%, and a 500 mb wind direction of 270° to 315° (NE quadrant of anticyclones) with a trapping probability of 85%.

The foregoing discussions provide abundant examples and support for confidence in a predictable synoptic-refractive relationship for general propagation assessments. This includes a sound basis for expecting ducting to be most prevalent in the eastern sides of anticyclones with some exceptions. In terms of REG development, a question remains of how quantitative and with what confidence can such relationships be made.

4.3 Recent Studies at PMTC

In an effort to provide a more quantitative basis for REG modification and development, and to document hypotheses with actual case studies, several separate studies have been conducted at PMTC. These utilized two data bases of radiosonde data received from the Navy Detachment at the NCC, Asheville, North Carolina, one for Ocean Stations NAN and PAPA for 1967, and one for 16 stations for the mid-season months for 1974 used in the REG. Both are supplemented with synoptic charts. These studies are briefly described as follows:

4.3.1 Use of 1967 NAN and PAPA Data Base

Computer programs were developed to calculate and graphically plot several meteorological and refractivity parameters. Data cards containing the basic sounding data were keypunched and processed on the CDC 3100 and Calcomp Plotter systems. Figure 14 is an example of the graphical output showing separate vertical profiles for NAN and PAPA. Parameters include Modified Refractivity (M), Temperature (T), Potential Temperature (PT) and Mixing Ratio (W). The plots on the left indicate the distributions through most of the troposphere from the surface to 25,000 feet. The plots on the right show the expanded scale distributions through the lower atmosphere from the surface to 6,000 feet. At the right-hand edge of each plot is a bar graph diagram reflecting the magnitude of the refractive index gradient between successive layers. Where the horizontal bars reach or exceed the dotted lines to the left, ducting is indicated. Ship names, latitude, longitude, date and both local and Greenwich time are also noted. These plots afforded the opportunity to examine refractivity profiles while comparing them with synoptic events depicted on facsimile charts.

One of the first studies attempted was to evaluate the performance of the REG by using NAN and PAPA data for verification. Synoptic charts were compared with the REG seasonal chart according to the prescribed procedure. The synoptic location of NAN and PAPA (the location of these stations on a given map with respect to synoptic features and air masses rather than geographic location) were then superimposed on a printed copy of the REG chart so that REG profile types could be determined. These REG solutions were then verified by comparison with sounding data actually obtained for the station. For the relatively few comparisons made, results were fair in prediction of elevated ducts at ship NAN. Elevated ducts occurred when they were predicted but the predicted heights were frequently too high by one profile classification. REG predictions for PAPA were fairly good but few ducts were encountered at this more northerly station. Since deficiencies in the initial REG were already apparent, the available effort was diverted towards more productive investigations.

One of these involved direct comparison of NAN and PAPA profiles with facsimile weather charts to determine if trends in height did in fact correlate with synoptic events. For the period studied, anticyclonic conditions were found to correlate with low duct heights and warm temperatures aloft. Two ships were involved in measurements at NAN (one on station and one in transit between the mainland and 30°N 140°W). When both ships' data were available, it was observed that the more northeastern-located vessel was more responsive to synoptic changes. This is consistent with what one might expect given the greater definition and amplitude of disturbances within the higher latitude belt of westerlies. The general experience with the NAN and PAPA data was that a fair correlation was noted between duct occurrence and the southeast quadrant of anticyclones but large variability was also noted.

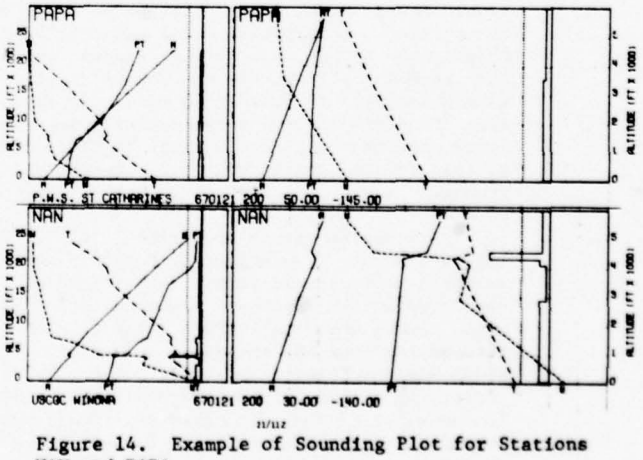

Figure 14. Example of Sounding Plot for Stations NAN and PAPA.

4.3.2 Use of 1974 Multi-Station Data Base

The comprehensiveness of the 1974 data bases used in developing the REG offers greater opportunities for finding meaningful synoptic-refractive relationships and case studies. In order to adequately manipulate the data, a large amount of radiosonde data from the 16 locations obtained were reviewed and punched on cards into digital form. As in the case with the NAN and PAPA data, computer programs were then developed to compute meteorological and refractive parameters from the basic data, and to graphically plot vertical profiles using the CDC 3100 and Cal Comp plotter. Tabular printouts listing pressure, height, temperature, potential temperature, relative humidity, mixing ratio and refractive index were also made for each sounding. The data bases are now on magnetic tape.

4.3.2.1 Case Studies

Based on inspection of the computer-generated vertical profiles, several sequences were selected for Bermuda in the Atlantic Ocean and Midway in the Pacific to study and illustrate the response of temperature and humidity structure (and hence refractivity) to synoptic influence. Temperature (solid lines) and humidity (dashed lines) were obtained directly from the original plots on the DODWPC 9-31A adiabatic diagrams. Small dashed and dotted lines generally indicate the height of the top and base of the inversion respectively based on isentropic analysis. Appropriate regions of synoptic influence were defined and obtained directly from the hemispheric surface analyses obtained from Asheville. The case studies all show a consistent pattern, with inversions (typically associated with ducts) being lowest when anticyclonic influence is greatest. Layers were found to rise and weaken with the approach of frontal systems. Figure 15 shows a time sequence of temperature and humidity profiles and accompanying surface charts in which this response to synoptic features is illustrated for a case study for Bermuda for the period 4-7 April 1974. On 4 April, even though a weak, dissipating front approaches and passes the station from the north, a low strong inversion and shallow marine layer are maintained with a Superior air mass above. This is due to the general increase in anticyclonic conditions over the area as reflected in higher surface pressures over the region. However, beginning on the 5th, the approach from the west of a more vigorous frontal system and the convergent flow in advance of it is reflected in a raising and weakening of the inversion with corresponding increase in marine layer depth. By 00Z on the 7th with the imminent passage of the front, the inversion has been destroyed. Although there is some humidity data missing, there is evidence of a general increase in moisture aloft in advance of the front. As high pressure begins to build once again at 12Z on the 7th shortly after frontal passage, weak inversions and a shrinking of the moist layer also reappear.

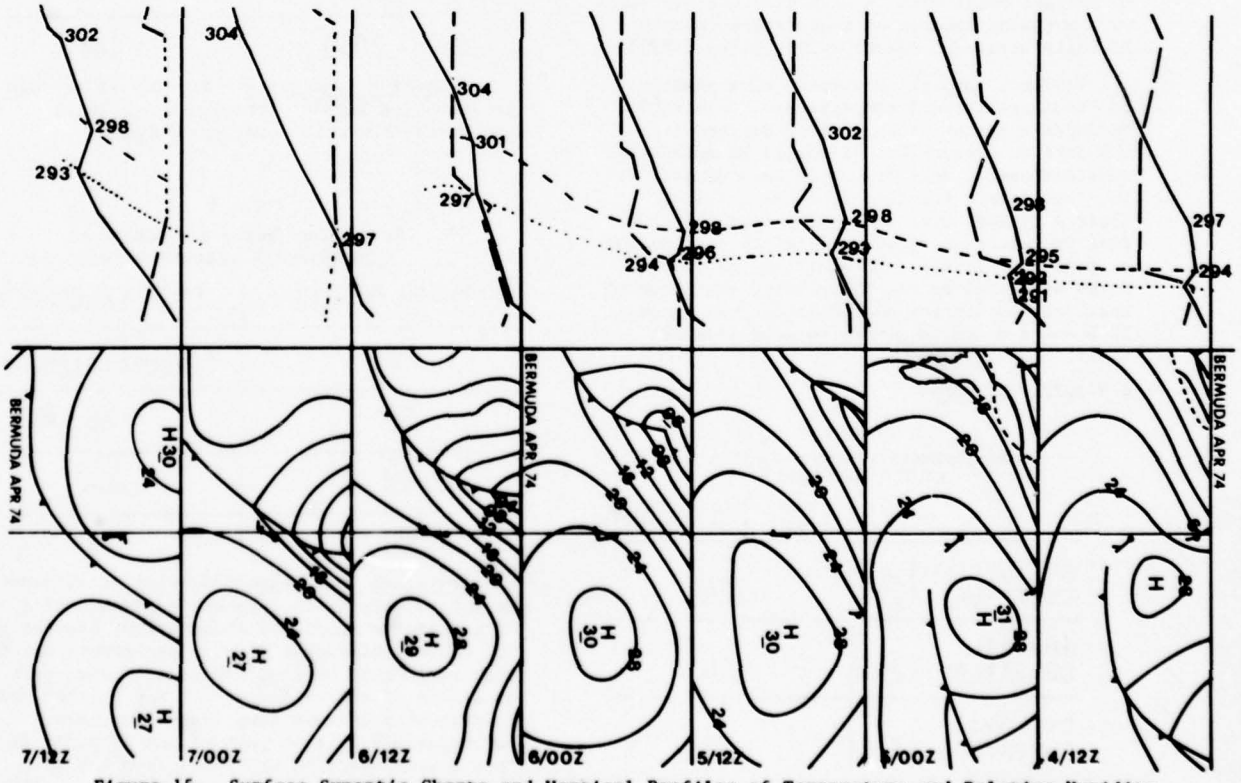

Figure 15. Surface Synoptic Charts and Vertical Profiles of Temperature and Relative Humidity for Bermuda, 4-7 April 1974 (Potential Temperatures on Profiles in Degrees Kelvin).

4.3.2.2 Objective Studies

The review of climatological statistics and patterns, physical considerations, models developed by other investigators, and individual case studies has provided strong encouragement that there is a synoptic-refractive relationship usable in a predictive sense. With this renewed optimism, objective studies have been initiated using the extensive 1974 data bases for the mid-season months with the goal of developing statistics which reflect the synoptic preferences for duct probability.

A variety of parameters have been defined based on strong suspicions or experience as correlators with ducting conditions. These include isobaric curvature (anticyclonic, neutral or cyclonic), proximity to anticyclone center, anticyclone quadrant, proximity to fronts, size of anticyclone, pressure increase to center of high, pressure gradients, distance to cyclones and others. These parameters must be determined for each station individually from actual synoptic charts. In addition, a variety of parameters directly available on tape from the digitized 1974 data bases were also considered such as station pressure, 850 mb temperature, surface wind direction, and the temperature difference between 700 mb and the surface. Since ducting is most frequent in the subtropical regions, emphasis was concentrated on comparative data from the five subtropical/temperate latitude radiosonde stations available, Bermuda, Terceira, Ship H, Midway Island and Ship NAN. Data for NAN and Ship H were available only for January and April. It should be pointed out that a few ducts formed solely by surface point effects on radiosonde soundings were excluded because of temperature-induced humidity errors as described by Helvey (1979).

Tables 1 through 18 present some examples of these statistical comparisons. Each table includes a tentative conclusion derived from the data as presented. It should be noted that computations of duct frequency were derived for 100-foot levels starting from the surface. Since a typical duct is usually more than 200 feet in thickness, ducts will often overlap two or more such levels. In addition, multiple ducts sometimes occur. Therefore, summation of duct frequencies for all altitudes may exceed 100% and some ducts may be counted several times.

4.3.2.2.1 Bermuda

Table 1
Bermuda Duct Frequency as Function of ISOBAR CURVATURE

	DUCT FREQUENCY
ANTICYCLONIC CURVATURE (1)	124
NEUTRAL CURVATURE (2)	104
CYCLONIC CURVATURE (3)	72

Tentative Conclusion - Ducting at Bermuda is more likely with anticyclonic surface isobar curvature.

Table 2
Bermuda Duct Frequency as Function of DISTANCE TO CENTER OF HIGH

DISTANCE (IN DEGREES LATITUDE)	DUCT FREQUENCY
0 TO 5	194
5 TO 10	122
10 TO 20	115
20 TO 40	84

Tentative Conclusion - Ducting at Bermuda is more likely with proximity to the center of high pressure areas.

*(It should be noted that category intervals are not equal in order to provide sufficient sample numbers for statistical significance.)

Table 3
Bermuda Duct Frequency as Function of SEA LEVEL PRESSURE

SEA LEVEL PRESSURE (MB)	DUCT FREQUENCY
1000 - 1012	49
1012 - 1020	89
1020 - 1050	141

Tentative Conclusion - Ducting at Bermuda is much more likely with higher sea level pressures than with lower pressures.

Table 4
Bermuda Duct Frequency as Function of HIGH PRESSURE AREA QUADRANT

QUADRANT OF HIGH	DUCT FREQUENCY
NE	(INSUFFICIENT DATA)
SE	66
SW	104
NW	147

Tentative Conclusion - Ducting at Bermuda is more likely in the western quadrants of a high pressure area. It is contrary, however to all other indications of duct occurrence which show ducting to be most likely in the eastern quadrants of anticyclones. It may be that this relationship is more complicated (or more inconclusive) in this part of the Atlantic due to a common westward extension from the main part of the Atlantic subtropical high usually referred to as the "Bermuda High".

Table 5

Bermuda Duct Frequency as Function of 700 MB TEMPERATURE

700 MB TEMPERATURE (°C)	DUCT FREQUENCY
-10 TO 0	51
0 TO 10	98
0 TO 5	126

Tentative Conclusion - Ducting at Bermuda is more likely with 700 mb temperatures just over 0° C.

Table 6

Bermuda Duct Frequency as Function of SURFACE WIND DIRECTION

"QUADRANT"	SURFACE WIND DIRECTION	DUCT FREQUENCY
SE	000° - 060°	50 (22 SOUNDINGS)
SW	060° - 120°	61 (18 SOUNDINGS)
SW - NW	120° - 180°	69 (23 SOUNDINGS)
NW	180° - 240°	35 (79 SOUNDINGS)
NE	240° - 300°	50 (68 SOUNDINGS)
NE - SE	300° - 360°	44 (27 SOUNDINGS)
	CALM	0
	ALL	47

Tentative Conclusion - A double maximum in Bermuda duct frequency is observed with primary maximum in the southwest to northwest quadrants which is in agreement with observations from Table 4. A secondary maximum is observed in the northeast quadrant.

*Anticyclone quadrant can be inferred from surface wind direction. Assuming that cyclonic wind systems are smaller in area and can be ignored for this purpose, quadrants can be assigned to different wind directions as shown in Table 6 and following tables. Cross isobaric flow of 30° is assumed. The number of soundings available for each category is indicated in parentheses.

Since most of the comparisons made were for the four mid-season months, January, April, July and October, considered together, computer processing was also accomplished for pure climatological statistics showing Bermuda duct frequencies for each of the four months considered separately, without regard to synoptic parameters. These are shown in Table 7.

Table 7

Bermuda Duct Frequency as Function of SEASON

SEASON	DUCT FREQUENCY
WINTER (Jan)	75
SPRING (April)	52
SUMMER (July)	31
FALL (October)	33
ANNUAL (4 Mon.)	50

Tentative Conclusion - Ducting at Bermuda is most frequent in winter and least frequent in summer even though the subtropical high is strongest and most persistent in summer. This distribution can be explained by the fact that in the warmer months, Bermuda is usually located within the western edge of the subtropical high and is influenced by a warm, somewhat unstable flow of tropical air.

4.3.2.2.2 Ship H

Ship H at 38°N 70°W is approximately 300 miles to the northwest of Bermuda (32°N 65°W) and serves as an interesting source of comparative data.

Table 8

Ship H Duct Frequency as Function of SURFACE WIND DIRECTION

QUADRANT	SURFACE WIND DIRECTION	DUCT FREQUENCY
SE	000-060°	40
SW	060-120°	(40)
SW-NW	120-180°	(25)
NW	180-240°	42
NE	240-300°	42
NE-SE	300-360°	54
	CALM	0
	ALL	43

Tentative Conclusion - Ducting at Ship H is most likely in the northeast and southeast quadrants of anticyclones and least likely in the southwest and northwest sectors. This is contrary to observations made for Bermuda. On the other hand it agrees with previous discussions which point to duct frequencies highest in the eastern quadrants of high pressure areas.

4.3.2.2.3 Terceira, Azores

Terceira (39°N 27°W) is on the eastern side of the Atlantic and provides another interesting point for comparison.

Table 9

Terceira Duct Frequency as Function of SEA LEVEL PRESSURE

SEA LEVEL PRESSURE (MB)	DUCT FREQUENCY
<1000	14
1000 - 1010	33
1010 - 1020	50
1020 - 1030	60

Tentative Conclusion - Ducting at Terceira is much more likely with higher sea level pressures and is therefore strongly correlated with anticyclone intensity.

Table 10
Terceira Duct Frequency as Function of SURFACE WIND DIRECTION

"QUADRANT"	SURFACE WIND DIRECTION	DUCT FREQUENCY
SE	000° - 060°	60
SW	060° - 120°	36
SW - NW	120° - 180°	50
NW	180° - 240°	32
NE	240° - 300°	36
NE - SE	300° - 360°	37
	CALM	0
	ALL	41

Tentative Conclusion - Duct frequencies at Terceira show a bi-modal distribution and are most likely in the southeast quadrant of a high in agreement with previous discussions. A secondary maximum occurs in the western sectors of highs which supports the Bermuda observations.

Table 11
Terceira Duct Frequency as Function of TEMPERATURE DIFFERENCE BETWEEN 700 MB AND SFC

700 MB TEMPERATURE MINUS SFC TEMP (°c)	DUCT FREQUENCY
-20 TO -15	25
-15 TO -10	58

Tentative Conclusion - Ducting at Terceira is more likely when temperatures at 700 mb are not more than 10 to 15 degrees colder than surface temperatures.

4.3.2.2.4 Ship NAN

Statistical studies were also made for Pacific Ocean stations. Results are shown below for Ship NAN (30°N 140°W).

Table 12
Ship Nan Duct Frequency as Function of SEA LEVEL PRESSURE (Jan & April only)

SEA LEVEL PRESSURE (MB)	DUCT FREQUENCY
< 1000	0
1000 - 1010	19
1010 - 1020	57
1020 - 1030	64
1030 - 1040	(100) - BASED ON ONLY 5 SOUNDINGS

Tentative Conclusion - Duct occurrence at NAN in winter and spring is much more likely with higher sea level pressure, or when anti-cyclonic conditions are strongest.

Table 13
Ship Nan Duct Frequency as Function of SURFACE WIND DIRECTION (Jan & Apr only)

"QUADRANT"	SURFACE WIND DIRECTION	DUCT FREQUENCY
SE	000° - 060°	82
SW	060° - 120°	60
SW - NW	120° - 180°	57
NW	180° - 240°	31
NE	240° - 300°	35
NE - SE	300° - 360°	62
	CALM	0

Tentative Conclusion - Duct frequencies at Ship NAN in winter and spring are more likely in the southeastern quadrant of highs and least likely in the northwest quadrant of highs in agreement with earlier discussions concerning regions of preferred subsidence.

Table 14
Ship Nan Duct Frequency as Function of TEMPERATURE DIFFERENCE BETWEEN 700 MB AND SFC

700 MB TEMPERATURE MINUS SFC TEMP (°c)	DUCT FREQUENCY
< -20	(0) only 5 soundings
-20 TO -15	47
-15 TO -10	72
7 TO 10	only 2 soundings

Tentative Conclusion - Ducting at Ship NAN is more likely when temperatures at 700 mb are not more than 10 to 15 degrees colder than surface temperature.

4.3.2.2.5 Midway Island

Midway Island (28°N 177°W) is located in the mid-Pacific Ocean.

Table 15
Midway Island Duct Frequency as Function of SURFACE WIND DIRECTION

"QUADRANT"	SURFACE WIND DIRECTION	DUCT FREQUENCY
SE	000° - 060°	33
SW	060° - 120°	28
SW - NW	120° - 180°	21
NW	180° - 240°	9
NE	240° - 300°	18
NE - SE	300° - 360°	33
	CALM	0
	OVERALL	25

Tentative Conclusion - Duct frequencies at Midway Island are most likely in the southeast quadrant of highs and least likely in the northwest quadrant in agreement with earlier discussions concerning regions of preferred subsidence.

4.3.2.2.6 All Stations (16)

A couple of comparative studies were made using data from all 16 stations contained in the 1974 data bases lumped together to obtain a more global view of statistical preferences. Results are shown below.

Table 16
Duct Frequency for all Stations Combined as Function of SEA LEVEL PRESSURE

SEA LEVEL PRESSURE (MB)	DUCT FREQUENCY
< 1000	7
1000 - 1010	19
1010 - 1020	33
1020 - 1030	40
1030 - 1040	(23) - BASED ON ONLY 34 SOUNDINGS

Tentative Conclusion - Duct frequencies for all stations combined are clearly more likely with high sea level pressures, but not extremely high pressures (> 1030 mb).

Table 17
Duct Frequency for all Stations Combined as Function of TEMPERATURE DIFFERENCE BETWEEN 700 MB and SFC

700 MB TEMPERATURE MINUS SURFACE TEMPERATURE (°C)	DUCT FREQUENCY
< -20°	12
-20 TO -15	25
-15 TO -10	31
-10	12

Tentative Conclusion - Duct frequencies for all stations combined are more likely when 700 mb temperatures are not more than 10 to 15 degrees colder than the surface.

4.3.2.2.7 Subtropical Stations (Bermuda, Terceira, Ship H, Midway, Ship NAN)

Since ducting is most frequent in the subtropical regions, comparative studies were made using data from the five subtropical/ temperate radiosonde stations available. Data for Ship NAN and Ship H was available only for January and April.

Table 18
Duct Frequency for Sub-Tropical Stations Combined as Function of Both SURFACE WIND DIRECTION AND SEA LEVEL PRESSURE

	"QUADRANTS" AND SURFACE WIND DIRECTION							
SEA LEVEL PRESSURE (MB)	"SE" 000-060	"SW" 060-120	"SW-NW" 120-180	"NW" 180-240	"NE" 240-300	"NE-SE" 300-360	CALM	ALL DIRECT SUMMED
1000	(0)	(0)	(0)	(0)	25	(33)	0	15
1000 - 1010	(40)	(16)	42	27	23	26	0	27
1010 - 1020	49	31	31	31	41	46	0	39
1020 - 1030	57	49	50	48	62	61	0	53
1030 - 1040	(100)	(100)	— NO DATA —			(50)	0	(77)
1040 - 1050	NO CASES							
1050 - 1060								
ALL PRESSURES	52	42	42	32	38	43	0	41

Tentative Conclusion - Ducting at the five subtropical/temperate stations combined is most likely in the southeast quadrant of highs (least likely in the northwest) and with higher sea level pressures (greater anticyclonic intensity). This picture arises even when the data for Bermuda are included which show a reverse dependency on quadrant.

5. DEVELOPMENT OF A NEW REG MODEL

The purpose of the objective studies and the previous review of models and atmospheric structure is to develop a basis for modifying the synoptic-refractive relationships used in the initial REG so that it will be more reliable and realistic. Based on experience with the REG and recent studies just discussed which show ducting to be consistently (but not exclusively) most frequent in the eastern quadrants and near the center of high pressure areas, a schematic diagram has been formulated of a proposed working model of REG solutions (Figure 16). In this diagram, a schematic view of a cyclone and associated frontal system is shown with a large subtropical high to the southeast and a continental-modified polar anticyclone to the west.

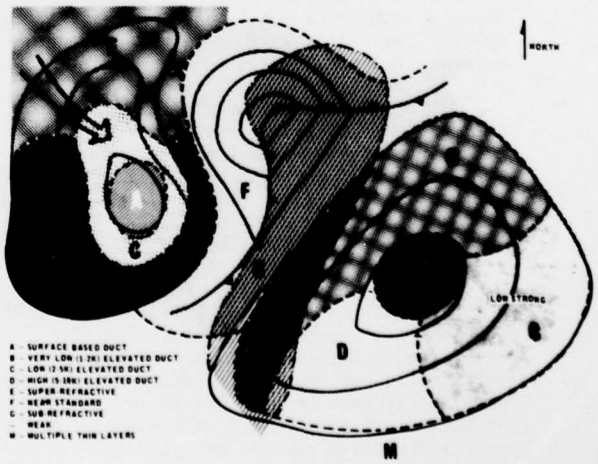

Figure 16. Preliminary Working Model of Synoptic-Refractive Relationships.

Within the subtropical anticyclone, a region of very low elevated ducts (Profile B) exists near the center of the anticyclone where pressure is high and subsidence strong. The southeast quadrant is a region of low, strong elevated ducts (designated as Profile C); as the air flows westward south of the center, it is heated by the warmer sea surface on the western sides of the oceans, and subsequent convection raises and weakens the elevated duct in the southwest quadrant (Profile D). North of the center of the anticyclone, subsidence is less, temperatures aloft are colder, and the refractivity gradient is assumed to be no more than super-refractive (Profile E). The line separating the E region from any of the duct regions may be thought of as a 50% duct-probability line.

The polar anticyclone is similar in refractivity characteristics except it is assumed that strong sinking motions and dryness of continental air may be manifested at times by a region of surface-based ducting (Profile A) near the center of the high. About this region is an area of low elevated ducts (Profile C) bounded to the south by weaker elevated ducts (C-), and to the north by super-refractive conditions.

Even though statistics have not yet been compiled to show that cyclones are associated mainly with near standard conditions, the instability and vertical mixing common in these regions has led to the assumption that refractivity conditions there and for some distance along the frontal surface are near standard (Profile F). As the pre-frontal flow increases, experience has shown that refractive layers rise and weaken markedly with proximity to the front. In addition, a region of moisture advection ahead of the cold front and into the cold air side of the surface warm front is both suspected and observed to result in sub-refractive layers and this region is designated as Profile G. It should be noted that G may overlap with any of the ducting or other defined regions. In addition, a region of multiple thin layers has also been defined in the tropics and is designated Profile M. It may be necessary to specify conditions in these low latitudes on a purely statistical basis.

Only general altitude classifications have been defined for each profile type in an attempt to simplify and generalize the REG predictions. These will be modified later as necessary from results of additional synoptic climatology studies. No altitudes have been specified for Profiles G or M.

The question of surface based ducts is still a difficult question with respect to REG development. Evaporative ducts were not incorporated into the initial REG and their relationship to synoptic events and large scale oceanic features is the subject of investigations at NEPRF. At some point, if a successful REG can be developed for the synoptically-induced layers, then evaporative duct conditions should be incorporated as part of the overall propagation assessment, - even if based purely on climatology.

There is also still the question of authenticity of surface-based ducts from the standpoint of radiosonde representativeness discussed by Helvey (1979). A proposed solution for this problem will also affect the nature of REG predictions.

6. MODIFIED REG PROCEDURES AND SOLUTIONS

6.1 REG Charts

Based on the proposed REG working model, REG charts have been modified for each of the four mid-season months for both the North Pacific Ocean and North Atlantic Ocean. Only these two ocean areas were selected in an attempt to focus on the nature of predictions and to allow for their proper evaluation, before going on to other ocean regions where data is sparce and firm knowledge is lacking. The REG charts were modified somewhat from the working model in order to account for some of the observations at Bermuda, and continue to be regarded as working solutions subject to results of continuing studies at PMTC. Figures 17a and b are examples of such maps for the Pacific and Atlantic, respectively, for selected seasons.

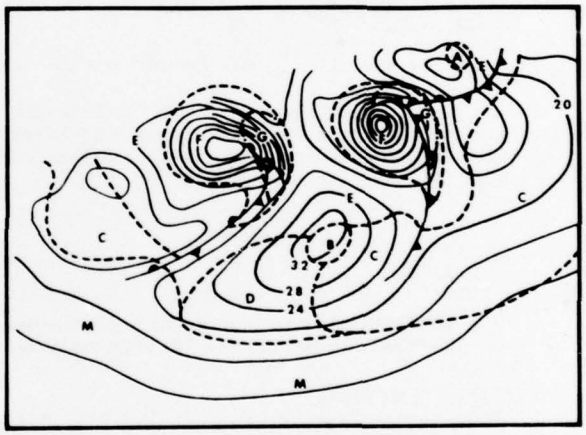

Figure 17a. Preliminary Modified REG Chart North Pacific, Spring.

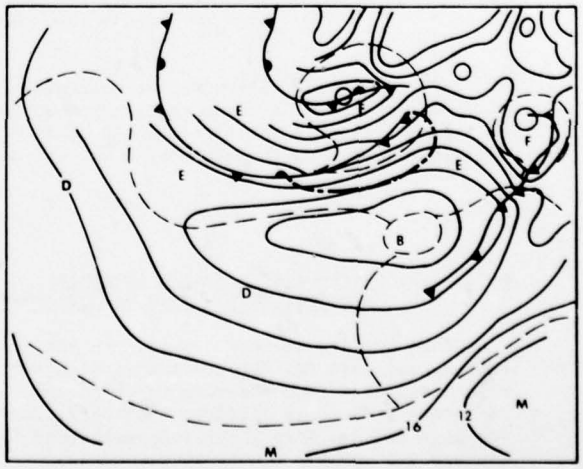

Figure 17b. Preliminary Modified REG Chart North Atlantic, Summer.

As the results of new objective studies and other knowledge or experience becomes available, the REG charts will be modified accordingly. One specific plan if possible is to incorporate a better definition of layer altitude on REG charts. This may require a different form of REG chart whereby the probability of occurrence and the probable altitude can both be displayed based on objective studies. Figure 18 shows an example of what such a chart feature might look like.

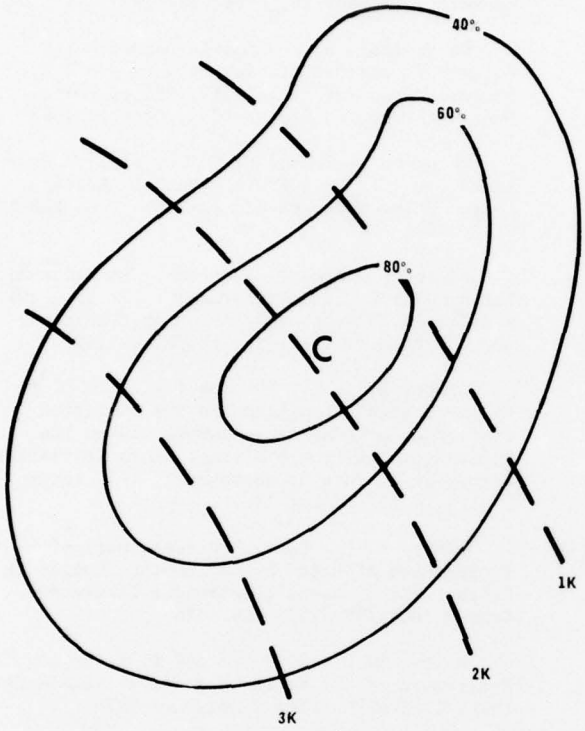

Figure 18. Depiction of Elevated Duct Altitude and Probability of Occurrence.

6.2 Systems Performance Assessment

While the scope of the present effort is to develop a firm basis for predicting refractive structure from a knowledge of synoptic weather features, some consideration must also be given to the modification of systems coverage diagrams for potential operational use. One possibility is to simplify the ray trace depiction by substitution with other related diagrams which may better describe coverage for an operational user. This may include other IREPS products or Fleet Numerical Weather Central (FNWC) displays. Figure 19 shows one type of pictorial display which is under consideration. These and other related aspects will be planned and discussed with NOSC and Fleet personnel at a suitable time prior to evaluation of the technique.

7. PLANNED EVALUATIONS

After additional objective input to the REG working model and charts, (possibly using an expanded 1974 data base) an evaluation will be performed to test the meteorological and operational improvement in skill over the earlier procedure. Such evaluations will include comparison of predicted refractive structure from modified REG charts (and other refractive predictive techniques under development by PMTC) with actual measured profiles determined from soundings at Point Mugu, San Nicolas Island and Hawaiian locations. If possible, these soundings will be corrected for temperature-induced humidity errors to minimize contamination by spurious surface-based ducts described by Helvey (1979).

Operational utility and significance of predictions will be tested by comparing REG systems performance solutions with actual performance conditions obtained from observations from radars from Point Mugu, San Nicolas Island, Barking Sands and other PMTC locations. Systems performance predictions will also be evaluated for specific sensors using the IREPS system developed by NOSC.

8. FUTURE PLANS

In the future, it is hoped to conduct a few aircraft flights across air mass boundaries to directly measure and document synoptic-refractive relationships due to large scale patterns over the North Pacific. With improvement in the REG's ability to predict refractivity conditions based on synoptic structure in the North Pacific and North Atlantic Oceans, attention will be directed to modifying the relationships for other ocean areas. Tests will also be made at several sites to determine the magnitude of temperature-induced humidity errors in radiosonde measurements and their impact on refractive structure. In addition, guidelines will need to be established to modify REG solutions for typical meso-scale or coastal influences that can be expected in the vicinity of major land masses. The incorporation of satellite imagery will also be attempted as an additional synoptic input from which to infer refractivity conditions. Ultimately, a successful REG can not only be used as stored synoptic solutions within IREPS, but could together with the PMTC Equivalent Altitude technique, and the Marine Planetary Boundary Layer model under development at NEPRF, be completely automated and used by FNWC as a valuable addition to other operational products.

9. CONCLUSION

The meteorological basis of a REG approach to predicting refractivity has been established with case studies and objective input from

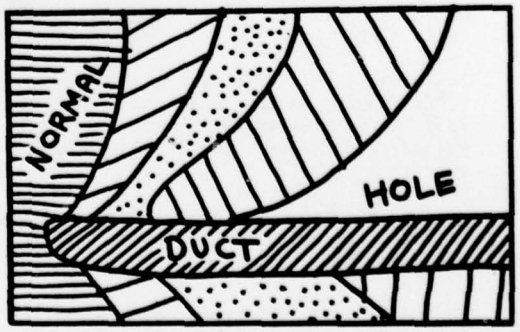

Figure 19. Simplified Depiction of Propagation Conditions Versus Altitude and Range.

synoptic climatologies. From this knowledge, a very general descriptive working model of a synoptic-refractive relationship has been constructed showing subsidence and higher duct probabilities in the southeast quadrant of subtropical anticyclones with lowest and most frequent ducts closest to the anticyclone center. A different pattern has been observed using Bermuda data which shows duct occurrence to be greatest at that station in the northwestern quadrants of anticyclones rather than in the southeastern quadrants as in most of the other stations studied. Stronger anticyclones in general result in a higher duct probability.

At low latitudes as air flows westward on the equatorward side of subtropical anticyclones, subsidence decreases and ducts rise and weaken as the air is heated convectively by warm seas. A region of super-refractive conditions covers the northwest quadrant of highs separating the ducting region from an area of near standard conditions associated with fronts and cyclones where air is well mixed. To the rear of fronts are air masses, partly of continental origin, which are also marked by low level ducting over the equatorward portions and super-refractive conditions in the poleward regions. If the air mass is very recently removed from the land, it is speculated that surface-based ducts may occur near the high center associated with dry continental air aloft.

It is concluded that refractive conditions and trends can be predicted by REG techniques but the quantitative extent to which this can be done depends on REG evaluation and further development, and may be limited in certain regions by local factors which do not conform to general trends. Other factors which affect REG performance include the various limitations of radiosonde data when used for refractive purposes, particularly as they apply to the authenticity of surface-based ducts over the ocean not caused by evaporation.

10. REFERENCES

Arvola, W., "Refractive Index Profiles and Associated Patterns", Bulletin of the American Meteorological Society, Vol. 38, No. 4, April 1957

Bean, B. R. and E. J. Dutton, "Radio Meteorology", National Bureau of Standards Monograph 92, U.S. Government Printing Office, March 1966

Bean, B. R., B. A. Cahoon, C. A. Samson and G. D. Thayer, "A World-Wide Atlas of Atmospheric Radio Refractivity", U.S. Government Printing Office, Washington, D. C., ESSA Monograph 1, 1966

Brookes, A., CDR, THIRD Fleet Environmental Effects Officer, "REG Evaluation", 1978-79 (in preparation)

Carr, T. R., "Certain Geophysical Phenomena Associated With the Subtropical Inversion", Pacific Missile Range, Point Mugu, California, PMR-TM-60-6, April 1960

Clarke, L., "Operational Radar Meteorology", Technical Note No. 27, Fleet Numerical Weather Facility, Monterey, California, March 1967

Cuming, M. J., F. G. Caton, and P. P. Kalinyak, "Development of a Synoptic Climatology of Tropospheric Refractive Conditions for the Eastern Pacific Ocean off the West Coast of the United States" (Task Three: The Assessment of Refractive Structures from Typical Synoptic Patterns) Meteorology International Incorporated, Monterey, California, September 1977

de Violini, R., "Climatic Handbook for Point Mugu and San Nicolas Island", Vol. 1, Surface Data, Pacific Missile Range, Point Mugu, California, PMR-MR-67-2, October 1967

Edinger, J. G. and M. G. Wurtele, "Marine Layer Over Sea Test Range", Pacific Missile Range, Point Mugu, Califonia Tech. Pub. PMR-TP-71-2, 1971

Elliott, R. and J. Thompson, "Relationships Between Tiros Cloud Patterns and Air Mass (Wind and Thermal) Structure", Aerometric Research, Inc., Goleta, California, September 1965

Gjessing, D. T., "On the Influence of the Meteorological Conditions on the Radiation Properties of Long Range Radars and on the Field Strength from a Distant Radio Transmitter", Norwegian Defence Establishment, FFIE Intern Report E-112, August 1967

Glevy, D. F., LCDR, "An Assessment of Radio Propagation Affected by Horizontal Changes in Refractivity", Naval Electronics Laboratory Center, NELC/TN 3153, May 1976

Glevy, D. F., LCDR and AGC L. E. Logue, "An Evaluation of the Refractive Effects Guidebook (REG)", NELC TN 3268, 2 December 1976

Glevy, D. F., LCDR, "An Evaluation of the Refractive Effects Guidebook (REG) in the Southern California Offshore Area from March-December 1977", enclosure (1) to NOSC ltr ser 035/09 of 9 March 1978

Godske, C., L. T. Bergeron, J. Bjerknes and R. C. Bundgaard, "Dynamic Meteorology and Weather Forecasting", American Meteorological Society, Boston, Massachusetts and Carnegie Institution of Washington, Washington, D. C., 1957

Gossard, E., J. H. Richter and D. Atlas, "Internal Waves in the Atmosphere from High Resolution Radar Measurements", Journal of Geophysical Research, Vol. 75, No. 18, 1970

Haurwitz, B. and J. Austin, "Climatology", McGraw-Hill Book Co., Inc., New York, 1944

Hargrave, M. F., AGC, "Refractive Effects Guidebook Evaluation", OA Division, USS ENTERPRISE, CPO memo of 18 June 1976

Helvey, R., "A Preliminary Assessment of Temperature-Induced Radiosonde Humidity Errors and Effects on Apparent Low-Level Refractive Structures", Pacific Missile Test Center, Point Mugu, California, PMTC-TP-79-09, February 1979

Hitney, H. V., "Propagation Modeling in the Evaporation Duct", Naval Electronics Laboratory Center, San Diego, California, NELC/TR 1947, April 1975

Hitney, H. V. and J. H. Richter, "Integrated Refractive Effects Prediction System (IREPS)", Naval Engineers Journal, April 1976

Jehn, K. H., "The Use of Potential Refractive Index in Synoptic-Scale Radio Meteorology", Journal of Meteorology, Vol. 17, June 1960

Lea, D. A., Some Climatological Aspects of the Stratus Season at Point Mugu," Pacific Missile Range, Point Mugu, California, Atmospheric Sciences Tech. Note No. 12, 1968

Namias, J. contributions to "Weather Analysis and Forecasting" by S. Petterssen, McGraw-Hill Book Co., Inc., 1940

Neiburger, M., D. S. Johnson, and Chen-Wu-Chien, "Studies of the Structure of the Atmosphere Over the Eastern North Pacific Ocean in Summer, Part I, The Inversion Over the Eastern North Pacific Ocean, University of California Publications in Meteorology, Vol. 1, No. 1, 1961

Noonkester, V. R. and H. V. Hitney, "Synoptic Prediction of Meteorological Factors Affecting Tropospheric Radio Propagation", Naval Electronics Laboratory Center, San Diego, NELC/TR 1934, October 1974

Ortenburger, L. N., "Radiosonde Data Analysis (May 1966-April 1969)", Final Report. GTE Sylvania, Electronic Systems Group, Western Division, Mt. View, California, 1 July 1973

Purves, C., "Geophysical Aspects of Atmospheric Refraction", Naval Research Laboratory, NRL Report 7725, June 1974

Richter, J., "High Resolution Radar Sounding", Radio Science, Vol. 4, No. 12, December 1969

Rosenthal, J., "Observed Inversion Fluctuations on the Synoptic Scale", presented at 239th National Meeting of the American Meteorological Society with the Pacific Division, American Association for the Advancement of Science, Riverside, California, June 1965

Rosenthal, J., "Point Mugu Forecasters Handbook", chapter 4, Pacific Missile Range, Point Mugu, California, Tech. Pub. PMR-TP-72-1

Rosenthal, J., "Refractive Effects Guidebook (REG)", Pacific Missile Test Center, Point Mugu, California, published by Naval Environmental Prediction Research Facility, Monterey, California, April 1976; promulgated as COMTHIRDFLEET TACMEMO 280-1-76 (cancelled in August 1978)

Rosenthal, J. and D. S. Posson, "Applications of Satellite Imagery to Test and Evaluation: Progress Report", Pacific Missile Test Center, Point Mugu, California, Tech. Pub. TP-78-04, September 1977

Samson, C. A., "Refractivity and Rainfall Data for Radio Systems Engineering", OT Report 76-105 Office of Telecommunications, U.S. Dept. Commerce, September 1976

Serebreny, S. M. and R. H. Blackmer, Jr., "Satellite-Viewed Cloud Cover as a Descriptor of Tropospheric Radio-Radar Propagation Conditions", Stanford Research Institute, Menlo Park, California, February 1974

Sweet, W., "A Summary of EASTPAC Refractive Structure Climatology", Naval Environmental Prediction Research Facility, TR-79-02, January 1979

U.S. Navy Weather Research Facility Meteorological Aspects of Radio-Radar Propagation, Norfolk, Virginia, NWRF-31-0660-035, June 1960

U.S. Naval Weather Service Command, Proceedings of COMTHIRDFLT's Navy Conference on Refractive Effects on Electromagnetic Propagation, prepared by Naval Weather Service Facility, San Diego, 22-24 May 1973

Wexler, H., J. Bjerknes, H. Panofsky, and E. Palmen contributions to the "Compendium of Meteorology" by T. Malone, American Meteorological Society, Boston, Massachusetts and Carnegie Institution of Washington, D. C., 1957

A PRELIMINARY ASSESSMENT OF TEMPERATURE-INDUCED RADIOSONDE HUMIDITY ERRORS AND EFFECTS ON APPARENT LOW-LEVEL REFRACTIVE STRUCTURES

Roger A. Helvey

Pacific Missile Test Center

Point Mugu, California

SUMMARY

Standard radiosonde measurements and procedures are subject to significant temperature-induced humidity errors in the near surface layer. These errors, when experienced at coastal locations and applied to open ocean conditions may result in spurious surface-based ducts which have serious implications for the authenticity and application of world-wide refractive climatologies in naval planning and operations, and in the development and verification of prediction techniques. Efforts are underway at the Pacific Missile Test Center to determine the magnitude of this problem, and to recommend modified measurement procedures and correction factors that can be applied to existing data.

1. PREFACE

Navy requirements exist for a prediction capability which will allow conversion of routine synoptic weather information to an assessment of meso-scale refractive structure and hence an inferred assessment of radar systems coverage. An initial subjective/objective effort based on world-wide radiosonde coverage and characteristic synoptic patterns resulted in the development of an initial Refractive Effects Guidebook (REG)[1]. While the prediction technique met with partial success, subsequent objective evaluations of REG performance indicated significant discrepancies in verification, particularly for surface-based ducts. These discrepancies can be explained by three factors: (1) A still incomplete understanding of synoptic-refractive relationships, (2) an overly detailed attempt to specify predicted profile types, and (3) deficiencies in radiosonde data when used for refractive purposes.

The first two problems are being addressed by PMTC in a continuing effort to develop improved prediction capabilities. The third problem is being simultaneously investigated and is the subject of this report.

2. A DAYTIME BIAS

In evaluating the performance of the REG,[1] doubt has arisen concerning the authenticity of many of the surface-based refractive ducts derived from radiosonde data. Statistical summaries of surface-based duct occurrence compiled from these data indicate an inordinately large diurnal variation. The global distribution of differences in relative frequency of occurrence of surface-based ducts is depicted in Figure 1, for "coastal" stations in a SYLVANIA[2] study covering the period May 1966 through April 1969. Locations where more ducts were noted at 00Z than at 12Z are indicated by squares; the reverse by "X"s; the size of the symbols is proportional to the differences in relative frequencies of occurrence observed between the two standard synoptic observation times, 00Z minus 12Z. It is immediately apparent that with very few exceptions, surface-based ducts were more frequent at 00Z on either side of the dateline between 90°E and 90°W, where 00Z occurs locally during daylight hours. The situation is reversed for the other side of the earth centered on the Greenwich meridian where 12Z is during daylight hours, although the pattern is not as clear-cut. The bias is greatest at low latitudes. Solar elevation angle is implicated as a direct or indirect cause, presumably by its effects on instrumentation or on actual conditions in the atmospheric boundary layer.

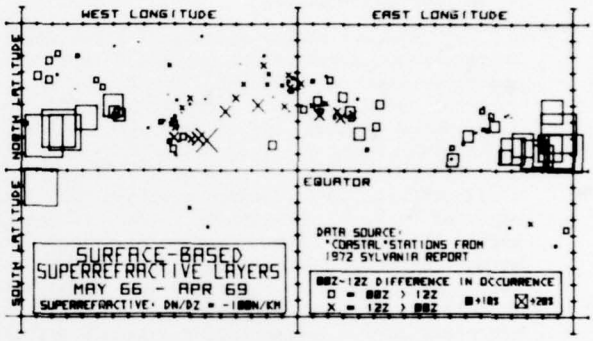

Figure 1. Global distribution of differences in occurrence of surface-based superrefractive layers between synoptic observation times.

Diurnal variations in atmospheric properties over the open ocean should generally be quite small; day-night sea surface temperatures typically vary by no more than a few tenths of a degree C.[3] Unfortunately, however, with the exception of a few ocean station vessels, the soundings regularly available from oceanic areas are actually made over land from islands or near the coasts of continents. Temporarily putting aside the question of whether such soundings are representative of open ocean conditions, the observed diurnal variations found from the Sylvania statistics seem meteorologically implausible.

The very limited extent of some of the island sites where the day-night variation is greatest suggests that changes in refractive layering due to diurnal variations in local winds are not the basic cause, especially since most of these surface-based ducts are very shallow. The establishment of daytime surface superadiabatic layers at land stations would be a common feature at nearly all sites, but except possibly in the case of wet soil,[4] the associated strong vertical mixing should destroy any humidity stratifications which could cause superrefraction, and the rapid decrease of temperature with height would tend to cause subrefraction.

3. SOURCE OF THE BIAS

3.1 Radiosonde Humidity

The apparent marked surplus of these daytime surface-based ducts can be explained as a consequence of instrumental error. Most of the stations shown in Figure 1 can be identified as sites where American radiosondes were employed. It has been known for some years that temperature-induced humidity errors have been responsible for a bias towards lower daytime relative humidities reported by U. S. radiosondes.[5] This is not merely the result of the inverse relationship between relative humidity and temperature, but represents a spurious reduction in daytime values of moisture in terms of dewpoint, mixing ratio, and other derived conservative moisture parameters. The cause is known to be warming of the hygristor (humidity element) due to solar radiation; the resultant increase in saturation vapor pressure of the air in contact with the hygristor leads to an erroneously low indication of relative humidity, which used in conjunction with the cooler temperatures from the sonde thermistor results in lowered calculated values for other moisture parameters. The microwave refractive index will also be too small. Above the surface layer this would have little effect on refractive gradient and duct calculations, since the bias would change slowly with altitude. But near the surface, significant refractive gradient errors could result. This follows from the fact that the surface point of soundings reduced according to standard procedures is obtained by psychrometer, as specified in FMH-3 (Federal Meteorological Handbook of Radiosonde Observations).[6] The value for surface refractivity would therefore presumably be relatively accurate. Because the refractivity at the top of the surface layer is obtained from the radiosonde and hence liable to be erroneously small (dry) during daytime, a negative bias in the apparent change in refractivity upward through the surface layer will result. This in turn leads to a tendency for fictitious superrefractive gradients in this lowest layer of the sounding.

Attempts to assess and correct for spurious daytime dryness in U. S. radiosonde data from the Line Island,[7] ATEX[7] and BOMEX[8] experiments led to introduction of a modified sonde[9] around 1971, designed to minimize hygristor heating by improving ventilation and shielding from sonde and solar heat sources. Although a considerable improvement in the accuracy of the upper-air humidities has been reported,[10, 11] a large diurnal variation in surface layer refractive conditions is still very much in evidence. Surface-based ducts continued in abundance during daytime hours in data obtained as late as 1974, as shown in Table 1.

	Lat	Long	Station	%(00Z)-%(12Z) Differences for Periods: 1966--1969	1974
00Z = DAY	71N	157W	BARROW, ALASKA	-2	+1
12Z = NIGHT	52N	177W	ADAK, ALASKA	0	+2
	30N	140W	SHIP "N"	+16	+6
	28N	177W	MIDWAY ISLAND	+2	+15
	15N	121E	CLARK AFB, PHILLIPINE IS.	+8	+1
	9N	138E	YAP, CAROLINE IS.	+35	(+6)
	7N	158E	PONAPE, E. CAROLINE IS.	+27	+33
	14S	171W	PAGO PAGO, AMERICAN SAMOA	+51	+21
00Z = NIGHT	77N	69W	THULE AFB, GREENLAND	0	0
12Z = DAY	64N	23W	KEFLAVIC, ICELAND	-1	-12
	39N	27W	TERCEIRA, AZORES (LAJES FIELD)	-7	-12
	38N	70W	SHIP "H"	*	+2
	32N	65W	ST. GEORGE, BERMUDA (USNAS)	*	-2
	"	"	" " " (KINDLEY AFB)	-1	*
	13N	60W	BARBADOS, W. INDIES (SEAWELL APT)	-24	-2
	9N	80W	BALBOA, CANAL ZONE (ALBROOK AFB)	*	+3
	"	"	" " " (HOWARD AFB)	-3	*
	7S	7W	DIEGO GARCIA (NAVCOMMSTA)	*	(-36)

* ASTERIX = NO DATA ( ) PARENTHESES = LESS THAN 40 SOUNDINGS AT ONE OR BOTH TIMES

1966-69 DATA FROM SYLVANIA REPORT (JULY 1972)

Table 1. Differences in percent frequency of occurrence of surface-based ducts reported at 00Z and 12Z (00Z minus 12Z), for periods May 1966 through April 1969, and Jan/Apr/Jul/Oct 1974.

The apparent lack of any overall decrease in daytime surface duct bias is understandable if we take into account the special nature of the atmosphere in the surface boundary layer, the manner in which the data is obtained, and the effect of hygristor thermal lag on indicated humidities. For temperatures typical of the lower atmosphere over temperate and tropical regions the humidity response of the carbon hygristor type of humidity element in use for some years is quite good, with a lag coefficient less than one second. The thermal response of the carbon hygristor is much worse, however, with a lag coefficient near sea level around 15 seconds in the improved sonde introduced around 1971[12, 13], and as much as a half-minute in the older sonde package[5, 7] formerly used by the National Weather Service. The lithium chloride element in use some years ago was likewise subject to considerable thermal lag. At times when the sonde is ascending through a region with negative temperature lapse rate, the hygristor temperature will be too warm and hence indicated humidity and refractivity will be too low. For the current sonde and normal ascent rates the theoretical hygristor temperature excess due to lag (15-second time constant) can be estimated at about 0.5C for an ambient lapse rate of -2C/1000 feet, with a corresponding relative humidity deficit around 3%, and refractivity deficit of roughly 3 N-units. In the free atmosphere the refractivity gradient structure will be affected very little, except during passage through inversions (when the biases will be reversed with the hygristor tending to be cooler than the environment). But the situation is entirely different near the earth's surface. There, very strong negative temperature lapse rates in the daytime superadiabatic layer and internal boundary layer near

coastlines during onshore flow will produce considerable reductions in apparent refractivity with height.

The influence of temperature lapse rate on refractivity is illustrated in Figure 2a, where refractivity gradient versus temperature gradient is plotted for the first layer of soundings for Ponape, 1974 data. In general, the greater the decrease of temperature, the stronger the refractive layer was found to be. This temperature-induced problem is aggravated by still another problem--the increasing sensitivity of the computed refractive gradients to noise in the data as layer thickness becomes smaller. As apparent in Figure 2b, even without noticeable correlation between layer thickness and refractive gradient, the larger scatter in the data for the thinner layers results in a greater number of extreme gradients - both superrefractive and subrefractive. Standard procedures dictate reduction of sonde data for mandatory pressure levels.[6] At most coastal and island stations the 1000mb level is as a rule within a few dozen feet of the surface, thus guaranteeing on reduced soundings a predominantly thin surface layer, with no direct physical basis for its reported depth.

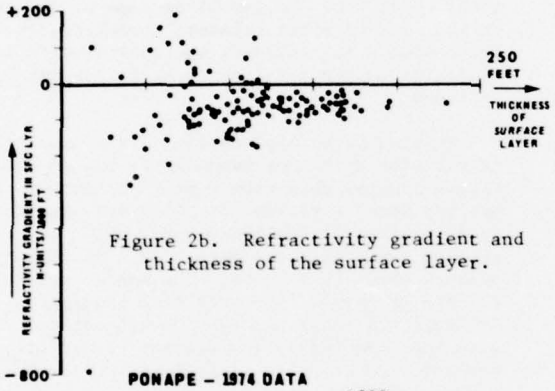

Figure 2b. Refractivity gradient and thickness of the surface layer.

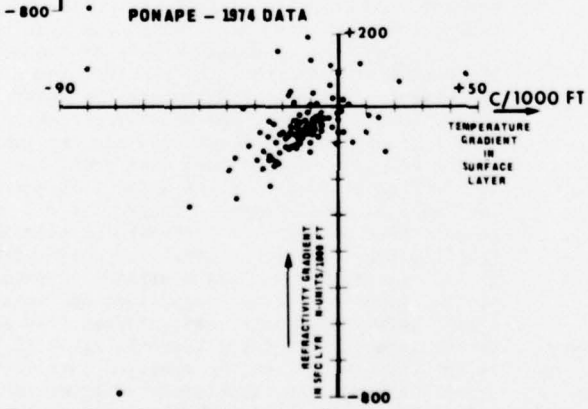

Figure 2a. Refractivity gradient and temperature gradient in the surface layer.

3.2 Sonde Exposure Before Release

Exposure of the sonde prior to release can also contribute to a bias towards daytime ducts. Although redesign of the sonde has minimized radiative contributions to the hygristor temperature excess aloft,[11] the hygristor remains vulnerable to heating by solar radiation during pre-release preparations because of inadequate ventilation. Cases are reported where a sonde has been allowed prior to release to lie outside on a hot surface such as the deck of a ship.[5] Even when reasonable care is exercised to avoid direct exposure to sunlight and relatively warm areas such as asphalt, substantial daytime warming of the sonde and hygristor can be expected before release under conditions of clear skies and light winds. Although according to FMH-3 the surface point would not be taken from the sonde in any event, a substantial period of time is required after release for recovery of the radiosonde from such overheating, due to the thermal lag of the hygristor and walls of the humidity duct. The contribution of this effect to the total humidity error is especially important when the first point from the sonde is selected within a few hundred feet of the surface, as when surface pressure is only slightly greater than 1000mb, or when a significant level is selected at the top of a shallow superadiabatic layer.

4. MAGNITUDE OF INITIAL ERROR

An estimate of the temperature of the hygristor element can be obtained for the moment of release if the radiosonde recorder chart and the surface psychrometer data are available. Regardless of temperature variations, and in the absence of wetting of the sonde and humidity element by precipitation, water vapor pressure should be essentially the same outside the sonde and in the air around the hygristor[12]. Thus the temperature of the latter is just that which together with the observed radiosonde initial ordinate value yields the same vapor pressure as that corresponding to the psychrometer data.

An example of a recorder chart for a sounding with substantial initial hygristor temperature excess is shown in Figure 3. Humidity increases to the left, temperature to the right, and time upwards. The sonde was released at Point Mugu at 1024 PST, 30 July 1973, and had been modified to permit greater vertical resolution by increasing the switching rate between temperature and humidity. Skies were overcast with low stratus (which was beginning to clear, however), and surface winds were two knots from the southwest (onshore).

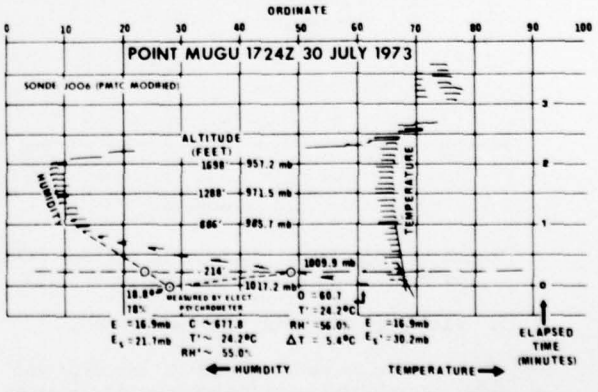

Figure 3. Radiosonde recorder chart for Point Mugu Sounding, 1724Z (1024 PST) 30 July 1973.

The sonde was one of the Weather Service types (J006) which had been modified at PMTC to reduce solar heating effects by covering the top of the hygristor duct with aluminum foil, and blackening the interior of the duct.

The surface humidity ordinate corresponding to the relative humidity reading of 78% obtained from electric psychrometer is shown as a circled point, far to the left and at a much higher humidity than that corresponding to the initial location of the sonde humidity trace. The latter indicated a relative humidity of 56%, using the psychrometer temperature of 18.8C. The discrepancy between these two humidities corresponds to a hygristor temperature excess in this case of about 5.5C. The sonde data indicate the top of a superadiabatic layer at 214 feet above the surface. (This level is indicated in Figure 3 by the long horizontal dashed line at about 1/4 minute into the sounding.) Use of the actual humidity contact value for this level together with the surface psychrometer data yields a surface-based superrefractive layer with refractivity gradient of -119 N-units/1000 feet. If the humidity ordinate for the top of the superadiabatic layer is obtained by interpolation between the surface psychrometer readings and higher sonde points, however, a refractivity gradient of only -35 N-units per 1000 feet is calculated. In this example use of the actual contact value for humidity would clearly have resulted in a spurious surface-base duct.

Hygristor initial temperature excesses calculated by the above method are shown in Figure 4 for Point Mugu soundings from September 1969, in which AMQ-9 military sondes were employed. This period was well before the introduction of extra radiation shielding. These values have been plotted against time of day, and clearly are separated into nighttime and daytime regimes. During the day the average temperature excess was around 4C, and reached as high as 7 to 8C on several occasions.

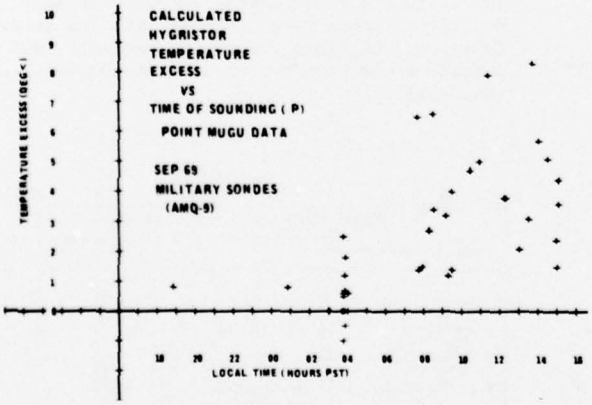

Figure 4. Hygristor temperature excess (calculated) for Point Mugu soundings, September 1969.

5. BIAS DUE TO INITIAL AND LAG ERRORS

In order to estimate actual humidity and refractivity distribution with altitude from radiosondes subject to initial and lag temperature-induced humidity errors, hygristor temperature must be known. First of all, it is required for reduction of the raw sonde hygristor data because of its effect on the relationship between hygristor resistance and relative humidity, but this effect is minor for the temperature range of concern here. Hygristor temperature is of much more importance, however, in correcting the apparent relative humidity for the difference in saturation vapor pressure between that in the free atmosphere and that in the air in immediate contact with the hygristor, when the temperature of the latter differs from the free air temperature as measured by the thermistor outside the sonde. Hygristor temperature can be measured directly by a thermistor placed on the hygristor, but this requires provision for transmitting the additional temperature to the surface. Another approach involves calculating theoretical hygristor temperature response to measured free air temperatures, considering hygristor temperature error at the moment of release, and the effective hygristor thermal time constant (due to the combined thermal lag characteristics of the hygristor element and the surrounding duct, corresponding to a ventilation rate appropriate for the type sonde used and ascent rate experienced). Although heating of the hygristor due to solar radiation is the source of its initial temperature bias, this is much diminished aloft (in the improved sondes about +0.6C near sea level) because of the increase in ventilation after release; therefore, in the discussion which follows, the contribution of radiation to the total error aloft has not been included.

Results of an application of the approach of calculating hygristor temperature are depicted in Figure 5 using data from a pair of improved J005 Weather Service radiosondes released simultaneously at PMTC at 1705Z (0905PST) 4 May 1977; at time of release sky conditions were 3/10 cumulus, with onshore winds of 6 knots. The sondes were altered at PMTC to permit finer vertical resolution. Although the sonde packages were identical, they were each handled in a different manner prior to release. An accurate estimate of free air temperatures was needed for computing hygristor temperatures. To minimize effects of radiation on temperatures indicated by the thermistor at the moment of release and through the lower part of the sounding, one sonde was force-ventilated in a thermoscreen for about five minutes just before release. Temperature data from this sonde is shown as profile 1 in the upper left section of Figure 5. This temperature profile was used to calculate a number of hypothetical examples of possible hygristor temperature variation with altitude, assuming various hygristor temperatures at the moment of release (expressed as "initial error" between hygristor and measured free air temperature), a hygristor thermal lag of 15 seconds, and ascent at the observed rate (858 ft/min) through the temperature environment indicated by profile 1. This value for thermal lag applies to the carbon hygristor in the J005 improved sonde package, as mentioned earlier; computed profiles 2, 3, and 4 differ solely as a result of different assumed initial hygristor temperature biases. In any event the effect of thermal lag in this situation with negative temperature lapse rates as shown by profile 1 would cause hygristor temperatures warmer than the free air, with consequences which are discussed below.

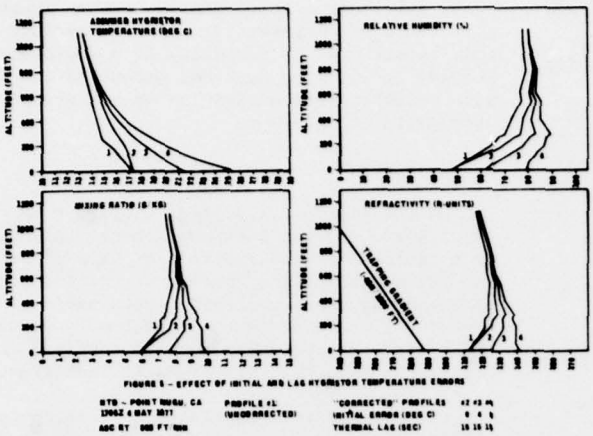

Figure 5. Calculated effects of initial and lag hygristor temperature errors.

The other radiosonde was used to obtain raw hygristor data under conditions which would enhance hygristor vulnerability to overheating, and which are suspected to occur at times with routine soundings. This sonde was allowed to sit in the sun for the same five minute period of time prior to release, on top of a wooden box about one and one-half feet above an asphalt pavement. A substantial bias of hygristor temperature above that in the free atmosphere was observed to develop by the time of release which may be characteristic of routine soundings where precautions against pre-flight heating may not be taken; as inferred from the radiosonde recorder chart by the method outlined previously (see section 4) it amounted to about +4C. This is the assumed initial error which resulted in generation of temperature profile 3; consequently that profile presumably comes closest to representing actual hygristor temperature behavior with altitude.

The sensitivity of some humidity-related parameters to hygristor temperature errors is demonstrated in the other boxed sections of Figure 5, by profiles of relative humidity, mixing ratio, and refractivity, numbered in accordance with the particular hygristor temperature profile assumed. The raw hygristor data was first reduced using each of the temperature profiles in turn to obtain four sets of apparent relative humidities. In the case of profiles 2, 3, and 4 these humidities were then tentatively corrected for differences between the assumed hygristor temperatures represented by the correspondingly numbered temperature profiles, and the free air temperatures represented by temperature profile 1. (Although the temperature and humidity information came from two separate sondes, it is believed that they sampled essentially the same volume of air due to their simultaneous release in close proximity.) Profiles of mixing ratio and refractivity were computed from these corrected relative humidities and free air temperatures. In the case of profile 1 for the humidity parameters, no corrections were applicable, the hygristor temperature being assumed identical to the free air temperature. Of the relative humidity, mixing ratio, and refractivity profiles shown, profile 3 is probably most representative of actual atmospheric conditions for this sounding, as it was determined by corrections based on the most appropriate hygristor temperature as pointed out above. On the other hand, except for the surface point (and the more detailed resolution of these soundings), profile 1 for the humidity-related parameters illustrates the kind of results to be expected under standard reduction procedures, which in effect assume zero hygristor thermal lag and initial bias by ignoring the effect of these sources of error on the humidity data after release. Under such procedures, the use of a psychrometer would have resulted in surface values close to the surface point of profile 1 for temperature, and profile 3 for the humidity-related parameters if the initial hygristor temperature bias was in fact about +4C as has been inferred. While in terms of gradients there is little difference between profiles 1 and 3, the substitution of psychrometer data for the surface point together with the use of uncorrected radiosonde data aloft necessarily introduces a negative bias in the daytime vertical gradients of humidity and refractivity in the surface layer. The first significant (or mandatory) level above the surface defines the top of the surface layer, and in this sounding would probably be selected as the top of the superadiabatic layer evident at about 250 feet altitude in temperature profile 1. But in practice the apparent altitude of a significant level is to some extent fortuitous since the radiosonde does not transmit each parameter continuously; also, resolution is ordinarily somewhat poorer than in our special example here. While conditions in the surface layer in this case actually appear to have been subrefractive as indicated by refractivity profile 3, selection of the top of the surface layer at any altitude lower than about 200 feet and reduction under standard procedures would have resulted in a fictitous surface-based trapping layer.

6. TRENDS IN THE BIAS AT PMTC

Major changes in statistics of humidity and refractive gradients over the years have been noted in Point Mugu radiosonde data which support the preceding indications of contamination by temperature-induced humidity errors. Alterations in radiosonde instrumentation and data reduction procedures at Point Mugu from 1967 through 1976 are noted in Figure 6, along with a plot of water vapor pressure variation with altitude through the first layer of selected soundings from that period, versus date. In order to provide a more homogeneous sample, the soundings represented were cases where the temperature decreased between 3 to 4C from the surface to the top of the surface layer, and for which the top of that layer was between 100 to 400 feet above the surface.

A substantial decline in magnitude of the reported vapor pressure differences over the years is obvious, with the greatest change occurring between about 1971 and 1975, probably reflecting adoption of two major changes: modification of sondes starting July 1971 to minimize radiational heating, and utilization of a fan-ventilated thermoscreen for pre-release conditioning of the sondes starting in November 1974. Changes in refractive gradient statistics for the surface layer are also evident, as shown

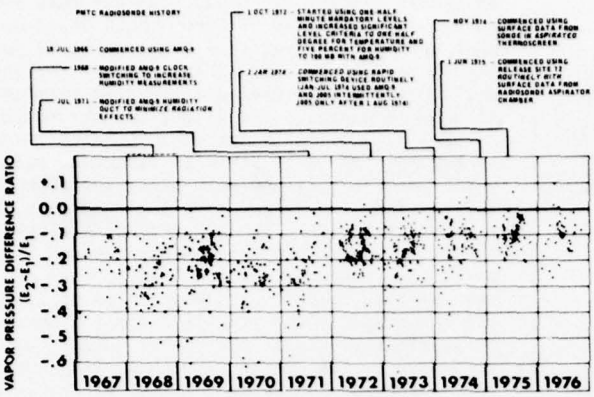

Figure 6. History of radiosonde instrumentation and reduction procedures at Point Mugu, and variation of vapor pressure through the surface layer, 1967-1976.

in Figure 7. A remarkable decline in the reported frequency of occurrence of the more extreme refractive gradients took place over this period. In 1968, almost 40% of all soundings indicated surface-based trapping, dropping to less than 10% in 1975 and 1976. The jump from 1967 to 1968 is believed due to an increase in emphasis at that time in reporting smaller features in the sounding, and in a switching modification to increase humidity measurements.

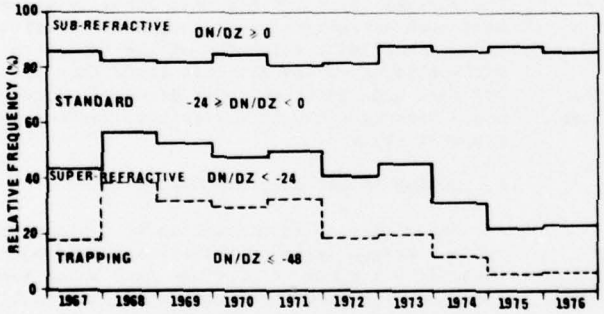

Figure 7. Relative frequencies by year of occurrence of specified refractive gradients within the surface layer at Point Mugu.

7. OTHER CONSIDERATIONS IN ASSESSING OCEANIC REFRACTIVE STRUCTURE

A number of other considerations are involved in assessment of the authenticity and behavior of low-level oceanic refractive structure based on radiosonde data. Advective and subsidence processes will bring about strong surface-based refractive gradients of substantial depth in certain regions and weather regimes. But structures due to local land/sea effects which appear in island and coastal radiosonde data and which may be completely real, nevertheless may not be representative of open ocean conditions. Although soundings from ships on the open ocean should be free of such influences, another source of misinformation may arise in the presence of an evaporative duct. This type of duct is characterized by a fairly shallow surface-based superrefractive region due to the frequently strong, evaporation-caused decrease in humidity with altitude in the atmosphere immediately above the ocean surface. A sufficiently intense evaporative duct could be mistaken for a deeper surface-based duct because of the inability of a radiosonde to resolve the limited vertical extent of the former, with possibly serious effects on assessment of propagation conditions.

8. CONCLUSION

On the basis of the large disparity in day/night surface-based duct occurrences calculated from radiosonde data reported at many stations, and the major decline in apparent duct occurrences accompanying improvements in instrumentation and procedures at Point Mugu, it is concluded that these ducts are probably much less prevalent over the oceans than has been formerly indicated.

This is due to a combination of reduction and handling procedures, and temperature-induced humidity errors in U. S. and other radiosondes susceptible to radiational heating and thermal lag effects on humidity measurements. The problem has serious implications for the authenticity and application of refractive climatologies in naval planning and prediction techniques.

Although it seems unlikely that soundings taken in the past can be satisfactorily corrected on an individual basis due to difficulty in reconstructing all the relevant procedural, instrumental, and meteorological factors in effect at the time, the climatological contamination may be substantially reduced by application of results of comparative studies which are planned at PMTC.

Such studies will involve comparing standard radiosonde soundings with near-simultaneous soundings employing modified sondes or procedures such as are used operationally or planned at PMTC. The modifications include the use of ventilated shelters prior to balloon release to minimize errors due to lag and radiation. Comparative soundings are planned for Point Mugu, California; San Nicolas Island, off the California coast; Barking Sands, Hawaii and possibly other locations. It is hoped that from these studies, correction factors will be developed which will improve the climatological data presently available on low-level atmospheric refractive structure over the oceans, and lead to a firmer basis on which to develop techniques of predicting refractive structure from air mass and weather considerations. In addition, it is anticipated that procedures will be recommended which will result in improved accuracy for future measurements.

9. REFERENCES

(1) Brousaides, F. J., An Assessment of the Carbon Humidity Element in Radiosonde Systems. AFCRL-TR-73-0423, Instrumentation Papers, No. 197, 18 July 1973.

(2) Brousaides, F. J. and J. F. Morrissey. Improved Humidity Measurements with a Redesigned Radiosonde Humidity Duct, Bull. Amer. Meteor. Soc., V. 52, No. 9, September 1971 (pp. 870-875).

(3) Brousaides, F. J. and J. F. Morrissey. Residual Temperature-Induced Humidity Errors in the National Weather Service Radiosonde, Final Report, Air Force Cambridge Research Laboratories, Hanscom AFB, Cambridge, MA, 28 February 1974.

(4) Holland, J. Z. Preliminary Report on the BOMEX Sea-Air Interaction Program, Bull. Amer. Meteor. Soc., V. 51, No. 9, September 1970 (pp. 815-816).

(5) Kerr, D. E. Propagation of Short Radio Waves, Radiation Laboratory Series, MIT, McGraw-Hill Book Co., 1951 (p. 255).

(6) Ortenburger, L. N. Radiosonde Data Analysis (May 1966-April 1969), Final Report. GTE Sylvania, Electronic Systems Group, Western Division, Mt. View, California 94040, Contract: DAAB03-72-C-0027, 1 July 1973.

(7) Ostopoff, F., W. W. Shinners, and E. Augstein. Some Tests on the Radiosonde Humidity Error, NOAA Technical Report ERL 194-AOML, December 1970.

(8) Radiosonde Observations. Federal Meteorological Handbook No. 3 (FMH-3), U. S. Dept of Commerce.

(9) Reihl, H., and A. K. Belts. Humidity Observation with the 1972 U. S. Radiosonde Instrument. Bull. Amer. Meteor. Soc., V. 53, No. 9, September 1972 (pp. 887-888).

(10) Rosenthal, J. Refractive Effects Guidebook (REG), (published by NEPRF in April 1976, promulgated as THIRD Fleet TACMEMO 280-1-76 in December 1976, cancelled in July 1978 due to ongoing effort on proposed revision).

(11) Shinners, W. W., G. E. Puttand, and P. B. Connors. Test of Modified Radiosonde Hygristor Duct. NOAA Tech. Report IRL AOML-15, 1971.

(12) Sverdrup, H. V., M. W. Johnson, and R. H. Fleming. The Oceans, Prentice-Hall, 1942 (pp. 133-134).

(13) Tewles, S. A Spurious Diurnal Variation in Radiosonde Humidity Records, Bull. Amer. Meteor. Soc., V. 51, No. 9, September 1970 (p. 836).

WORLD-WIDE STATISTICS OF TROPOSPHERIC DUCTING CHARACTERISTICS

Leigh N. Ortenburger

GTE Sylvania Inc.

P.O. Box 205

Mountain View, California 94042

ABSTRACT

Utilizing a data base of all world-wide radiosonde soundings during a five year period, numerous statistics of tropospheric ducts and super-refracting layers (SRLRs) have been compiled by extensive computer processing. The basic pressure, temperature, and dewpoint profile from each of the 2,300,000 soundings has been expanded and converted into refractive index profile with 2 mb increments. A search of each expanded profile was conducted to locate occurrence of gradients less than -157 N units/km (in the case of ducts) or less than -100 N units/km (in the case of SRLRs). Monthly estimates of the probability of occurrence of ducts and SRLRs were then computed for each of 924 radiosonde stations. Characteristics such as height, thickness, intensity, and minimum trapping frequency have been computed. Extensive results are displayed in tabular form and as CALCOMP plots for each individual station; these portray the statistical distributions of ducting parameters as well as seasonal variations. Regional maps showing 22 parameters have been prepared to show geographical relationships. The reportage from this project should be useful for applications in which expected ducting characteristics are required at an arbitrary location anywhere in the world.

1. INTRODUCTION

For the past several years GTE Sylvania has been conducting a large-scale analysis of radiosonde data for the Department of Defense. The purpose of our three projects has been the generation of statistics on the characteristics of tropospheric ducting through the computer analysis of worldwide radiosonde sounding reports over a five year period. This massive effort was based on radiosonde data, not because the superiority of refractometer measurements was not recognized, but because the analysis was desired on a global basis so that the entire synoptic climatology of tropospheric ducting could be depicted. Radiosonde soundings form the only available world-wide data base for such an investigation.

A significant portion of the effort has been devoted to the condensation and formatting of the output in a variety of ways, including listings, CALCOMP plots, and world or regional maps. In the following sections brief descriptions will be given of the input data, data acceptance criteria, refractivity profile expansion, search for ducts and super-refracting layers (SRLRs), and computation of ducting parameters. Descriptions will also be provided of the various types of output which were produced.

2. COMPUTATIONAL PROCEDURES

2.1 Input Data

The basic radiosonde sounding data were obtained from two time periods: May 1966 through April 1969, and January 1973 through December 1974. A total of about 300 magnetic tapes containing these data were provided by the USAF Environmental Technical Applications Center (ETAC). The initial processing program for all these tapes was run on the CDC3200 computer. This program first unpacked the records, tested the data for acceptability, computed profiles of refractive index, searched for ducts and SRLRs, and computed the parameters of the ducts and SRLRs which were present. By carrying out all these processes in the initial program it was possible to read each input tape only once.

2.2 Acceptability Testing

Each sounding was subjected to several tests before it was accepted for further processing. Initial syntactical tests were imposed on record length and invalid characters within each record. Pressure, temperature, and dewpoint values were tested to determine whether they were within limits. Soundings were then rejected if a) fewer than three accepted data levels were found between the surface and the 100 mb level; b) pressure values not monotonically decreasing; c) no height or station elevation data were contained in the record; or d) the data did not contain at least one significant level other than the surface level.

2.3 Primary Output Tapes

Two types of output tapes were produced by the initial computer program. The first provided one record for each accepted sounding, and contained indicators of data quality and duct (SRLR) presence, as well as other significant quantities such as surface pressure, temperature, and dewpoint; wind speed and direction; and surface refractivity gradients. The second tape provided one record for each duct or SRLR found during the search process, containing parameters such as heights, M values, minimum trapping frequency and average gradient. After completion of these computations, the output tapes were fed into a SORT/MERGE program which sorted all the records first by WMO station number,

and second by date-time group. The resulting sorted tapes contain a total of 2,262,447 records of accepted soundings on 14 reels, and 606,266 records of ducts and SRLRs on two reels.

2.4 Profile Expansion

Each accepted sounding profile was expanded to provide temperature and dewpoint values for every 2 mb level from the lowest to the highest pressure value in the input data; linear interpolation in temperature and dewpoint, relative to pressure, was used for this expansion. The standard hypsometric formula was applied to input height data contained in the record to determine heights associated with each 2 mb level. Next the refractivity, N, and modified refractivity, M, were computed for each 2 mb level, using the standard expressions for refractivity in terms of pressure, temperature, and saturation water vapor pressure at the dewpoint. When surface data were provided in the radiosonde sounding record, the average refractivity gradients were calculated for the first 50, 100, 500, and 1000 meters, in units of N units per kilometer.

2.5 Duct (SRLR) Search

A search upward through the modified refractivity profile was performed to determine whether one or more ducts and/or SRLRs were present. In accordance with standard practice a duct is defined as the height interval within which the refractivity gradient is less than -157 N units/km, or within which the modified refractivity gradient is negative. An SRLR is defined as the height interval within which the refractivity gradient is less than -100 N units/km, or the modified refractivity gradient is less than 57 M units/km.

Three types of ducts (SRLRs) were defined, on the basis of the location of the inflection points of the M profile; it is these inflection points which define the duct boundary in height. If the M gradient is negative at the earth surface, the layer is defined to be a surface duct. If the first inflection point is not on the surface, and if the abscissa (M value) of the second inflection point is less than the M value at the surface, the layer is defined to be an elevated-surface duct. If the abscissa (M value) of the second inflection point is greater than the M value at the surface, it is an elevated duct. Similar definitions hold for superrefracting layers (SRLRs). While a given sounding or profile may contain at most one surface duct (SRLR), it may contain several elevated-surface and/or elevated ducts (SRLRs). At some radiosonde stations the occurrence of multiple ducts (SRLRs) is not rare.

2.6 Parameter Calculation

The output record for each duct (SRLR) contains the heights and M values at the layer bottom, optimum coupling height, and top. For an elevated or elevated-surface duct or SRLR the height at which the M gradient first becomes negative is called the optimum coupling height; for surface layers this optimum coupling height is undefined. The average gradient in N units/km from the first inflection point to the duct (SRLR) top is calculated and also given in the record. Finally the minimum trapping frequency is computed, using a numerical approximation to the standard phase integrals for surface and elevated ducts.

3. STATISTICAL OUTPUT

All of the volumes of results from the Radiosonde Data Analysis projects were produced by the analytical processing of these two sets of primary output tapes, one set containing one record per accepted sounding, and the other set containing one record for each duct or SRLR. The first of two analysis programs using these tapes as input produced two lengthy output records for each radiosonde station, containing fundamental duct (or SRLR) occurrence and surface parameter statistics, given on a monthly basis so that seasonal variations could be observed. Some of these basic station statistics such as the percent of station soundings which were accepted, were generated so that the reliability of the station might be evaluated.

The second analysis program produced five output records for each radiosonde station. The first two records contain overall histograms of parameters of surface and elevated ducts (SRLRs), as well as monthly medians with associated confidence intervals for additional parameters. Histogram parameters include top, optimum coupling, and bottom height for elevated ducts (SRLRs); thickness, intensity, average N-gradient, and minimum trapping frequency for both elevated and surface ducts (SRLRs). The last three records contain monthly histograms of elevated duct (or SRLR) thickness, optimum coupling height, and coverage height. The (pseudo) histogram of coverage height provides the probability that each specified height interval will be contained within a duct (SRLR).

3.1 Listings

This massive quantity of statistical information was listed on a total of 10 pages per station for each of the 924 accepted radiosonde stations. A station reporting fewer than 100 soundings over the five year period was deleted from this and subsequent processing. These 9240 pages have been formed into a set of 26 volumes which contain the most extensive detail of the various forms of the published reports.

3.2 CALCOMP Plots

To display a portion of these results graphically a set of 10 CALCOMP plots for each station was generated, showing monthly percent occurrence and various parameter distributions associated with the ducts (SRLRs). One plot displayed results for elevated ducts, one for surface ducts, one for elevated SRLRs and one for surface SRLRs. Three of the remaining plots provided monthly histograms of elevated duct thickness, optimum coupling height, and coverage height. The remaining three plots provided the same histograms for elevated SRLRs.

3.3 Condensed, Sorted Listings

The results for all 924 stations were condensed into two volumes containing two kinds of listings in eight formats. The first type provides one line per station with statistics for both reporting periods (00Z and 12Z) pooled. The second type provides separate lines for the two reporting periods so that diurnal differences can be observed. The eight distinct formats list different categories of data so that the reader may select that which is the most useful to his purposes. Separate formats are provided for input data statistics, monthly per-

cent occurrence, duct or SRLR parameters, and elevated or surface ducts or SRLRs. These listings have been sorted in several ways to facilitate the study of ducting climatology.

3.4 Regional Parameter Plots

The final and most elaborate presentation of the results is in a single volume consisting of 260 pages with 17 plots on each page. For each of 20 geographical regions there are 13 pages; these 13 pages display a total of 22 distinct parameters. The purpose of this volume is to permit a geographical understanding of the variations of these paremeters and to permit an estimate of the value of one of these parameters at points where there is no radiosonde station.

The world was divided into 20 regions which were defined by the number of reliable radiosonde stations each contained as well as some degree of geographical unity. Each of the 13 pages given for a region contains a central map showing the region, and the location of each of the 17 stations selected as the best representatives for the region. Around the perimeter of the map are 17 individual plots, one for each selected station and connected to the station by a line with an arrow. In general two parameters are displayed on each plot, one with a solid line and the second with a dashed line. On each plot are given the station number and elevation, and the sample size of the displayed data.

The following parameters for each of the 17 stations are displayed in these thirteen pages:

1) Monthly percent occurrence of elevated ducts
2) Monthly percent occurrence of elevated SRLRs
3) Monthly median optimum coupling height, with confidence intervals, for elevated ducts
4) Monthly median minimum trapping frequency, and surface-to-duct bottom M gradient
5) Distribution of coverage height for elevated ducts
6) Distribution of coverage height for elevated SRLRs
7) Distribution of optimum coupling height for elevated ducts
8) Distribution of optimum coupling height for elevated SRLRs
9) Distribution of thickness for elevated ducts
10) Distribution of thickness for elevated SRLRs
11) Distribution of minimum trapping frequency for elevated ducts
12) Distribution of intensity of elevated ducts
13) Distribution of intensity of elevated SRLRs
14) Monthly percent occurrence for surface ducts
15) Monthly percent occurrence for surface ducts
16) Monthly median surface refractivity (N_s)
17) Monthly median dN/dH over the first 1000 meters
18) Distribution of thickness for surface ducts
19) Distribution of thickness for surface SRLRs
20) Distribution of minimum trapping frequency for surface ducts
21) Distribution of intensity of surface ducts
22) Distribution of intensity of surface SRLRs

4. SUMMARY

The completion of this very large-scale data analysis effort by GTE Sylvania has produced a reliable set of world-wide statistics on ducting characteristics as extractable from standard radiosonde soundings. Radiosonde data, however, have known limitations. Because of time-lags and other inaccuracies in the humidity sensing element in standard instruments, radiosonde data tend to provide an underestimate of ducting occurrence percentages. A second difficulty is the difference between instruments used in different countries. Nevertheless, the results of this effort show the long-term statistical regularities of tropospheric ducting, and as such they will be useful in those common situations in which radiowave propagation estimates are required but there are not available any actual measurements, either from refractometers or even radiosonde soundings. Our results contain the first world-wide presentation for some of the ducting parameters and so provide the opportunity for new insight into the climatology of tropospheric ducting.